

WESTFÄLISCHE
WILHELMS-UNIVERSITÄT
MÜNSTER

› Spectroscopy of the hyperfine transition in lithium-like bismuth at the ESR at GSI and an APD-based single-photon detector for laser spectroscopy on highly charged ions

Raphael Jöhren, Dissertation 2013

Experimentelle Physik

Dissertationsthema

Spectroscopy of the hyperfine transition in lithium-like bismuth at the ESR at GSI and an APD-based single-photon detector for laser spectroscopy on highly charged ions

Inaugural-Dissertation
zur Erlangung des Doktorgrades
der Naturwissenschaften im Fachbereich Physik
der Mathematisch-Naturwissenschaftlichen Fakultät
der Westfälischen Wilhelms-Universität

vorgelegt von
Raphael Jöhren
aus Lippstadt

- 2013 -

Dekan:

Prof. Dr. M. Donath

Erster Gutachter:

Prof. Dr. Chr. Weinheimer

Zweiter Gutachter:

Prof. Dr. A. Khoukaz

Tag der mündlichen Prüfung: 24.06.2013

Tag der Promotion: 24.06.2013

TO ELIAS

Abstract

Quantum Electro Dynamics (QED) is known to be the most accurate physics theory and has been verified in a large number of precision experiments in the laboratory. To extend tests of QED predictions to strong-field QED, especially in the magnetic sector, laser spectroscopy experiments on heavy highly charged ions are performed at GSI. In these ions the electrons are exposed to electric and magnetic fields, whose strengths exceed the available artificially generated field strengths of pulsed lasers or superconducting magnets by orders of magnitude.

Within this work, dedicated detector systems are presented, that were developed to allow for efficient fluorescence light detection in laser spectroscopy experiments that aim at precision tests of QED in highly charged ions. This is an essential contribution to the success of experiments aiming for the determination of hyperfine structure transitions in the observed ions. With the transition wavelength of the hyperfine states known for both the hydrogen-like ($1s$ splitting) and the lithium-like ($2s$ splitting) ion of the same isotope, the major uncertainty in the determination of QED contributions to the transition energy, the Bohr-Weiskopf effect, can be eliminated. The best isotope candidate to achieve this is ^{209}Bi , where both transitions of interest can be accessed by means of laser spectroscopy.

While the $1s$ transition in hydrogen-like $^{209}\text{Bi}^{82+}$ has been determined previously, the $2s$ hyperfine transition in lithium-like $^{209}\text{Bi}^{80+}$ was observed for the first time in the LIBELLE experiment. There bismuth ions were orbiting the Experimental Storage Ring (ESR) and were excited by a tunable laser system. A novel detector system applying a movable parabolic mirror with a slit was used to efficiently detect fluorescence photons emitted under small polar angles. The transition wavelength of hydrogen-like bismuth was also measured again. In the first part of this work, the data of the LIBELLE beamtime are analyzed and the transition wavelengths for the two charge states are determined.

To improve the accuracy of spectroscopy measurements performed at the ESR by several orders of magnitude, the SpecTrap experiment aims to store the ions under observation inside a Penning trap to eliminate the main uncertainty of the storage ring experiments, i.e. the velocity distribution of the ions, which leads to a Doppler broadening of the resonance signal. The SpecTrap experiment will allow for laser spectroscopy of a variety of fine and hyperfine transitions of highly charged ions, which are cooled down to mK temperatures. To achieve this, detectors capable of single photon detection, covering the wavelength region from ultra violet (UV) to the near infrared (NIR), are necessary. A detector system for the UV region has already successfully been used during the first commissioning measurements at SpecTrap, which were performed on Mg^+ ions to investigate the systematics of the experimental setup. Additionally, a test setup has been built to characterize several types of silicon avalanche photodiodes (APDs) in order to achieve stable single-photon counting conditions with these devices. APDs of the type S0223 manufactured by Radiation Monitoring Devices (RMD) have been found to be suitable for wavelengths from 400 nm up to 1100 nm. It has been shown, that under suitable conditions these devices are capable of single-photon detection with an efficiency of the order of their quantum efficiency. Subsequently, an APD detector system has been developed based on the test setup to allow for the use of the S0223 APDs at the SpecTrap experiment.

Zusammenfassung

Die Quantenelektrodynamik (QED) gilt als die präziseste Theorie der Physik im Bereich niedriger elektrischer und magnetischer Felder. An der GSI werden derzeit Laserspektroskopie-Experimente an schweren, hochgeladenen Ionen durchgeführt, um die Vorhersagen der QED in starken Feldern zu testen. In hochgeladenen Ionen sind die Elektronen elektrischen und magnetischen Feldern ausgesetzt, deren Feldstärken die von künstlich durch gepulste Laser oder gepulste Magnete erzeugten Feldern um mehrere Größenordnungen übertreffen.

In der vorliegenden Arbeit werden Detektorsysteme vorgestellt, die entwickelt wurden, um in Laserspektroskopie-Experimenten einen effizienten Nachweis von Fluoreszenzlicht zu ermöglichen, was einen wesentlichen Beitrag zu diesen Experimenten darstellt. Das Ziel hierbei ist die Bestimmung von Hyperfeinstruktur-Übergängen in den betrachteten Ionen. Sind die Übergangswellenlängen des 1S -Übergangs im wasserstoff-ähnlichen und des 2S -Übergangs im lithium-ähnlichen Ion desselben Isotops bekannt, kann die größte Unsicherheit der theoretischen Berechnung der QED-Beiträge zum Hyperfein-Übergang der beiden Ionen, die aus der Berechnung des sog. Bohr-Weißkopf-Effekts stammt, eliminiert werden. Das dazu am besten geeignete Isotop ist ^{209}Bi , bei dem sowohl der 1S -, als auch der 2S -Übergang für Laserspektroskopie zugänglich sind und die Übergangswellenlängen mit gängigen Detektortypen nachweisbar sind.

Während der 1S -Übergang in wasserstoff-ähnlichem $^{209}\text{Bi}^{82+}$ bereits vor mehreren Jahren bestimmt wurde, ist es dem LIBELLE-Experiment nun zum ersten Mal gelungen, auch den 2S -Übergang im lithium-ähnlichen $^{209}\text{Bi}^{80+}$ nachzuweisen. In diesem Experiment wurden die Bi-Ionen im Experimentierspeicherring (ESR) gespeichert und mit einem durchstimmbaren Laser angeregt. Um die unter kleinen Polarwinkeln in Vorwärtsrichtung emittierten Fluoreszenzphotonen effizient nachzuweisen wurde ein neuartiges Detektorsystem eingesetzt, bestehend aus einem mit einem Schlitz versehenen Kupfer-Parabolspiegel, der in den Ionenstrahl gefahren werden kann. Neben dem Hyperfein-Übergang in $^{209}\text{Bi}^{80+}$ wurde auch der Übergang in $^{209}\text{Bi}^{82+}$ erneut vermessen. Im ersten Teil dieser Arbeit wird die Analyse der LIBELLE-Daten vorgestellt, aus denen die Übergangswellenlängen der beiden Bismuthionen bestimmt wurden.

Um die durch Experimente am ESR gewonnenen Werte der Hyperfeinübergänge mit höherer Präzision zu bestimmen, wird das SpecTrap-Experiment die hochgeladenen Ionen in einer Penning-Falle speichern. Durch eine Iontemperatur von einigen mK in der Falle wird die größte Messunsicherheit der Experimente am Speicherring unterdrückt, die in der Geschwindigkeitsverteilung der Ionen und der daraus resultierenden Doppler-Verbreiterung der Resonanzlinien liegt. Das SpecTrap-Experiment kann dazu genutzt werden, eine Vielzahl von Fein- und Hyperfein-Übergängen in hochgeladenen Ionen zu vermessen. Hierzu ist es allerdings notwendig, dass der Wellenlängenbereich vom ultravioletten (UV) bis zum nahen Infrarot (NIR) mit Detektoren nachgewiesen werden kann, die in der Lage sind, einzelne Photonen zu detektieren. Für den UV-Bereich wurde ein solches System bereits erfolgreich bei Testmessungen mit MG^+ Ionen am SpecTrap-Experiment eingesetzt. Zusätzlich wurde ein Teststand zur Charakterisierung verschiedener Typen von Avalanche Photodioden (APDs) aufgebaut. APDs vom Typ S0223 der Firma Radiation Monitoring Devices (RMD) konnten unter geeigneten Bedingungen mit sehr niedrigen Dunkelzählraten und hohen Verstärkungen betrieben werden, was den Nachweis niedriger Einzelphotonenraten im Wellenlängenbereich

von 400 nm bis 1100 nm ermöglicht. Die Photodetektionseffizienz liegt dabei im Bereich der Quanteneffizienz der APDs. Für deren Einsatz am SpecTrap-Experiment wurde ein geeigneter Detektoraufbau entworfen und gebaut.

Contents

1. Introduction	1
2. Hyperfine structure and QED tests	5
2.1. Hyperfine structure and transitions	5
2.1.1. Energy structure of one-electron atoms	6
2.1.2. The hyperfine structure of one electron atoms	9
2.1.3. The hyperfine structure of highly charged ions	10
2.2. Test of QED	12
2.2.1. Eliminating the Bohr-Weisskopf error contribution	12
2.3. Transition probabilities and lifetimes	14
Part I. EVALUATION OF THE HFS TRANSITION WAVELENGTH IN $^{209}\text{Bi}^{80+}$ AND $^{209}\text{Bi}^{82+}$ IN THE LIBELLE EXPERIMENT	15
3. The LIBELLE Experiment	17
3.1. Experimental setup	17
3.1.1. The Experimental Storage Ring (ESR)	17
3.1.2. Ion excitation	19
3.1.2.1. Dye laser control program	21
3.2. Fluorescence light detection at the ESR	24
3.2.1. The segmented mirror section	24
3.2.2. Emission characteristics of relativistic excited ions	25
3.2.2.1. Relativistic Doppler-effect and forward boost	25
3.2.2.2. Number of excited ions	29
3.2.2.3. Simulated signal rates and detection times	30
3.2.3. New detector systems	33
3.2.3.1. The parabolic mirror system	34
3.2.3.2. The forward detection system	36
3.3. LIBELLE Data acquisition	37
3.3.1. The DAQ system	37
3.3.2. Recorded signals	37
3.3.2.1. Photon detectors	37
3.3.2.2. Laser status and wavelength step	40
3.3.2.3. Machine and ion beam parameters and timing	40
3.3.3. Data format	41
4. LIBELLE beamtime and data analysis	43

4.1.	LIBELLE beamtime	43
4.1.1.	Beamtime schedule and experimental data	43
4.1.2.	Parabolic mirror system performance	44
4.2.	Analysis	47
4.2.1.	Extracting the laser steps	48
4.2.1.1.	Finding the scan steps	49
4.2.1.2.	Processing the TDC data	51
4.2.2.	Associating a wavelength to the laser steps	51
4.2.3.	Obtaining count rate differences from stacked TDC data	52
4.2.4.	Fitting the resonances	54
4.2.4.1.	Error of the wavelength fit	56
4.3.	Resonance wavelengths in the laboratory system	58
4.3.1.	The $^{209}\text{Bi}^{80+}$ hyperfine transition (Li-like)	58
4.3.2.	The $^{209}\text{Bi}^{82+}$ hyperfine transition (H-like)	63
5.	Resonance wavelengths in the ion rest frame	67
5.1.	Calculating the ion velocity	67
5.1.1.	Calibration of the electron cooler voltage	68
5.1.2.	Space charge corrections	73
5.1.3.	Misaligned bunching frequency	74
5.1.4.	Results for the ion velocity β	74
5.2.	Calculating the transition wavelengths in the ion rest frame	75
 Part II. AN APD BASED SINGLE PHOTON DETECTOR FOR THE		
SPECTRAP EXPERIMENT		81
6.	The SpecTrap Experiment	83
6.1.	Experimental setup	84
6.1.1.	The SpecTrap Penning trap	85
6.1.2.	Superconducting magnets and vacuum system	86
6.1.3.	SpecTrap beamline and ion sources	87
6.1.4.	Ion excitation	88
6.2.	Fluorescence light detection at SpecTrap	88
6.2.1.	Estimated photon rates at the detector	89
6.2.1.1.	Simulations of the optics and the influence of the detector size	90
6.2.1.2.	Photon and signal rates	92
6.2.2.	Magnetic field at the detector position	93
6.2.3.	Detector types for different wavelength regions	93
6.2.3.1.	240 nm to 400 nm: CPM 1993 P Channel Photomultiplier .	94
6.2.3.2.	400 nm to 1100 nm: Silicon (Si) APDs	95
6.2.3.3.	1100 nm to 1600 nm: Possible detectors	97
7.	Detector test setup	99
7.1.	The detector test setup	99
7.1.1.	Vacuum chamber and detector mount	99

7.1.2.	Low noise preamplifier	102
7.1.3.	Test setup control and DAQ	105
7.1.3.1.	The main control program	106
7.1.3.2.	Gain measurements	109
7.1.3.3.	Signal and dark count rate measurements	111
7.2.	Single-photon sources	113
7.2.1.	Single-Photons from a pulsed low level light source	113
7.2.2.	A pulsed 628 nm LED with aperture	115
7.2.3.	A grating spectrograph with light bulb	117
8.	RMD S0223 Avalanche Photo Diodes as single-photon detectors	119
8.1.	Avalanche photo diodes	119
8.1.1.	Dark counts and experimental measuring time	120
8.1.2.	Linear and Geiger mode operation	121
8.2.	Basic APD characterization	122
8.2.1.	Dark current	123
8.2.2.	Relative gain	124
8.2.3.	Determination of the APD's operation bias	124
8.3.	Determination of single-photon detection efficiency	125
8.3.1.	Single-photon detection efficiency at 628 nm	126
8.3.2.	Single-photon detection efficiency at 1020 nm	128
8.3.3.	Detection time at SpecTrap	129
9.	An APD detector setup for SpecTrap	131
9.1.	Detector vacuum chamber	132
9.2.	Detector flange	133
9.3.	Optics and shutter mechanism	134
9.4.	Setup remote control	135
10.	Conclusion and outlook	139
	Appendix	143
A.	Operating procedure for the APD setup	143
B.	Circuit diagrams	145
B.1.	Preamplifier	147
B.2.	PT 1000 transducer	149
B.3.	APD setup NIM size control module	150
C.	Datasheets	155
	List of figures	159
	List of tables	163

INTRODUCTION

Since its development, Quantum Electrodynamics (QED) has proven to be one of the most precise theories in physics [Bei00]. QED is the quantum field theoretical extension of classical electrodynamics. Its success is based on the accurate description of the effects weak external fields have on electrons, like the anomalous magnetic moment of the electron. The latter is one of the most commonly known examples for the precision of QED. The g -factor of the free electron connects its spin with its magnetic moment. The Dirac theory predicts a value of exactly 2 for the g -factor, while experiments revealed a slightly higher value. This deviation can be explained by the introduction of the basic QED processes (*self energy*, *vacuum polarization*, *vertex correction*, depicted in figure 1.1). These higher order terms lead to an increase of the electrons magnetic moment. This effect can be calculated with high accuracy and presents a remarkable consistency with the experimentally determined value:

$$(g/2)_{\text{theoretical}} = 1.001\,159\,652\,175\,86\,(10)(26)(848) \quad [\text{Kin06}]$$

$$(g/2)_{\text{experimental}} = 1.001\,159\,652\,180\,73\,(28) \quad [\text{Gab08}]$$

While this example shows the success of QED, it has to be remarked that precision tests have, up to now, been performed in relatively small electric and magnetic fields, where theoretical calculations can be performed using perturbation theory. In strong fields that exist e.g. in the vicinity of the nucleus in heavy highly charged ions, however, this approach is no longer valid [Bei00]. In hydrogen-like systems, i.e. nuclei stripped of all but one electron, the coupling of the electron to the external field scales with the nuclear charge to $Z\alpha \approx 0.6$ in hydrogen-like bismuth ($Z = 83$), where $\alpha \approx \frac{1}{137}$ is the fine structure constant. In the latter ion, the $1s$ electron is exposed to electric fields up to 10^{16} V/cm and magnetic fields up to 10^4 T, which renders the investigation of hyperfine splittings in hydrogen-like systems suitable to

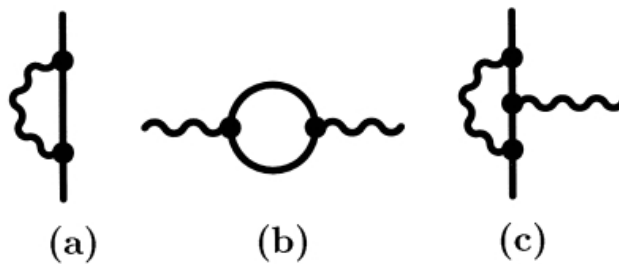


Figure 1.1.: The basic quantum electrodynamical processes, depicted as Feynman diagrams. Plain lines denote free electrons or positrons, wavy lines denote photons. (a) Emission and re-absorption of a virtual photon by an electron, called *self energy*. (b) creation and annihilation of a virtual electron-positron pair, termed *vacuum polarization*. (c) Modification of a basic electron-photon interaction by an additional virtual photon, known as *vertex correction*. [Bei00]

test QED predictions in those strong fields. Since the high field strength of the electric and magnetic fields leads to an increased overlap of the electron orbit with the nuclear volume, nuclear structure effects, which also influence the hyperfine structure, have to be accounted for. However, the calculation of the corrections to the hyperfine splitting in heavy ions due to the nuclear structure, especially the contribution due to the distribution of the nuclear magnetic moment (Bohr-Weisskopf effect), hampers precise QED tests. To circumvent this problem it has been suggested by Shabaev et al. [Sha01], that the determination of both the $1s$ hyperfine splitting in the hydrogen-like charge state and the $2s$ splitting in the lithium-like charge state of the same isotope will enable the elimination of the Bohr-Weisskopf correction terms from the equations. This would allow for high precision QED tests in strong fields. An isotope of special interest in this case is bismuth, since both the hyperfine transitions in the hydrogen-like ion ($^{209}\text{Bi}^{82+}$, $\lambda_{0,1s} \approx 244$ nm) and in the lithium-like ion ($^{209}\text{Bi}^{80+}$, $\lambda_{0,2s} \approx 1555$ nm) are accessible to laser spectroscopy experiments.

This approach is pursued at GSI¹, a research facility specialized on heavy ion research. With the possibility to store ions at high velocities, up to $\beta \approx 0.7$, inside the Experimental Storage Ring (ESR), the transition wavelengths can be Doppler shifted upwards or downwards to experimentally well-accessible values providing ideal conditions for application of laser spectroscopy on the ions of interest.

Over the last years experiments to determine the $1s$ hyperfine splitting in several hydrogen-like systems have successfully been performed at the ESR, e.g. in hydrogen-like bismuth [Kla94] or hydrogen-like lead ($^{207}\text{Pb}^{81+}$) [See99]. While the hyperfine transition in $^{209}\text{Bi}^{82+}$ has already been observed in 1994, several attempts to measure the $2s$ transition in lithium-like bismuth $^{209}\text{Bi}^{80+}$ have not been successful [Win99, San09]. The LIBELLE experiment

¹GSI Helmholtzzentrum für Schwerionenforschung GmbH, Planckstraße 1, 64291 Darmstadt, <http://www.gsi.de>

performed in August 2011 is the latest attempt and has finally been able to determine the wavelength of the latter transition due to a novel fluorescence light detection system.

These successful measurements are the prerequisite for an even more precise determination of the transition wavelengths in trap experiments like the SpecTrap setup, which is currently in the commissioning phase. It is a high precision Penning trap experiment which makes use of the HITRAP facility currently under construction at GSI. HITRAP will allow for the deceleration of heavy highly charged ions ejected from the ESR. These ions will then be delivered among others to the SpecTrap experiment. The storage of the ions in a Penning trap has the advantage of a very small velocity distribution of the ions. On the other hand, the Doppler shifting of the transitions to the optical regime is not possible anymore, leaving both laser excitation and fluorescence light detection with potentially inconvenient transition wavelengths to deal with.

This thesis will deal with aspects of both experimental approaches at the ESR and at SpecTrap, and is therefore divided into two parts. Subsequent to this introductory chapter, a short introduction to the theoretical background of this work will be given in **chapter 2**. The hyperfine structure of one electron atoms will be derived shortly before explaining the additional corrections to the hyperfine splitting energy in heavy ions. To motivate the experiments dealt with in part I and part II, Shabaev's idea to cancel the Bohr-Weisskopf contribution to the hyperfine splitting will be briefly described. The outline of the parts I and II is shown in the following:

Part I: Evaluation of the HFS transition wavelength in $^{209}\text{Bi}^{80+}$ and $^{209}\text{Bi}^{82+}$ in the LIBELLE experiment: In this part the data of the LIBELLE experiment are analyzed, which is the latest attempt to determine the hyperfine splitting in lithium-like bismuth at the ESR.

- **Chapter 3** will introduce the LIBELLE experiment. One particular focus of the chapter lays on the fluorescence light detection at the ESR. Investigations of the previously existing light detection system, which will be discussed briefly, led to the development of a novel detector system for fluorescence photons at the ESR. The characteristics and the design of the new detection system are presented as well as its implementation in the data acquisition at the LIBELLE experiment.
- **Chapter 4** deals with the analysis of the LIBELLE beamtime data. The analysis structure will be described and the transition wavelength of the $1s$ hyperfine splitting in $^{209}\text{Bi}^{82+}$ and the $2s$ splitting in $^{209}\text{Bi}^{80+}$ in the laboratory frame will be determined.

- To obtain the velocity of the ions, which is determined by the velocity of the electrons in the electron cooler at the ESR, the calibration of the electron cooler voltage was evaluated in **chapter 5**. Finally, the obtained transition wavelengths in the ions' rest frame are presented.

Part II: An APD based single photon detector for the SpecTrap experiment:

The second part of this work deals with the development of a detection system for optical and near-infrared wavelengths for fluorescence light detection at the SpecTrap experiment. This work concentrates on the detection of near infrared wavelengths up to 1100 nm, which is needed in the proposed precision measurements of the 1020 nm $1s$ hyperfine transition in Pb^{81+} at SpecTrap.

- **Chapter 6** will introduce the SpecTrap experiment. The experimental setup will be described and the challenges concerning fluorescence light detection at SpecTrap will be discussed. Previous simulation results regarding the demands on detection systems will be summarized and detector types under investigation to cover different wavelength regimes will be introduced.
- **Chapter 7** explains the well-shielded and cryogenically cooled test setup built to investigate one of the detector types, i.e. avalanche photo diodes (APDs). Additionally, a custom made extremely low noise preamplifier has been developed based on a design from the Mainz Neutrino Mass Experiment [Sch90, Wei90] to minimize the electronic noise. Finally, a simple concept of a single-photon source is presented and two realizations of the concept are introduced, which have been used in the following chapter.
- After introducing APDs and their operation principle, **chapter 8** presents the performance results obtained for type S0223 APDs manufactured by Radiation Monitoring Devices (RMD). Basic measurements to characterize the devices were performed. It will also be shown, that this APD type is capable of detecting single-photons and the photodetection efficiency (PDE) is determined for different wavelength.
- **Chapter 9** will present the dedicated APD detector setup designed for the application of the RMD S0223 APDs at the SpecTrap experiment. Its components and functions are explained.

The work will be summarized in **chapter 10** and a brief outlook on the development progress of the topics of the two parts will be given.

HYPERFINE STRUCTURE AND QED TESTS

This chapter will give a short overview over the theoretical background concerning the hyperfine structure of highly charged ions, which is investigated in the experiments presented later on. The $2s$ hyperfine transition wavelength in lithium-like bismuth ($^{209}\text{Bi}^{80+}$), observed for the first time in the LIBELLE experiment, can in combination with the corresponding wavelength of the $1s$ transition in hydrogen-like bismuth ($^{209}\text{Bi}^{82+}$) be used to determine the QED contribution to the hyperfine splitting. Therefore, the hyperfine transition will be derived for the case of one electron atoms before the extended hyperfine splitting equation for highly charged ions will be explained.

To test QED, the contribution of one particular nuclear structure effect, the Bohr-Weisskopf effect, which accounts for the spatial distribution of the nuclear magnetization, has to be eliminated from the equations due to its large uncertainty. V.M. Shabaev et al. have presented a solution to the latter [Sha01], which will be discussed briefly.

2.1. Hyperfine structure and transitions

In this section the hyperfine splitting will be derived for one electron atoms. Starting with the Schrödinger equation, the basic energy levels of one electron atoms are presented. The fine structure corrections to these energy levels are described and analog to the spin orbit coupling the hyperfine structure is introduced. Additional corrections to the hyperfine splitting due to nuclear structure and QED effects as well as corrections to the hyperfine splitting in lithium-like systems are explained briefly.

2.1.1. Energy structure of one-electron atoms

In 1913, Nils Bohr presented his atomic model, which allowed the electrons to be located only on certain energy levels, to explain experimental results indicating that atoms can only absorb and emit light of certain wavelengths. His equation to calculate these energy levels has been confirmed by quantum mechanics if the electron spin and the nuclear spin are not accounted for. In the case of a hydrogenic atom consisting of a nucleus of the charge Ze and an electron of charge $-e$, the one-body time-independent Schrödinger equation with the Hamiltonian H_0 ,

$$H_0\psi(\vec{r}) = E\psi(\vec{r}) \quad \text{with} \quad H_0 = -\frac{\hbar^2}{2\mu}\nabla^2 - \frac{Ze^2}{4\pi\epsilon_0 r}, \quad (2.1)$$

has to be solved, where $\mu = \frac{m_e \cdot m_N}{m_e + m_N}$ is the reduced mass, m_e the electron mass and m_N the mass of the nucleus, r the distance of the spatial coordinate of the electron wave function to the nucleus and $\hbar = \frac{h}{2\pi}$ the reduced Planck constant. The solution of equation (2.1), which can be found in detail e.g. in [Bra83], leads to the energy eigenvalues

$$E_n = -Ry^* \cdot \frac{Z^2}{n^2}, \quad (2.2)$$

where $Ry^* = \frac{\mu e^4}{8\epsilon_0^2 \hbar^2}$ is the Rydberg constant in units of energy, ϵ_0 the vacuum permittivity, h the Planck constant and $n \in \mathbb{N}$ the principal quantum number, denoting the energy level. The energies E_n can also be expressed in terms of the rest mass energy μc^2 using the representation $Ry^* = \frac{1}{2}\mu c^2 \alpha^2$,

$$E_n = -\frac{1}{2}\mu c^2 \frac{(Z\alpha)^2}{n^2}, \quad (2.3)$$

which is convenient for discussing the relativistic corrections in the following. Here $\alpha = \frac{e^2}{(4\pi\epsilon_0)\hbar c} \approx \frac{1}{137}$ is the fine structure constant. Equation (2.2) is identical to the energy formula classically derived by Bohr and describes the energy levels of simple systems like the Hydrogen atom very accurately. However, experiments with high spectral resolution discovered, that the energy levels slightly differ from the values given by the latter equation. Corrections to E_n have to be considered originating in the following relativistic effects [Dem10]:

1. The relativistic mass increase of the electron mass due to the the electron's motion in the Coulomb field, which leads to a small change in the kinetic energy. This effect results in a shift of the energy levels of [Dem10]

$$\Delta E_{\text{rel}} = -E_n \frac{(Z\alpha)^2}{n^2} \left(\frac{3}{4} - \frac{n}{l + \frac{1}{2}} \right), \quad (2.4)$$

where l is the orbital quantum number.

2. The "smearing" of the electron charge over a volume $\lambda_c^3 = (\frac{\hbar}{m_e c})^3$ with the Compton wavelength λ_c , which applies only for s -states ($l = 0$), leads to a change in the potential energy (*Darwin term*) [Bra83]

$$\Delta E_{\text{Dar}} = -E_n \frac{(Z\alpha)^2}{n} \quad (2.5)$$

3. The interaction of the electron's orbital angular momentum \vec{l} and spin \vec{s} results in a small shift and splitting of the energy levels, the *spin orbit coupling*, ΔE_{so} .

A detailed discussion of ΔE_{rel} and ΔE_{Dar} can be found e.g. in [Dem10, Bra83]. The spin-orbit coupling, however, will be briefly explained, since the hyperfine structure introduced later on is derived in the same way. From the electron's point of view the nucleus is a moving charge, which according to the Biot-Savart law creates a magnetic field \vec{B} at the electron's position [Dem10],

$$\vec{B} = \frac{\mu_0 Z e}{8\pi r^3 m_e} \vec{l}, \quad (2.6)$$

which interacts with the magnetic spin moment of the electron $\vec{\mu}_s$

$$\vec{\mu}_s = -g \cdot \frac{\mu_B}{\hbar} \cdot \vec{s}. \quad (2.7)$$

Here g is the electron g -factor and μ_B is the Bohr magneton. This interaction leads to a shift ΔE_{so} of the energy levels:

$$\begin{aligned} \Delta E_{\text{so}} &= -\vec{\mu}_s \cdot \vec{B} \\ &= g\mu_B \frac{\mu_0 Z e}{8\pi\hbar m_e \langle r^3 \rangle} (\vec{s} \cdot \vec{l}) \\ &\approx \frac{\mu_0 Z e^2}{8\pi m_e^2 \langle r^3 \rangle} (\vec{s} \cdot \vec{l}) \end{aligned} \quad (2.8)$$

Introducing the total angular momentum $\vec{j} = \vec{l} + \vec{s}$, with $|\vec{j}| = \sqrt{j(j+1)}\hbar$, equation (2.11) can be written as

$$\Delta E_{\text{so}} = \frac{a}{2} [j(j+1) - l(l+1) - s(s+1)], \quad (2.9)$$

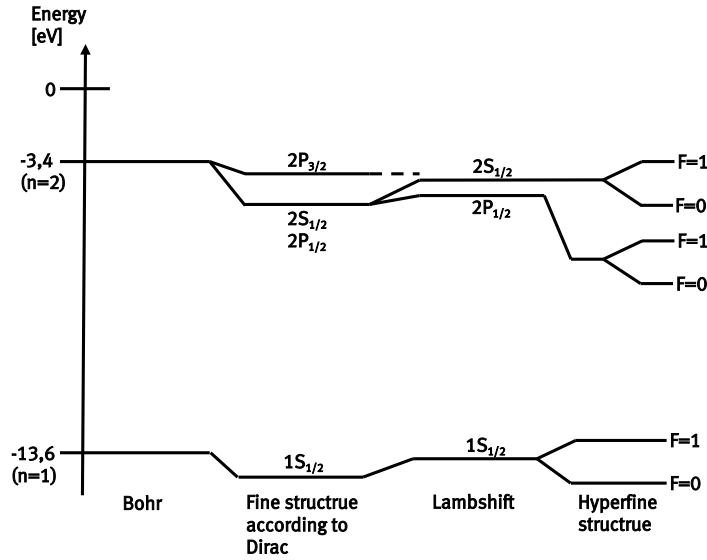


Figure 2.1.: Scheme of the two lowest energy levels of the Hydrogen atom. The splittings are not to scale. The fine structure contains the spin-orbit interaction correction ΔE_{so} , the Darwin term ΔE_{Dar} and the relativistic mass correction ΔE_{rel} . The fine structure splitting of the $n = 2$ level is in the order of 10^{-5} eV, while the first two hyperfine splittings are about 10^{-6} eV and 10^{-7} eV, respectively [Pov06].

with the spin orbit coupling constant

$$a = \frac{\mu_0 Z e^2 \hbar^2}{8\pi m_e^2 r^3}. \quad (2.10)$$

Adding the three relativistic corrections ΔE_{rel} , ΔE_{Dar} and ΔE_{so} to the non-relativistically obtained energies E_n of equation (2.3), this leads to [Dem10]

$$E_{n,j} = E_n + \Delta E_{rel} + \Delta E_{Dar} + \Delta E_{so} = E_n \left[1 + \frac{Z^2 \alpha^2}{n} \left(\frac{1}{j + \frac{1}{2}} - \frac{3}{4n} \right) \right]. \quad (2.11)$$

An additional shift of the energy levels is caused by the interaction of the electron with the virtual radiation field, the so called *Lamb shift*, which is a QED effect. This interaction results in fluctuations of the potential energy of the electron without a change of the electron's energy level.

The different contributions to the overall energy level scheme are shown in figure 2.1 for the two lowest energy levels of the Hydrogen atom. The hyperfine structure will be introduced in the next section.

2.1.2. The hyperfine structure of one electron atoms

The hyperfine structure (HFS) is comprised of the interaction of both the electric quadrupole moment Q and the magnetic dipole moment $\vec{\mu}_I$ of the nucleus with the electron shell. In the following the hyperfine structure of spherical symmetric ns -states will be discussed, where the electric contribution does not matter. Analog to the fine structure the hyperfine structure is then derived from the interaction of the nuclear magnetic moment

$$\vec{\mu}_I = g_I \cdot \frac{\mu_N}{\hbar} \cdot \vec{I}. \quad (2.12)$$

with the magnetic field \vec{B}_j generated by the electron at the position of the nucleus. Here g_I is the nuclear g -factor, μ_N the nuclear magneton and \vec{I} the nuclear spin. Like in the case of the fine structure, this interaction results in a splitting of the energy levels given by [Dem10]

$$\begin{aligned} \Delta E_{\text{HFS}} &= -\vec{\mu}_I \cdot \vec{B}_j \\ &= -|\vec{\mu}_I| \cdot B_j \cdot \cos(\angle(\vec{\mu}_I, \vec{B}_j)) \\ &= g_I \mu_N \sqrt{I(I+1)} B_j \cdot \cos(\angle(\vec{I}, \vec{j})). \end{aligned} \quad (2.13)$$

Introducing the total angular momentum of the atom $\vec{F} = \vec{j} + \vec{I}$ and using the law of cosines in quantum mechanical notation, $\cos(\angle(\vec{I}, \vec{j}))$ can be expressed by

$$\cos(\angle(\vec{I}, \vec{j})) = \frac{F(F+1) - I(I+1) - j(j+1)}{2\sqrt{j(j+1)}\sqrt{I(I+1)}}. \quad (2.14)$$

Combining equations (2.13) and (2.14), the hyperfine splitting can be written as

$$\Delta E_{\text{HFS}} = \frac{A_{\text{hf}}}{2} [F(F+1) - I(I+1) - j(j+1)], \quad (2.15)$$

with the hyperfine constant

$$A_{\text{hf}} = \frac{g_I \mu_N B_j}{\sqrt{j(j+1)}}. \quad (2.16)$$

For s -states A_{hf} can be written as [Bra83]

$$A_{\text{hf}} = \frac{\mu_0}{4\pi} 4g_I \mu_B \mu_N \frac{1}{j(j+1)(2l+1)} \frac{Z^3}{a_\mu^3 n^3}, \quad (2.17)$$

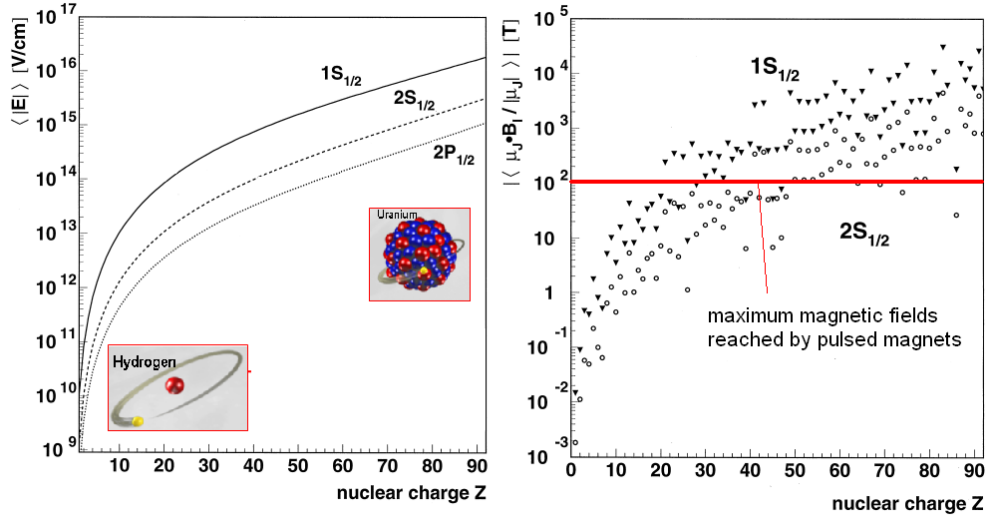


Figure 2.2.: Expectation values of the electric and magnetic field strengths in highly charged ions depending on the nuclear charge Z [Bei00]. The horizontal line represents the highest field artificially achievable by pulsed magnets [Mei12].

where a_μ is modified Bohr radius

$$a_\mu = \frac{4\pi\epsilon_0\hbar^2}{\mu e^2}. \quad (2.18)$$

With the representation of A_{hf} from equation (2.17) and the introduction of the fine constant α , equation (2.15) can thus be rewritten to the form [Bra83, Bei00]

$$\Delta E_{\text{HFS}} = \alpha g_I \frac{m_e}{m_p} \frac{F(F+1) - I(I+1) - j(j+1)}{2j(j+1)} m_e c^2 \cdot \frac{(Z\alpha)^3}{n^3(2l+1)}. \quad (2.19)$$

The hyperfine splitting in Hydrogen corresponds to the well known wavelength of $\lambda \approx 21$ cm and a lifetime of about $\tau \approx 8 \cdot 10^6$ a [See99]. As ΔE_{HFS} is in the first order proportional to Z^3 , the transition wavelengths of some heavy ions are shifted to the optical regime, making them accessible to laser spectroscopy. On the other hand, the lifetime τ is proportional to Z^{-9} [Nör11], which drastically reduces the lifetimes in heavy ions.

2.1.3. The hyperfine structure of highly charged ions

With increasing nuclear charge Z , several effects that could have been neglected in the case of low Z ions now have to be accounted for. Due to the spatial expansion of the nucleus, its charge radius increases with $\sqrt[3]{A}$, while due to the increase of the potential the Bohr radius of the $1s$ electron decreases with $1/Z$. Therefore, the electrons in the K -shell of heavy ions are more sensitive to the nuclear structure. To account for the effects of the extended nucleus

and other effects, corrections to the hyperfine splitting have to be applied, which are [Bei00]:

- Due to the finite mass of the nucleus it moves around a common center of mass with the electrons, which is accounted for by the nuclear mass correction \mathcal{M} .
- The relativistic factor $A(Z\alpha)$ accounts for relativistic corrections.
- The finite size of the nucleus also implies a finite distribution of its charge, known as Breit-Rosenthal effect, denoted by $(1 - \delta)$.
- The Bohr-Weisskopf effect describes the influence of spatial distribution of the nuclear magnetization on the hyperfine splitting and is accounted for by the factor $(1 - \epsilon)$.
- Finally, corrections to the hyperfine splitting introduced by QED effects like self-energy and vacuum polarization are described by an additional higher order term $\frac{\alpha}{\pi}\Delta\epsilon_{\text{QED}}$.

With these corrections equation (2.19) is extended to:

$$\Delta E_{\text{HFS}} = \alpha g_I \frac{m_e}{m_p} \frac{F(F+1) - I(I+1) - j(j+1)}{2j(j+1)} m_e c^2 \cdot \frac{(Z\alpha)^3}{n^3(2l+1)} \cdot \mathcal{M} \left[A(Z\alpha)(1-\delta)(1-\epsilon) + \left(\frac{\alpha}{\pi}\right) \Delta\epsilon_{\text{QED}} \right]. \quad (2.20)$$

The electrons are also exposed to high electric and magnetic fields, which surpass the field strengths of artificially generated fields by orders of magnitude. Figure 2.2 shows the field strengths of electric and magnetic fields depending on the nuclear charge Z . The electric fields can reach values of up to 10^{16} V/cm. Also the magnetic field strengths of up to 10^4 T exceed fields generate by pulsed magnets (up to 10^2 T [Mei12]) by far. Hydrogen-like highly charged ions are therefore an ideal candidate to test QED in strong electric and magnetic fields as has been proposed e.g by V.M. Shabaev et al. [Sha01]. As will be shown in the next section, also the hyperfine splitting in lithium-like heavy ions is essential for precision QED tests. For the calculation of the hyperfine splitting in lithium-like ions equation (2.20) has to be modified to account for the interelectronic interactions [Bei00]:

$$\Delta E_{\text{HFS}-2s_{1/2}} = \frac{1}{6} \alpha g_I \frac{m_e}{m_p} \frac{F(F+1) - I(I+1) - 3/4}{2} m_e c^2 \cdot \mathcal{M} \left\{ \left[(A_{2s_{1/2}}(Z\alpha)(1 - \delta_{2s_{1/2}})(1 - \epsilon_{2s_{1/2}}) + \frac{\alpha}{\pi} \Delta\epsilon_{\text{QED},2s_{1/2}}) \right] + \frac{1}{Z} B(Z\alpha) + \frac{1}{Z^2} C(Z\alpha) + \dots \right\}. \quad (2.21)$$

$B(Z\alpha)$ and $C(Z\alpha)$ are the terms accounting for the interelectronic interactions. Also the other correction terms denoted by the lowered $2s_{1/2}$ have to be recalculated. A detailed discussion of the terms is given in [Bei00].

2.2. Test of QED

With large progress in the experimental investigations of the Lamb shift, the hyperfine splitting and the bound-electron g factor in heavy ions to test QED in a strong Coulomb field, the uncertainty of the theoretical calculations of the observed quantities becomes crucial to the precision of these tests. Especially the uncertainty introduced by theoretical calculations of the Bohr-Weisskopf (BW) correction, which is of the same order as the QED correction itself, limits the achievable accuracy. Thus the QED effects on the hyperfine splitting can not be determined by measurements of the latter in just hydrogen-like ions. In the following it will be shown that the Bohr-Weisskopf correction can be eliminated following V.M. Shabaev et al. [Sha01], which allows for the investigation of QED effects on the level of a few percent. This involves the knowledge of the hyperfine transition wavelengths of H- and Li-like ions of the same isotope.

2.2.1. Eliminating the Bohr-Weisskopf error contribution

In order to demonstrate the cancellation of the Bohr-Weisskopf effect in the equations allowing for tests of QED, the ground-state hyperfine splitting in H- and Li-like ions can be written as

$$\text{H-like: } \Delta E^{(1s)} = \Delta E_{\text{Dirac}}^{(1s)} (1 - \epsilon^{(1s)}) + \Delta E_{\text{QED}}^{(1s)} \quad (2.22)$$

$$\text{Li-like: } \Delta E^{(2s)} = \Delta E_{\text{Dirac}}^{(2s)} (1 - \epsilon^{(2s)}) + \Delta E_{\text{int}} (1 - \epsilon^{(\text{int})}) + \Delta E_{\text{QED}}^{(2s)} + \Delta E_{\text{int-QED}}, \quad (2.23)$$

where $\Delta E_{\text{Dirac}}^{(1s)}$ and $\Delta E_{\text{Dirac}}^{(2s)}$ are the one-electron relativistic values of the $1s$ and $2s$ hyperfine splitting including the nuclear charge distribution correction. The BW corrections for the $1s$ and $2s$ states are labeled $\epsilon^{(1s)}$ and $\epsilon^{(2s)}$, $\Delta E_{\text{QED}}^{(1s)}$ and $\Delta E_{\text{QED}}^{(2s)}$ are the one-electron QED corrections to the $1s$ and $2s$ hyperfine splitting, ΔE_{int} is the interelectronic-interaction contribution to the ground-state hyperfine splitting in the Li-like ion, $\epsilon^{(\text{int})}$ indicates the BW effect on the interelectronic-interaction contribution, and finally $\Delta E_{\text{int-QED}}$ denotes the combined interelectronic-interaction QED correction, called "screened QED effect" [Sha01]. It has been shown that the ratios $\epsilon^{(2s)}/\epsilon^{(1s)}$ and $\epsilon^{(\text{int})}/\epsilon^{(2s)}$ almost solely depend on the electronic structure and can be written as:

$$\frac{\epsilon^{(2s)}}{\epsilon^{(1s)}} = f(\alpha Z) \quad \Rightarrow \quad \epsilon^{(2s)} = f(\alpha Z)\epsilon^{(1s)} \quad (2.24)$$

Table 2.1.: Previous theoretical and experimental values of the 2s hyperfine splitting in $^{209}\text{Bi}^{80+}$. The experimental value in [Bei98] was obtained at an electron beam ion trap (EBIT) in Livermore and is not suited for a QED test due to its large uncertainty. The calculations in [Sha00] and [Sap01] were performed using experimental results of $\Delta E^{(1s)}$ in hydrogen-like bismuth.

hyperfine splitting (meV)	transition wavelength (nm)	determination	reference
797.1±0.2	1555.4±0.4	theoretical	[Sha00]
797.15±0.13	1555.3±0.3	theoretical	[Sap01]
783.9±3.0	1581.6±6.0	theoretical	[Tom00]
820.0±26.0	1512±48	experimental	[Bei98]
791.2±5.0	1567±10	experimental	[Nör08]

$$\frac{\epsilon^{(\text{int})}}{\epsilon^{(2s)}} = f_{\text{int}}(\alpha Z) \Rightarrow \epsilon^{(\text{int})} = f_{\text{int}}(\alpha Z) f(\alpha Z) \epsilon^{(1s)}. \quad (2.25)$$

Since $f(\alpha Z)$ and $f_{\text{int}}(\alpha Z)$ can be calculated with a high accuracy, equations (2.22) and (2.23) can be expressed in terms of only $\epsilon^{(1s)}$. On the other hand, with the experimental value of the hyperfine splitting $\Delta E^{(1s)}$ known for the H-like ion of a certain isotope, $\epsilon^{(1s)}$ can be expressed in terms of $\Delta E^{(1s)}$ using equation (2.22). Now this value can be substituted for $\epsilon^{(1s)}$ in equation (2.23), which allows for a very accurate calculation of $\Delta E^{(2s)}$. Some values for $\Delta E^{(2s)}$ in lithium-like bismuth calculated this way are listed in table 2.1 along with two experimental values. However, these calculations still depend on $\epsilon^{(1s)}$. To completely exclude the uncertainty of the BW effect and to allow for QED tests in the strong fields of highly charged ions with higher accuracy, the following specific difference is introduced:

$$\Delta' E = \Delta E^{(2s)} - \xi \Delta E^{(1s)}. \quad (2.26)$$

The parameter ξ in this equation has to be chosen to cancel the BW correction on the right hand side and can be obtained using equations (2.22), (2.23), (2.24) and (2.25):

$$\xi = f(\alpha Z) \frac{\Delta E_{\text{Dirac}}^{(2s)} + f_{\text{int}}(\alpha Z) \Delta E_{\text{int}}}{\Delta E_{\text{Dirac}}^{(1s)}}. \quad (2.27)$$

With the BW corrections $\epsilon^{(1s)}$, $\epsilon^{(2s)}$ and $\epsilon^{(\text{int})}$ dropped from equation (2.26), the specific difference $\Delta' E$ can be calculated with high accuracy. For $Z = 83$ in the case of bismuth this yields $\xi = 0.16885$ [Sha01]. Equation (2.26) can be utilized to test QED on the percent level at these strong fields, in case the hyperfine splitting values of the H-like and the Li-like ion of an isotope are known with a precision of $\Delta\lambda/\lambda = 10^{-7}$ [Krä07]. This precision is expected to be reached at the SpecTrap experiment [And10]. Also, with $\Delta E^{(1s)}$ and $\Delta E^{(2s)}$ known for the H-like and Li-like ions of a certain isotope and the QED contribution derived from the calculation above, conclusions on the nuclear structure and the BW effect can be drawn.

Table 2.2.: Transition wavelengths λ and lifetimes τ of the hyperfine states of three highly charged ions of interest to test QED. The hyperfine splitting of $^{209}\text{Bi}^{80+}$ has finally also been observed at the ESR, where the results are presented in part I of this work. All transitions are to be observed with high accuracy at the SpecTrap experiment.

Type	Ion	Transition	λ (nm)	τ (ms)
H-like	$^{209}\text{Bi}^{82+}$	F=4 \rightarrow F=5	243.87(4), ESR [Kla94]	0.351(16), exp. [Kla94]
H-like	$^{207}\text{Pb}^{81+}$	F=0 \rightarrow F=1	1019.7(2), ESR [See99]	49.5(65), exp. [See99]
Li-like	$^{209}\text{Bi}^{80+}$	F=4 \rightarrow F=5	1511(48), EBIT [Bei98]	82.2(14), theo. [Sha98]

2.3. Transition probabilities and lifetimes

As parts of this work deal with the detection of fluorescence light emitted in the decay process of excited hyperfine states, it is necessary to estimate the photon rates to properly dimension the detectors. The fluorescence photon rate emitted by a transition between two hyperfine states depends on the transition probability $\Gamma_{F \rightarrow F'}$. For hydrogen-like ions this probability is given by [Bei00]

$$\Gamma_{F \rightarrow F'} = \frac{\alpha \omega^3 \hbar^2}{3m_e^2 c^4} \cdot \frac{I}{2I+1} \left[g - g_I \frac{m_e}{m_p} \right]^2, \quad (2.28)$$

where the contribution of nuclear g -factor g_I is negligible compared to the contribution of the electron g -factor. ω is the transition frequency given by $\hbar\omega = \Delta E_{\text{HFS}}$. The transition probability for an electron in an s -state is given by [Sha98]

$$\Gamma_{F \rightarrow F'} = \frac{\alpha \omega^3 \hbar^2}{m_e^2 c^4} \frac{4}{27} \cdot \frac{I}{2I+1} \left[\frac{2E_{n,\kappa}}{m_e c^2} + 1 \right]^2, \quad (2.29)$$

where $E_{n,\kappa}$ are the energy eigenvalues of the Dirac equation. The transition probability for the $1s_{1/2}$ state is given by [Bei00, Vog05]:

$$\Gamma = \frac{\alpha \omega^3 \hbar^2}{m_e^2 c^4} \frac{4}{27} \cdot \frac{I}{2I+1} (2\kappa + 1)^2 \quad (2.30)$$

with $\kappa = \sqrt{1 - (Z\alpha)^2}$ and Z the nuclear charge number. To obtain transition probabilities for lithium-like systems, additional corrections to account for the interelectronic interaction have to be implemented [Bei00]. The lifetime of a state is the inverse of the transition probability. The lifetimes and transition wavelengths of the hyperfine states of three dedicated highly charged ions, which have been investigated at the ESR and are also to be investigated at SpecTrap to test QED, are listed in table 2.2.

Part I.

EVALUATION OF THE HFS TRANSITION WAVELENGTH IN $^{209}\text{Bi}^{80+}$ AND $^{209}\text{Bi}^{82+}$ IN THE LIBELLE EXPERIMENT

THE LIBELLE EXPERIMENT

The purpose of the LIBELLE experiment has been the determination of the wavelength of the hyperfine splitting of the $2s$ -state in lithium-like bismuth ($^{209}\text{Bi}^{80+}$) at the ESR by means of laser spectroscopy. Several attempts to measure this transition were undertaken over the last 13 years [Gep12]. The recent measurement was finally successful in finding the resonance signal due to the introduction of a novel fluorescence light detection system. Also the $1s$ -transition in hydrogen-like bismuth $^{209}\text{Bi}^{82+}$ was observed again.

3.1. Experimental setup

The LIBELLE experiment has been performed at the Experimental Storage Ring (ESR) at GSI. Highly charged $^{209}\text{Bi}^{82+}$ and $^{209}\text{Bi}^{80+}$ ions were delivered by the GSI accelerator infrastructure (see fig. 3.1). To create these charge states, bismuth ions were produced in a Metal Vapour Vacuum Arc (MeVVA) ion source, injected into the UNILAC linear accelerator and further accelerated by the SIS synchrotron to energies of about 400 MeV/u. Subsequently, they were shot through a copper stripper foil where most of the electrons were removed, producing various charge states. The ions of the desired charge state were then selected by a dipole magnet and injected into the ESR, where they were stored at a velocity of $\beta = 0.71$. A tunable laser system has been set up to excite HFS transitions in the stored ions. To detect the fluorescence signal several detector systems were installed including a novel movable parabolic mirror system.

3.1.1. The Experimental Storage Ring (ESR)

The Experimental Storage Ring (ESR, schematically shown in figure 3.2) is shaped like a stretched hexagon with a circumference of about 108 m . The ions are deflected by six 60° -

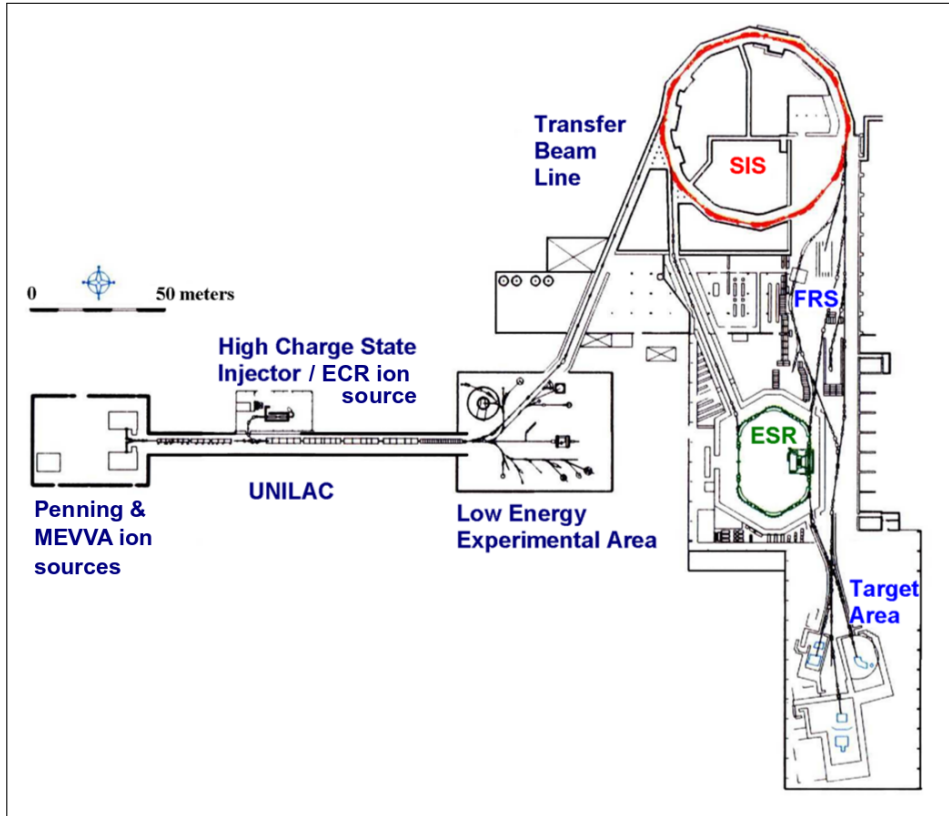


Figure 3.1.: Overview of the GSI accelerator infrastructure. In the LIBELLE experiment the ions were produced in the MeVVA ion source and injected into the UNILAC. After transport through the Transfer Beam Line, they were further accelerated by the SIS. The final charge states were subsequently produced using a stripper foil and a dipole magnet and were then injected into the ESR [Bra00].

dipole magnets with a B -field of 1.6 T each and thus stored on a closed orbit. In addition, twenty multipole magnets are distributed along the length of the storage ring to focus the ion bunches in both transversal directions. To reduce the velocity spread of the stored ions, the ESR features an electron cooling system. There, a beam of electrons with well defined velocity is overlapped with the ion beam over a 2.5 m long segment of the beam pipe. With this technique the momentum distribution of the ions can be reduced within 10 s to the uncertainty of the momenta of the cooling electrons and is then of the order of $\delta p/p \approx 10^{-4}$ [Nör12]. In order to match the ion velocity of $\beta = 0.71$, the electron cooler was operated at $U_{e\text{-cool}} \approx 214$ kV, which is close to the maximum voltage allowed for stable operation. RF cavities in the ESR were operated using the second harmonic of the ion's revolution frequency (≈ 2 MHz), forcing the stored ions to split up into two bunches of about 10 m length. One of these bunches (the signal bunch) was excited by a tunable laser system (see section 3.1.2), while the other bunch (the reference bunch) was used for background determination.

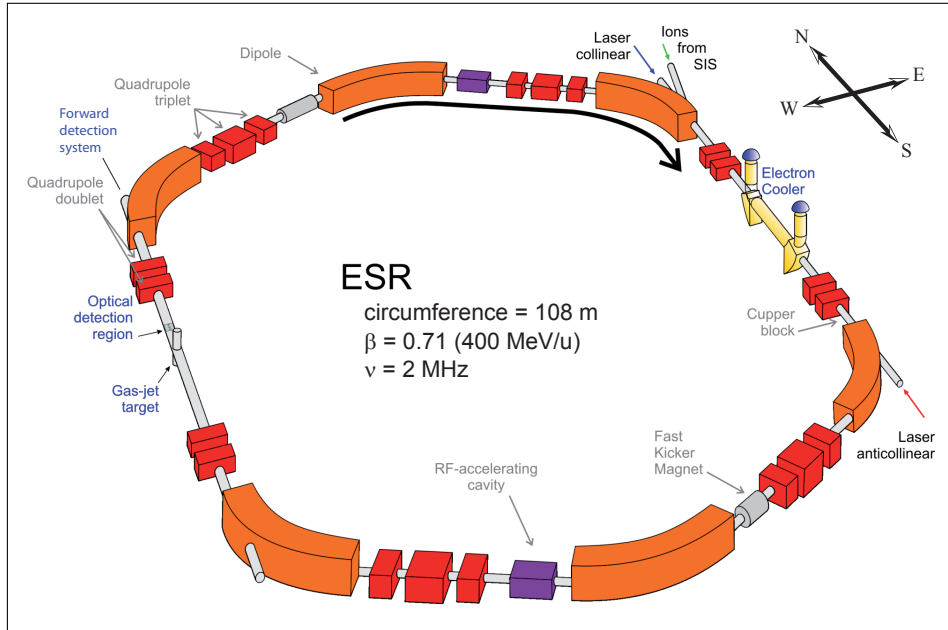


Figure 3.2.: Overview of the Experimental Storage Ring (ESR) at GSI. In the LIBELLE experiment the HCI were excited by a laser on the eastern straight section in the electron cooler. The fluorescence detection was set up on the opposite side of the ESR right behind the gas-jet target and at the north western end of the straight section [San12].

3.1.2. Ion excitation

The laser system used to excite the signal bunch coasting in the ESR consisted of two lasers, a Spectra Physics Quanta Ray Pro 290-30 pulsed Nd:YAG pumping laser and a custom made SIRAH Cobra Stretch dye laser. The setup of the laser system is shown in figure 3.3. The SIRAH dye laser was used to provide the necessary wavelength to excite HFS transitions in the ions, which is in the laboratory frame $\lambda_H \approx 590$ nm in the hydrogen-like case and $\lambda_H \approx 640$ nm in the lithium-like case. The dye laser was pumped with about 600 mJ of the second harmonic of the Nd:YAG pumping laser.

Inside the dye laser, the pumping laser beam is divided into three separate beams. The first is focused onto a cubic dye cell, which is the active medium of the oscillator. One end of the oscillator is composed of a prism array and a mirror with diffraction grating in Littrow configuration with a line density of 1800 cm^{-1} , which can be rotated by a step motor to allow for wavelength selection. Two exchangeable prism sets were used to switch between a broad-band mode with a linewidth of with 54 GHz and a narrow-band mode with 18 GHz linewidth. After decoupling from the resonator, the laser beam is bend upwards to pass the cubic cell again on an elevated level, thus being amplified by the second of the pumping laser beams. In the main amplification cell (cylindrical cell), the widened beam is further amplified by the third pumping beam containing most of the Nd:YAG's pumping power,

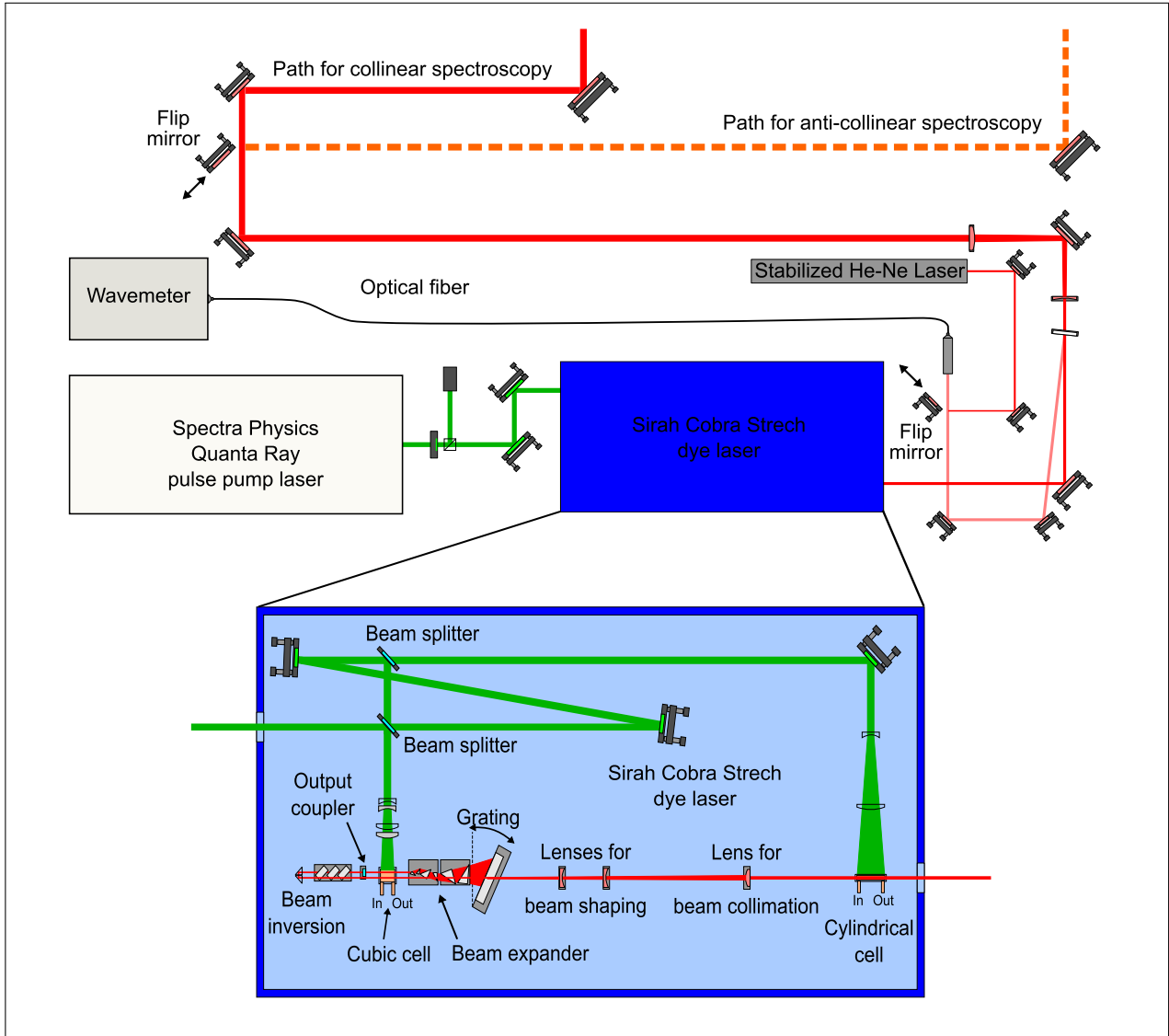


Figure 3.3.: Scheme of the laser setup used in the LIBELLE experiment [San12].

before exiting the laser housing. A more detailed description of the laser system can be found in [Loc13].

The laser was overlapped with the ion bunch inside the electron cooler over a length of roughly 2.5 m. The pulses of the laser had to be synchronized with the bunches. This was achieved by connecting the frequency signal given by the master oscillator driving the ESR RF cavities divided by a factor of two to a coincidence unit along with the properly delayed output of the lamp trigger of the Spectra Physics pumping laser. While the lamp trigger was running with 30 Hz, the Q-switch of the pumping laser was triggered by the output of the coincidence unit, which then caused the dye laser to emit a light pulse synchronized to the signal bunch. Typical pulse energies of the dye laser were around 140 mJ at a pulse length of 4-7 ns [Nör12]. While searching for the transitions, initially the broad-band mode was

used, whereas afterwards high resolution measurements with the narrow-band mode were performed.

The laser wavelength was measured by an Atos lambdameter LM-007. This device consists of four neon-filled, temperature stabilized Fizeau interferometers with different base lengths. The interference patterns behind the interferometers were recorded by four linear CCD sensors and afterwards the laser wavelength was determined from the interference patterns. Depending on the line width of the laser, only one (broad-band) or two (narrow-band) interferometers were used. Logfiles of the measured laser wavelength along with information on the intensity of the laser as measured by the lambdameter and a timestamp of the measurement were generated by a LabVIEW program used to control the Atos lambdameter. The logfiles written by this program and by the dye laser control program were recorded on separate computers not related to the main DAQ system described in section 3.3.

To be able to access the lasers during operation of the ESR they were located in a laboratory outside the ESR hall. The laser beams had thus to be transported over rather large distances of about 70 m in the case of collinear excitation and 40 m in the case of anti-collinear excitation. Due to the high laser power this was not possible with optical fibers. The beam was instead guided by a system of mirrors installed in the laser laboratory and in the ESR hall. In the process the laser beam was enlarged in diameter with a telescope and reduced again directly in front of the entrance windows of the ESR to a diameter of about 16 mm in the interaction region [Nör12]. The overlap of the laser beam with the ion bunches was checked in the transversal plane by measuring the ion beam position with scraper-blades before and after the electron cooler and subsequent visual adjustment of the laser beam to the same position. To compensate for fluctuations of the laser beam position caused by temperature and pressure gradients along the path a beam stabilizing system manufactured by TEM Messtechnik was installed in front of both entrance windows on the eastern straight section of the ESR.

3.1.2.1. Dye laser control program

The SIRAH dye laser was controlled by a custom made LabVIEW program (“Cobra Control“) developed within this work using LabVIEW driver libraries provided by the manufacturer. The wavelength of the dye laser was scanned over a certain wavelength range in 51 steps with increments of 0.01 nm, 0.02 nm and 0.04 nm, respectively. The duration of a scan step was set in the control program to be 180 times the pulsed laser trigger period (33.3 ms), resulting in an average measurement time of 6 s per wavelength. Since the program might be reused for other applications of the SIRAH dye laser, its functions will be described briefly. The user interface is shown in figure 3.4.

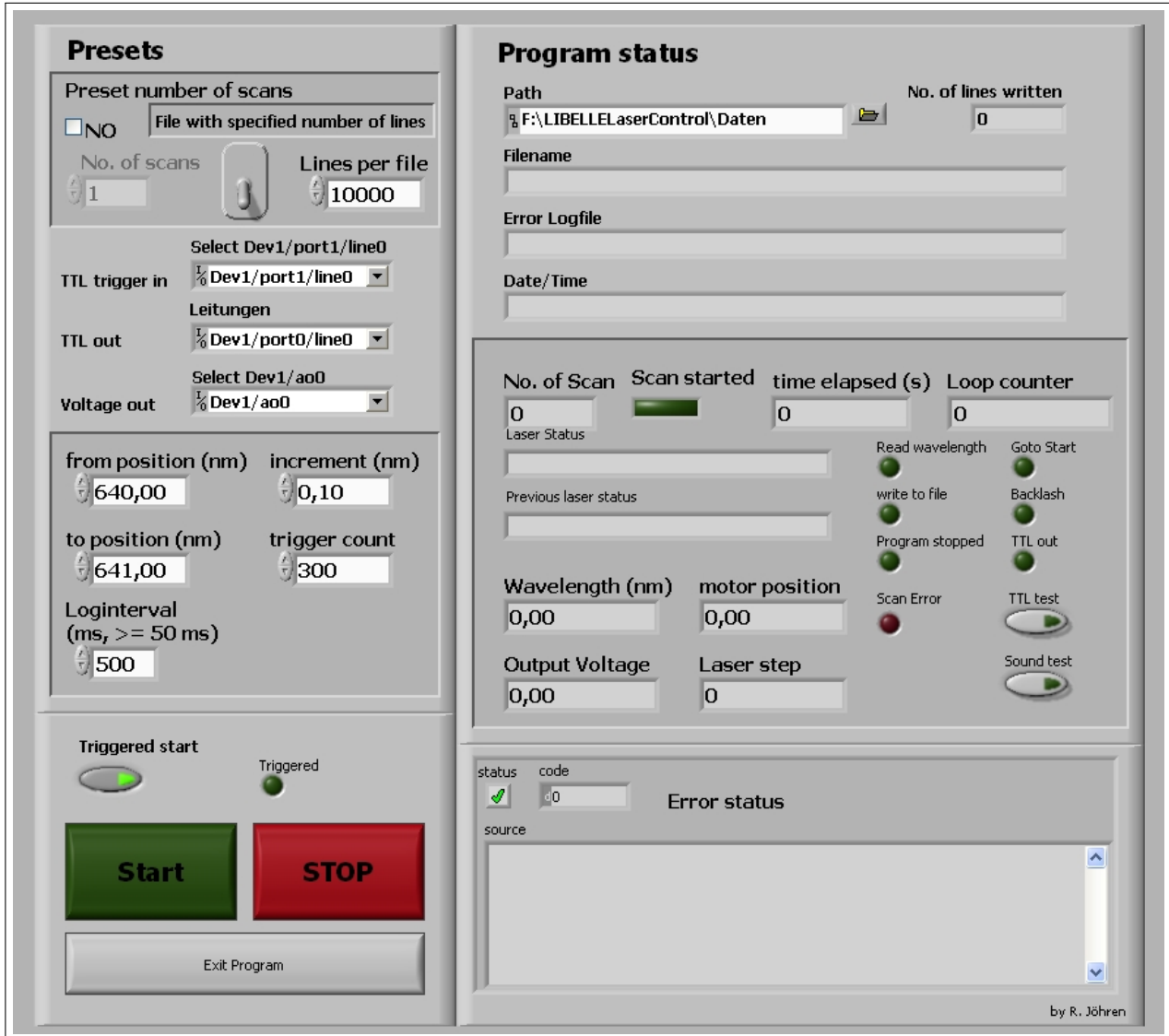


Figure 3.4.: User interface of the “Cobra Control” laser control program.

Presets: The left side of the interface comprises various parameters, that can be specified in order to perform the desired scan cycle.

- **Preset number of scans:** Enabling the check box activates the *No. of scans* field below. In this case the program will repeat a scan cycle with the given parameters the specified number of times.
- **Lines per file:** To prevent log-files from getting too big, the number of lines written to a single file can be limited to a certain value. This applies only if the lever is in the lower position, otherwise the file size of the log-file is not limited.
- **TTL trigger in:** Selection of the device and channel used to acquire the TTL trigger signal of the pumping laser. (During the beamtime one of the digital inputs of a

NI USB-6008 14-Bit Multifunction DAQ was used for this purpose.)

- **TTL out:** Used to propagate the laser status. High level: Laser is scanning. Low level: laser is busy shifting wavelength.
- **Voltage out:** Selection of the DAC output channel used to provide a voltage between 0 V and 5 V, corresponding to the current wavelength step, where 0 V corresponds to the initial and 5 V to the final step of the selected scan region. (During beamtime: analog output of the NI USB-6008.)
- **from position (nm):** Initial wavelength of the scan cycle.
- **to position (nm):** Final wavelength of the scan cycle.
- **increment (nm):** Step size in nm.
- **trigger count:** Defines the time the laser stays on a wavelength by specifying the number of incoming TTL trigger signals of the pumping laser (30 Hz) to count before shifting to the next wavelength, e.g. 180.
- **Loginterval:** Specifies the interval with which the laser status is written to a log-file. This file consists of seven columns:
 1. the number of the current scan (starts at 1 when the program is started)
 2. current date
 3. current time
 4. current LabVIEW timestamp¹
 5. the laser wavelength of the dye laser calculated from the motor position using the current calibration
 6. the motor position
 7. a string containing the laser status information
- **Triggered start:** Allows to chose whether the scan start should be triggered manually or by an external TTL signal, e.g. the status signal of the parabolic mirror system confirming the mirror position inside the beam pipe.

Program status: Besides the text field to choose the file path for log files, a TTL output and a sound test button, the right side of the interface contains only status information, which are self-explanatory by their titles.

¹seconds elapsed since midnight UTC, January 01 1912

3.2. Fluorescence light detection at the ESR

This section deals with the problems and solutions regarding the detection of fluorescence light emitted by relativistic lithium-like bismuth ions ($^{209}\text{Bi}^{80+}$) at the ESR. Prior to the 2011 beamtime the question arose, whether the existing detection system used in the previous beamtimes 1999 and 2003 was sufficiently sensitive to photons emitted in the very forward direction. These investigations have been performed in the diploma thesis of D. Anielski [Ani10] and led to the conclusion, that the segmented mirror section installed in the ESR mainly detects sideways emitted photons. Therefore, a decision was taken to build a novel detection system specialized for the detection of photons emitted under small angles relative to the beam direction. The main part of this new system is an off-axis parabolic mirror with a central slit, that can be moved into the beam. Thus, it is able to reflect photons emitted under small polar angles towards a detector. This system will be referred to as parabolic mirror system and it will be introduced in detail in section 3.2.3 along with another new detector system. Beforehand, the older detection system will be described and the assumptions made and the conclusions drawn in [Ani10] will be presented in this section.

3.2.1. The segmented mirror section

The so called mirror section has been the system used for fluorescence light detection in the previous experiments in 1999 and 2003 [See99]. The system has an overall length of 650 mm and features 10 mirror segments, each with a length of 55 mm. The segments consist of conically shaped upper and lower parts, that have an opening angle of 15° towards the beam direction. Detectors can be placed on the outside of three optical viewports equipped with re-entrance windows² with a diameter of 60 mm and a distance of 80 mm to the beam axis, enhancing the accessible solid angle. The system has, among others, been used for the detection of the $1s$ HFS transition in hydrogen-like lead ($^{207}\text{Pb}^{81+}$) and hydrogen-like bismuth ($^{209}\text{Bi}^{82+}$). However, the detection of the $2s$ hyperfine transition in $^{209}\text{Bi}^{80+}$ has been tried at GSI several times with this system, but no fluorescence signal was observed so far. The reasons for this problem were investigated by modeling the mirror section in an optical simulation using the GEANT4 software package (diploma thesis D. Anielski [Ani10]). It turned out, that the mirror section is not efficiently collecting forward emitted photons, but mainly detects sideways emitted photons, which, in the case of $^{209}\text{Bi}^{80+}$, have wavelength above 900 nm that are outside the range of the PMTs used in the experiment as will be shown in the following sections. During the LIBELLE beamtime the mirror section was

²The window is attached to the end of a piece of pipe, that extends on the vacuum side of the mounting flange.

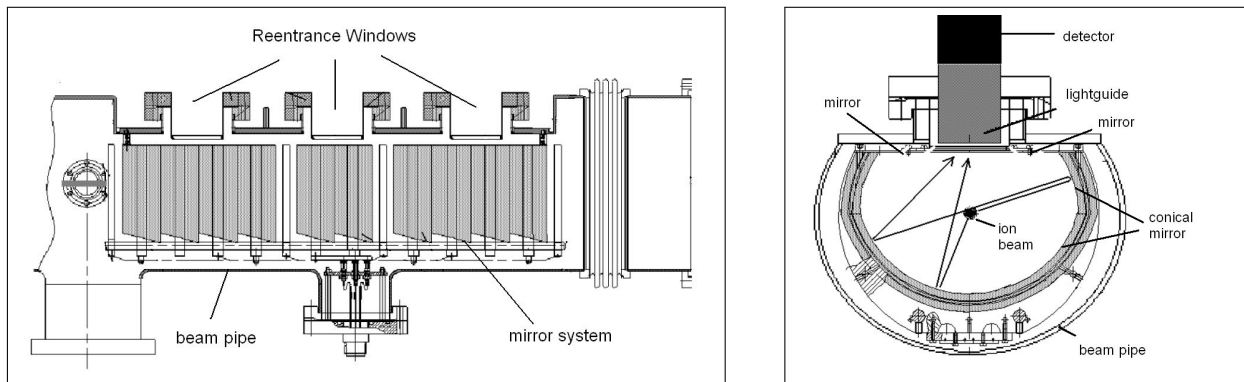


Figure 3.5.: Left: longitudinal section of the 650 mm long mirror section. Each of the ten mirror segments has a length of 55 mm an opening angle of 15° . Right: cross section of the mirror system showing the conical lower and upper part of the mirrors [See99].

used as primary detection system for the verification of the fluorescence signal of hydrogen-like bismuth. In the case of lithium-like bismuth, however, it was only used as secondary system in favor of the new parabolic mirror system.

3.2.2. Emission characteristics of relativistic excited ions

To estimate signal rates at the detectors, the emission characteristics of relativistic light sources have to be considered. Time dilation results in a longer lifetime of the excited hyperfine states. Also, the emission wavelengths are shifted, depending on the emission angle, due to the relativistic Doppler effect. The isotropic emission of fluorescence photons in the rest frame of the ions becomes forward peaked in the laboratory frame due to the Lorentz transformation between the systems, thus enhancing the number of short wavelength photons. In advance of the LIBELLE beamtime these effects were investigated regarding their influences on the efficiency of the existing detector system and on the layout of a possible new system. Simulations of the detector efficiencies have been performed in [Ani10]. In the following only the basic considerations will be explained and the results of the simulations will be discussed briefly.

3.2.2.1. Relativistic Doppler-effect and forward boost

In the following the ion is assumed to move only in z -direction. Starting with the Lorentz transformation [Dem10]

$$ct' = \gamma \cdot (ct - \beta z) \quad (3.1)$$

$$x' = x \quad (3.2)$$

$$y' = y \quad (3.3)$$

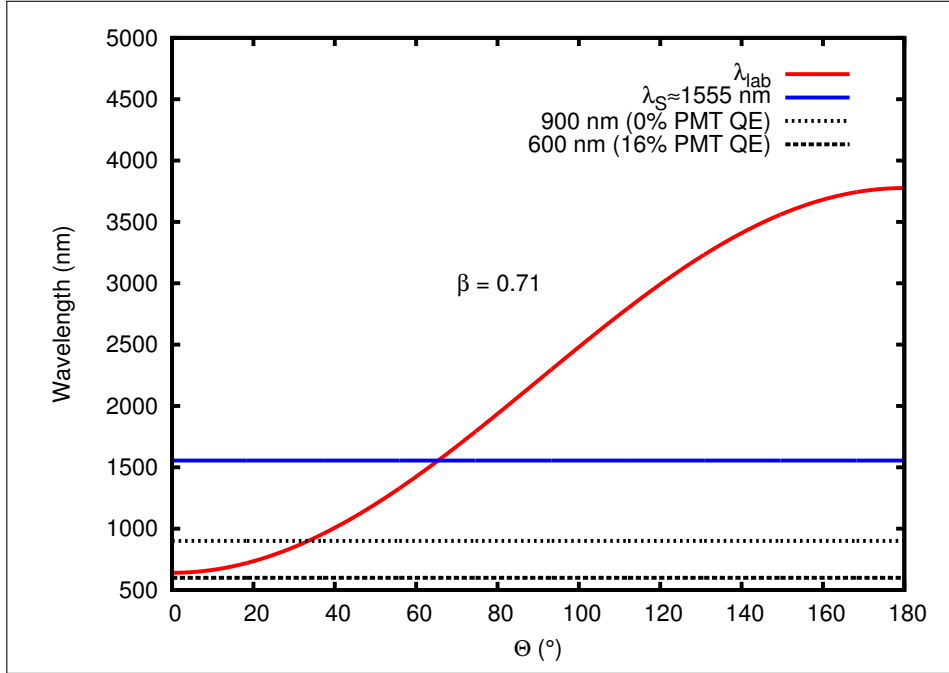


Figure 3.6.: Implications of the relativistic effects for $^{209}\text{Bi}^{80+}$ ions with a velocity $\beta = 0.71$: The wavelength λ_{lab} of the detected photons is Doppler-shifted depending on their detection angle Θ (red). The lowest detectable wavelength is about 640 nm at a polar angle of 0° , where the quantum efficiency of the selected Hamamatsu R1017 PMT is about 16%. The wavelength increases for greater polar angles, thus only angles up to 35° can be observed due to the vanishing PMT quantum efficiency at about 900 nm wavelength. The wavelength in the co-moving reference frame is about $\lambda_S \approx 1555$ nm (blue).

$$z' = \gamma \cdot (z - \beta ct), \quad (3.4)$$

which transfers the four-vectors (ct, x, y, z) from the laboratory rest frame to the primed four-vectors of the co-moving ion reference frame (ct', x', y', z') , which moves with the relativistic velocity $\beta = \frac{v_z}{c}$ in z -direction, it can be seen that time differences Δt in the rest frame appear longer than time differences $\Delta t'$ in the co-moving system (time dilation):

$$\Delta t = \gamma \cdot \Delta t'. \quad (3.5)$$

Since the emission rate of fluorescence photons depends on the inverse of the mean lifetime of the hyperfine state, a prolonged lifetime in the laboratory frame leads to a lower photon rate. This is important for the estimation of the measurement time needed to detect a fluorescence signal above background, as will be discussed later in this section. In the experiment the light source, i.e. the ions, is moving towards the static detectors with the velocity v_z . Therefore, the wavelength λ the detectors should classically observe is given by the oscillation period $T_S = \frac{1}{\nu_S} = \frac{\lambda_S}{c}$ of the source and the relative speed of source and detector, which is in this

case $c - v_z \cdot \cos(\Theta)$, taking into account the angle Θ between the velocity and the emission vectors:

$$\lambda = T_S \cdot (c - v_z \cos(\Theta)). \quad (3.6)$$

For a relativistic source the time dilation has to be considered in addition. In this case the period T_S has to be transformed according to equation (3.5), which leads to the relativistic Doppler effect

$$\lambda = \lambda'_S \cdot \gamma(1 - \beta \cos(\Theta)), \quad (3.7)$$

$$\nu = \nu'_S \cdot \frac{1}{\gamma(1 - \beta \cos(\Theta))}. \quad (3.8)$$

The implications of the Doppler shift for the fluorescence light detection in the LIBELLE experiment are depicted in figure 3.6. The red line shows the wavelength of photons emitted at an ion velocity of $\beta = 0.71$ as a function of the detection angle in the laboratory frame. The fine dotted black line represents the maximum wavelength detectable by a Hamamatsu R1017 PMT that will be used as detector, which corresponds to a maximum detectable polar angle of the photons of 35.6° .

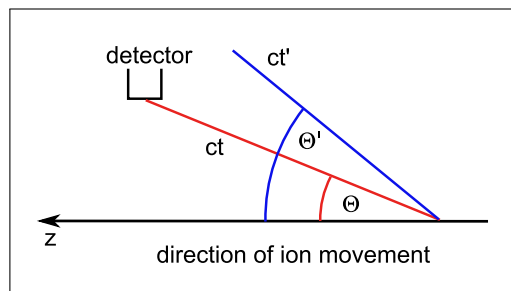


Figure 3.7.: Photons emitted by a relativistic light source under a polar angle Θ' are detected under an angle Θ in the detector's rest frame.

Another effect caused by special relativity is the fact that the detection angle Θ of photons emitted by relativistic light sources is smaller in the laboratory frame than the emission angle Θ' in the co-moving system (see figure 3.7). Since smaller angles in the frame of the detectors correspond to smaller wavelength according to equation (3.7), this is an advantage as smaller wavelength are easier to detect. The polar angles in the corresponding reference frames are given by [Ani10]:

$$\Theta' = \arccos\left(\frac{\cos \Theta - \beta}{1 - \beta \cos \Theta}\right) \quad (3.9)$$

$$\Theta = \arccos\left(\frac{\cos(\Theta') + \beta}{1 + \beta \cos(\Theta')}\right). \quad (3.10)$$

The enhanced emission rate in the forward direction is called relativistic boost, i.e. the relativistic light source, isotropic in the co-moving system, is no longer isotropic in the

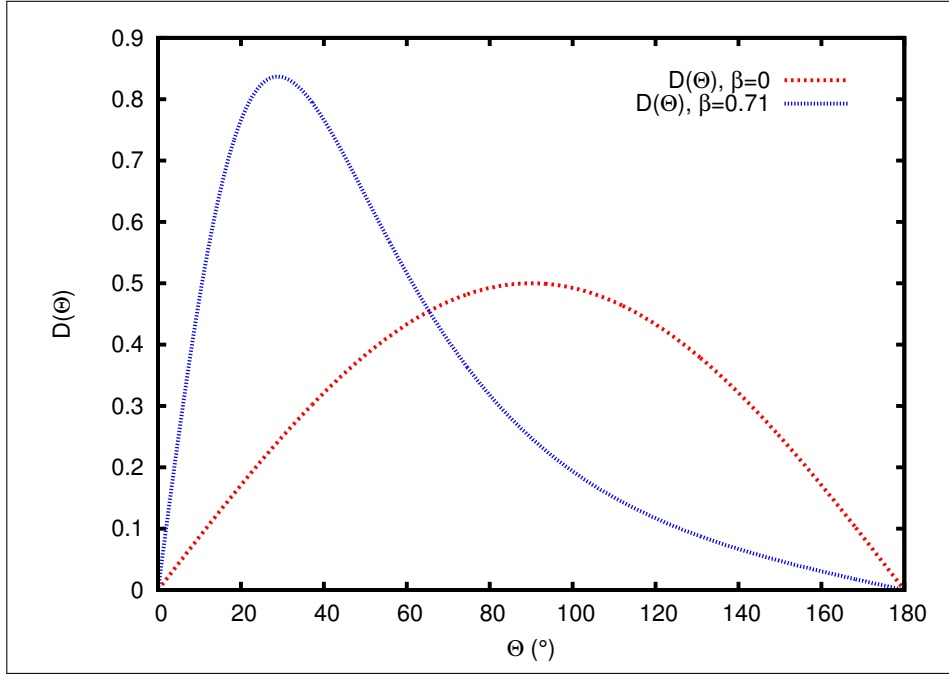


Figure 3.8.: Implications of the relativistic effects for $^{209}\text{Bi}^{80+}$ ions with a velocity $\beta = 0.71$: The relativistic boost, increases the fraction of photons emitted under small polar angles. The maximum of the distribution shifts from a polar angle of 90° for a source at rest to about 30° in the case of $\beta = 0.71$. The angular distribution $D(\Theta) = \frac{1}{2}R_{\Delta\Omega}(\Theta, \beta) \sin(\Theta)$ is shown for $\beta = 0$ and $\beta = 0.71$.

laboratory frame. With increasing β this effect also increases. This can be seen when looking at the ratio $R_{\Delta\Omega}$ of the solid angles Ω and Ω' . For the calculations spherical coordinates are used with the direction of motion of the light source along the z -axis. In this case the azimuthal angles have the same value in both the co-moving system and the rest frame, i.e. $\phi = \phi'$ as well as $d\phi = d\phi'$. Therefore, using equation (3.9) and expressing $\sin(\Theta')$ through Θ , $R_{\Delta\Omega}$ is given by:

$$R_{\Delta\Omega}(\Theta, \Theta') = \frac{\Delta\Omega'}{\Delta\Omega} = \frac{\sin \Theta' d\Theta' d\phi'}{\sin \Theta d\Theta d\phi} \quad \Rightarrow \quad R_{\Delta\Omega}(\Theta, \beta) = \frac{1 - \beta^2}{(1 - \beta \cos(\Theta))^2} \quad (3.11)$$

Now assuming a point-like photon source, where the distribution of the photons is rotationally symmetric with respect to the z -axis, the fraction of the photons emitted with angles between Θ_{\min} and Θ_{\max} , $F(\Theta_{\min}, \Theta_{\max})$, is given by:

$$F(\Theta_{\min}, \Theta_{\max}) = \int_{\Theta_{\min}}^{\Theta_{\max}} D(\Theta) d\Theta, \quad (3.12)$$

where

$$D(\Theta) = \frac{1}{2}R_{\Delta\Omega}(\Theta, \beta) \sin(\Theta) d\Theta \quad (3.13)$$

is the angular distribution of the photons, which depends on $R_{\Delta\Omega}(\Theta, \beta)$. $D(\Theta)$ is shown for $\beta = 0$ and $\beta = 0.71$ in figure 3.8. The Lorentz boost increases the fraction of photons emitted under small polar angles.

3.2.2.2. Number of excited ions

In order to estimate the signal rate, the number of excited ions present in the ESR has to be known. Prior to the beamtime the foreseen ion current in the LIBELLE experiment was 3 mA. The simulations performed in [Ani10] and [Han13] are based on this value. During the beamtime the average ion current was about 1.8 mA, half of which was concentrated in the signal bunch. The number of excited ions in that bunch depends on some assumptions [Nör09]:

1. Due to a beam shift caused by the dipole magnets of the electron cooler, the straight section that can be used for laser excitation on the east side of the ESR is the length of 2.5 m of the electron cooler itself. In combination with the bunch profile and the pulse duration of the anti-collinear laser beam, only about 25% of the ions could be geometrically reached [Win99].
2. Due to the velocity distribution of the ions the resonance is Doppler-broadened. Thus only a fraction of 5% [See99] to 25% [Win99] of the accessible ions can be excited by the narrow-band laser.
3. In the time span between the laser pulses the ions interact with each other. This results in a change of velocity and some of the ions previously not in the bandwidth region of the laser can now be excited. Therefore, the effective bandwidth of the laser is enhanced.
4. Collisions of the ions with residual gas molecules result in a decreasing ion current. Storage times of some 10 s up to several minutes are expected depending on the experimental conditions.
5. Due to the effect of stimulated emission only 50% of the suitable ions can be transferred into the excited state in equilibrium.

The ion current I_{ion} is given by the number of ions N , the charge of the ions Q and their revolution period T_{cycle} . With T_{cycle} depending on the ESR circumference l_{ESR} and the ion

Table 3.1.: Estimated photon rates for 3 mA and 1.8 mA ion current. The values for 3 mA are taken from [Ani10]. The values for 1.8 mA are estimated with the same assumption for the mean ion current during the $^{209}\text{Bi}^{80+}$ measurements at the LIBELLE experiment. The fluorescence photons N_p are equally distributed over the circumference of the ESR.

ion current (mA)	$N_{exc.,0}$	f_{laser} (Hz)	N_p (s^{-1})
3	$2 \cdot 10^5$	50	$1.58 \cdot 10^6$
1.8	$1.2 \cdot 10^5$	30	$8.93 \cdot 10^5$

velocity β , $T_{\text{cycle}} = \frac{l_{\text{ESR}}}{\beta \cdot c}$, it can be derived:

$$I_{\text{ion}} = \frac{N \cdot Q}{T_{\text{cycle}}} \quad (3.14)$$

$$\Rightarrow N = \frac{I \cdot T_{\text{cycle}}}{Q} = \frac{I \cdot l_{\text{ESR}}}{Q \cdot \beta \cdot c}, \quad (3.15)$$

where c is the speed of light. An ion current of 3 mA of $^{209}\text{Bi}^{80+}$ at a velocity $\beta = 0.71$ in the ESR with an orbit length of about $l_{\text{ESR}} = 108$ m then leads to

$$N = \frac{3 \cdot 10^{-3} \frac{\text{C}}{\text{s}} \cdot 108 \text{m}}{80 \cdot 1.6 \cdot 10^{-19} \text{C} \cdot 0.71 \cdot 3 \cdot 10^8 \frac{\text{m}}{\text{s}}} = 1.2 \cdot 10^8 \quad (3.16)$$

$^{209}\text{Bi}^{80+}$ ions in the ESR, divided into two bunches with about $6 \cdot 10^7$ ions each. With the above assumptions after several laser shots the number of excited ions in the signal bunch should balance around $2 \cdot 10^5$ after each laser pulse [Nör09]. These values have been used in the simulations. However, during the beamtime the average ion current was only around 1.8 mA. In this case the number of excited ions would drop to about $1.2 \cdot 10^5$.

In [Ani10] also the number of fluorescence photons emitted by the excited ions between two laser pulses was calculated. The number of emitted photons is given by the difference of the number of initially excited ions just after the laser pulse $N_{exc.,0}$ and the number of excited ions $N_{exc.,t}$ at the time $t = 1/f_{laser}$:

$$N_p = N_{exc.,0} - N_{exc.,t} = N_{exc.,0} - N_{exc.,0} \cdot e^{-\frac{t}{\gamma\tau}} = N_{exc.,0} \cdot \left(1 - e^{-\frac{1}{\gamma\tau f_{laser}}}\right), \quad (3.17)$$

where $\tau = 82$ ms is the life time of the $2s$ hyperfine state in $^{209}\text{Bi}^{80+}$ [Sha98], that has to be multiplied with the relativistic γ factor, due to the time dilation.

3.2.2.3. Simulated signal rates and detection times

To check the performance of the existing mirror section and of the newly designed detection system, GEANT4 [All03] based optical tracking simulations have been performed [Ani10,

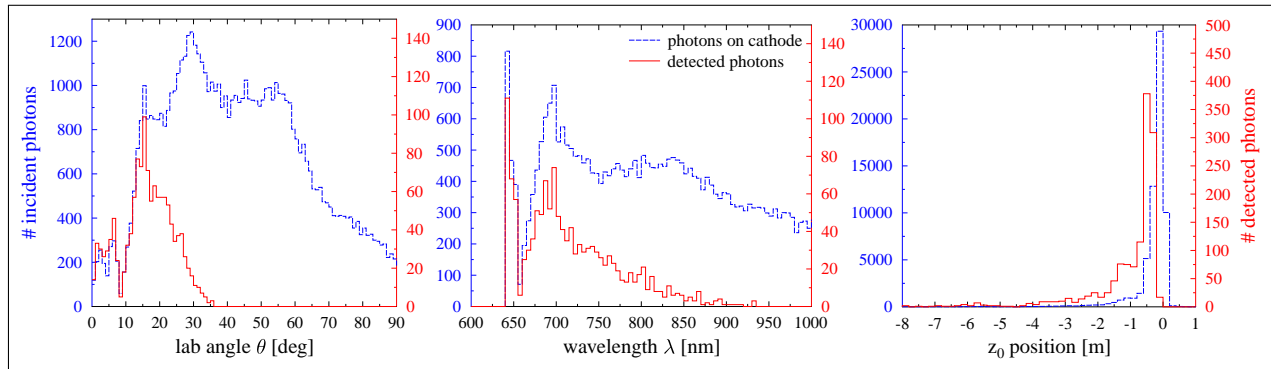


Figure 3.9.: Simulation results for the mirror section. Only the results for the third detector are shown, which collected the highest number of photons. The dashed blue curves represent the distributions of emission angles, wavelengths and starting distances of those photons that are guided onto the photocathode of the PMT. The red curves are the corresponding distributions of the photons that are actually detected, given the quantum efficiency of the PMT used [Han13].

Han13]. An ion velocity of $\beta = 0.71$ was assumed along with a number of excited ions of $N_{\text{exc},0} = 2 \cdot 10^5$. The event generator of the simulation software produced fluorescence photons emitted along the 11 m long straight section of the ESR beampipe before the mirror section [Han13]. For the stainless steel of the beampipe a reflectivity of 25% was assumed. The background was simulated by applying a simple model of excited residual gas molecules, homogeneously distributed in the beampipe. The results of the simulations for the mirror section are shown in figure 3.9 and the corresponding results for the parabolic mirror system in figure 3.10. For the mirror section only the results for the last of the three detectors are shown, since in the simulations it had the highest count rate. It can be seen that only a small fraction of the photons that hit the PMT's photocathode are emitted under a detectable angle resulting in a detectable photon wavelength. The results for the parabolic mirror show a better situation. Besides the overall higher count rate, the largest part of the fluorescence photons hitting the photocathode feature detectable angles and wavelengths in the region from 640 nm to 700 nm, where the QE of the R1017 is still above 5%. As intended by the design, the small polar angles of the photons are collected very efficiently.

For an experiment relying on the assignment of beamtime at an accelerator facility, it is important to prove, that the aim of the experiment can be achieved in the available time. For the mirror section as well as the new parabolic mirror system, signal and background rates were extracted from the simulations, allowing an estimation of the time needed to detect a resonance signal with a significance of n times the uncertainty of the signal. Considering two bunches coasting in the ESR, where one of the bunches is excited by the laser (signal bunch) and the other is not (reference bunch), the signal rate S at the detectors caused by

3. The LIBELLE Experiment

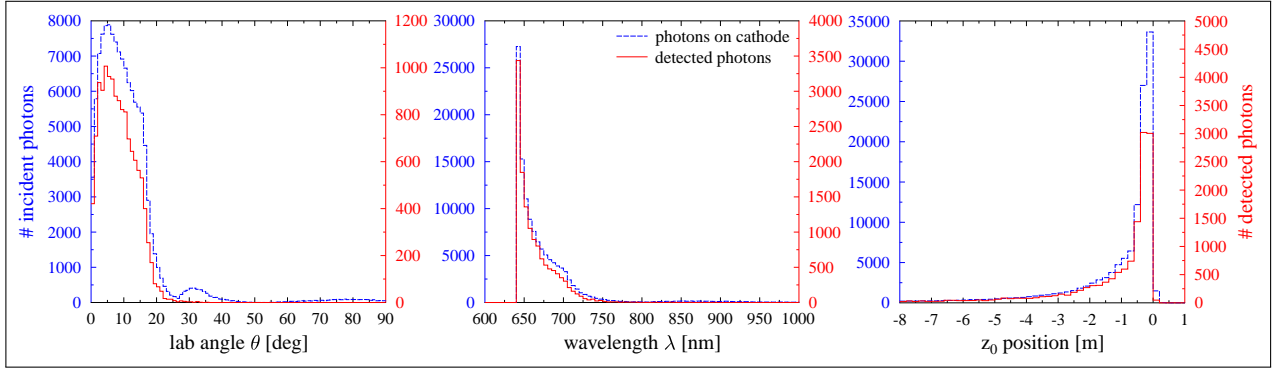


Figure 3.10.: Simulation results for the parabolic mirror system. The dashed blue curves represent the distributions of emission angles, wavelengths and starting distances of those photons that are guided onto the photocathode of the PMT. The red curves are the corresponding distributions of the photons that are actually detected, given the quantum efficiency of the PMT used [Han13].

the fluorescence photons is given by

$$S = R_S - R_R, \quad (3.18)$$

where R_R is the count rate recorded with the reference bunch passing the detectors and $R_S = R_R + S$ is the equivalent count rate of the signal bunch. If the signal bunch is not excited, the signal rate is $S = 0$ and the background rates of the two bunches should more or less cancel out. The error of the signal rate S is given by:

$$\Delta S = \sqrt{R_S + R_R}. \quad (3.19)$$

Since the signal rate S is small compared to the background rate ($S \ll R_R$), we have $R_S \approx R_R$ and therefore $\Delta S \approx \sqrt{2R_R}$. The rate R_R of the reference bunch can be written as the sum of the background induced by photons in the ESR B_{ESR} , e.g. from rest gas excitation, and the dark count rate D of the detector:

$$R_R = B_{\text{ESR}} + D. \quad (3.20)$$

To obtain an estimate of the time needed to detect a signal with a significance $n \cdot \sigma$, the signal $S \cdot t$ recorded in a certain time t has to be larger than n times its uncertainty:

$$S \cdot t \geq n \cdot \sqrt{2 \cdot (B_{\text{ESR}} + D) \cdot t} \quad (3.21)$$

$$\Leftrightarrow t \geq \frac{2 \cdot n^2 \cdot (B_{\text{ESR}} + D)}{S^2} \quad (3.22)$$

The required measurement times in table 3.2 have been calculated using equation (3.22)

Table 3.2.: Simulated signal and background count rates for the mirror section (combined results of all three detectors) and the parabolic mirror system. The reflectivity of the beam pipe is expected to be $R = 25\%$. The detector simulated was a selected Hamamatsu R1017 with the quantum efficiency increased by factor 1.4 compared to a standard R1017. The quoted measurement times are calculated using equation (3.22) with the significance multiple $n = 3$ [Ani10].

	signal rate (s^{-1})	background rate (s^{-1})	measurement time (s)
Mirror section	15.4 ± 0.5	626 ± 7	47.6 ± 0.9
Parabolic mirror	86.0 ± 0.6	453 ± 9	1.1 ± 0.01

with $n = 3$. The signal and background rates needed for the calculation have been extracted from the GEANT4 simulations and are presented in table 3.2 along with the corresponding measurement times. Based on the data acquisition system used in previous experiments, for the simulations it was implied that the data acquisition is only active during those intervals when the two bunches are actually passing the detector. The resulting duty cycle of the data acquisition was assumed to be 20%.

Finally, the simulations of the two detector systems result in an improved signal rate observed with the new setup, which is more than 5 times higher than for the mirror section. At the same time the background is significantly reduced as well as the measurement time per wavelength step required to detect the fluorescence signal, which is lowered by more than a factor 40 for the new detector system.

3.2.3. New detector systems

In order to detect photons emitted under small polar angles, which experience the maximum Doppler shift to smaller wavelength, more efficiently, two new systems were developed and built:

- A forward detection system that is located at a window at the upstream end of the western straight section of the ESR, which detects photons emitted by the ion bunch under the smallest angles (including 0°) just before the ions are bent around the corner by the north western dipole (see figure 3.2).
- The already mentioned off-axis parabolic mirror with a central slit, which can be moved into the beam and reflects photons emitted under small polar angles towards a detector.

While the expected count rates of the forward detection system are rather low due to the small solid angle covered, high expectations laid on the movable mirror system, since the results of the simulations regarding the performance and efficiency of this system were promising.

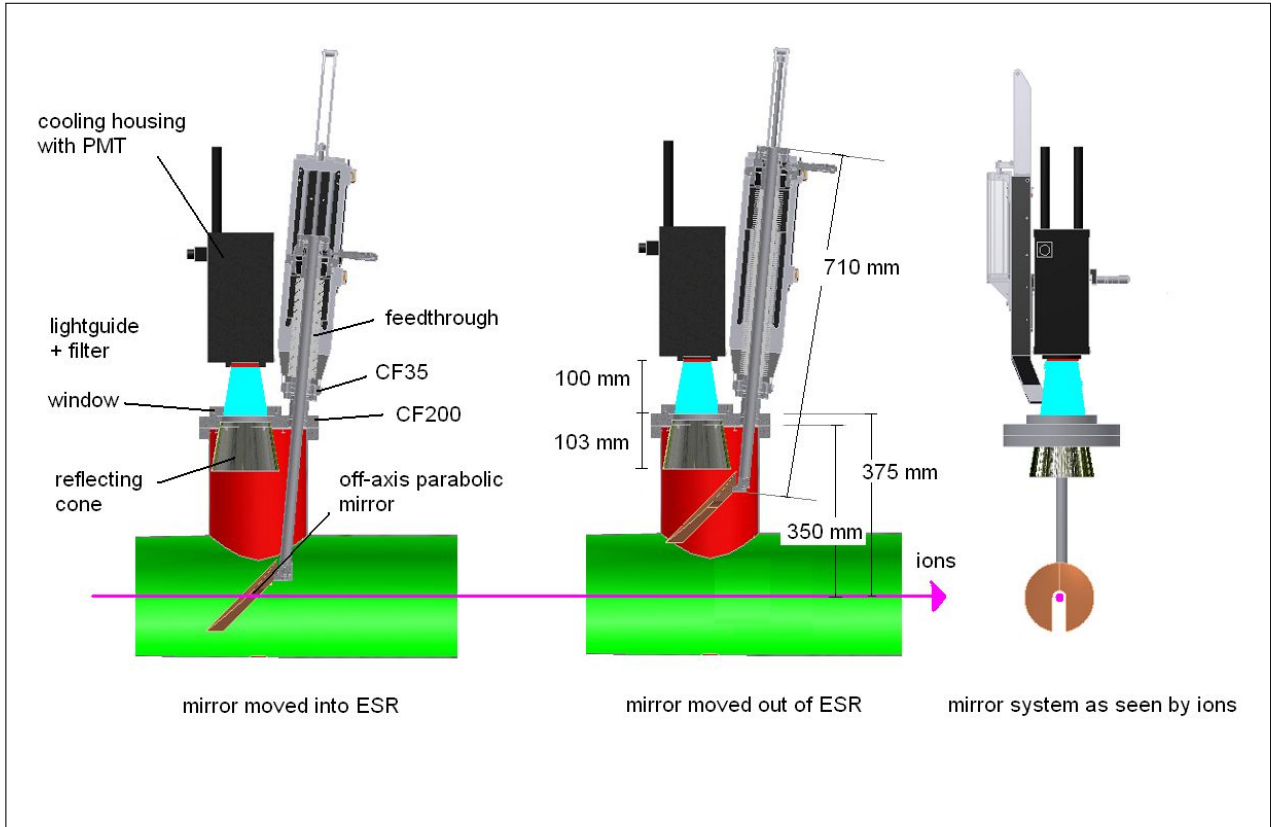


Figure 3.11.: Setup of the parabolic mirror system. The mirror is moving horizontally, thus the cross sections shown represent the view from above the ESR. Left: mirror in the extended state. Middle: mirror in the retracted state. Right: mirror as seen by the ions, tilted counter-clockwise by 90° when installed at the ESR [Ani10].

3.2.3.1. The parabolic mirror system

With the parabolic mirror system a novel detection system was introduced to the ESR in the LIBELLE beamtime. The main element of the system is an off-axis parabolic mirror with a diameter of 150 mm made of oxygen free, high conductivity (OFHC) copper that can be moved into the beamline to collect photons emitted by the coasting ions under small polar angles. The mirror features a central hole with 3 cm diameter, extended on one side to a 3 cm wide slit. The width of the slit has been chosen such that it can be moved into a pre-cooled ion beam only disturbing it sparsely [Ani10].

The mirror was manufactured by LT Ultra Precision Technology GmbH [LTU12] and has a finish roughness of less than 20 nm with an overall shape accuracy of about $2 \mu\text{m}$. The reflectivity of the material has been measured to be $R > 95\%$ above 635 nm [Lop10].

When placed inside the beam line the mirror reflects fluorescence photons emitted by the ions orbiting the ESR towards a VAb model SFK100 CF 100 kodial glass window with a diameter of 89 mm, mounted on a CF 200 flange connected to the ESR beam tube (see figure 3.11

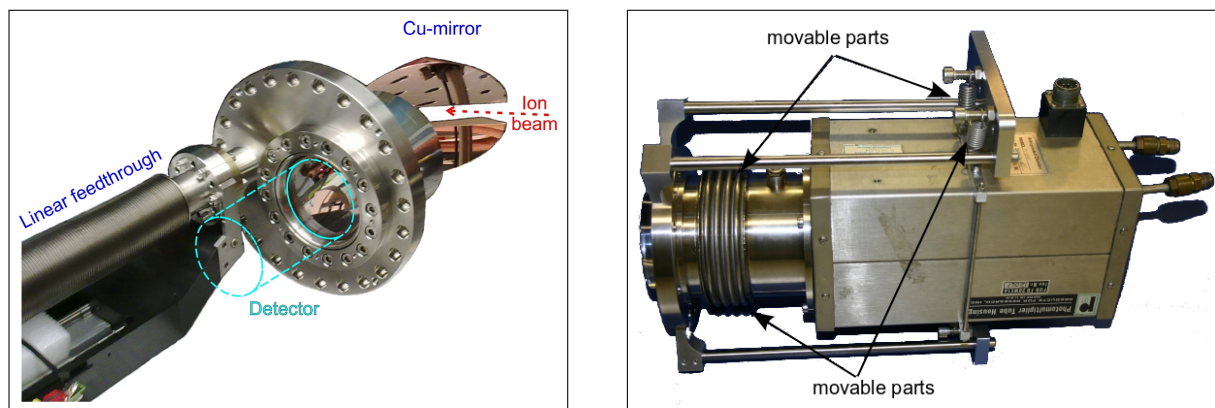


Figure 3.12.: Left: The mirror system without the detector module. Right: The detector module, consisting of the light guide, the PMT cooling housing and the PMT (inside the housing).

and 3.12). A 160 mm plexiglass lightguide attached to the window on the outside collects the photons and focuses them on a Hamamatsu R1017 PMT placed in a PR-TE104RF cooling system, cooling the PMT to $T = -20^{\circ}\text{C}$. The light guide itself is surrounded by a stainless steel bellow pressing it onto the window. Between the PMT's photo cathode and the light guide an optical bandpass filter is placed, consisting of a Schott OG long pass filter [Sch08] and a Balzers CALFLEX X heat protection filter [Bal08]. The bandpass removes background photons outside the region of interest by only transmitting wavelengths from 590 nm to 725 nm. On the vacuum side of the window a cone made of MIRO-2 aluminum alloy is installed to enhance the solid angle of the detector. An additional CF 35 flange attached to the CF 200 base flange is used for the mounting of a linear feedthrough based on a VAb model KPM 12-200 [VAb12], which has a range of movement of 180 mm and is driven by a pneumatic cylinder with end position dampening (Festo, ADVU-32-180-P-A) to avoid vibrations of the mirror mounted on the feedthrough. A special double walled stainless steel rod has been manufactured to hold the weight of ca. 3 kg of the copper mirror. The transversal position of the mirror can be adjusted up to ± 12.5 mm by micrometer screws, that move the mounting base of the rod transversal to the feedthrough direction, to adjust the mirror slit to the beam position. Additionally, a counter weight on a pulley has been installed to compensate for the torque of the mirror and the pull of the vacuum on the feedthrough and thus smoothening the mirror movement.

The system has to adhere to ESR vacuum policies. It is not allowed to introduce a leak rate $> 1 \cdot 10^{-10}$ mbar l/s to the ESR vacuum system and has to be suitable for bake out cycles heating up the surfaces of the beampipe to 350°C , while the rest of the system will reach temperatures of about 230°C .

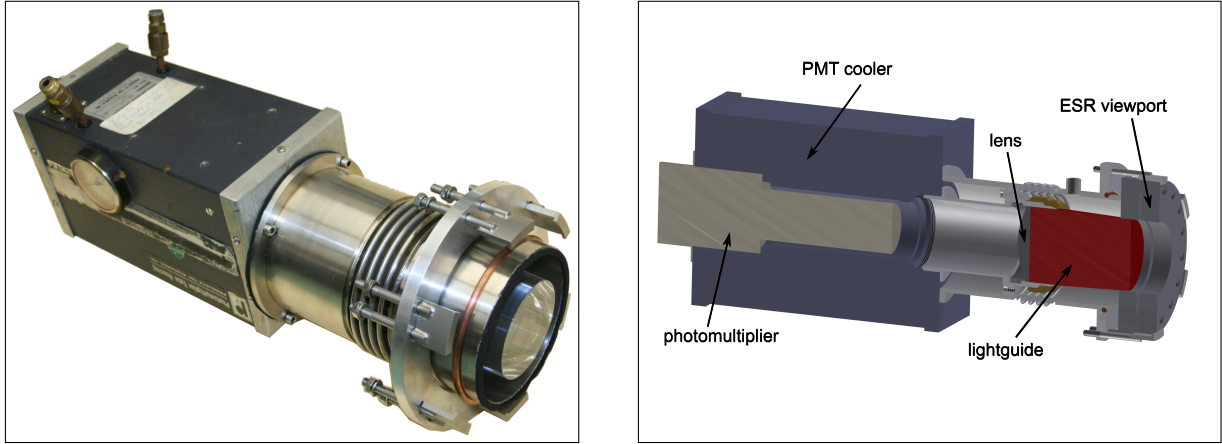


Figure 3.13.: The forward detection system. Left: Photograph of the system. Right: Cross section.

3.2.3.2. The forward detection system

The forward detection system (figure 3.13) was introduced as another secondary detection system in the LIBELLE beamtime [Ani10, Lop10]. It is placed in forward direction with respect to the beam orbit on an exit window, normally used for coupling laser beams into the ESR on the westward straight section, located near to the north-west dipole. The system was mounted on a DN 100 CF window flange with a window diameter of 89 mm. A stainless steel adapter keeps the system light tight and houses a light guide which transports the light exiting the window onto a LA 1002 N-BK7 plano-convex uncoated lens from Thorlabs [Tho12] that focuses it to the detector. The detector used in the forward detection system is a Hamamatsu PMT R943-02 with an active area of 10×10 mm and a gain of about $5 \cdot 10^5$. It is housed in a TE-210RF PMT cooler, which allows for operation of the PMT at temperatures 60° below the cooling water temperature, thus reducing the PMT temperature to around -35° and the dark count rate to about 20 s^{-1} . The PMT is also equipped with two optical filters creating an optical bandpass filter around the wavelength region of interest, attached to the PMT entrance window with optical grease.

Simulations of the efficiency of the forward detection system estimated a signal rate of $S = (2.1 \pm 0.1) \text{ s}^{-1}$ with an overall background of $B = (29.7 \pm 1.4) \text{ s}^{-1}$, resulting in a measurement time of about 120 s for a signal with 3σ significance [Ani10]. The main purpose of this system was therefore to be used as a diagnostic tool and as fallback should the other system exhibit too high background rates.

3.3. LIBELLE Data acquisition

This section will describe the Data Acquisition (DAQ) system set up for the LIBELLE beamtime, schematically shown in figure 3.14. Firstly, the hardware and cabling will be explained and secondly the structure of the data taken will be shown.

3.3.1. The DAQ system

The main components of the DAQ system were a VUPROM and an E7 CPU board, both VME based modules. The VUPROM was used for gathering and buffering the incoming signals. It features 32 input channels, all operated as scalers, where the first 16 channels were additionally configured as multi-hit double-buffer TDC operated in common stop mode. The E7, a Motorola 68040 based VME computer board running the GSI Multi Branch System (MBS) software [Du96], was used to read and reset the TDC buffers and scaler channels of the VUPROM and arrange the data to events with an event builder triggered by a 200 Hz clock. The events were written to a network storage in data files of a maximum size of 100 MB.

The TDC channels of the VUPROM were started by the detector signals while the common stop signal was provided by the output of a rate divider, scaling down the frequency of the HF master oscillator by a factor of 200 (see figure 3.14). The values written to the TDC buffer represent the number of the clock cycles before common stop with a clock period of 3.33 ns, which is the TDC time resolution [Min12]³.

3.3.2. Recorded signals

During the beamtime several detector signals and status values were recorded. Table 3.3 shows the input configuration of the VUPROM VME module. The TDC was used to tag the signals of the photon detectors, while the slow-control parameters were recorded using the remaining scaler channels.

3.3.2.1. Photon detectors

The signals of 12 detectors were recorded by the VUPROM's TDC. Six of these detectors were dedicated to scan for the fluorescence signal. They were located at the mirror section (solar blind PMT, R1017_1, R1017_2, R1017_3), at the parabolic mirror system (PMT mirror system, also an R1017) and at the forward detection system (Hamamatsu PMT R943-02).

³The exact time resolution of $\frac{10}{3}$ ns is given by a 300 MHz clock.

Table 3.3.: VUPROM TDC and scaler channel assignment.

	VUPROM channel	comment
TDC & scaler	0	PMT mirror system (selected Hamamatsu R1017)
	1	Solar blind PMT (mirror section)
	2	R1017_1
	3	R1017_2
	4	R1017_3
	5	Forward detection system (Hamamatsu R943-02)
	6	UV PMT bottom
	7	UV PMT horizontal
	8	Channeltron
	9	Target PMT
	10	Photo diode north east (entrance collinear)
	11	Photo diode south east (entrance anti-collinear)
	12-14	unused
	15	Pumping laser Q-switch
	scaler	16
17		Injection
18		U electron cooler (U_{EC})
19		I electron cooler (I_{EC})
20		p_{gun} pressure @ electron cooler
21		p_{coll} pressure @ electron cooler
22		divided RF cavity frequency (1/200)
23		clock (1 MHz)
24		Cu mirror inner switch
25		Cu mirror outer switch
26		SIRAH laser scan start
27		SIRAH laser trigger out (inverted: logic 1 = busy)
28		next wavelength bin
29		frequency representing wavelength step of the dye laser
30-31		unused

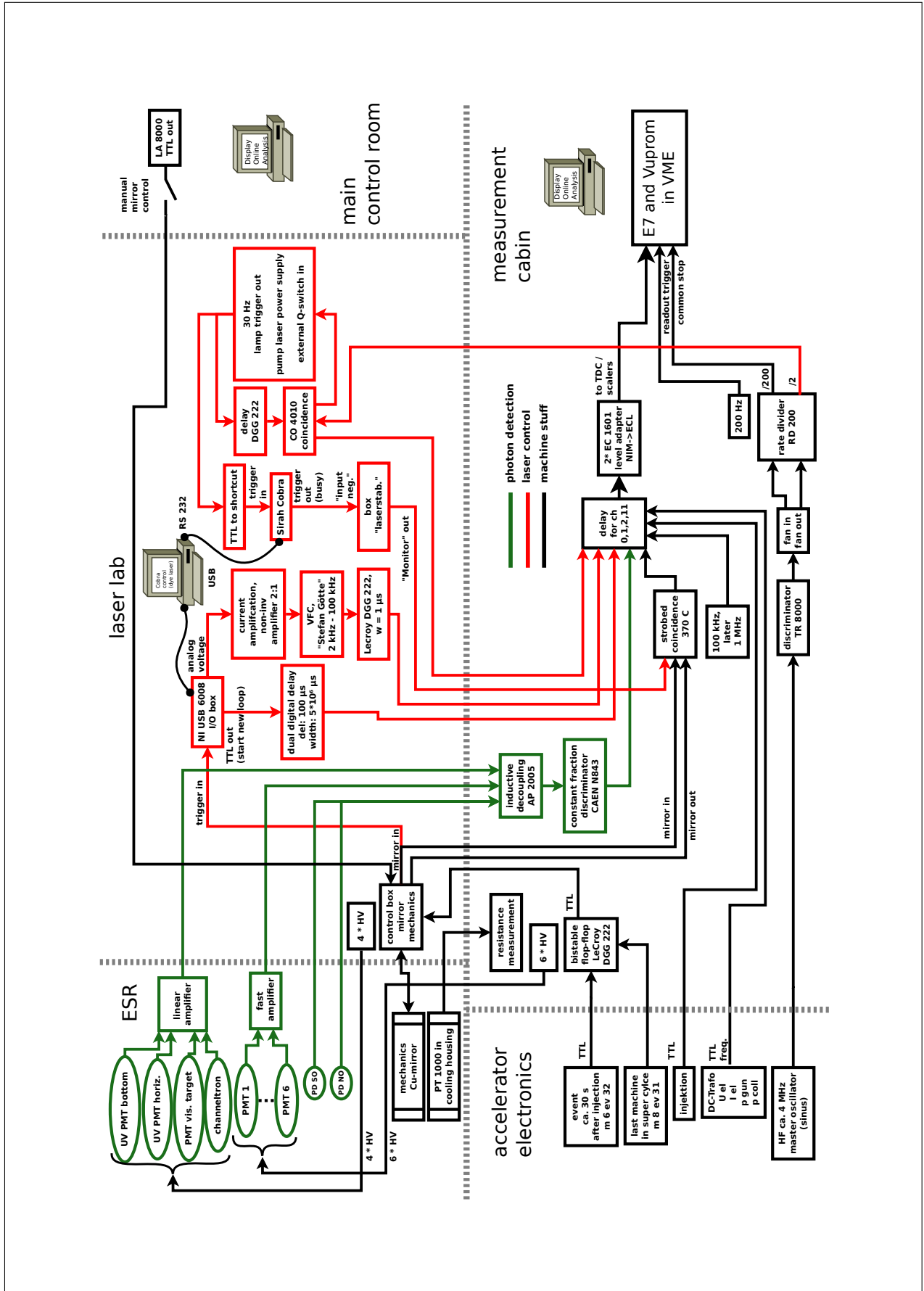


Figure 3.14.: Schematic overview of the cabling of the LIBELLE control and DAQ system.

The signals of these photomultipliers were amplified by a CAEN Mod. 979 16 channel fast amplifier before signal transfer to the measurement cabin (figure 3.14) and there fed to a AP 2005 inductive decoupling unit before being processed by a CAEN model N843 16 channel constant fraction discriminator. Four additional detectors were mounted at various places of the ESR. Another photomultiplier was located at the gas-jet target, whereas two UV PMTs and a channeltron were located between the gas-jet target and the mirror section [Loc12]. The signals of these detectors were amplified and also passed to the inductive decoupling unit and the constant fraction discriminator. For accurate timing the signal travel times of all detectors were matched with delay units as needed before being translated for the VUPROM input by two EC 1601 NIM to ECL level adapters.

In order to determine the moment of the entrance of the laser pulse into the ESR, photo diodes were placed near the laser entrance windows of the ESR. The signals of these diodes were also recorded using the TDC. Besides the various photon detectors the only other parameter recorded by the TDC was the Q-switch signal of the pumping laser.

3.3.2.2. Laser status and wavelength step

For analysis issues, especially for improved online analysis during the beamtime, an additional signal representing the current wavelength step was implemented in the dye laser control program. The “Cobra Control“ program used a NI USB-6008 12 bit multifunction DAQ connected to the laser control computer to deliver a voltage proportional to the current laser wavelength. This voltage output was processed by a voltage to frequency converter (VFC) to obtain frequencies between 2 kHz for the initial and 100 kHz for the final wavelength step, which were then recorded by one scaler channel of the VUPROM.

3.3.2.3. Machine and ion beam parameters and timing

Also several other parameters of the ESR were recorded by the scaler inputs. This includes the DC-Trafo value, from which the ion current can be calculated, the acceleration voltage U_{EC} and the electron current I_{EC} of the electron cooler and the pressures p_{gun} and p_{coll} at either side of the electron cooler, which were all provided as TTL frequency signals. Also a TTL signal triggered by the injection of ions into the ESR was recorded.

The TDC common stop signal was provided by the 200th fraction of the HF master oscillator (≈ 4 MHz), which was also recorded, whereas the VUPROM readout was triggered by an external 200 Hz pulser. To determine the duration of an event or a wavelength scan step, the signals of a 1 MHz clock were counted.

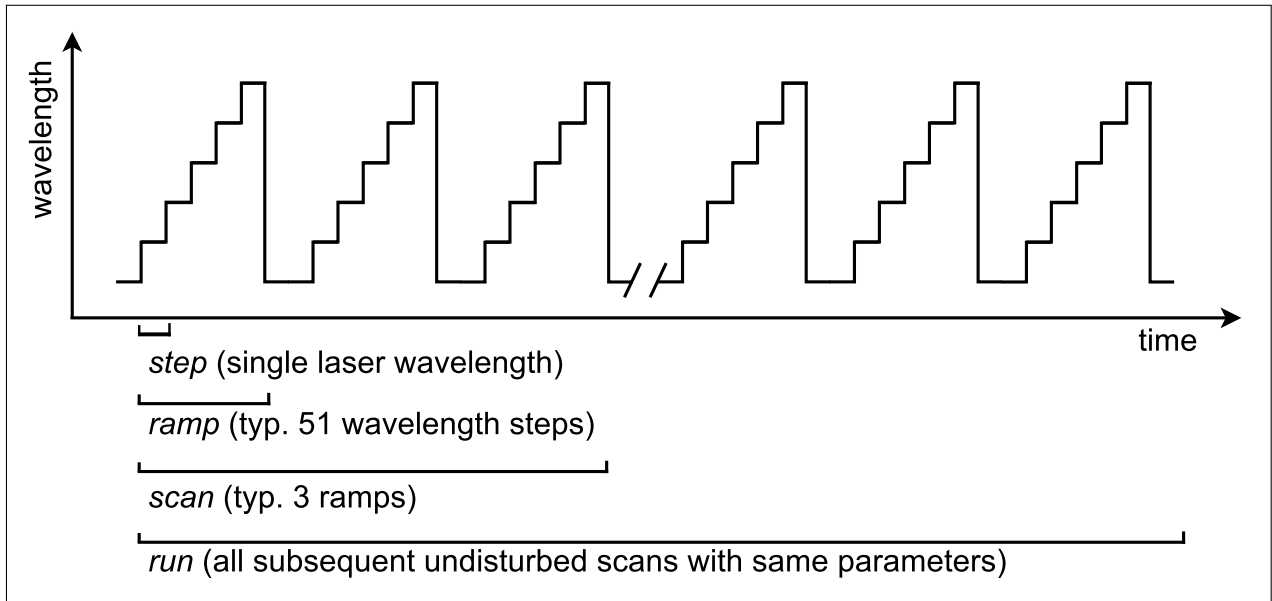


Figure 3.15.: Structure of the data taking during the $^{209}\text{Bi}^{80+}$ measurements of the LIBELLE beamtime. Per *scan* cycle three laser *ramps* of each 51 wavelength *steps* were recorded. Afterwards the MBS was reset and new ions were injected to the ESR. All *scans* subsequently taken with the same parameters are summarized to a *run*.

3.3.3. Data format

As already mentioned, the data taken by the VUPROM were read out and written to disk by the GSI MBS software running on a E7 VME Processor board. It stored the events to “.lmd” files with a maximum size of 100 MB.

Since the event builder was running at a frequency of 200 Hz, several TDC common stop periods were recorded within one event. The TDC data contain integer numbers representing the number of TDC clock cycles to the next common stop signal and are written to one of two buffer memories. When the event is built the buffer memory is read and reset. Thus the TDC data of the several common stops per event can not be re-assigned to an absolute time, but the relative time to the common stop stays true. A single event in the data files is comprised of several elements:

- An array of integer values labeled `scalerSubEvent[MAX_SCA]`, where `MAX_SCA=32` for the number of scaler channels of the VUPROM.
- A vector of “TArrayI”-type integer arrays labeled `tdcSubEvent[MAX_TDC]` and containing the TDC data, where `MAX_TDC=16` since the TDC consists of 16 channels. Each of the array elements contains another array of varying size, comprised of the integer values of the clock cycles prior to a common stop signal, where an event in the corresponding detector was registered.

- A `time_t` value containing the UNIX time stamp⁴ of the event building time, labeled `eventTime`.
- An integer value `eventTimeMilliSec`, adding a millisecond scale to the event time.
- An integer value labeled `eventCount` used as index for the events.
- Another integer value labeled `eventSizeMbs`, referring to the size of the data package.

A scan pattern was introduced in order to deal with certain problems, that arose during the beamtime. It is shown in figure 3.15. To account for the decreasing ion current and stability problems of the MBS software, a *scan* consisting of three subsequent wavelength *ramps* of the laser, each comprised of 51 wavelength *steps*, was performed. After each *scan* the MBS was reset and new ions were injected into the ESR. Therefore, the mirror had to be retracted from the beam until sufficient ion cooling after the injection. The data taken during a single *scan* were accumulated by the MBS to typically 2-3 `.lmd` files. The analysis described in the next chapter partially resorts to this *scan*, *ramp*, *step* structure introducing an additional superordinated *run* object, including all *scans* subsequently recorded with the same scan parameters.

⁴seconds elapsed since midnight UTC, January 01 1970

LIBELLE BEAMTIME AND DATA ANALYSIS

This chapter deals with the data analysis of the LIBELLE beamtime. The first section will briefly lay out the beamtime schedule and analyze the performance of the new parabolic mirror system. The second section will discuss the steps of the data analysis in detail and present the obtained results for the transition wavelengths in the laboratory frame in both H-like and Li-like bismuth. The transformation of these wavelengths to the ions' rest frame will be carried out in chapter 5.

4.1. LIBELLE beamtime

In this section the beamtime parameters and the DAQ system along with the structure of the data taken at the LIBELLE experiment will be discussed briefly. The beamtime took place from Monday, 1st of August 2011 to Tuesday, 9th of August 2011 at GSI. It was divided into three phases, looking for the resonance in H-like $^{209}\text{Bi}^{82+}$, the resonance in Li-like $^{209}\text{Bi}^{80+}$ and for the lifetime of the upper $2s$ hyperfine state in $^{209}\text{Bi}^{80+}$, respectively.

4.1.1. Beamtime schedule and experimental data

The first of the three phases was used to scan for the resonance of the $1s$ hyperfine transition in H-like $^{209}\text{Bi}^{82+}$. It started in the afternoon of Monday, 1st of August and ended at noon on Friday, 5th of August 2011. The aim of the second phase was the detection of the $2s$ hyperfine transition in Li-like $^{209}\text{Bi}^{80+}$. This phase started on the afternoon of Saturday, 6th of August. Caused by a huge delay of the second phase due to problems during the scan for the H-like transition and additional difficulties during the second phase, the verification of the Li-like resonance was only achieved early at the 8th of August. In order to collect more

Table 4.1.: Assignment of the data files.

Measurement	file indices
$^{209}\text{Bi}^{82+}$, 1s transition	009 - 307
$^{209}\text{Bi}^{80+}$, 2s transition	308 - 678
$^{209}\text{Bi}^{80+}$, HFS lifetime	679 - 695

data on the resonance, the third phase of the beamtime was reduced to only three hours of measurement right before the end of the beamtime.

During the beamtime the data acquisition system MBS running on the E7 computer board generated data files that were labeled “Libelle’index’.lmd”, with the ‘index’ ranging from 0009 to 0695, including the data of the three different measurements. Files 0009 to 0307 were taken while scanning for the transition in hydrogen-like bismuth, files 0308 to 0678 while scanning for the one in lithium-like bismuth and files 0679 to 0695 contain data taken during the measurement of the lifetime of the upper hyperfine state in lithium-like bismuth (see also table 4.1). While the data of the first two phases will be investigated in this work, the lifetime data will be subject for another independent analysis [Vol13].

4.1.2. Parabolic mirror system performance

The parabolic mirror system has been installed at the ESR in summer 2010 and its operability has been parasitically tested during the beamtime of a special relativity (SRT) experiment [Nov09], where a Li^+ beam with $\beta = 0.338$ was circulated in the ESR. The main purpose of these tests was to determine the influence of the mirror insertion on the stored ion beam and the study of the sources and characteristics of background photons in the ESR [Lop10]. During the LIBELLE beamtime, the system was used as primary detector in an experiment for the first time.

Corresponding to section 3.3.3, during the measurements, at a low ion current, the mirror had to be withdrawn from the beam in order to inject new ions into the ESR and moved back into the beam after a sufficient ion cooling time. The evolution of the detector count rates at the parabolic mirror system over such a cycle is shown in figure 4.1. At about 30 s the mirror is moved out and the background count rate immediately drops. With the ion injection (at about 40 s) the background count rate increases significantly. The initially uncooled ions are then cooled by the electron cooler for the next 40 s, reducing the ions’ velocity spread and beam radius. After cool-down, the mirror is re-inserted into the beam (at about 80 s). The sharp increase in the detector count rate is caused by the impact of ions from the beam halo on the copper mirror, which contributes to the experimental background due to the slow but constant re-population of the halo. The actual laser spectroscopy measurements can be resumed once the high background from ion impacts has decreased to a level that

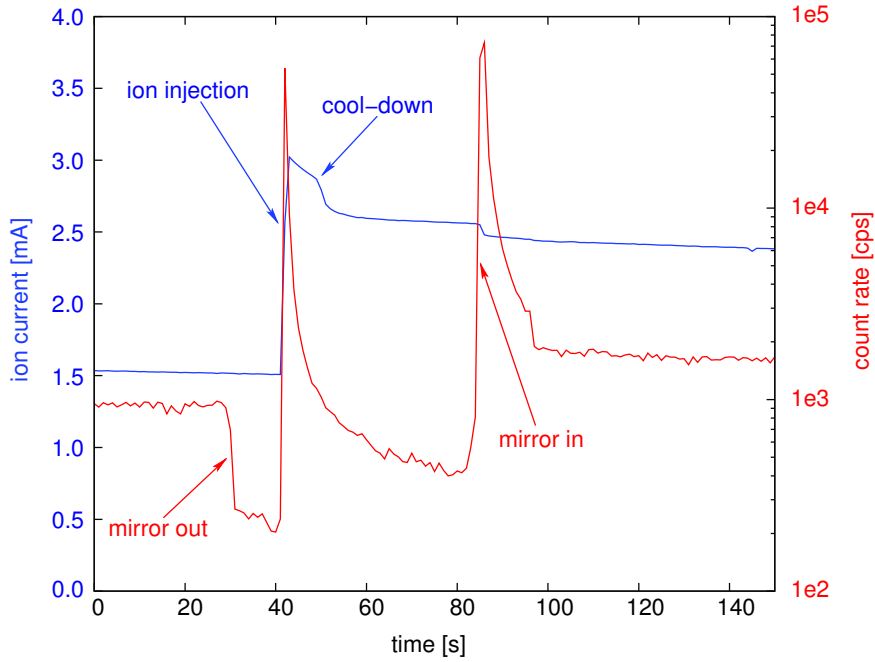


Figure 4.1.: Time evolution of the detector count rates and the corresponding ion current in the ESR during movement of the mirror and injection of new $^{209}\text{Bi}^{80+}$ ions. [Han13]

then slowly drops with the ion current (at about 110 s).

The overall background rate can be written as the sum of four contributions [Han13]:

$$D(I) = D_{\text{PMT}} + D_{\text{ll}} + D_{\text{rg}}(I) + D_{\text{h}}(I), \quad (4.1)$$

with the dark count rate of the PMT detector D_{PMT} , which is for the cooled PMT < 100 cps, and photons originating from light leaks in the ESR D_{ll} , both independent of the ion current. The other two background sources depend on the ion current, i.e. the fluorescence photons from residual gas excitation by the ion beam $D_{\text{rg}}(I)$, which is assumed to be proportional to the ion current, and the photons produced by the mentioned impact of ions from the beam halo onto the mirror $D_{\text{h}}(I)$. The latter can be derived by calculating the number of ions outside a certain radius r_0 from a simple two dimensional Gaussian beam profile $f(r, \phi) = A \cdot \exp\left(-\frac{r^2}{2\sigma^2}\right)$:

$$\int_0^{2\pi} \int_{r_0}^{\infty} A \exp\left(-\frac{r^2}{2\sigma^2}\right) r dr d\phi = 2\pi A \sigma^2 \exp\left(-\frac{r_0^2}{2\sigma^2}\right), \quad (4.2)$$

with the Gaussian's amplitude A and the RMS radius σ , which is assumed to be the same for both horizontal and vertical beam axis. The dependence of σ of the ion current I can be described by $\sigma = \alpha I^\beta$ [Ste04], summarizing equations 4.1 and 4.2 to the background model:

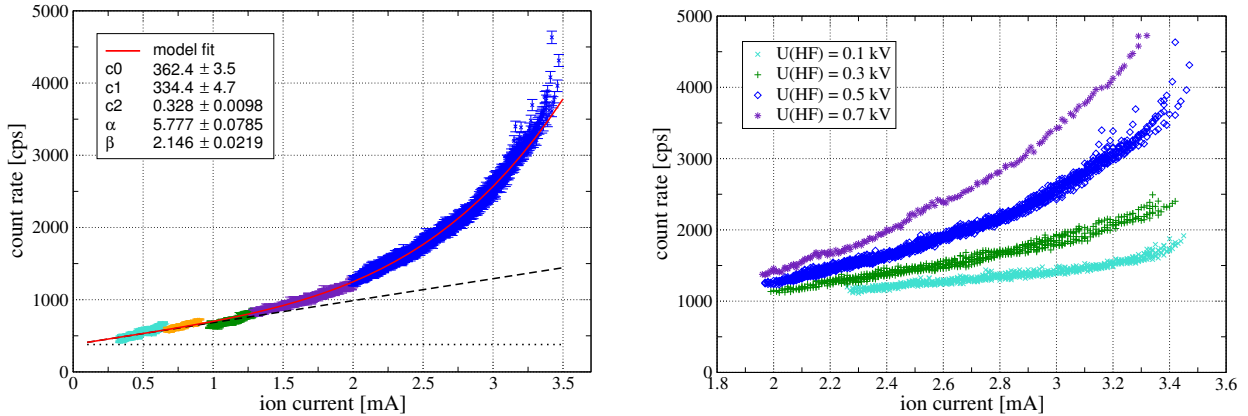


Figure 4.2.: Left: Measured PMT count rates as a function of the ion current in the ESR. The red line represents the model fit, while the dotted and the dashed lines display the constant and linear contributions to the fit, respectively. To cover the range of ion currents displayed, data from several measurements were used, indicated by different data point colors. Right: Dependence of the background rate on the voltage of the pulse driving the RF bunching cavities. [Han13]

$$D(I) = c_0 + c_1 \cdot I + c_2 \cdot \alpha^2 I^{2\beta} \exp\left(-\frac{r_0^2}{2\alpha^2 I^{2\beta}}\right). \quad (4.3)$$

The background as a function of the ion current is shown in figure 4.2. The combined background rate of the PMT dark counts D_{PMT} and light leaks D_{ll} is given by the constant term c_0 , which amounts to (362.4 ± 3.5) cps. As will be explained in detail in section 4.2, the TDC hits from individual cycles of the ion bunches in the ESR were stacked for each wavelength scan step on top of each other in a timing histogram covering the time of a single revolution. The count rate increase induced by the passing bunches shows up as two peaks. Fitting the histogram with a constant background with two Gaussians on top, the difference of the peak area of the right (reference bunch) and the left Gaussian (signal bunch) gives the number of fluorescence photons. In case of figure 4.3 the laser wavelength was on resonance frequency and the extracted number of 344 ± 78 fluorescence photons from the HFS transition detected within 5.94 s leads to a signal rate of (58 ± 13) cps. To compare this with the simulation results from table 3.2 of the previous chapter, this result has to be scaled to the ion current of 3 mA assumed in the simulation, since the ion current during the shown wavelength step was only 2.2 mA, which results in (79 ± 18) cps. This compares well with the 86 cps obtained from the simulations. Also the background rate can be extracted from the histogram to be (1304 ± 13) cps. This number has to be scaled with the ratio of actual and simulated current, and also the duty cycle of 20% that was assumed in the simulations for the data acquisition as stated in section 3.2 has to be taken into account. The simulated background of 453 cps then has to be compared to the experimental background rate of then

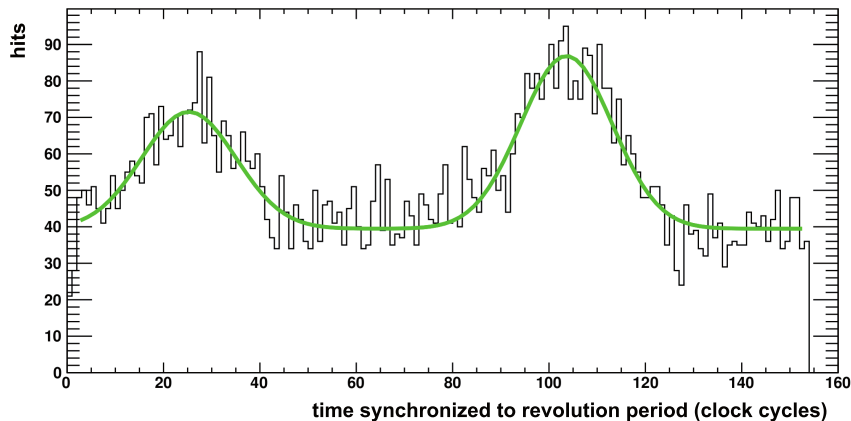


Figure 4.3.: Timing spectrum of PMT signals accumulated during a 5.94 s interval with the laser wavelength being on resonance with the HFS transition in $^{209}\text{Bi}^{80+}$, recorded with the parabolic mirror system. The time is given in cycles of the 300 MHz clock of the TDC used for readout. The green line corresponds to a fit of a constant background with two Gaussians representing the signals from the reference bunch (left peak) and the signal bunch (right peak). [Han13]

(356 ± 4) cps, which is reasonably close to the simulations based on a simplified background model.

The predictions and the performance of the novel parabolic mirror system agree well with the experimental results and, as will be shown in the following sections, the expectations on the new system of allowing the determination of the HFS transition in $^{209}\text{Bi}^{80+}$ were satisfied.

4.2. Analysis

During the LIBELLE beamtime it was decided that the analysis of the experimental data should be done independently by two teams at GSI [Loc13] and Münster (this thesis). While the analysis in [Loc13] was performed using the GSI analysis framework Go4¹ and additional software, the analysis in this work was exclusively done with the ROOT² analysis framework. This enhances the degree of independence between the two analyses. Only the initial conversion of the .lmd data files taken by the DAQ system during the beamtime to ROOT trees, necessary to make the data usable within the ROOT framework, resorted to a dedicated unpacking routine requiring the use of Go4 specific headers and functions.

The two different measurements with $^{209}\text{Bi}^{82+}$ and $^{209}\text{Bi}^{80+}$ ions had overall the same data structure, such that a general analysis code developed for e.g. the hydrogen-like data had to be adjusted to the lithium-like data only in some minor details. However, as more data were taken for the lithium-like case, these were chosen to be analyzed first. The procedure

¹GSI Object Oriented On-line Off-line system, <http://go4.gsi.de>

²Root: An object-Oriented Data Analysis Framework, <http://root.cern.ch/drupal>

of the analysis described in the following was later also used on the hydrogen-like data, which proved to be a little more complicated than expected due to the small number of files containing useful data. To develop the basic analysis code a subset of the lithium-like data was used (files 0481 to 0489), which already showed a resonance signal in the online analysis during the beamtime.

The final analysis cycle consists of seven steps:

1. Convert the .lmd data files to .root data files.
2. Unpack the single events from the .root data files and simultaneous assignment of the event data to a certain wavelength step.
3. Extract the laser wavelength for each step from the logfiles of the wavemeter and the “Cobra Control” program on the basis of the timestamps contained in the files.
4. Determination of the rate of fluorescence photons for each wavelength step, i.e. the count rate difference of the signal and the reference bunch.
5. Write the gathered data of all wavelength steps to a single file.
6. From these data fit the resonance.
7. Transform the fitted wavelength from the laboratory frame to the transition wavelength in the rest frame.

In order to organize the analysis according to the structure of the data taking described in section 3.3.3, a class labeled *Step* is introduced. It is used to gather all information on a single scan step, e.g. the values of the laser wavelength, the ion current or the TDC data histograms, for further processing.

4.2.1. Extracting the laser steps

The first part of the analysis is to extract the step-like structure of the wavelength scans done by the laser as depicted in fig 3.15. The aim is to fill an array of the specific class *Step* with all relevant data recorded for each particular scan step. This comprises the name of the .root file containing the starting event of the step, the .root file with the last event of the step, the number of these events within the corresponding files, the start and stop time stamps and information on the recorded scaler and TDC values and hence derived experimental parameters at that wavelength step.

Some of the information have to be derived from the data of all events belonging to a certain wavelength scan step, like the average values of the ion current or the bunching RF, which are assumed to be rather constant during a scan step of typically 6 s.

4.2.1.1. Finding the scan steps

In the data, the smallest structures are the events. To assign events to a certain wavelength step the scaler channel representing the trigger output of the dye laser is evaluated. In case the count rate for this channel is non-zero for a certain event, the laser was busy shifting wavelength. Therefore, data files are loaded subsequently and the events contained are investigated for the laser status as shown in fig 4.4, searching for all events in between two periods of laser wavelength shifts and assigning these to one step. At the same time other scaler data of the events are summed up, e.g. to get the overall clock counts of the 1 MHz clock to determine the step duration or to divide the sum of e.g. the divided RF cavity frequency channel (see table 3.3) by the number of events to obtain the mean value Div_{RF} . In particular the routine did the three following steps:

1. For each event the status of the laser is checked by reading the corresponding scaler value.
2. Depending on the status value of it is decided whether the event is rejected (in case of laser busy) or accepted:
 - a) If it is rejected, it is checked whether the previous event was accepted, making the latter the last event of the current step. In this case the accumulated data of the events belonging to the current step are processed in the *Step* class: The mean values of the scaler channels are calculated except for the clock and the TDC data are stacked as described in the next section. Afterwards the values of the buffer variables are reset.
 Otherwise, the event is just rejected without anything being done.
 - b) If it is accepted, it is checked whether the previous event was rejected. In that case the current event is the first one of the step and parameters like the starting time of the step are defined by the event's values. Also the sums of the scaler channels are initiated with the current values as well as the TDC histograms.
 Otherwise, only the scaler channels are summed up and the TDC histograms are expanded.
3. The procedure is applied to the next event.

The scaler channels summed up are the DC-Trafo channel, the divided RF channel, the 1 MHz clock channel (*Clk*) and the channel of the frequency representing the laser wavelength. The average values (i.e. the sum of the corresponding scaler channel entries divided by the number of events for a single step) of all parameters but the clock are determined and are in

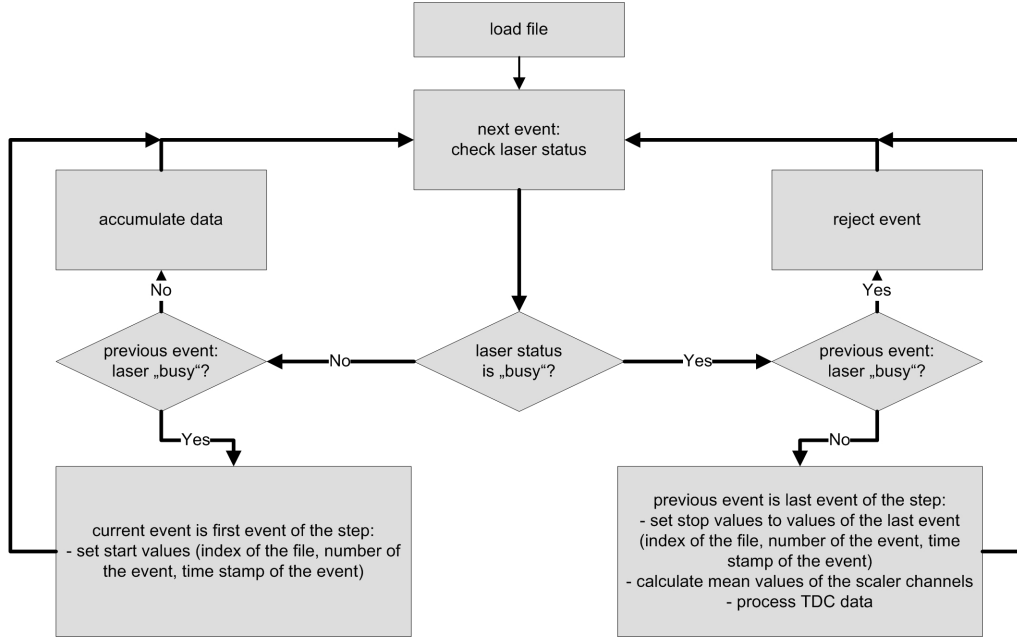


Figure 4.4.: Flow chart of the scan step extraction. For each event the laser status was checked and according to it the data contained in several other TDC and scaler channels were processed to get all relevant information of the step.

the following labeled as DC_{trafo} for the average DC-Trafo value, Div_{RF} for the mean value of the divided RF and n_{laser} for the average count rate of the frequency representing the wavelength step of the dye laser. For the further analysis these values are used to calculate the mean ion current I_{ion} in mA, the bunch revolution time t_{bunch} in s, the number of TDC time bins per ion revolution n_{TDCbin} and a frequency label f_{step} for each wavelength step:

$$\text{mean ion current (mA): } I_{\text{ion}} = \left(\frac{DC_{\text{trafo}} \cdot 10^6}{Clk} - DC_{\text{offset}} \right) \cdot \frac{1}{DC_{\text{prop}}} \quad (4.4)$$

$$\text{bunch revolution time: } t_{\text{bunch}} = \frac{1}{f_{\text{bunch}}} = \left(\frac{(Div_{\text{RF}} \cdot n_{\text{div}})}{n_{\text{bunch}}} \cdot \frac{1 \cdot 10^6}{Clk} \right)^{-1} \quad (4.5)$$

$$\text{bins per ion revolution: } n_{\text{TDCbin}} = \frac{t_{\text{bunch}}}{\Delta t_{\text{TDC}}} \quad (4.6)$$

$$\text{frequency label: } f_{\text{step}} = \frac{n_{\text{laser}} \cdot 10^6}{Clk} \quad (4.7)$$

In these equations $n_{\text{div}} = 200$ is the value of the fraction of the bunching RF provided by a rate divider, $DC_{\text{offset}} = 2059.3$ mA and $DC_{\text{prop}} = 1 \cdot 10^5$ are offset and proportional factor of the calibration of the ion current, $n_{\text{bunch}} = 2$ is the number of bunches in the ESR and $\Delta t_{\text{TDC}} = 3.33$ ns is the width of a TDC time bin.

4.2.1.2. Processing the TDC data

As mentioned above, the TDC data representing the time information of the photons detected have to be processed further. The TDC data of each accepted event are first accumulated to a single histogram for each detector channel with about 15,000 bins corresponding to the inverse of the common stop signal frequency divided by the TDC's time resolution. Since the ions orbit the ESR with about 2 MHz, which corresponds to about 150 time bins in the histograms, their contents have to be stacked according to the revolution time in order to obtain the bunch structure. Therefore, the exact bunch revolution time t_{bunch} and the corresponding number of TDC time bins n_{TDCbin} are calculated for each scan step according to equations 4.5 and 4.6. From these values the number of bins representing a single ion revolution is obtained. For each TDC bin the time relative to the start of the corresponding revolution can be calculated:

1. First the index number i_{bin} of the current TDC bin is divided by the exact number of bins per ion revolution n_{TDCbin} , which is in general a real number.
2. Then the fractional digits of this value are multiplied again with n_{TDCbin} to obtain the index of the bin relative to the starting time of the corresponding revolution.
3. Finally, since the bin number is still a real number, for further histogram processing it has to be rounded to a non-negative integer.

An example for the "stacking" of the TDC histograms is shown in figure 4.5. As can be seen, the stacked histogram clearly shows a structure consisting of two Gaussians with a general offset. This represents the bunch structure of the ions orbiting the ESR. The offset corresponds to the constant photon background in the ESR.

4.2.2. Associating a wavelength to the laser steps

The data files containing the wavelength given by the Sirah laser as well as the log files of the ATOS lambdameter (see section 3.1.2) were written to the local hard disks of the computers used to control these devices. Therefore, the wavelength of a certain scan step has to be extracted from these data.

Each line of the Sirah log files contains, besides other information, date, time and a time stamp of the entry, the motor position and the derived wavelength and a laser status string. Unfortunately, the wavelength given by the control software of the Sirah laser is only derived from the position of the motor rotating the diffraction grating and thus is not to be used as the real wavelength value. Still the laser status string can be used to determine start and stop time of each scan step.

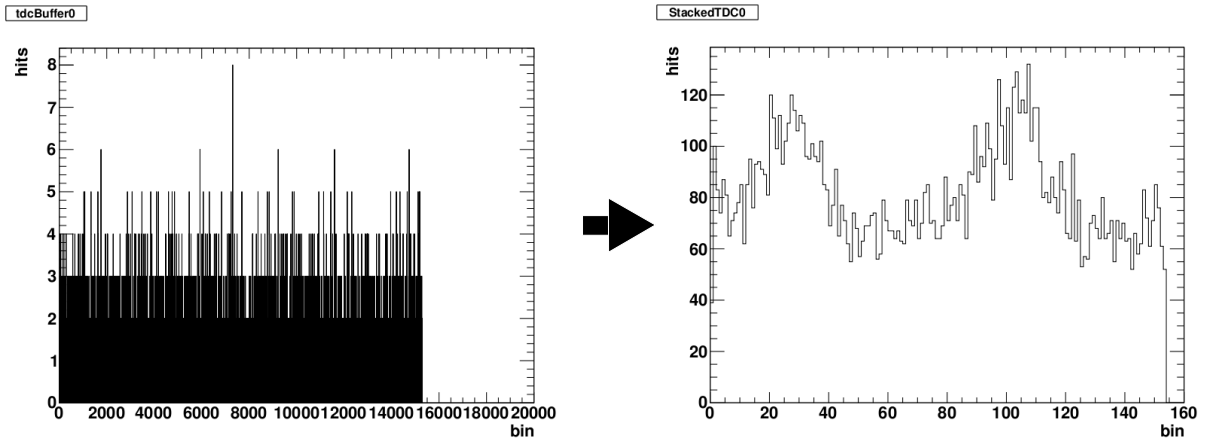


Figure 4.5.: The raw TDC histogram (lefthand side) contains the data of all TDC common stop periods of the wavelength step. The timing bins are stacked with respect to the bunch revolution time to obtain the fluorescence detection time structure (right).

The Atos files also contain a time stamp as well as a measured wavelength value and an intensity value giving the light intensity as recorded by the lambdameter as a measure of the reliability of the wavelength value. With the start and stop times of each step extracted from the Sirah log files, the Atos files are then checked for time stamps falling within the boundary times of an extracted step. For each step the mean laser wavelength λ_{step} along with its RMS $\Delta\lambda_{\text{step}}$ and the mean intensity I_{laser} is calculated and written to a single file, now comprising the start and stop time as well as the mean wavelength and the mean intensity for all scan steps recorded during the beamtime.

The start and stop times of these scan steps are then compared with the start and stop times of the steps extracted from the .root files, associating the mean wavelength and the intensity value to the corresponding *Step*-class object.

4.2.3. Obtaining count rate differences from stacked TDC data

As shown in section 4.2.1.2, all TDC data belonging to a wavelength are stacked to a histogram displaying the bunch structure. Now, after the *Step*-class objects are built with all relevant information including the wavelength information extracted from the lambdameter data, these histograms are fitted by two Gaussians and a constant offset. The fit function is parametrized such that the difference $p_{\Delta\text{area}}$ of the areas of the Gaussians, i.e. the signal rate, is a fit parameter itself:

$$f(x) = p_{\text{offset}} + \frac{p_{\text{area1}}}{\sqrt{2\pi}p_{\sigma1}} \exp\left[-\frac{(x - p_{\text{mean1}})^2}{2p_{\sigma1}^2}\right] + \frac{(p_{\text{area1}} + p_{\Delta\text{area}})}{\sqrt{2\pi}p_{\sigma2}} \exp\left[-\frac{(x - p_{\text{mean2}})^2}{2p_{\sigma2}^2}\right] \quad (4.8)$$

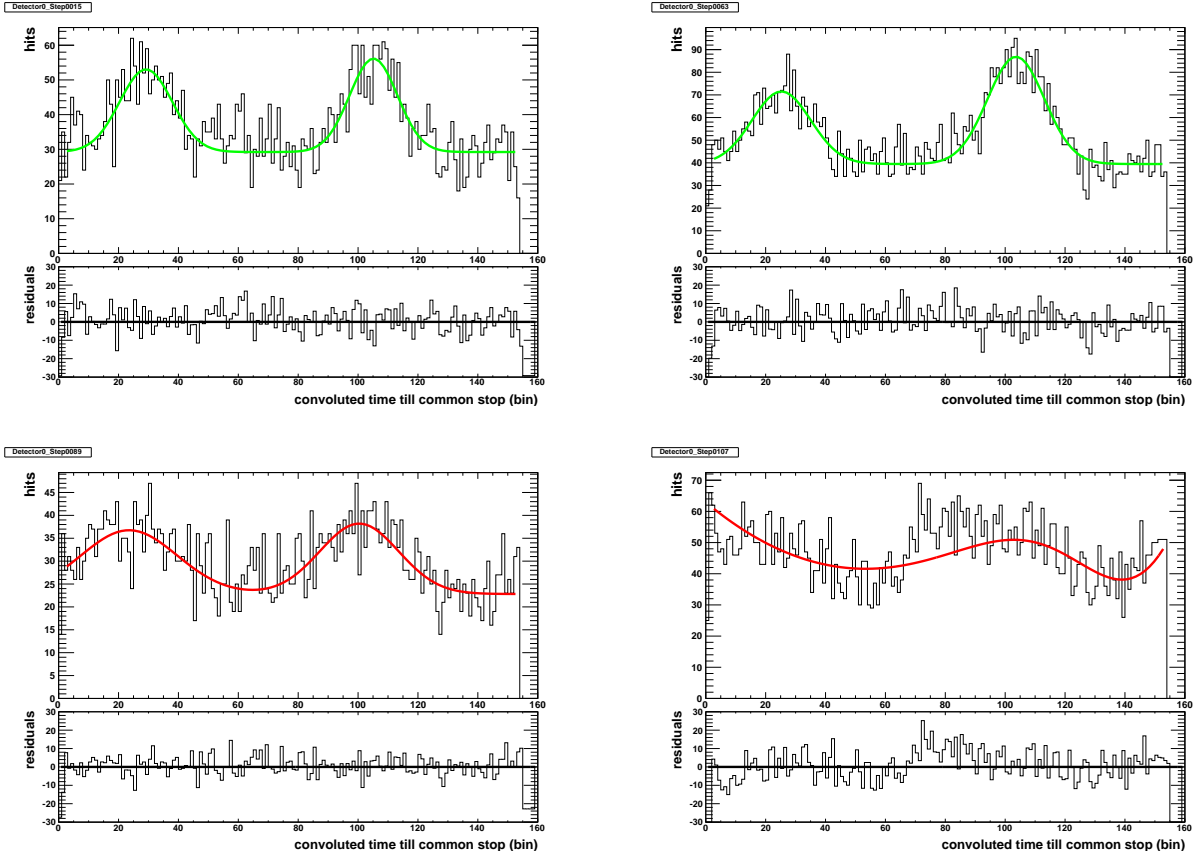


Figure 4.6.: Examples of the TDC histogram fits. The fits of the two upper plots were processed with error code 0 showing two separate peaks. The left is slightly off resonance since the peak of the reference bunch nearly has the same area as the signal bunch peak, whereas in the right plot the area of the signal bunch peak is obviously larger. The two lower plots show fits with error code 2, meaning the Gaussians are not detached from each other.

Thus, the area difference and the corresponding error are obtained directly from the fitted parameters without the need to perform an error propagation of correlated uncertainties. Figure 4.6 shows some examples of fitted TDC histograms. The fits are performed using the Minuit2 minimizing routine implemented in the ROOT framework.

The fits are also checked for eventual errors and inconsistencies that may cause problems during the further analysis. Depending on the criterion failed, the program returns an integer value (error code). The error codes with the corresponding criteria applied to the check are:

- **error code 0:** Fit ok.
- **error code 1:** The reduced χ^2 ($\chi_{\text{red}}^2 = \frac{\text{chi}^2}{N_{\text{dof}}}$) was not between 0.5 and 1.7. This is introduced as rough measure for the goodness of the fit. The number of degrees of freedom is $N_{\text{dof}} = 146$ and $\sigma_{\chi_{\text{red}}^2} = \sqrt{\frac{2}{N_{\text{dof}}}} = 0.12$. The χ_{red}^2 -distribution for all bunch fits of the narrow-band data of H-like Bi^{82+} is exemplary shown in figure 4.7.

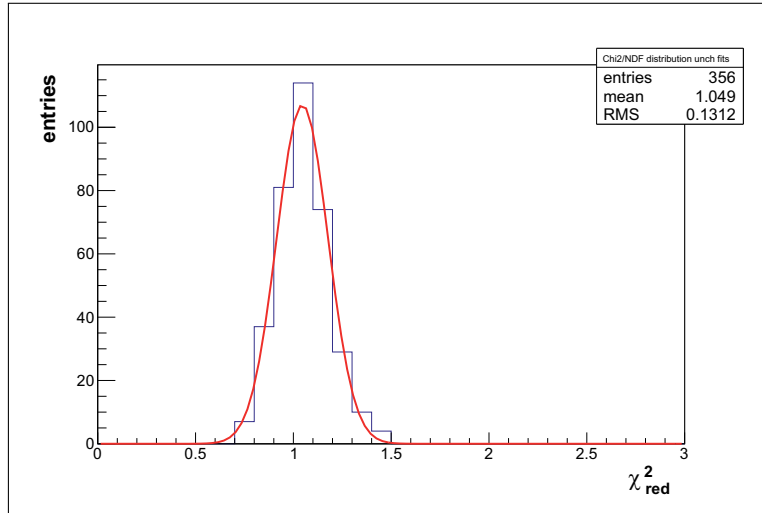


Figure 4.7.: χ_{red}^2 -distribution of the bunch fits of the narrow-band data of H-like Bi⁸²⁺.

- **error code 2:** The $\pm 2\sigma$ region of one of the Gaussians has to be smaller than half of the bunch cycle, ensuring two separate bunches.
- **error code 4:** Either $p_{\text{area}1} < 0$ or $(p_{\text{area}1} + p_{\Delta\text{area}}) < 0$, corresponding to Gaussians with negative amplitude.
- **error code 5:** The fit did not converge.

Besides the area difference of the Gaussians $p_{\Delta\text{area}}$, also the difference of the bin contents belonging to the 2σ region of the peaks is calculated, both representing the count rate difference between signal and reference bunch. Due to good consistency of both values, in the following only the area difference $p_{\Delta\text{area}}$ will be used for the analysis.

The obtained fit parameters, the error code the area difference and the bin content difference are written to the *Step*-class objects. Now having a set of *Step*-class objects with all necessary information to search for the resonance, these data are extracted to an ASCII-spreadsheet for backup and further processing.

4.2.4. Fitting the resonances

Up to this point information on the wavelength scan steps has been accumulated in the *Step* class objects. Now, the resonance wavelengths have to be obtained from these data. The main values needed per step are the ion current I_{ion} , the measuring time per step, which can be calculated from the clock counts *Clk*, the laser wavelength of the step as extracted in section 4.2.2, the count rate difference between signal and reference bunch, given by $p_{\Delta\text{area}}$, and the error code as outlined in section 4.2.3. The fitting of the resonance is separated from the previous steps and uses the just mentioned ASCII file containing the step information.

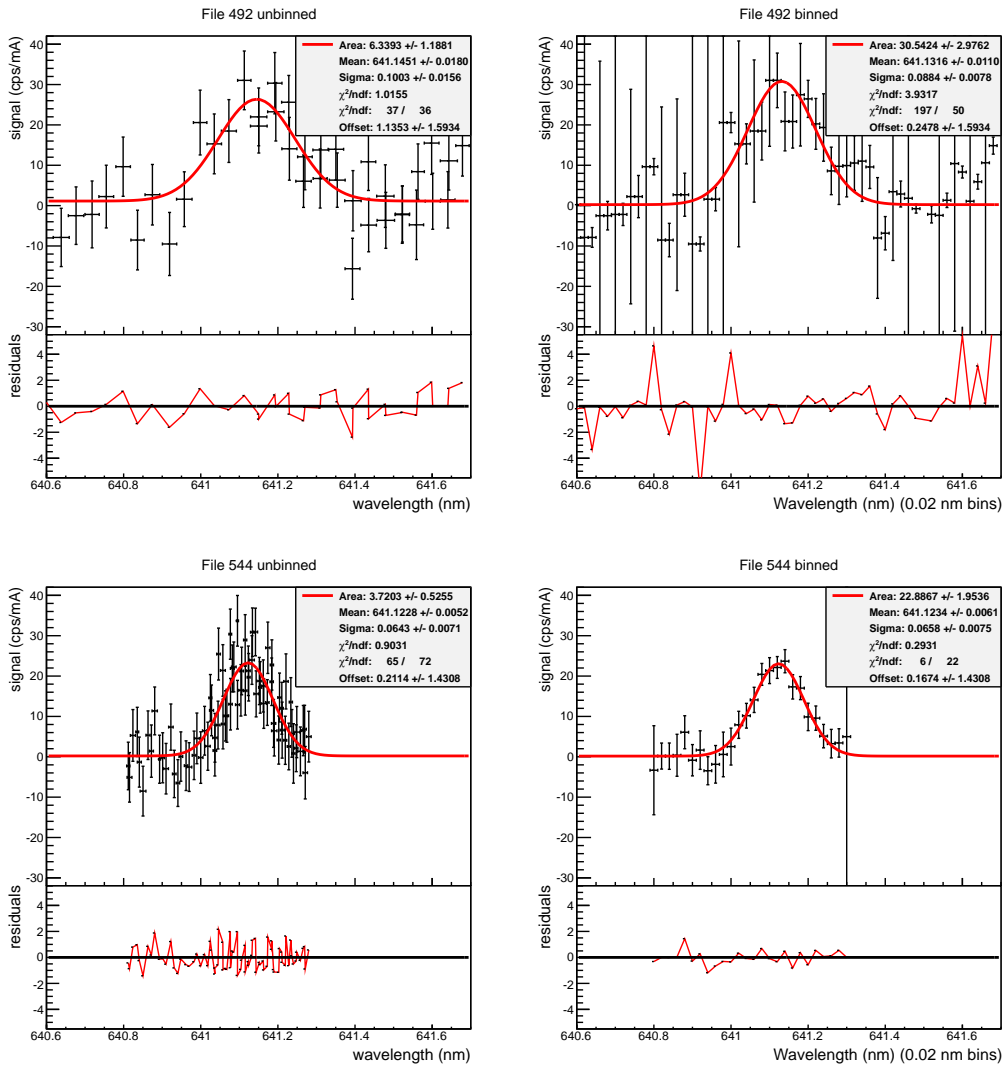


Figure 4.8.: Two examples of a resonance fit of a single file. The left plots show the fits of the unbinned data, while the right ones are binned with a bin width of 0.01 nm.

The file is opened and an algorithm searches for usable steps based on several criteria. The steps were only processed further, if all of the following criteria are met:

- The fit error code had to be 0.
- The mean intensity I_{laser} has to be larger than 50 (arbitrary units) to ensure, that the measurement of the laser wavelength is accurate.
- $\Delta\lambda_{\text{step}}$, given by the RMS of the lambdameter wavelength values belonging to a certain step, has to be smaller than 0.1 nm. This should prevent to account for steps with a large spread of the single wavelength measurements.

The resonance wavelength is now obtained by fitting two different arrangements of the *Step* data (see figure 4.8):

1. To avoid binning problems for each *Step* the signal rate, i.e the count rate differences normalized to the ion current and the measuring time, was plotted against the wavelength into a simple graph (ROOT TGraphError object), leading to signal rates in units of cps/mA.
2. For low signal rates, where the above mentioned simple graph exhibits scattered data points without a clear peak structure, a binned version of the data is produced. There the count rate of each *Step* is split into two fractions depending on the relative position of the *Step*'s wavelength between two neighboring bins of the histogram. By also dividing the measuring time in the same fashion, the signal rates are again normalized to cps/mA. Due to difficulties in dividing wavelength error to different bins, this arrangement along with its fit was mainly used to illustrate the resonance conveniently.

These two datasets are prepared for each *Scan* and each *Run* (see figure 3.15) and fitted with a single Gaussian parametrized to contain the area A , the position μ and the standard deviation σ as parameters:

$$f(x) = \frac{A}{\sqrt{2\pi}\sigma} \cdot \exp\left[-\frac{(x - \mu)^2}{2\sigma^2}\right]. \quad (4.9)$$

Figure 4.8 shows a plot of the datasets and the fits. The central value of the Gaussian along with its error denotes the fitted transition wavelength λ_{fit} with the error $\Delta\lambda_{\text{fit}}$. The residuals are given by

$$res_i = \frac{(y_i - f(x_i))}{\sigma_i}, \quad (4.10)$$

where y_i is the y-value of the data point i , $f(x_i)$ is the corresponding value of the fit function and σ_i is the y-error of data point i .

4.2.4.1. Error of the wavelength fit

Now, the error propagation from the initial data to error $\Delta\lambda_{\text{fit}}$ will be looked at. Two error contributions can be distinguished, that can be handled independently to a certain degree: The statistical error on the one hand and the systematic uncertainty on the other hand. To determine the transition wavelength λ_{fit} , the signal rate is normalized to the measuring time and the ion current and is plotted against the laser wavelength, hence the errors of the signal rate, the measuring time, the ion current and the laser wavelength determination have to be discussed.

Starting with the statistical error of the signal rates, originating in the method of data taking. Since the DAQ consisted mainly of a 32-channel scaler and a 16-channel TDC of

the VUPROM, the initial data are basically count rates with the statistical error of the square root of these rates. The wavelength of the transition in the laboratory system λ_{fit} is determined by applying a Gaussian fit to the *Step* data, plotted as signal rate versus wavelength (see figure 4.8). The signal rate is derived only from values taken with the TDC or the scalers, respectively. After stacking the TDC data the histogram class of the ROOT framework automatically assigns the square root of the bin content as error of the bin. Thus, the two-Gaussian fit to these histograms (see figure 4.6) handles the error of the parameters in the correct way. By parametrizing the fit function as shown in equation 4.8, the parameter of the area difference of the two bunches $p_{\Delta\text{area}}$ is uncorrelated to the other parameters and its error $\Delta p_{\Delta\text{area}}$ can be adopted in the further analysis.

The statistical error bars of the wavelength values, which can be seen as horizontal error bars in the plots of the resonance fits, e.g. in figure 4.8, originate in the spreading of the laser wavelength measurements at a certain wavelength scan step. For the duration of a single scan step about five to six wavelength measurements have been done by the Atos lambdameter. The mean value of these measurements serves as wavelength value of the step and the RMS as its statistical error. An additional systematic uncertainty is introduced by the lambdameter concerning the accuracy of the measured wavelength, which depends on the number of interferometers used. Unfortunately, during the measurements with the laser set to broad-band mode, only one interferometer could be operated, resulting in an uncertainty of the determined wavelength of $\lambda_{\text{lab,broad}}^{\text{Atos}} = 0.219$ nm, whereas the measurements with narrow-band settings were done with two interferometers, reducing the uncertainty to $\lambda_{\text{lab,narrow}}^{\text{Atos}} = 0.016$ nm [Loc12]. The systematic uncertainty is only taken into account in the final wavelength results for the broad-band and the narrow-band measurements, respectively, as described later on. The ion current calculated from the DC_{trafo} values ranges from about 3 mA to around 1 mA and has small fluctuations of 0.004 mA. An additional systematic error in the small percent range is assumed [Loc12]. Altogether, the error of the ion current is very small compared to the other errors and is thus neglected in the analysis. Since the measuring time is derived from the scaler counts of a 1 MHz clock, the error of the counts is ± 1 count, corresponding to an uncertainty of 1 μs and is also negligible. Thus, the error bars of each entry in the resonance plots, taken into account by the resonance fit are comprised of:

- x-direction: The RMS of the Atos lambdameter laser wavelength measurements associated to the corresponding scan step.
- y-direction: The error $\Delta p_{\Delta\text{area}}$ of the area difference fit parameter of the TDC histogram fits.

These are the error bars seen in e.g. figure 4.10. The fit applied to these data points accounts

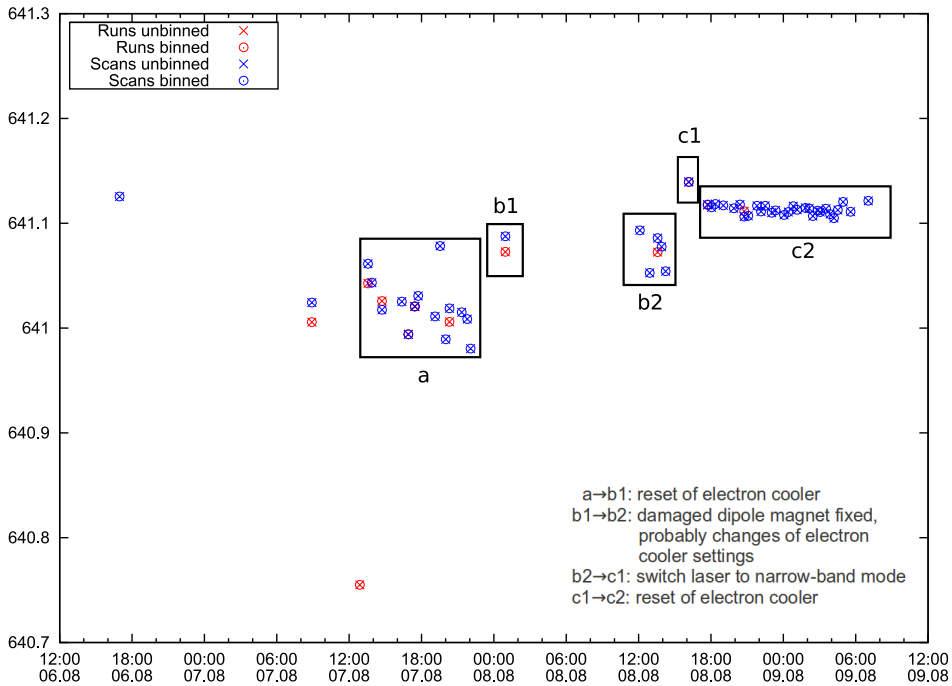


Figure 4.9.: The plot shows the wavelength values obtained from the analysis of the *Runs* (red) and the corresponding *Scans* (blue). The two different point types for both the *Runs* and the *Scans* represent the different methods of fitting the resonance as described in section 4.2.4. The different regions are marked and the changes of the experimental conditions are listed.

for the statistical errors. The value of the resonance wavelength in the laboratory system obtained from the fits λ_{fit} along with its statistical error $\Delta\lambda_{\text{fit}}$ is therefore given by the position parameter μ of the Gaussian fit and its error.

4.3. Resonance wavelengths in the laboratory system

In the previous section the concept of the analysis was explained in detail. In the following section the results of this analysis structure applied to the experimental data of both the hydrogen-like and the lithium-like bismuth will be presented. The more complicated part of the analysis is to extract the transition wavelength from the hydrogen-like data, since during the hydrogen-like part of the beamtime the scan structure described in 3.3.3 was not completely evolved at the beginning. Therefore, the analysis of the lithium-like data are done first, resulting in some re-arrangement of the final wavelength fit.

4.3.1. The $^{209}\text{Bi}^{80+}$ hyperfine transition (Li-like)

The files containing the data of the Lithium-like data were assigned to 19 *Runs* with several *Scans* each as shown in table 4.2. The first four runs did not contain much data and were

Table 4.2.: Association of the data files containing the lithium-like data to *Runs* and the time regions.

region	run	files
	1	319 - 324
	2	325 - 336
	3	345 - 348
	4	349 - 359
a	5	360 - 371
	6	372 - 375
	7	376 - 384
	8	385 - 401
	9	402 - 405
	10	406 - 407
	11	408 - 423
	12	424 - 440
b1	13	441 - 456
b2	14	463 - 480
	15	481 - 489
c1	16	491 - 500
c	17	507 - 545
	18	547 - 575
	19	577 - 678

therefore not further investigated in the analysis. During the first test runs of the lithium-like analysis, the resonances were fitted for each *Scan* as well as for each *Run*. That resulted in several values for the transition wavelength and ideally the mean value should represent the final result. However, when the fit results for the *Scan* and *Run* fits were plotted against time, several separate time intervals were observed, where the fits of the resonance wavelength more or less stay the same with shifts of the mean wavelengths in between (figure 4.9). After investigation of the logs of the ESR and the LIBELLE experiment, the wavelength shifts were linked with changes of experimental conditions. The shift of the wavelength between region b2 and c1 could be correlated to the switching of the laser bandwidth, whereas the shifts between region a, b1 and b2 as well as between c1 and c have to originate in another statistical uncertainty, most likely related to resets of the electron cooler noted in the experiment's logbook at the corresponding times. Since these changes obviously influence the resonance position, they add another systematical error source to the analysis.

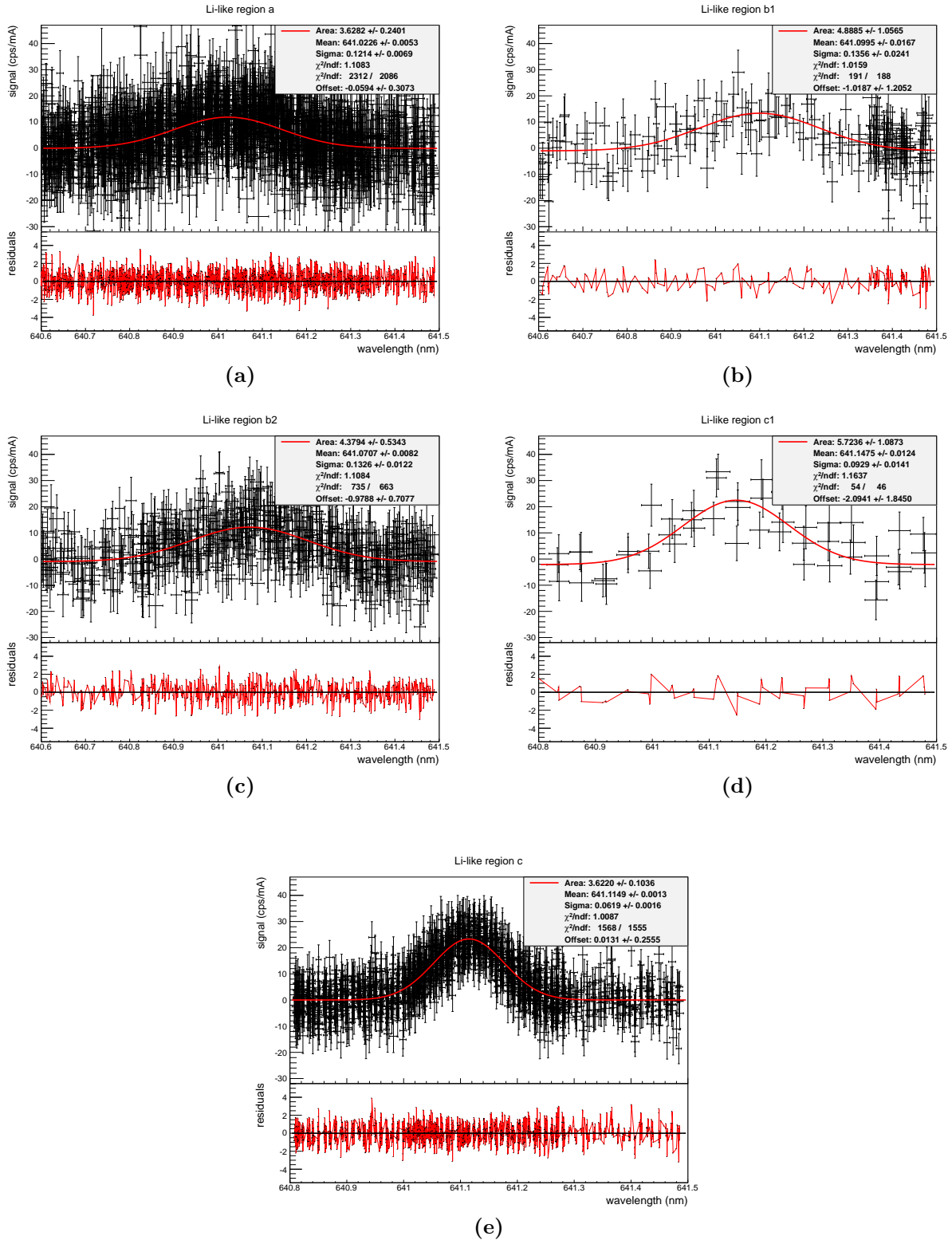


Figure 4.10.: Fits of the five scan regions. In the time regions a, b1 and b2 the scans were performed with the laser set to broadband mode, while in region c1 and c the narrowband mode was applied. The results are also listed in table 4.3

Table 4.3.: Results of the resonance fits of the five time regions of the lithium-like measurements as shown in figure 4.10.

region	scan mode	λ_{fit} (nm)	σ	χ^2/ndf
a	broadband	641.0226 ± 0.0053	0.1214 ± 0.0069	1.1083
b1	broadband	641.0995 ± 0.0167	0.1356 ± 0.0241	1.0159
b2	broadband	641.0707 ± 0.0082	0.1326 ± 0.0122	1.1084
c1	narrowband	641.1475 ± 0.0124	0.0929 ± 0.0141	1.1637
c	narrowband	641.1149 ± 0.0013	0.0619 ± 0.0016	1.0087

The analysis structure of the Lithium-like data was hence changed from analyzing and fitting the single *scans* and *ramps* to analyzing the complete data of each of these five time regions, a, b1, b2, c1 and c, at once, obtaining one value $\lambda_{\text{fit}} \pm \Delta\lambda_{\text{fit}}$ for each of the regions. The fits of the corresponding data are shown in figure 4.10 and the results of the fits are listed in table 4.3. In order to obtain a single transition wavelength value for the $^{209}\text{Bi}^{80+}$ measurements, the wavelength fits of all five time regions a, b1, b2, c1 and c, are accounted for. Therefore, in a first step a mean wavelength value for the measurements done in broad-band mode as well as for the measurements done in narrow-band mode are calculated. Since the number of data points in region a is much larger than in region b1 and b2, and also the error of the fitted wavelength is much smaller, as can be seen in figure 4.10 and table 4.3, which also applies for region c compared to c1, instead of the arithmetic means the the weighted means [Jam06] of regions a, b1 and b2, $\lambda_{\text{lab,broad}} \pm \Delta\lambda_{\text{lab,broad}}^{\text{stat.}}$ and of c1 and c, $\lambda_{\text{lab,narrow}} \pm \Delta\lambda_{\text{lab,narrow}}^{\text{stat.}}$, were calculated using:

$$\lambda_{\text{lab}} = \frac{\sum_i \frac{\lambda_{\text{fit},i}}{(\Delta\lambda_{\text{fit},i})^2}}{\sum_i \frac{1}{(\Delta\lambda_{\text{fit},i})^2}} \quad (4.11)$$

$$\Delta\lambda_{\text{lab}}^{\text{stat.}} = \sqrt{\left(\sum_i \frac{1}{(\Delta\lambda_{\text{fit},i})^2}\right)^{-1}} \quad (4.12)$$

with $i = \text{a, b1, b2}$ for the broad-band and $i = \text{c1, c}$ for the narrow-band case. The results obtained from these equations are:

$$\lambda_{\text{lab,broad}}^{\text{Li-like}} = (641.0409 \pm 0.0043) \text{ nm}$$

$$\lambda_{\text{lab,narrow}}^{\text{Li-like}} = (641.1153 \pm 0.0013) \text{ nm}$$

Now, additional error contributions to the values $\lambda_{\text{lab,broad}}$ and $\lambda_{\text{lab,narrow}}$ are discussed. The

spread of the wavelength values λ_{fit} of regions a, b1 and b2 is much bigger than their error bars $\Delta\lambda_{\text{fit}}$. As described above, this spread originates in the statistical fluctuations of the fitted wavelengths introduced by resets of the electron cooler. The spread of the values $\lambda_{\text{fit},c1}$ and $\lambda_{\text{fit},c}$ should be aroused from the same systematic. To account for this uncertainty the RMS of the wavelength values λ_{fit} of the broad-band measurements with respect to $\lambda_{\text{lab,broad}}$ was calculated. Also the systematic uncertainty of the Atos lambdameter $\lambda_{\text{lab}}^{\text{Atos}}$ is now added. Thus, two error contributions are added to the final error of the wavelengths $\lambda_{\text{lab,broad}}$ and $\lambda_{\text{lab,narrow}}$ in the laboratory frame:

$$\Delta\lambda_{\text{lab}}^{\text{e-cooler}} = \sqrt{\frac{\sum_{i=a,b1,b2} (\lambda_{\text{lab,broad}} - \lambda_{\text{fit},i})^2}{N-1}} = 0.0482 \text{ nm} \quad (4.13)$$

$$\Delta\lambda_{\text{lab}}^{\text{Atos}} = \begin{cases} 0.219 \text{ nm} & \text{(broad-band)} \\ 0.016 \text{ nm} & \text{(narrow-band)} \end{cases} \quad (4.14)$$

where $N = 3$ is the number of data points. Since there are only two data points for the narrow-band region, the calculation of the RMS for the mean of these two points is not reasonable. However, the statistical uncertainty induced by electron cooler resets should also apply for the narrow-band region. Thus, the uncertainty $\Delta\lambda_{\text{lab}}^{\text{e-cooler}}$ is also added to the narrow-band value. The overall error of $\lambda_{\text{lab,broad}}$ and $\lambda_{\text{lab,narrow}}$ is then given by:

$$\Delta\lambda_{\text{lab,broad}}^{\text{Li-like}} = \sqrt{(\Delta\lambda_{\text{lab,broad}}^{\text{stat.}})^2 + (\Delta\lambda_{\text{lab}}^{\text{e-cooler}})^2} + \Delta\lambda_{\text{lab,broad}}^{\text{Atos}} \quad (4.15)$$

$$\Delta\lambda_{\text{lab,narrow}}^{\text{Li-like}} = \sqrt{(\Delta\lambda_{\text{lab,narrow}}^{\text{stat.}})^2 + (\Delta\lambda_{\text{lab}}^{\text{e-cooler}})^2} + \Delta\lambda_{\text{lab,narrow}}^{\text{Atos}}. \quad (4.16)$$

Here, the statistical contributions $\Delta\lambda_{\text{lab}}^{\text{stat.}}$ and $\Delta\lambda_{\text{lab}}^{\text{e-cooler}}$ are summed up in quadrature while the systematic uncertainty $\Delta\lambda_{\text{lab}}^{\text{Atos}}$ is added linearly. This leads to the following values:

$$\begin{aligned} \lambda_{\text{lab,broad}}^{\text{Li-like}} &= (641.0409 \pm 0.0043(\text{stat.}) \pm 0.0482(\text{e-cooler}) \pm 0.219(\text{Atos})) \text{ nm} \\ &\stackrel{(4.15)}{=} (641.0409 \pm 0.2674) \text{ nm} \end{aligned}$$

$$\begin{aligned} \lambda_{\text{lab,narrow}}^{\text{Li-like}} &= (641.1153 \pm 0.0013(\text{stat.}) \pm 0.0482(\text{e-cooler}) \pm 0.016(\text{Atos})) \text{ nm} \\ &\stackrel{(4.16)}{=} (641.1153 \pm 0.0642) \text{ nm} \end{aligned}$$

Again, due to the different size of the errors of these values, the weighted mean according to equations (4.11) and (4.12) is calculated to obtain the final value $\lambda_{\text{lab}}^{\text{Li-like}}$ for the transition

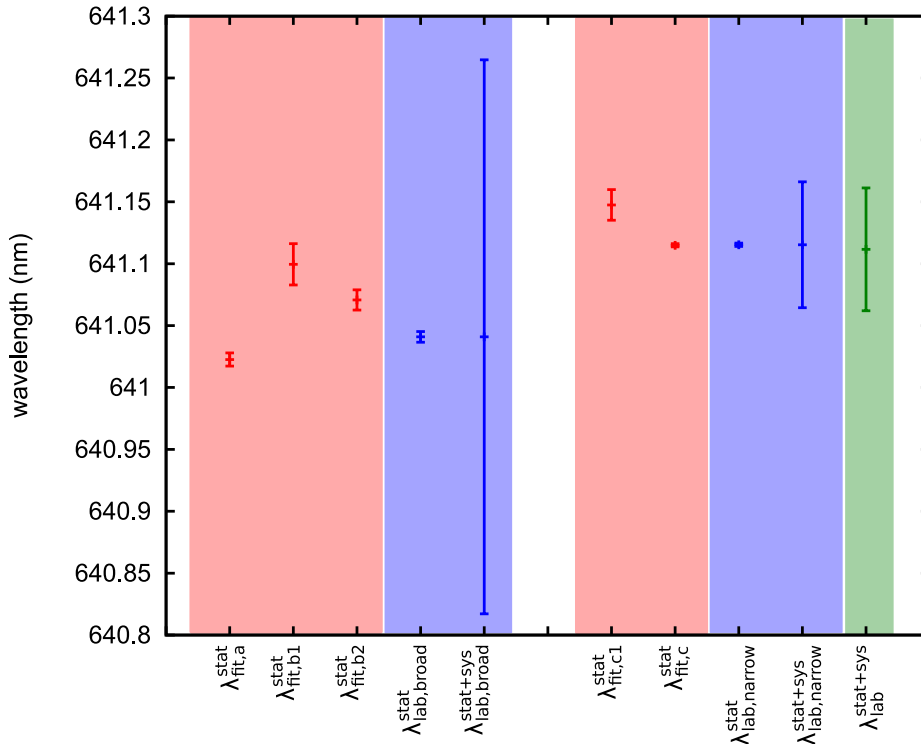


Figure 4.11.: The different values and the evolution to the final laboratory wavelength $\lambda_{\text{lab}}^{\text{Li-like}}$. The designations of the values state the contribution to the corresponding error bars.

wavelength in lithium-like bismuth in the laboratory frame:

$$\lambda_{\text{lab}}^{\text{Li-like}} = (641.1112 \pm 0.0627) \text{ nm.}$$

Figure 4.11 shows the different values and the evolution to the final laboratory wavelength $\lambda_{\text{lab}}^{\text{Li-like}}$. The designations of the values state the contribution to the corresponding error bars. It can be seen that the final wavelength $\lambda_{\text{lab}}^{\text{Li-like}}$ is mainly determined by the value of the narrow-band measurements $\lambda_{\text{lab,narrow}}^{\text{Li-like}}$ due to the large systematic uncertainty of the Atos lambdameter in the broad-band case. Also the overall error is mainly given by the error of $\lambda_{\text{lab,narrow}}^{\text{Li-like}}$. The main contribution to the latter, is the systematic uncertainty induced by the electron cooler resets, that applies for both the broad-band and the narrow-band measurements.

4.3.2. The $^{209}\text{Bi}^{82+}$ hyperfine transition (H-like)

No similar regions were found in the hydrogen-like data. Only the wavelength shift between the broad band and the narrow band mode of the laser was observed. The overall amount of usable data of the hydrogen-like measurements is very small compared to the usable data

Table 4.4.: Association of the data files of the hydrogen-like measurements to the broadband and narrowband measurement phases.

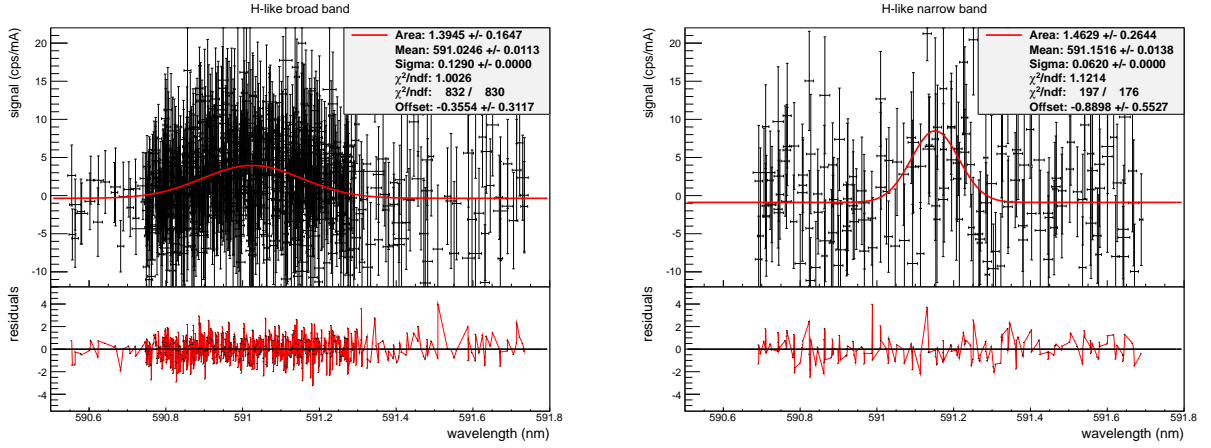
scan mode	files	files used in the analysis
broad band mode	215 - 287	217, 218, 220, 227, 238, 239, 242, 243, 244, 245, 248, 249, 250, 251, 253, 259, 260, 262, 263, 267, 268, 270, 271
narrow band mode	288 - 299	295, 296, 298

of the lithium-like measurements. The primary detector used for the H-like measurements was, as in previous measurements of this transition, a type 9422A ("solar blind") PMT manufactured by Thorn EMI, which was mounted at the first window of the mirror section. The signal rate per *Step* at the solar blind PMT was smaller by a factor two and the number of steps containing enough data for proper stacking and fitting of the TDC histograms was about five times smaller. The reason for this decreased count rates is, that prior to the beam time the window of the mirror section viewports were replaced. In this turn a wrong window of a standard material was placed at the flange used for the "solar blind" PMT, which has a decreased transmission in the 240 nm ultraviolet region [Loc12]. Thus, the statistics of the hydrogen-like data is not very good and the extraction of a resonance wavelength proved to be more complicated. Fitting the complete data of each the broad band and the narrow band region did not show a reasonable resonance. Since the widths of the resonance in the broad and narrow band case are already known from the lithium-like measurements, each of the files listed in table 4.4 in column "files" were fitted with a Gaussian function as given by equation (4.10) with the σ fixed to the corresponding mean value. Afterwards, all files showing a proper resonance fit were processed in a single fit for each the broad band and the narrow band region, also keeping the σ fixed at the value. The resulting plots are shown in figure 4.12(a) and for convenience with a 0.02 nm binning in figure 4.12(b). The fit results are also listed in table 4.5.

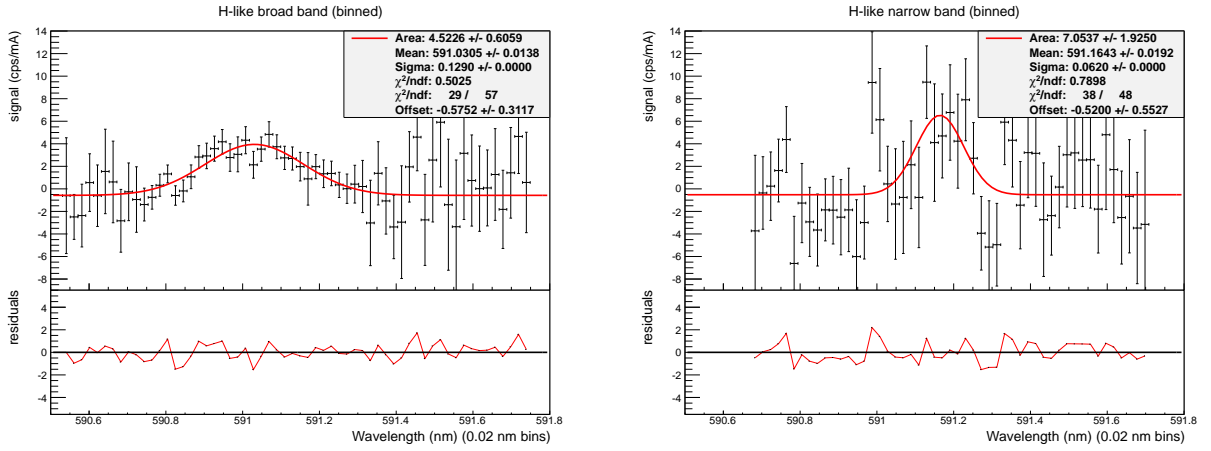
Table 4.5.: Results of the resonance fits of the four time regions of the hydrogen-like measurements.

region	λ_{fit} (nm)	σ	χ^2/ndf
broad band	591.0246 ± 0.0113	0.1290 (fixed)	1.0026
narrow band	591.1516 ± 0.0138	0.0620 (fixed)	1.1214

In contrast to the lithium-like case, now only one wavelength fit value was obtained for the broad-band ($\lambda_{\text{fit,broad}}^{\text{H-like}}$) and the narrow-band ($\lambda_{\text{fit,narrow}}^{\text{H-like}}$) measurements. Again, like in the lithium-like case, the systematic uncertainty of the lambdameter $\Delta\lambda_{\text{lab}}^{\text{Atos}}$ for the corresponding laser bandwidth has been added to $\lambda_{\text{fit,broad}}^{\text{H-like}}$ and $\lambda_{\text{fit,narrow}}^{\text{H-like}}$. Also the uncertainty due to the wavelength shifts induced by the electron cooler resets $\Delta\lambda_{\text{lab}}^{\text{e-cooler}}$ obtained from the broad-



(a) Unbinned H-like resonance fits.



(b) Binned H-like resonance fits.

Figure 4.12.: Resonance fits of the broadband and narrowband data of the H-like measurements. (a) unbinned fits, (b) binned fits.

band measurements in the lithium-like case have been added. The combined error is again comprised of the individual contributions summed up corresponding to equations (4.15) and (4.16):

$$\begin{aligned}\lambda_{\text{lab,broad}}^{\text{H-like}} &= (591.0246 \pm 0.0113(\text{stat.}) \pm 0.0482(\text{e-cooler}) \pm 0.219(\text{Atos})) \text{ nm} \\ &= (591.0246 \pm 0.2680) \text{ nm}\end{aligned}$$

$$\begin{aligned}\lambda_{\text{lab,narrow}}^{\text{H-like}} &= (591.1516 \pm 0.0138(\text{stat.}) \pm 0.0482(\text{e-cooler}) \pm 0.016(\text{Atos})) \text{ nm} \\ &= (591.1516 \pm 0.0665) \text{ nm}\end{aligned}$$

Subsequently, again the weighted mean has been calculated using equations (4.11) and (4.12)

giving the final value of the laboratory transition wavelength in hydrogen-like bismuth:

$$\lambda_{\text{lab}}^{\text{H-like}} = (591.1442 \pm 0.0645) \text{ nm.}$$

Again, as in the lithium-like case, the dominating contribution to the overall value $\lambda_{\text{lab}}^{\text{H-like}}$ is the wavelength obtained from the narrow-band measurements $\lambda_{\text{lab,narrow}}^{\text{H-like}}$ again due to the large uncertainty of the Atos lambdameter.

RESONANCE WAVELENGTHS IN THE ION REST FRAME

In this chapter the results concerning the resonance wavelengths in the laboratory system are transferred to the ion rest frame. Therefore, the ion velocity has to be known, which is predominantly determined by the velocity of the electrons in the electron cooler. The latter can be calculated from the electron cooler acceleration voltage and the electron current. Also space charge effects of the electrons and ions inside the electron cooler have to be taken into account. As in previous experiments ([Kla94, See99]), the uncertainty of the calibration of the electron cooler voltage is the dominating error contribution to the wavelength in the ion rest frame.

5.1. Calculating the ion velocity

The velocity β of the ions inside the ESR approaches the velocity of the electrons in the electron cooler during the cooling process. The electron velocity can be calculated from the effective acceleration potential U_{eff} and the electron current I_{e^-} . U_{eff} accounts for several effects that lead to a deviation from the preset value U_{set} :

$$U_{\text{eff}} = U_{\text{e-cool}} + \Phi_{\text{ges}} + dU, \quad (5.1)$$

where $U_{\text{e-cool}}$, Φ_{ges} and dU denote the following contributions:

- The high voltage actually applied to the electron cooler $U_{\text{e-cool}}$, which differs from the electron cooler voltage setting U_{set} . $U_{\text{e-cool}}$ is calibrated in the following.
- Corrections for space charge effects in the electron beam and the ion cloud, Φ_{ges} .

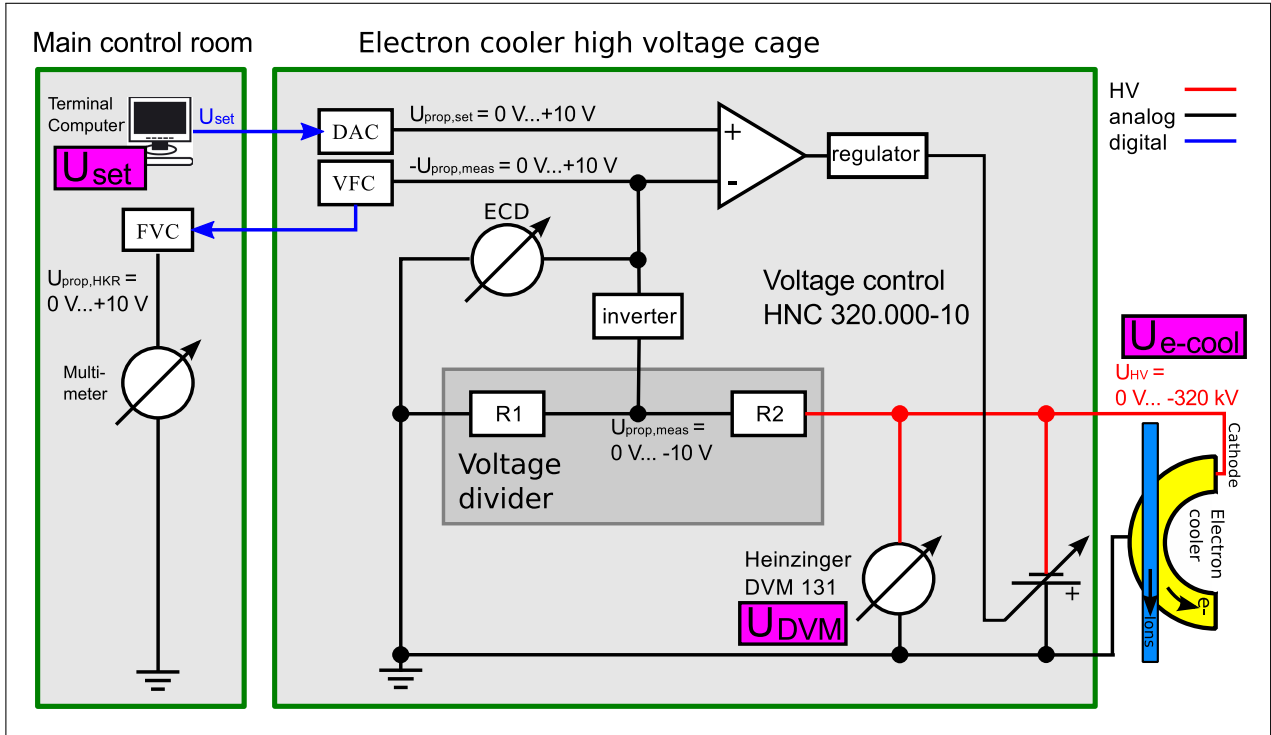


Figure 5.1.: Schematic overview of the electron cooler voltage control. The output voltage of the Heinzinger HNC 320.000-10 high voltage supply is set at a terminal computer in the GSI’s main control room by choosing U_{set} . The voltage applied to the electron cooler cathode is divided by a voltage divider and compared to the voltage setting to regulate the HNC 320.000-10. The Heinzinger DVM 131 digital voltmeter is not connected during regular operation. Two calibration steps are done to obtain $U_{\text{e-cool}}$: $U_{\text{set}} \rightarrow U_{\text{DVM}}$ and $U_{\text{DVM}} \rightarrow U_{\text{PTB}}$, where U_{PTB} is the voltage reference of the PTB used for calibration of the DVM 131 module [Loc13].

- Corrections due to a misaligned bunching frequency during the Li-like measurements, dU .

These three contributions will be discussed in the following. The results presented for the space charge correction and the misaligned bunching frequency are in detail discussed and derived by M. Lochmann [Loc13].

5.1.1. Calibration of the electron cooler voltage

A schematic overview of the electron cooler high voltage system is shown in figure 5.1. The preset voltage U_{set} of the electron cooler is set with a resolution of 1 V in the main control room at GSI. U_{set} is translated to a voltage between 0 V and +10 V that controls the output of the high voltage supply of the electron cooler, a custom-made device based on the ”HNC” series by Heinzinger (labeled HNC 320.000-10). The output voltage can be monitored up to 130 kV by a digital voltmeter with an internal voltage divider (Heinzinger DVM 131), in

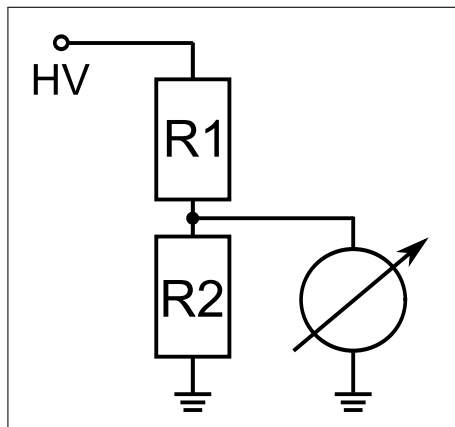


Figure 5.2.: Scheme of a high voltage voltmeter consisting of a voltage divider and a low voltage voltmeter.

the following denoted DVM, which has been calibrated at the PTB¹ in 2001 for positive and negative voltages up to 120 kV and 100 kV, respectively, and in 2012 for positive voltages up to 100 kV. During calibration of the negative voltages in the latter measurement, the DVM device got damaged. This means, that for negative voltages it has to be relied on the assumption, that the drift in the calibration of the DVM for positive voltages observed between the years 2001 and 2012 also holds for the negative branch of the device. Under this assumption a high voltage correction for U_{DVM} at the experimental cooler voltage of -213.9 kV can then be extrapolated.

In order to determine the actual electron cooler voltage $U_{\text{e-cool}}$ from the electron cooler set voltage U_{set} , two calibration steps have to be done:

1. $U_{\text{set}} \rightarrow U_{\text{DVM}}$: Conversion of the voltage setting U_{set} of the terminal computer in the main control room to the voltage measured by the Heinzinger DVM 131 U_{DVM} . The corresponding measurement has been performed on June 18th 2012.
2. $U_{\text{DVM}} \rightarrow U_{\text{PTB}}$: Conversion of U_{DVM} to the reference voltage U_{PTB} determined during calibrations of the DVM at the PTB in 2001 and 2012.

The calibrations in the following two steps have been performed for $U_{\text{set}} = -213900$ V, which is the voltage setting that has been applied during the measurements with H-like Bi⁸²⁺. The voltage setting in the Li-like case was $U_{\text{set}} = -213890$ V. Since the voltages corrections for both U_{set} -values differ negligibly by < 0.1 V, the extrapolations in the following are performed only for $U_{\text{set}} = -213900$ V.

In order to extrapolate the voltages measured with the DVM to the actual preset voltage, both calibration steps are in the following fitted with 2nd order polynomials $f(U) = aU^2 +$

¹Physikalisch-Technische Bundesanstalt, Abteilung 2, Bundesallee 100, 38116 Braunschweig

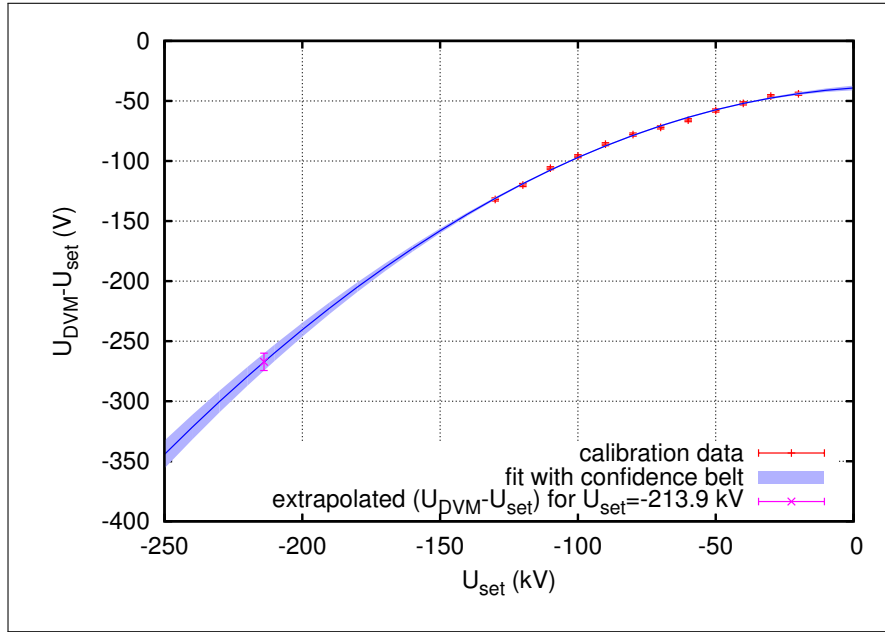


Figure 5.3.: Calibration fit for the calibration $U_{\text{set}} \rightarrow U_{\text{DVM}}$. The fit is shown with the corresponding confidence belt. For convenience the extrapolated value for $U_{\text{DVM}}(U_{\text{set}} = -213900 \text{ V})$ is separately plotted.

$bU + c$. A typical high voltage voltmeter consists of a voltage divider connected to a low voltage voltmeter as shown in figure 5.2, where typically $R1 \gg R2$. Due to the quadratic dependence of the heating power $P = U \cdot I = \frac{U^2}{R}$ on the voltage, a quadratic dependence of the correction terms on the voltages measured with the DVM is expected. Linear effects might occur due to heat dissipation at the resistors and an offset is allowed to account for unknown device systematics of the DVM. The fits have been performed using ROOT.

Step 1: $U_{\text{set}} \rightarrow U_{\text{DVM}}$ The voltage measured by the DVM, U_{DVM} , has been measured for different preset voltages U_{set} in June 2012. The fitted data are shown in figure 5.3, where $U_{\text{DVM}} - U_{\text{set}}$ is plotted against U_{set} . The fit is developed around $U_0 = -213900 \text{ V}$ using the fit function

$$f_{[U_{\text{DVM}}-U_{\text{set}}]}(U_{\text{set}}) = a(U_{\text{set}} - U_0)^2 + b(U_{\text{set}} - U_0) + c \quad (5.2)$$

to directly obtain parameter $c = f_{[U_{\text{DVM}}-U_{\text{set}}]}(-213900 \text{ V})$ along with its error. The fit results in

$$f_{[U_{\text{DVM}}-U_{\text{set}}]}(-213900 \text{ V}) = (-267.2 \pm 10.2_{\text{stat.}}) \text{ V}, \quad (5.3)$$

and therefore

$$U_{\text{DVM}}(U_{\text{set}} = -213900 \text{ V}) = (-214167.2 \pm 10.2) \text{ V}, \quad (5.4)$$

Step 2: $U_{\text{DVM}} \rightarrow U_{\text{PTB}}$ As already mentioned, the DVM has been calibrated at the PTB in 2001 for positive and negative voltages up to 120 kV and 100 kV, respectively, and in 2012 for positive voltages again up to 100 kV. The data are given as relative deviations of U_{DVM} from the voltage measured by the PTB reference voltmeter U_{PTB} . A significant drift is observed between the positive voltage calibration from the years 2001 and 2012. The same kind of drift is assumed to be present in the calibration of the negative DVM measurements but could not be verified due to the breakdown of the device during the measurements. Since the LIBELLE beamtime took place in August 2011, the calibration data of 2012 are assumed to be valid for the beamtime. However, the 2001 data can be used to estimate a value of the difference $[U_{\text{PTB}} - U_{\text{DVM}}]$ for $U_{\text{DVM}} = -214167.2 \text{ V}$ which corresponds to $U_{\text{set}} = -213900 \text{ V}$ (see equation (5.4)).

To be able to fit the data with 2nd order polynomials, the calibration data of 2001 for positive and negative voltages as well as the 2012 data for positive voltages are plotted as $[U_{\text{DVM}} - U_{\text{PTB}}]$ against U_{PTB} , where the 2001 negative data are mirrored to be displayed alongside the positive data (see figure 5.4). Thus, U_0 is in this case also positive. The three datasets are each fitted with

$$f_{[U_{\text{DVM}}-U_{\text{PTB}}]}(U_{\text{PTB}}) = a(U_{\text{PTB}} - U_0)^2 + b(U_{\text{PTB}} - U_0) + c, \quad (5.5)$$

where $U_0 = 231900 \text{ V}$.

Having obtained a fit function $f_{[U_{\text{DVM}}-U_{\text{PTB}}]}(U_{\text{PTB}})$ for the 2012 data, this function is used to determine the voltage U_{PTB} where $[U_{\text{DVM}} - U_{\text{PTB}}] + U_{\text{PTB}} = U_{\text{DVM}} = 214167.2$, which leads to a value of $U_{\text{PTB}} = 213978.4 \text{ V}$. The fits of the data using the 1σ error as given by the PTB result in $0.02 < \chi_{\text{red}}^2 < 0.09$. This indicates that the size of the error bars as stated by the PTB is governed by systematics. To separate the statistical analysis and the systematic effects, the errors of each dataset are scaled down by a factor 5.7, which corresponds to the mean deviation to $\chi_{\text{red}}^2 = 1$ of the three fits. The error of the fit parameters is this way almost solely statistical. The systematic uncertainty will be discussed later on.

Now, the three datasets are again fitted with function (5.5), this time with $U_0 = 213978.4 \text{ V}$, which results in the values and statistical errors for the parameter $c = f_{[U_{\text{DVM}}-U_{\text{PTB}}]}(U_0)$:

$$c_{2001,\text{neg}} = (67.5 \pm 7.7_{\text{stat}}) \text{ V} \quad (5.6)$$

$$c_{2001,\text{pos}} = (93.7 \pm 4.7_{\text{stat}}) \text{ V} \quad (5.7)$$

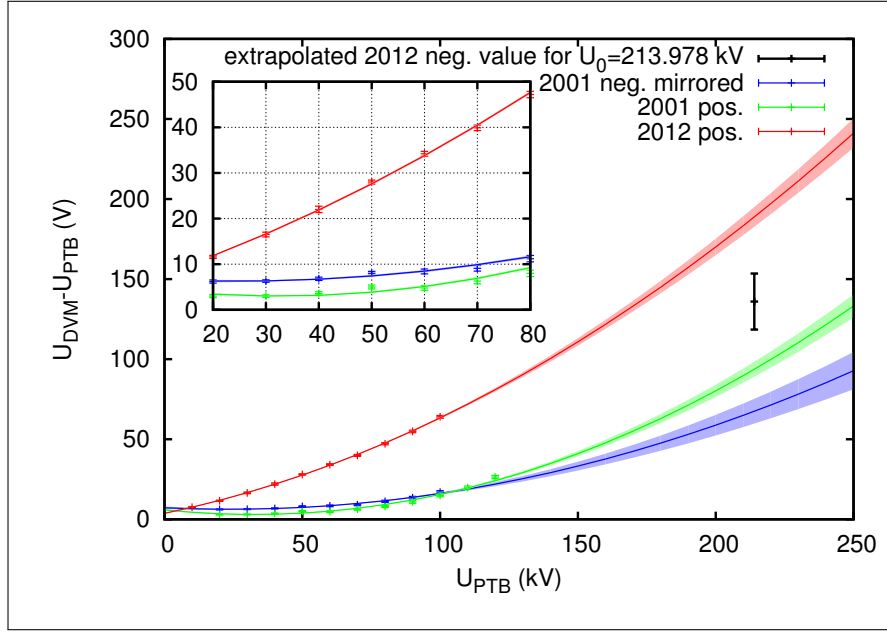


Figure 5.4.: Calibration fit for the calibration $U_{\text{DVM}} \rightarrow U_{\text{PTB}}$. The error bars of the three datasets are scaled down by a factor 5.7. The fits are shown with the corresponding confidence belt and the extrapolated value for $c_{2012,\text{neg,est.}}$ is depicted.

$$c_{2012,\text{pos}} = (188.8 \pm 6.2_{\text{stat}}) \text{ V}, \quad (5.8)$$

Assuming that the ratio $\frac{c_{2001,\text{pos}}}{c_{2001,\text{neg}}} = 1.39 \pm 0.17$ is still the same in 2012, the corresponding estimated value for $c_{2012,\text{neg,est.}}$ can be calculated to be

$$\begin{aligned} c_{2012,\text{neg,est.}} &= c_{2012,\text{pos}} \cdot \frac{c_{2001,\text{pos}}}{c_{2001,\text{neg}}} \\ &= \frac{(188.8 \pm 6.2) \text{ V}}{1.39 \pm 0.17} \\ &= (136.0 \pm 17.5_{\text{stat}}) \text{ V}. \end{aligned} \quad (5.9)$$

As mentioned, the scaling of the error bars of the datasets ignores the systematic uncertainty, which is a probable shift of the obtained fit functions $f_{[U_{\text{DVM}}-U_{\text{PTB}}]}(U_{\text{PTB}})$. This systematic uncertainty also has to be added to the extrapolated parameters $c_{2001,\text{neg}}$, $c_{2001,\text{pos}}$ and $c_{2012,\text{pos}}$, and is given by the PTB as a relative error of $1 \cdot 10^{-4}$ of the absolute voltage values. Thus

$$\Delta c^{\text{sys}} = U_0 \cdot 10^{-4}. \quad (5.10)$$

The obtained values for the three fits are

$$\Delta c_{2001,\text{neg}}^{\text{sys}} = \Delta c_{2001,\text{pos}}^{\text{sys}} = \Delta c_{2012,\text{pos}}^{\text{sys}} = 21.4 \text{ V}, \quad (5.11)$$

resulting in an overall systematic uncertainty $\Delta c_{2012,\text{neg,est.}}^{\text{sys}}$ of

$$\Delta c_{2012,\text{neg,est.}}^{\text{sys}} = \Delta c_{2001,\text{neg}}^{\text{sys}} + \Delta c_{2001,\text{pos}}^{\text{sys}} + \Delta c_{2012,\text{pos}}^{\text{sys}} = 64.2 \text{ V}. \quad (5.12)$$

These systematic uncertainties are not added quadratically but linearly to account for possible correlations of the uncertainties.

Since the negative data have been mirrored to the positive side, the voltage difference $[U_{\text{DVM}} - U_{\text{PTB}}]$ at $U_{\text{PTB}} = -213978.4 \text{ V}$ becomes $(-136.0 \pm 17.5_{\text{stat}} \pm 64.2_{\text{sys}}) \text{ V}$.

Now, the electron cooler voltage $U_{\text{e-cool}}$ corresponding to $U_{\text{set}} = -213900 \text{ V}$ can be calculated by

$$\begin{aligned} U_{\text{e-cool}} &= U_{\text{set}} + [U_{\text{DVM}} - U_{\text{set}}] + [U_{\text{PTB}} - U_{\text{DVM}}] \\ &= U_{\text{set}} + [U_{\text{DVM}} - U_{\text{set}}] - [U_{\text{DVM}} - U_{\text{PTB}}] \\ &= U_{\text{set}} + [(-267.2 + 136.0) \pm (\sqrt{(17.5_{\text{stat}})^2 + (10.2_{\text{stat}})^2} + 64.2_{\text{sys}})] \text{ V} \\ &= U_{\text{set}} - (131.2 \pm 84.5) \text{ V}, \end{aligned} \quad (5.13)$$

where the statistical error contributions are summed up in quadrature and the systematic uncertainty is added linearly.

5.1.2. Space charge corrections

The electrons in the cooler are influenced by space charge effects in the electron beam, which lead to a potential variation resulting in a change of the effective electron cooler voltage. This directly influences the electron velocity, which in turn determines the ion velocity. The direct influence of the potential variation on the ions can be neglected due to their higher mass. The potential introduced by the space charge of either the electron beam Φ_e or the ion beam Φ_i at the beam center (radial distance $r = 0$) have both been investigated by M. Lochmann and can be calculated by [Win96, Loc13]

$$\Phi_{(e,i),0} = \Phi_{e,i}(r = 0) = -\frac{I_{e,i}}{4\pi\epsilon_0\beta_e c} \left(1 + 2 \ln \frac{R_D}{R_{e,i}} \right) \quad (5.14)$$

where $I_{e,i}$ is the electron current or the ion current, respectively, ϵ_0 the electrical field constant, β_e the velocity of the electrons in terms of the speed of light c , $R_{e,i}$ the diameter of the electron beam or the ion beam, respectively, and R_D is the diameter of the drift tube of the

electron cooler. Equation (5.14) presumes cylindrically symmetrical electron and ion beams with homogeneous charge distributions and well-known beam radii as well as coaxial alignment of the electron and ion beams, which then leads to an overall space charge correction of [Loc13]

$$\Phi_{\text{ges}}(r) = \Phi_{\text{e},0} + \Phi_{\text{i},0} = \begin{cases} 27.2 \pm 4.2 \text{ V} & (\text{Bi}^{82+}) \\ 19.4 \pm 4.2 \text{ V} & (\text{Bi}^{80+}) \end{cases}. \quad (5.15)$$

The simplified assumptions in equation (5.14) are accounted for by the uncertainty of $\Phi_{\text{ges}}(r)$.

5.1.3. Misaligned bunching frequency

The ion velocity only depends solely on the electron cooler voltage, if it is not altered by another mechanism. During the measurements the ions were divided into two bunches by a high frequency (HF) voltage signal at the bunching cavity, providing such a mechanism. Only in the case that the free revolution frequency of the ions ν_{rev} without any HF signal applied matches the bunching frequency ν_{HF} (in the case of two bunches $\nu_{\text{HF}} = 2\nu_{\text{rev}}$) the ion velocity can still be derived from the electron cooler voltage. Unfortunately, during the measurements the revolution frequency ν_{rev} , which was only checked three times throughout the beamtime, changed by 112.9 Hz after changing the ion species, resulting in a discrepancy of ν_{HF} and $2\nu_{\text{rev}}$ of

$$\frac{d\nu}{\nu} = \frac{\nu_{\text{rev}} - \frac{\nu_{\text{HF}}}{2}}{\nu_{\text{rev}}} = 5.759 \cdot 10^{-5}. \quad (5.16)$$

The influence on the ion velocity has been investigated by M. Lochmann [Loc13], stating that this shift of ν_{rev} during the measurements with the $^{209}\text{Bi}^{80+}$ beam corresponds to an additional voltage shift of

$$dU = (67 \pm 5) \text{ V}$$

that has to be accounted for. However, for the H-like measurements, ν_{HF} and $2\nu_{\text{rev}}$ seem to have been well adjusted, thus $dU = 0$ in that case.

5.1.4. Results for the ion velocity β

In order to calculate the effective electron cooler voltage U_{eff} , the previous corrections to U_{set} are applied resulting in

$$U_{\text{eff}} = U_{\text{e-cool}} + \Phi_{\text{ges}} + dU \quad (5.17)$$

Table 5.1.: Electron cooler settings during the LIBELLE beamtime as calculated above.

	Bi ⁸²⁺	Bi ⁸⁰⁺
electron current I_{e-}	200 mA	150 mA
U_{set}	-213,900 V	-213,890 V
calibration correction	(-132 ± 84.5) V	(-132 ± 84.5) V
$U_{\text{e-cool}}$	(-214031.2 ± 84.5) V	(-214021.2 ± 84.5) V
space charge correction Φ_{ges}	(27.2 ± 4.2) V	(19.4 ± 4.2) V
misaligned bunching freq. corr. dU	–	(67 ± 5) V
U_{eff}	(-214004.0 ± 88.7) V	(-213934.8 ± 93.7) V
calculated ion velocity β	$(70.93830 \pm 0.02940)\%$	$(70.93161 \pm 0.03106)\%$

with the systematic uncertainties of the values added linearly to

$$\Delta U_{\text{eff}} = \Delta U_{\text{e-cool}} + \Delta \Phi_{\text{ges}} + \Delta dU. \quad (5.18)$$

With U_{eff} , now the ion velocity β is calculated according to

$$\beta = \sqrt{1 - \frac{1}{\gamma^2}} = \sqrt{1 - \left(1 + \frac{E_{\text{kin}}}{m_e \cdot c^2}\right)^{-2}} = \sqrt{1 - \left(1 + \frac{-e \cdot U_{\text{eff}}}{m_e \cdot c^2}\right)^{-2}}, \quad (5.19)$$

Table 5.1 gives an overview of the parameters.

5.2. Calculating the transition wavelengths in the ion rest frame

With the ion velocity determined in the previous subsection, the transition wavelength in the laboratory system λ_{lab} obtained by the fit of section 4.2.4 can now be used to calculate the transition wavelength λ_0 in the ions' rest frame. The laser wavelength seen by the ions is Doppler-shifted depending on the relative directions of the ion velocity and the laser beam. For collinear excitation in the case of lithium-like bismuth the excitation wavelength in the ion rest frame is given by

$$\lambda_{\text{lab}}^{\uparrow\uparrow} = \lambda_0 \frac{1}{\gamma(1 + \beta)} \quad \Leftrightarrow \quad \lambda_0 = \lambda_{\text{lab}}^{\uparrow\uparrow} \gamma(1 + \beta), \quad (5.20)$$

whereas for anti-collinear excitation in the hydrogen-like case

$$\lambda_{\text{lab}}^{\uparrow\downarrow} = \lambda_0 \frac{1}{\gamma(1 - \beta)} \quad \Leftrightarrow \quad \lambda_0 = \lambda_{\text{lab}}^{\uparrow\downarrow} \gamma(1 - \beta) \quad (5.21)$$

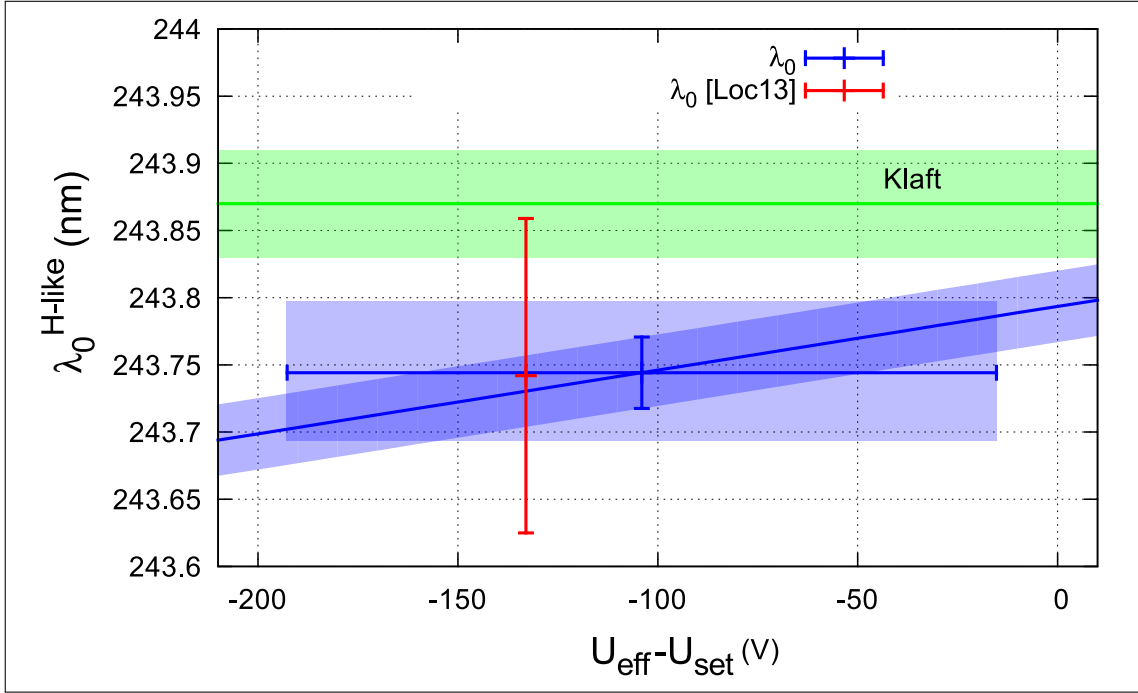


Figure 5.5.: Wavelength results as a function of $U_{\text{eff}} - U_{\text{set}}$ for Bi^{82+} : The sloped blue band corresponds to $\lambda_0^{\text{H-like}}$ with the thickness representing the error contribution labeled *lab* in equation (5.24). The wavelength obtained for the reconstructed value of $U_{\text{eff}} - U_{\text{set}}$ listed in table 5.1 is highlighted as blue datapoint and its error bars represent the uncertainties due to the calibration of U_{eff} (horizontal), and due to the laboratory wavelength (vertical). The height of the surrounding blue rectangle corresponds to the overall uncertainty as listed in table 5.2. The $\lambda_{0,\text{Lochmann}}^{\text{H-like}}$ value derived in [Loc13] is shown as the red data point with its error bar including an uncertainty of $U_{\text{eff}} - U_{\text{set}}$ of ± 244 V. The green band corresponds to the experimental value $\lambda_{0,\text{Klaft}}^{\text{H-like}}$ obtained by Klaft et al. [Kla94].

applies. The uncertainty has been calculated using

$$\Delta\lambda_0 = \sqrt{\underbrace{\left(\frac{\partial\lambda_0}{\partial\lambda_{\text{lab}}} \cdot \Delta\lambda_{\text{lab}}\right)^2}_{\text{lab}} + \underbrace{\left(\frac{\partial\lambda_0}{\partial\beta} \cdot \Delta\beta\right)^2}_{\text{cal}}}, \quad (5.22)$$

where *lab* denotes the error contribution due to the laboratory wavelength and *cal* the error contribution due to the effective acceleration potential U_{eff} . With these equations applied to the resonance wavelengths $\lambda_{\text{lab}}^{\text{Li-like}}$ and $\lambda_{\text{lab}}^{\text{H-like}}$, the transition wavelengths in the rest frame are:

$$\begin{aligned} \lambda_0^{\text{H-like}} &= (243.744 \pm \underbrace{0.042}_{\text{cal}} \pm \underbrace{0.027}_{\text{lab}}) \text{ nm} \\ &= (243.744 \pm 0.050) \text{ nm} \end{aligned} \quad (5.23)$$

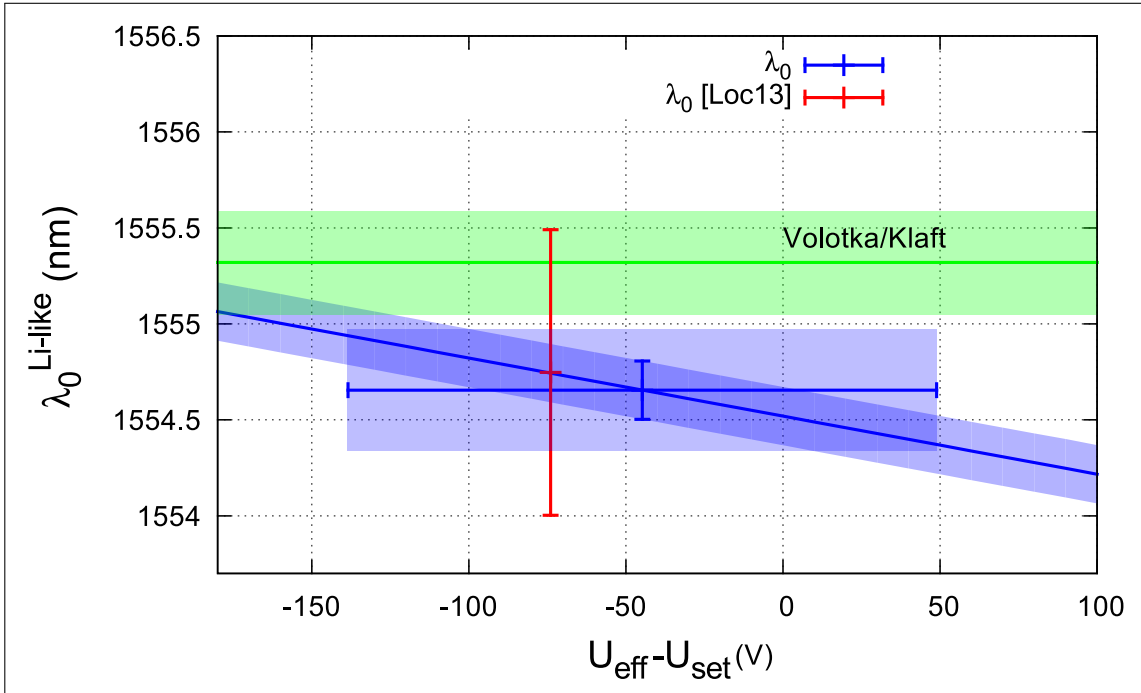


Figure 5.6.: Wavelength results as a function of $U_{\text{eff}} - U_{\text{set}}$ for Bi^{80+} : The sloped blue band corresponds to $\lambda_0^{\text{Li-like}}$ with the thickness representing the error contribution labeled *lab* in equation (5.24). The wavelength obtained for the reconstructed value of $U_{\text{eff}} - U_{\text{set}}$ listed in table 5.1 is highlighted as blue datapoint and its error bars represent the uncertainties due to the calibration of U_{eff} (horizontal), and due to the laboratory wavelength (vertical). The height of the surrounding blue rectangle corresponds to the overall uncertainty as listed in table 5.2. The $\lambda_{0,\text{Lochmann}}^{\text{Li-like}}$ value derived in [Loc13] is shown as the red data point with its error bar including an uncertainty of $U_{\text{eff}} - U_{\text{set}}$ of ± 244 V. The green band corresponds to the theoretical value $\lambda_{0,\text{Volotka}}^{\text{Li-like}}$ calculated by Volotka et al. [Vol11].

$$\begin{aligned} \lambda_0^{\text{Li-like}} &= (1554.655 \pm \underbrace{0.283}_{\text{cal}} \pm \underbrace{0.152}_{\text{lab}}) \text{ nm} \\ &= (1554.655 \pm 0.322) \text{ nm} \end{aligned} \quad (5.24)$$

These results are compared in both the H-like and the Li-like case to the results obtained by Lochmann [Loc13]. The H-like result is also compared to the transition wavelength in Bi^{82+} obtained by Klaft et al. [Kla94]. The Li-like result is compared to the theoretical calculation of the transition wavelength by Volotka et al. [Vol11], which is based on the H-like wavelength value obtained by Klaft and theoretical calculations of the QED contributions in equation (2.26). The values are plotted in figures 5.5 and 5.6 and listed in table 5.2. In these plots the sloped blue band corresponds to λ_0 with the thickness representing the error contribution labeled *lab* in equations (5.23) and (5.24), respectively. The λ_0 obtained for

Table 5.2.: Transition wavelength values for Bi^{82+} and Bi^{80+} obtained in this work and in [Loc13] compared to other experimental and theoretical results. The results in [Loc13] and in this work are obtained from the same experimental dataset.

Bi^{82+}			
wavelength (nm)	$\Delta\lambda_0/\lambda_0$	deviation to this work (pm)	reference
243.744 ± 0.050	$2.1 \cdot 10^{-4}$		ESR, this work
243.742 ± 0.117	$4.8 \cdot 10^{-4}$	2	ESR, [Loc13]
243.87 ± 0.04	$1.6 \cdot 10^{-4}$	126	ESR, [Kla94]
Bi^{80+}			
wavelength (nm)	$\Delta\lambda_0/\lambda_0$	deviation to this work (pm)	reference
1554.655 ± 0.322	$2.1 \cdot 10^{-4}$		ESR, this work
1554.747 ± 0.744	$4.8 \cdot 10^{-4}$	92	ESR, [Loc13]
1555.32 ± 0.27	$1.7 \cdot 10^{-4}$	665	theor., [Vol11]

the $U_{\text{eff}} - U_{\text{set}}$ values listed in table 5.1 is highlighted as blue datapoint and its error bars represent the uncertainties due to the calibration of U_{eff} , *cal* (horizontal), and due to the laboratory wavelength, *lab* (vertical). The error bars are surrounded by a blue rectangle, whose vertical size corresponds to the total uncertainty of λ_0 stated in equations (5.23) and (5.24), respectively, obtained using equation (5.22). The λ_0 value derived in [Loc13] is shown in red with its overall uncertainty including the uncertainty of U_{eff} , which has been conservatively estimated in both the H-like and the Li-like case to be ± 244 V. In figure 5.5 the green band corresponds to the value $\lambda_{0,\text{Klaft}}^{\text{H-like}}$ obtained by Klaft et al. [Kla94], while in figure 5.6 it represents the value $\lambda_{0,\text{Volotka}}^{\text{Li-like}}$ calculated by Volotka et al. [Vol11].

H-like The obtained $\lambda_0^{\text{H-like}}$ value of this work, in the following labeled $\lambda_{0,\text{Jöhren}}^{\text{H-like}}$, does not correspond within its error bars in to the value obtained by Klaft et al. [Kla94] as listed in table 5.2. In contrast, the value $\lambda_{0,\text{Lochmann}}^{\text{H-like}}$ obtained in [Loc13] is, assuming a very conservative uncertainty of the effective acceleration potential $\Delta U_{\text{eff}} = \pm 244$ V, within its error bars compatible to the Klaft value $\lambda_{0,\text{Klaft}}^{\text{H-like}}$, which features the smallest error bars of the three values. The deviation of the value obtained in this work to the value obtained in [Loc13],

$$D_{\text{Lochmann}}\lambda_0^{\text{H-like}} = |\lambda_{0,\text{Lochmann}}^{\text{H-like}} - \lambda_{0,\text{Jöhren}}^{\text{H-like}}| = 2 \text{ pm}, \quad (5.25)$$

is very small compared to the deviation to the value obtained by Klaft,

$$D_{\text{Klaft}}\lambda_0^{\text{H-like}} = |\lambda_{0,\text{Klaft}}^{\text{H-like}} - \lambda_{0,\text{Jöhren}}^{\text{H-like}}| = 126 \text{ pm}. \quad (5.26)$$

The deviations of the wavelength values of Lochmann, Klaft and Volotka to the values obtained in this work are also listed in table 5.2. During calculations of the specific difference $\Delta'E$ (see chapter 2.2) performed by M. Lochmann [Loc13], doubts arose about the calibration of the electron cooler voltage U_{e-cool} in the Klaft measurements, since the DVM was first calibrated by the PTB in 2001 while the experiment described by Klaft et al. was performed in 1994 (see discussion in [Loc13]). That would have an impact on both $\lambda_{0,Klaft}^{H-like}$ and $\lambda_{0,Volotka}^{Li-like}$, since the calculation of $\lambda_{0,Volotka}^{Li-like}$ is based on the value $\lambda_{0,Klaft}^{H-like}$ and might explain the discrepancy.

Li-like In the lithium-like case the value $\lambda_{0,Jöhren}^{Li-like}$ of this work is also not compatible within its error bars to the value $\lambda_{0,Volotka}^{Li-like}$ calculated by Volotka et al. [Vol11]

Again the deviations of the wavelength values of Lochmann and Volotka to the ones obtained here can be compared:

$$D_{Lochmann}\lambda_0^{Li-like} = |\lambda_{0,Lochmann}^{Li-like} - \lambda_{0,Jöhren}^{Li-like}| = 92 \text{ pm}, \quad (5.27)$$

which is again very small compared to the third value listed in table 5.2:

$$D_{Volotka}\lambda_0^{Li-like} = |\lambda_{0,Volotka}^{Li-like} - \lambda_{0,Jöhren}^{Li-like}| = 665 \text{ pm}. \quad (5.28)$$

The laboratory wavelength values λ_{lab}^{H-like} and $\lambda_{lab}^{Li-like}$ obtained by the analyses performed largely independently in this work and in [Loc13] agree very well. The different size of the error bars of the rest-frame wavelength is induced by a somewhat different analysis strategy of the laboratory wavelength and a different extrapolation of the effective acceleration potential of the electron cooler.

The uncertainty in the order of $\mathcal{O}(10^{-4})$ obtained in this work and by Lochmann [Loc13], as listed in table 5.2, does not allow yet for a precision test of QED predictions. However, the experimental verification and determination of the $2s$ transition wavelength in Bi^{80+} enables future experiments like SpecTrap, with uncertainties on the $\mathcal{O}(10^{-7})$ level, to pursue high precision QED tests. The size of the errors both in [Loc13] and in this work are dominated by the uncertainties in the determination of the ion velocity β and, in turn, by the uncertainty of the effective acceleration potential U_{eff} of the electron cooler. The uncertainty of U_{eff} stems from the unsatisfactory calibration of the negative electron cooler voltage U_{e-cool} , which has been discussed earlier in this chapter, and fluctuations of the electron cooler voltage after electron cooler resets, which have been discussed in section 4.3.1. The latter fluctuations are in this work already accounted for by the error contribution of λ_{lab} , while in [Loc13] they are

part of the error contribution due to the calibration of the effective acceleration potential, which has there been estimated very conservatively.

To increase the precision of future experiments at the ESR, it is crucial to further investigate the systematics of the electron cooler and increase the effort in calibrating and monitoring the parameters determining the effective acceleration potential U_{eff} .

Part II.

AN APD BASED SINGLE PHOTON DETECTOR FOR THE SPECTRAP EXPERIMENT

THE SPECTRAP EXPERIMENT

The SpecTrap experiment is designed as multi-purpose experiment, providing the infrastructure to perform laser spectroscopy on a variety of charged ions with a suitable transition wavelength. By cooling the ions stored in the central Penning trap of the experiment to very low temperatures, SpecTrap will be able to increase the precision of the transition wavelength measurements of predecessor experiments performed at the ESR or an EBIT¹ by several orders of magnitude to a relative accuracy of several parts in 10^{-7} [And10]. The setup is suitable for excitation and detection of transitions spanning wavelengths from about 240 nm ultraviolet light up to 1600 nm near infrared light. The limitations are given by transmission properties of non-exchangeable optical components on the ultraviolet side and the increasing difficulties in the detection of single-photons in the infrared regime. At the boundaries of the wavelength regime hyperfine transitions in H-like and Li-like bismuth are found, which are of special interest for laser spectroscopy measurements providing precision tests of QED in high magnetic and electric fields as laid out in chapter 2. A list with additional measurement

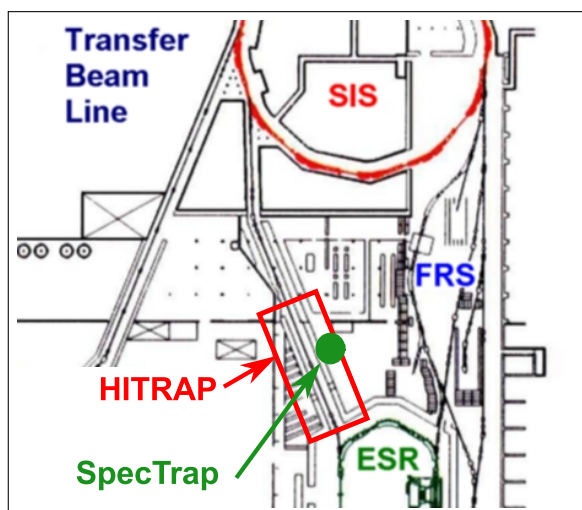


Figure 6.1.: Location of the HITRAP beamline and the SpecTrap experiment at GSI.

¹Electron Beam Ion Trap

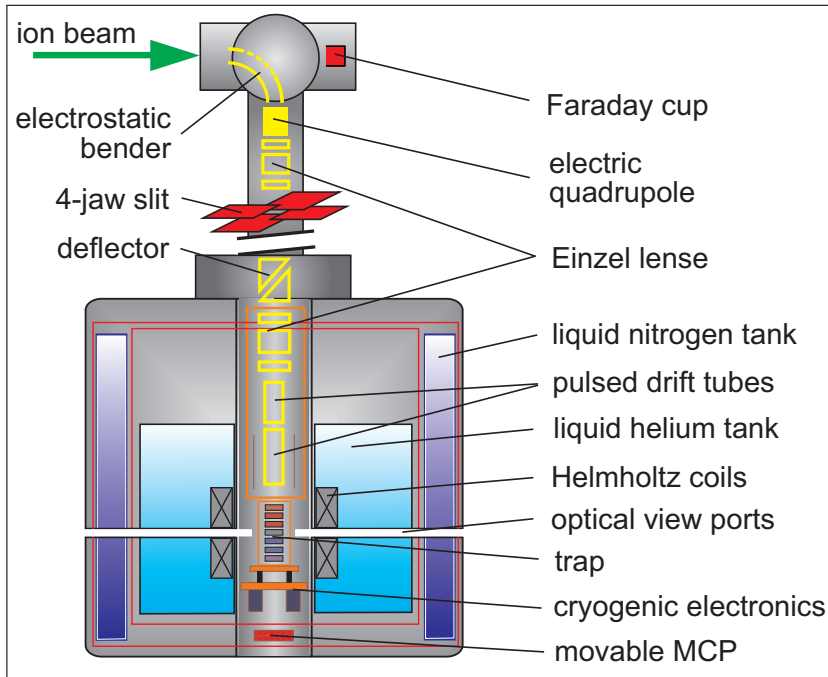


Figure 6.2.: Overview of the SpecTrap setup (not to scale). Ions are injected either from HITRAP or from a local ion source and are captured in the central Penning trap located inside two superconducting magnets in a Helmholtz configuration. Light from tunable lasers can enter the trap from below the setup once the multichannel plate (MCP) detector which is used for diagnostic purposes is removed. Fluorescence photons can be detected through two pairs of optical view ports, perpendicular to each other. [And10]

candidates for fine and hyperfine transitions can be found in [And12].

6.1. Experimental setup

The SpecTrap experiment is one of several experiments that will make use of the HITRAP decelerator facility, which is currently being built in place of the SIS re-injection channel (see figure 6.1). HITRAP will be used to slow down (heavy, highly charged) ions produced by the GSI accelerators for use in high precision trap experiments. After the deceleration stages the HITRAP beamline bends upwards and is continued on top of the re-injection cavern in the opposite direction, where several experiments are located, one of them the SpecTrap experiment. A schematic cross section of the SpecTrap experiment is shown in figure 6.2. SpecTrap consists of a superconducting magnet and a liquid helium (LHe) cryostat formerly used in the RETrap experiment and consigned to GSI². It is equipped with a newly designed Penning trap, laser systems and photon detectors to allow laser spectroscopy of fine and hyperfine transitions in highly charged ions to be delivered by the HITRAP facility. SpecTrap is set up on an elevated platform next to the HITRAP cavern. Since a very detailed description of the experimental setup can be found in [And12, Caz12], this section introduces the experiment only briefly.

²In collaboration with Lawrence Livermore National Laboratory and Texas A&M University

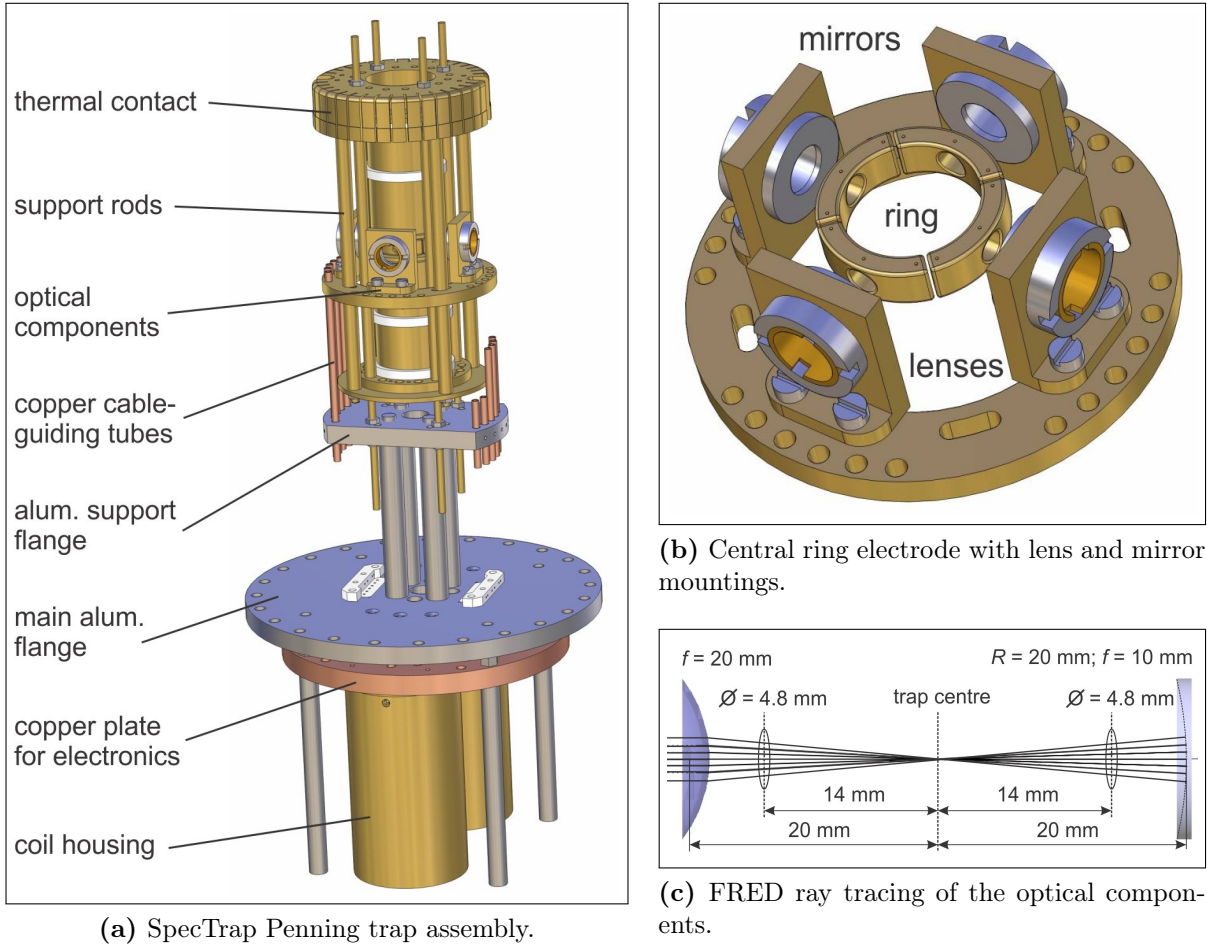


Figure 6.3.: (a) Technical drawing of the SpecTrap Penning trap assembly without cables and electronic components. The trap is mounted vertically as depicted. Ions are introduced from the top while the laser beam is injected along the vertical axis from the bottom. (b) The perforated ring electrode with the mounting of the light collection system. (c) Ray tracing of the light collection system consisting of a spherical mirror, a plano-convex lens and the two holes in the ring electrode segments; done with FRED [And12].

6.1.1. The SpecTrap Penning trap

The central part of the SpecTrap setup is a 5-pole, cylindrical, open-endcap Penning trap. It is designed to capture ion bunches in-flight and to store them for use in laser spectroscopy experiments. The complete trap assembly is shown in figure 6.3(a). The trap consists of a central ring electrode and, from the center outwards, of a pair of correction electrodes, a pair of endcaps and an additional pair of capture electrodes. The latter ones are used as first capture stage thus enhancing the *trap acceptance*, which is the maximum bunch size that can be captured by reflecting an incoming ion bunch at the second capture electrode and rapidly raising the potential of the first one. The trap has an inner radius of $r_0 = 10.6$ mm and an overall length of about 110 mm. The electrodes are made of oxygen free high conductivity

(OFHC) copper and were first silver coated and then gold plated.

The central ring electrode is divided into four segments (see figure 6.3(b)). This allows for ion cyclotron frequency detection, ion excitation and for the implementation of the rotating wall technique used to compress the ion cloud [Bha12]. Each of the segments is perforated with a 4.8 mm hole, to allow optical access to the trap volume perpendicular to the trap axis.

A system of mirrors and lenses located outside the trap volume and mounted on the trap support structure was designed by Z. Anđelković [And12] to enhance the photon flux at two perpendicular viewports. As shown in Fig 6.3(c) a plano-convex lens on one side is used to collect and collimate the light emitted from the trap center for detection. On the other side a spherical mirror reflects light emitted in the opposite direction back towards the trap center such that it can then also be collected by the lens. This should ideally double the light yield at the optical exits equipped with detectors (not taking into account imperfections of the optical system). The fluorescence detection has to deal with a very small accessible solid angle of 0.09 sr, which corresponds to a fraction of $7.2 \cdot 10^{-3}$ of the total solid angle of 4π . Further details concerning the Penning trap specifications, especially electronics and signal processing for non-destructive ion detection, can be found in [And12].

6.1.2. Superconducting magnets and vacuum system

To allow the Penning trap to function, a magnetic field parallel to the trap axis is needed. This is provided by a Nalorac NMR, vertical, cold-bore, split-coil superconducting magnet (see figure 6.2) [And12]. It is mounted inside a 50 l liquid helium reservoir, which has a central bore of 76.2 mm to mount the trap and additional equipment as needed. Direct optical access to the inner bore is provided by six optical viewports with a minimum diameter of 15.9 mm, four of them oriented like a cross and the other two in line with an angle of 30° with respect to one of the cross axes. Therefore the coil of the superconducting magnet is split into two parts made of a single Niobium-Titanium wire, arranged in Helmholtz configuration, i.e. the spacing between the coils equals the coil radius. To avoid direct thermal contact to the environment, the liquid helium reservoir is surrounded by several intermediate temperature stages. The first stage is a passive radiation heat shield, followed by a 100 l liquid nitrogen vessel. Another passive heat shield is the last stage before the outer vacuum chamber.

The complete inner cryostat system is suspended from the upper flange with 800 mm diameter, which houses two pairs of liquid helium (LHe) and liquid nitrogen (LN) fill ports, one of each used for filling and the other one for venting. The bottom flange has the same diameter but has no direct contact to any component of the cryostat system. It is equipped with several smaller flanges used for vacuum pumps and gauges as well as for electrical con-

nection of the Penning trap. The central flange is used for ion ejection from the trap, which can be detected with a movable MCP, and for injecting a laser beam into the trap.

The SpecTrap vacuum system was designed to provide favorable conditions for long storage times of ions inside the Penning trap, which directly depend on the residual gas pressure. Therefore, the vacuum tubing and the magnetic housing were constructed of type 304 and 316 stainless steel which allow for low outgassing rates. The system is evacuated by two turbomolecular pumps, mounted on the top and on the bottom of the system, followed by rotary vane pumps. Additionally, two ion getter pumps were installed. To reach optimum vacuum conditions, the system was baked out at maximum temperatures below 150°C to avoid damage on some temperature sensitive components. This way a pressure of $2 \cdot 10^{-8}$ mbar was achieved. When cooling with liquid helium the pressure measured with the gauges located outside the cold region drops to $5 \cdot 10^{-9}$ mbar. However, life time measurements performed with Mg^+ ions indicate a vacuum of 10^{-11} mbar in the trap region, which is achieved by cooling the trap to LHe temperature [And12].

6.1.3. SpecTrap beamline and ion sources

The T-shaped SpecTrap beamline (see figure 6.2) is directly connected to the central DN CF 100 flange of the upper 800 mm flange. The horizontal part is separated into two sections. One of these will later be used to connect SpecTrap to the HITRAP beamline. The opposite end of the horizontal beamline can be used for installation of off-line ion sources as used in the first systematic tests of the setup [And12, Caz12]. Ions from either side of the horizontal beam pipe can be transferred to the trap by the implemented ion optics. For local ion sources this consists of two einzel lenses to shape the ion beam followed by a quadrupole bender guiding the ions into the vertical section. A multipole is used to correct for beam deformations after bending down, while two following einzel lenses are guiding the beam towards two drift tubes used to decelerate the ion bunch right in front of the trap. Between the quadrupole bender and the magnet, a channeltron is placed to check the efficiency of the ion transport before entering the strong magnetic field of the trap.

Since the beamline from HITRAP as well as a local EBIT source is currently being assembled, testing of the setup has so far only been done with local sources that produce Mg^+ ions. The EBIT will be able to provide several charge states of isotopes in the mid-Z to high-Z region with fine and hyperfine transitions suitable for laser spectroscopy experiments and can be used to set up an intermediate experimental schedule until the completion of the HITRAP facility.

6.1.4. Ion excitation

In contrast to measurements at the ESR, where a single laser system can be used to excite different ions due to the possibility of Doppler-shifting the transition to the laser wavelength by adapting the ion velocity, various laser systems are needed to cover the wide wavelength range from 240 nm to 1600 nm on the excitation side. Therefore, the laser system has to be considered for each transition separately. To provide a safe and well controlled environment for the operation of precise laser systems close to the Penning trap, a laser laboratory was built under the SpecTrap platform where the vacuum vessel is placed. It has first been used during measurements with trapped Mg^+ ions [And12, Caz12], where a 1.2 W 1118 nm single-mode fiber laser with two cavities for second harmonic generation was applied to obtain a frequency quadrupling to 279 nm.

6.2. Fluorescence light detection at SpecTrap

Since the aim of the SpecTrap experiment is to determine transitions spanning the wavelength region from the ultraviolet to the near infrared, suitable detector systems are required which together are able to cover this range. Of particular importance are the HFS transitions in hydrogen-like bismuth ($^{209}\text{Bi}^{82+}$) at 244 nm and in lithium-like bismuth ($^{209}\text{Bi}^{80+}$) at 1555 nm. These transitions, at the opposite edges of the spectrum, can be used for a precision test of QED predictions. In the following, another transition of importance is the HFS transition in hydrogen-like lead ($^{207}\text{Pb}^{81+}$) at 1020 nm. Besides the broad wavelength range, additional demands come from the small solid angle accessible to fluorescence light detection and the relatively high magnetic field at the exit windows of the optical viewports that pose a problem for classical photomultipliers. The following section will discuss estimated photon rates at the exits of the optical viewports, which are based on simulations of the optics used to focus the fluorescence light onto the detector (diploma thesis of D. Hampf [Ham08]). The assumptions made in the simulations along with updated results are introduced in section 6.2.1. Section 6.2.2 will briefly deal with the magnetic field present at the SpecTrap experiment in which the detectors have to operate. Finally, section 6.2.3 will introduce the different detector types that are or will be used at the SpecTrap experiment.

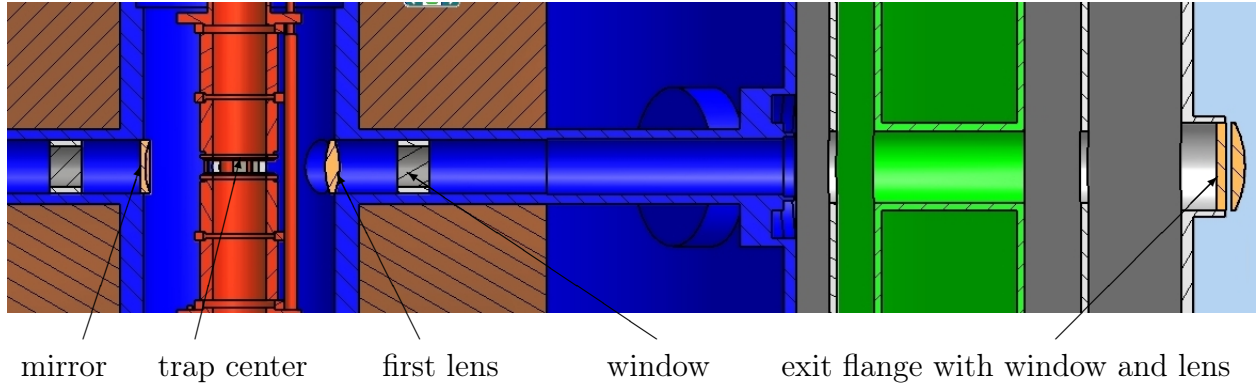


Figure 6.4.: Cross section of one of the light tunnels of the SpecTrap cryostat (technical drawing): The trap can be seen on the left hand side (red) with the first lens and the mirror (yellow) mounted close to the trap center. A window separating two vacuum stages is placed at the left end of a tube (gray). The exit flange of the cryostat later equipped with a window and a second lens (yellow) is shown on the right side.

6.2.1. Estimated photon rates at the detector

In order to establish the demands on the detectors to be used at SpecTrap, it is necessary to estimate the amount of fluorescence light, which is exiting the optical viewports and which can be guided to the detectors. Assuming that the excitation laser is able to saturate the transition under study, such that about half of the trapped ions is in the upper state, the number of spontaneously emitted photons per time is mainly determined by three factors:

- The photon rate should be proportional to the number N_{ions} of trapped ions.
- It should depend inverse proportionally on the lifetime τ of the upper state.
- Losses due to solid angle and light transport by the optics are accounted for by $\varepsilon_{\text{transp}}$.
- The detection efficiency $\varepsilon_{\text{det}} = \text{QE} \cdot \varepsilon_{\text{size}}(r)$ incorporating the detector's quantum efficiency (QE) and its acceptance $\varepsilon_{\text{size}}(r)$ depending on the detector radius r , which determines the fraction of photons that can be counted.

Thus, the total rate of photons that are detected, \dot{N}_{det} , is given by

$$\dot{N}_{\text{det}} = \frac{1}{2} \cdot N_{\text{ions}} \cdot \frac{1}{\tau} \cdot \varepsilon_{\text{transp}} \cdot \varepsilon_{\text{det}}. \quad (6.1)$$

According to M. Vogel [Vog05] the number of ions stored inside the trap will be of the order $N_{\text{ions}} \approx 10^5$. The factor $\varepsilon_{\text{transp}}$ accounts for several losses of fluorescence light, that will occur due to the properties of the experimental setup and its components:

$$\varepsilon_{\text{transp}} = \varepsilon_{\text{comp}} \cdot \varepsilon_{\text{sa}} \cdot \varepsilon_{\text{optics}}, \quad (6.2)$$

where the factors $\varepsilon_{\text{comp}}$, ε_{sa} and $\varepsilon_{\text{optics}}$ are accounting for the following light losses:

- $\varepsilon_{\text{comp}}$: Describes the losses due to the transmission properties of the lenses and windows used in the setup. The optics system consists of two lenses and two windows, where the first lens is located near the Penning trap as depicted in figure 6.4. The figure also shows the first window, which is inserted in the light tunnel to separate the vacuum stages. This window is made of *fused quartz*, as are the two lenses and the window mounted at the exit flange. The transmission of the material stays above 90% between 300 nm and 2000 nm, while for the 244 nm of the transition in Bi^{82+} the transmission is about 80%. The estimates in [Ham08] assumed all optical components to be made of the same material. The second lens, however, was supposed to be glued on the exit window with optical grease to eliminate one of the optical transitions to act as a single optical element. These three components with each 90% and 80% transmission, respectively, lead to an overall transmission of $(0.9)^3=0.73$ or $(0.8)^3=0.51$. Also the previous trap design included a meshed central electrode with 30% coverage leading to overall factors of $\varepsilon_{\text{comp}}^{\text{Pb}^{81+},\text{Bi}^{80+}}=(51\pm 12)\%$ and $\varepsilon_{\text{comp}}^{\text{Bi}^{82+}}=(36\pm 9)\%$. Since the design of the central electrode has changed, i.e the mesh is exchanged with a hole, and also the second lens is no longer attached to the exit window, the overall transmission has to be adapted to $\varepsilon_{\text{comp}}^{\text{Pb}^{81+},\text{Bi}^{80+}}=(66\pm 10)\%$ and $\varepsilon_{\text{comp}}^{\text{Bi}^{82+}}=(41\pm 10)\%$.
- ε_{sa} : The solid angle accessible to fluorescence light detection was assumed in [Ham08] to be 0.23 sr, due to the size and the position of the first lens, resulting in $\varepsilon_{\text{sa}} = 1.8\%$. Additionally, the mirror placed on the opposite side of the first lens was not taken into account. In the final setup the solid angle is given by the size of the hole in the central trap electrode. A solid angle of 0.09 sr would lead to a fraction of all fluorescence photons of $\varepsilon_{\text{sa}} = 0.72\%$ available for detection. Without accounting for re-absorption of photons in the ion cloud and for a non-perfect reflection at the mirror on the opposite side of the first lens, the light yield is ideally doubled, which can be expressed by doubling the solid angle to $\varepsilon_{\text{sa}} = 1.44\%$
- $\varepsilon_{\text{optics}}$: Accounts for losses during light transport to the detector and is derived from optical simulations as described in the next section. Assuming that the minor changes in the final lens setup do not drastically change the transmission from the first to the second lens, the geometric efficiency of the optics $\varepsilon_{\text{optics}}$ is not re-evaluated.

6.2.1.1. Simulations of the optics and the influence of the detector size

To determine the efficiency of the viewport optics, simulations have been performed in the diploma thesis of D. Hampf [Ham08] using *Kojac*, a java-based freeware tool for ray tracing

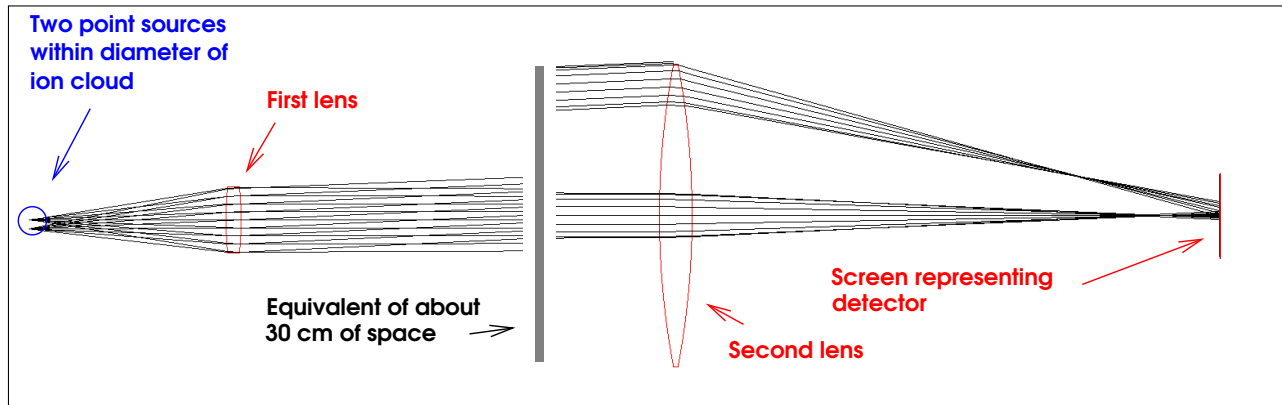


Figure 6.5.: Light rays of two point sources within the ion cloud to the detector. One of the sources is located in the center of the ion cloud, the other is shifted downwards by 1.2 mm. [Ham08]

in optical systems. The simulations have been used to investigate firstly the transmission of photons from the trap center to the outside and secondly the percentage $\varepsilon_{\text{size}}(r)$ of these photons that can be focused onto a detector of a certain size r .

Transmission from the first to the second lens: The simulations assume an extended ion cloud inside the trap as light source. The ion cloud is supposed to be spherical and homogeneous with a radius of 1.5 mm, where the ion density sharply drops at the cloud's perimeter and no photons are reabsorbed inside the cloud. The extension of the light source is implemented by placing a certain number of point-like light sources throughout the defined ion cloud volume. As shown in figure 6.3, the penning trap is equipped with plano-convex lenses, which are adjusted to ideally collimate light emitted from the trap center. Since the light source is extended, light that is emitted outside the cloud center leaves the first lens under a certain angle to the surface normal, as depicted in figure 6.5, where the light rays emitted by a point source 1.2 mm off the center of the ion cloud only hit the outer rim of the second lens. Since the light tunnel has various diameters and gaps as shown in figure 6.4 and its reflectivity is unknown, photons reflected from the tube can either be lost in the hollow spaces or would hit the second lens under large angles, making it difficult to focus them onto the detector. Therefore, the simulation only accounts for light rays emerging from the first lens that directly hit the second lens. The simulations result in $\varepsilon_{\text{optics}} = (77 \pm 2)\%$ [Ham08].

The influence of the detector size: The second lens focuses the light collimated by the first lens onto the detector. The main problem here is not the lens aberrations but incident non parallel light rays originating from the extension of the light source. Hence, the focal point of the second lens varies for light emitted from different locations in the ion cloud, which again can be seen in figure 6.5. The optimum detector position will therefore be

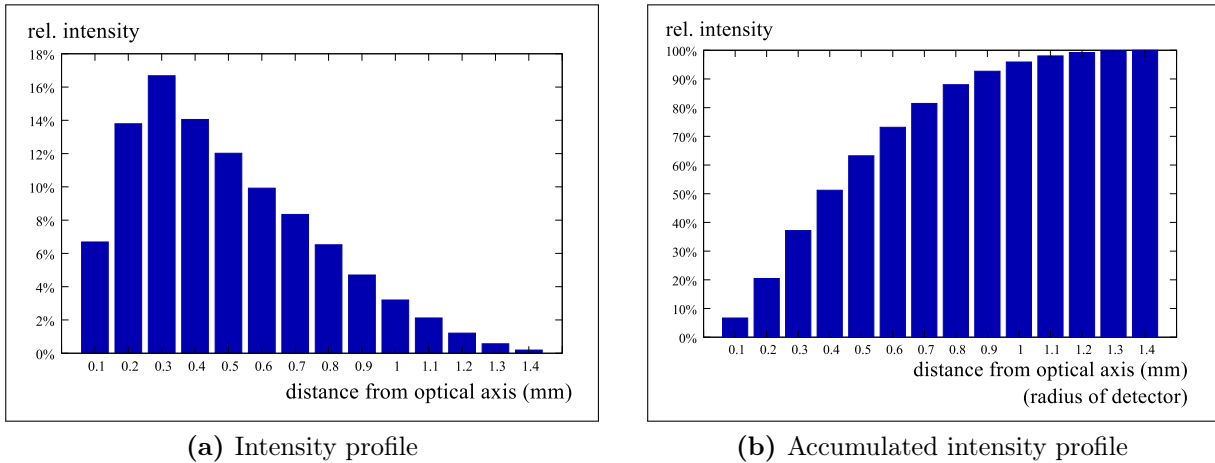


Figure 6.6.: Simulation results: (a) Intensity profile of the two lens system at the detector, (b) accumulated intensity profile to display the relative intensity as a function of the detector’s radius. [Ham08]

slightly behind the focal length of the second lens. To determine the minimum detector size needed to detect a certain amount of the emitted photons a screen with a radius of 5 mm that was segmented in annuli with a width of 0.1 mm each was implemented in the simulation representing the detector. Figure 6.6(a) shows the intensity profile at the detector.

Figure 6.6(b) shows the accumulated intensity profile to obtain the amount of the light that can be focused by the second lens onto a detector with an active area of a certain radius. To detect 100% of that light ($\varepsilon_{\text{size}}(r) = 1$) a detector with at least $r = 1.4$ mm is needed, while e.g. the RMD S0223 APD, which is currently foreseen as a broad band detector covering the wavelength range from 400 nm to 1100 nm has an active area of $2 \times 2 \text{ mm}^2$ and will therefore be able to detect about $\varepsilon_{\text{size}}(r \approx 1 \text{ mm}) \approx 95\%$ of the focused light when accurately aligned [Ham08].

6.2.1.2. Photon and signal rates

With $\varepsilon_{\text{comp}}$, ε_{sa} and $\varepsilon_{\text{optics}}$ the number of photons exiting the second lens can be calculated using equation (6.1), not accounting for ε_{det} . The lifetimes of several hyperfine states of special interest to the experiment listed in table 2.2 have been used to obtain the values listed in table 6.1. The count rates given in the table are based on simulation results taken from [Ham08] and have been adapted for changes in the trap design. The signal rates in the last column are obtained by also taking detection efficiencies ε_{det} for typical detector sizes and quantum efficiencies of the stated detector types into account.

Table 6.1.: Count rate estimates for some of the HFS transitions of interest originating from a kojac-simulation [Ham08] that have been adapted for changes in the trap design. The numbers are based on the assumption of 10^5 Ions in the trap and saturating laser bursts leading to $5 \cdot 10^4$ ions in the excited state. In column 3 detector efficiencies ε_{det} are not taken into account. The results in the last column are taking into account detection efficiencies and active areas of some suitable detector types.

isotope	wavelength	photon rate (kHz)	detector type	signal rate (kHz)
$^{209}\text{Bi}^{82+}$	244 nm	566 ± 180	CPM	60 ± 18
$^{207}\text{Pb}^{81+}$	1020 nm	7.0 ± 2.2	Si APD	1.3 ± 0.39
$^{209}\text{Bi}^{80+}$	1555 nm	4.4 ± 1.4	InGaAs APD NIR PMT	0.24 ± 0.07 0.44 ± 0.13

6.2.2. Magnetic field at the detector position

The experimental runs at the SpecTrap experiment will be conducted with B -fields ≥ 4 T. With the optical exits of the cryostat being at a radial distance of $r \approx 400$ mm from the trap center, the magnetic field of the superconducting magnet at this distance is still high enough to influence the detector performance. The magnetic field strength depending on the radial distance to the trap center has been simulated in [And12] and is expected to be about 30 G at the optical viewport exits as shown in figure 6.7. Since the space on the SpecTrap platform is limited and the light transport becomes more complicated with increasing distance to the light source, placing the detector at larger distances than roughly 1 m to the trap center should be avoided. Therefore, only detectors that can safely be operated at several Gauss are considered. This means that head-on type PMTs that suffer from efficiency losses of up to 50% when exposed to magnetic fluxes above 1 G [Ham07] either have to be shielded or should not be used.

6.2.3. Detector types for different wavelength regions

In this section the detector types chosen for the SpecTrap experiment will be introduced. To cover the whole wavelength region from about 240 nm up to 1600 nm several different detectors will be needed. One of the quantities of interest is the quantum efficiency (QE), which is the ratio of generated electron hole pairs to the number of incident photons. Since due to recombination not every primary electron hole pair will trigger a detector signal. Another value, the photo detection efficiency (PDE), is introduced that takes this effect into account. The PDE is given by the ratio of the background corrected detector signal rate to the number of photons incident on the detector. Thus, the PDE can at best be equal to the QE, but is in general smaller.

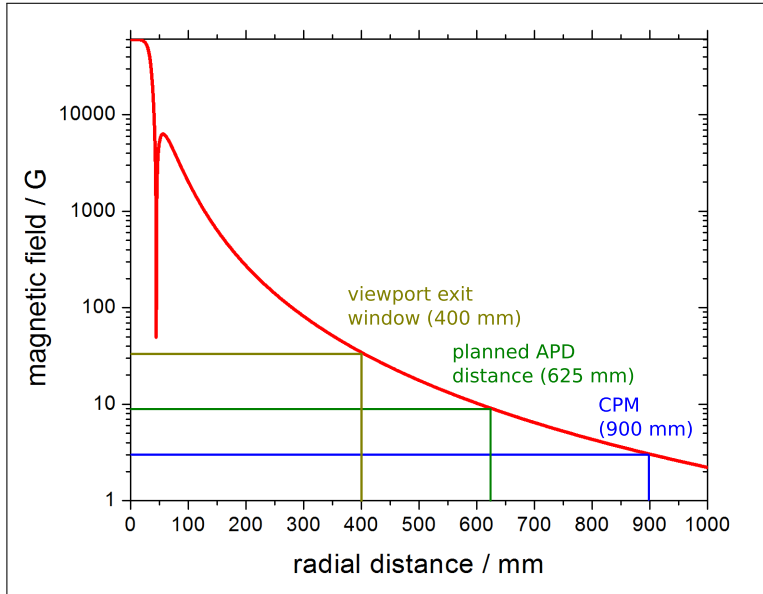


Figure 6.7.: Simulation of the magnetic field of the SpecTrap Helmholtz coils in the plane of the trap center, i.e. the plane of fluorescence detection. The field drop around $r = 40$ mm is inside the region of the coils themselves. The field strength at a radial distance of $r \approx 400$ mm, i.e. at the optical viewports, is about 30 G. The field strength at the radial distances of two of the detectors that are introduced in the next section is also highlighted. [And12]

6.2.3.1. 240 nm to 400 nm: CPM 1993 P Channel Photomultiplier

Channel Photomultipliers (CPMs) manufactured by PerkinElmer³ will be used to cover the ultraviolet part and wavelengths up to blue visible light. Compared to PMTs, these detectors have an extremely low dark current, leading to a very low dark count rate, and are less sensitive to magnetic fields [Perk3]. Tests have shown that the CPM signal rate exponentially drops in the presence of magnetic fields above 13 G [Ani10]. The devices are very compact with a length of about 90 mm and have, depending on the device type, active areas up to 21.5 mm. They can be obtained as bare CPM with an additional high voltage supply module of about the same size as the CPM itself, or assembled as CPM module, containing the CPM, the high voltage supply and a discriminator and are therefore suited for photon counting by providing logical signals. Both a bare C 1993 P CPM and the corresponding CPM module have been procured (see figure 6.8(a)).

The channel photomultiplier is in principle a channeltron type detector with a photocathode in front of the channel entrance, of which the primary electron is ejected. This electron is accelerated towards the channeltron's semiconductive channel surface by an electric potential applied between the cathode and the end of the channel, where multiple secondary electrons are emitted at each hit, leading to an avalanche effect with a gain exceeding 10^8 [Perk3].

The CPM module has been equipped with a mounting structure for attachment at the SpecTrap experiment at GSI, shown in figure 6.8(b) and (c). The CPM module is surrounded by a μ -metal shielding to reduce the effects of the magnetic field. A 500 mm long pipe connects the shielded housing with the exit window of the SpecTrap setup. A $f = 500$ mm lens is placed inside the aluminum piece connecting the pipe to the exit window, focusing the

³Excelitas, formerly PerkinElmer Optoelectronics, <http://www.excelitas.com>

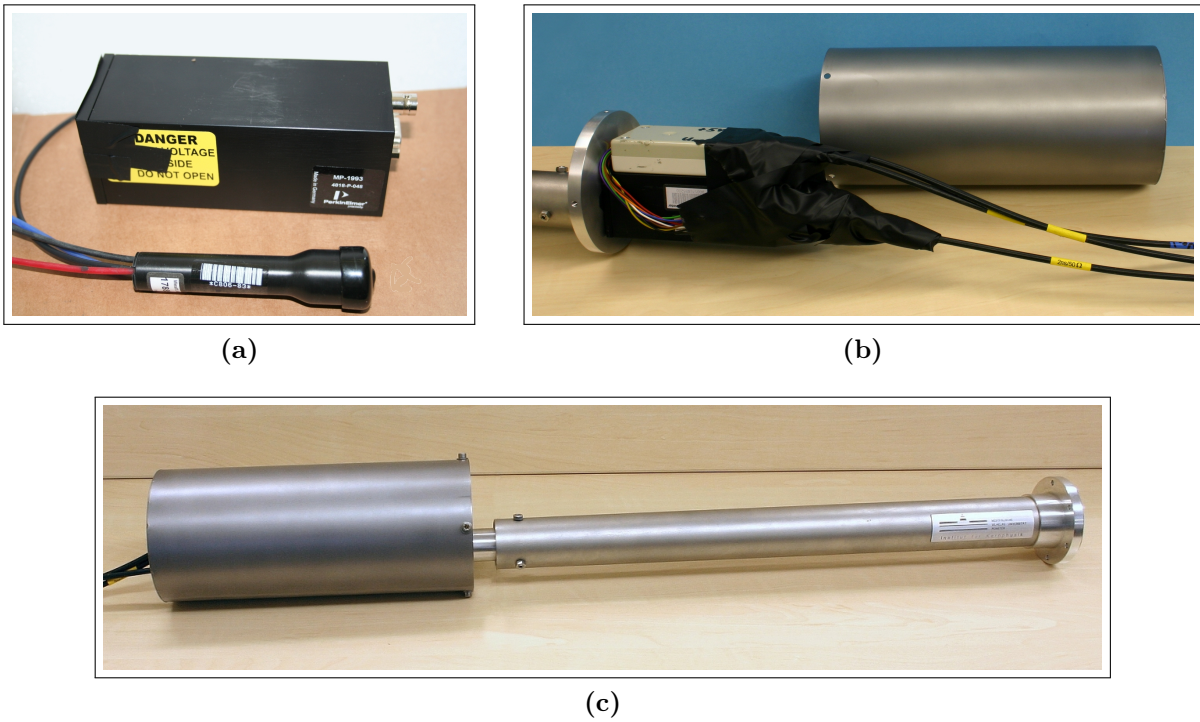


Figure 6.8.: (a) Top: A CPM module containing a CPM 1993 P channel photomultiplier and a HV supply, in use at the SpecTrap experiment. Bottom: A bare CPM 1993 P channel photomultiplier, used as reference detector at the detector test setup. (b) The CPM module attached to the mounting structure for the use at SpecTrap. (c) The complete mounting structure.

light from the viewport onto the CPM’s photocathode, which is located in about 900 mm distance to the trap center. The unshielded magnetic field at this distance is expected to be < 5 G.

This detector setup has already successfully been used at SpecTrap during the first commissioning measurements, where Mg^+ ions from a local ion source were stored inside the trap and excited by a tunable laser. The Mg^+ ions were produced in an ion source developed for pulsed extraction and transfer into SpecTrap and delivers up to 50 Mg^+ ions per shot. Up to 180 successively extracted ion bunches were stacked up inside the trap resulting in up to 2600 particles trapped over times up to 145 s, which were cooled down to about 0.1 K. The optimum loading parameters of the trap have been obtained by optimization of the fluorescence signal taken with the CPM module.

6.2.3.2. 400 nm to 1100 nm: Silicon (Si) APDs

Typically, in the optical regime, Photomultiplier Tubes (PMTs) are the most commonly used photon detectors capable of single-photon detection. They have, however, the disadvantage of being sensitive to magnetic fields and have, especially at long wavelengths, low quantum

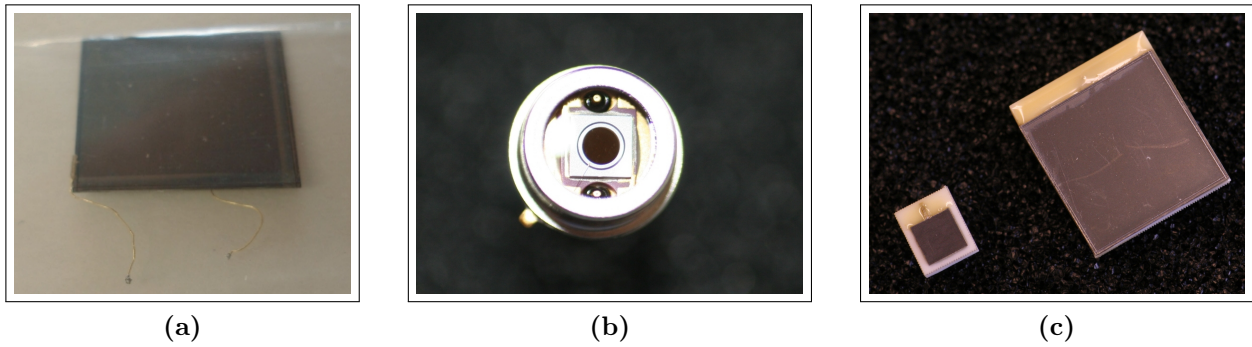


Figure 6.9.: Investigated silicon APD types: (a) RMD S1315 APD without aluminum oxide backing, (b) Hamamatsu S8664-20k APD in TO package, (c) RMD S0223 (left) and S0814 (right).

efficiencies compared to semiconductor detectors. Another detector type capable of covering the optical regime are silicon avalanche photodiodes (APDs). They are in general light sensitive from about 300 nm up to 1100 nm and feature high quantum efficiencies of about 75% in the peak region and still about 20% at 1064 nm [RMD03]. At room temperatures, APDs have been operated in high magnetic fields up to the Tesla region without an effect on the observed amplification [Mar00, Gen11]. As already stated, the magnetic field due to the superconducting magnet at the detector mounting position at SpecTrap is below 100 Gauss and therefore no negative effects on the APD performance are expected. With gains typically in the region of up to 10^3 [Ham04], normal silicon APDs are in general not suited for single-photon detection. To achieve operating conditions allowing for single-photon detection, the APDs have to be cryogenically cooled in order to achieve high gains in the vicinity of the breakdown voltage, which also lowers the APD's dark current [Jöh12]. In addition, extremely low noise preamplifier electronics are needed to amplify the small charge pulses of the APD induced by single-photon events.

Up to now, five different silicon APD types have been purchased, four of them have already been investigated (see figure 6.9):

- RMD S1315 (13 mm \times 13 mm active area)
- Hamamatsu S8664-20k (2 mm diameter)
- Hamamatsu S11518-30 (3 mm diameter)
- RMD S0223 (2 mm \times 2 mm active area)
- RMD S0812 (8 mm \times 8 mm active area, currently being investigated)

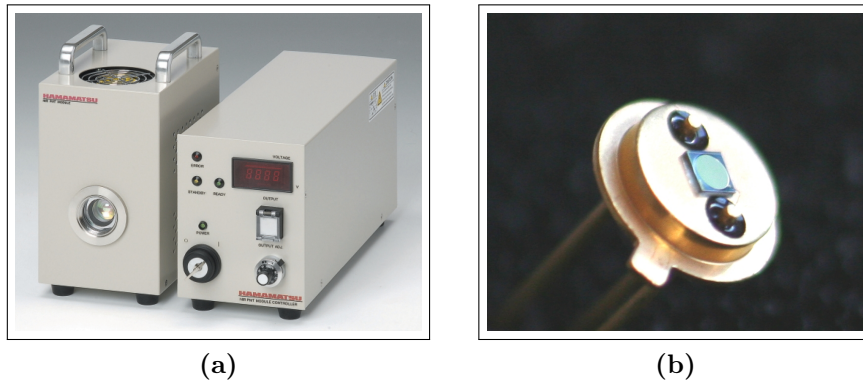


Figure 6.10.: (a) Hamamatsu NIR PMT module [Ham11], (b) Spectrolab InGaAs/InAlAs APD

6.2.3.3. 1100 nm to 1600 nm: Possible detectors

For this wavelength region so far two detector types are considered (shown in figure 6.10) and the investigation of both device types is ongoing:

- A Hamamatsu H10330-75 NIR-PMT module with an InGaAs/InP photocathode, that has a spectral response from about 950 nm up to 1700 nm. The PMT module at hand has been selected by Hamamatsu for a high a quantum efficiency of about 10% at the Bi^{80+} transition wavelength of about 1555 nm. This easy to handle detector system consists of two devices. Firstly, the PMT, which has an active area with a diameter of 1.6 mm, is contained in a thermally insulated sealed-off housing with an internal thermoelectric cooler and secondly, a controller that also provides the high voltage. The input window of the module uses a condenser lens to provide a virtually larger photosensitive area allowing easy optical coupling. Adapters for connection to an optical fiber or a monochromator are available [Ham11].
- Infrared sensitive InGaAs APDs that cover wavelengths up to 1650 nm have recently become available with active diameters of up to 1 mm. Two different types of such APDs are available for testing:
 1. Spectrolab InGaAs/InAlAs APDs (active area: $\varnothing = 1$ mm)
 2. Princeton Lightwave type PLA-208 InGaAs/InP APDs (active area: $\varnothing = 0.8$ mm)

These devices are sensitive up to about 1650 nm, with a quantum efficiency of 64% (Spectrolab) or 68% (Princeton Lightwave) at 1550 nm. Like the Hamamatsu APDs, they are delivered in TO package but without a glass window. The advantage of using another type of APD is that, besides the experience gathered during the characterization of several Si APDs, also the already existing APD detector setup built for the SpecTrap experiment, which will be described in chapter 9, can be re-used by simply

replacing the APD holding piece. However, first it needs to be proven that it is possible to achieve sufficiently large amplification for single-photon counting with these devices.

DETECTOR TEST SETUP

The test setup described in the first section of this chapter was built to investigate the possibilities for single-photon detection with APDs. For this purpose it is necessary to cool the APDs to cryogenic temperatures (in this case near liquid nitrogen temperature). The operation at low temperatures allows to set the bias voltage very close to the breakdown voltage of the APD and, therefore, reach high gain values. Secondly it also reduces electronic noise in the preamplifier used to read out the APD signals.

For the test measurements two simple single photon sources were set up, one based on a pulsed LED and another one based on a grating spectrograph with a light bulb as continuous light source. The second section of this chapter will deal in detail with the idea and the realization of these light sources.

7.1. The detector test setup

The detector test setup consists of a small vacuum chamber which includes a mounting structure for the detector and preamplifier and associated control and DAQ electronics. It provides, in principle, a controllable environment to test several types of detectors, as long as they can be mounted within the available space inside the vacuum chamber.

7.1.1. Vacuum chamber and detector mount

The test setup is used to cool the APDs and the first stage of the preamplifier down to near liquid nitrogen temperature in order to minimize the thermal noise of the APD and the preamplifier FET. It mainly consists of a small vacuum chamber, which provides vacuum conditions down to $3 \cdot 10^{-7}$ mbar, necessary to prevent condensation of gas molecules on the detector. With viewports and electrical feedthroughs using ceramic insulations being

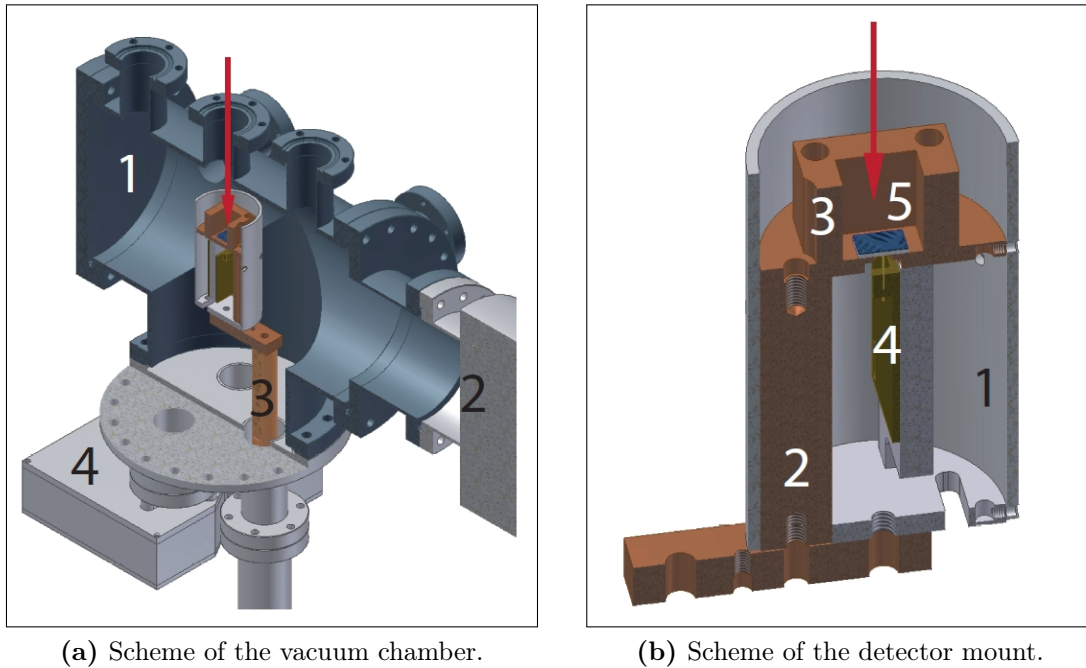
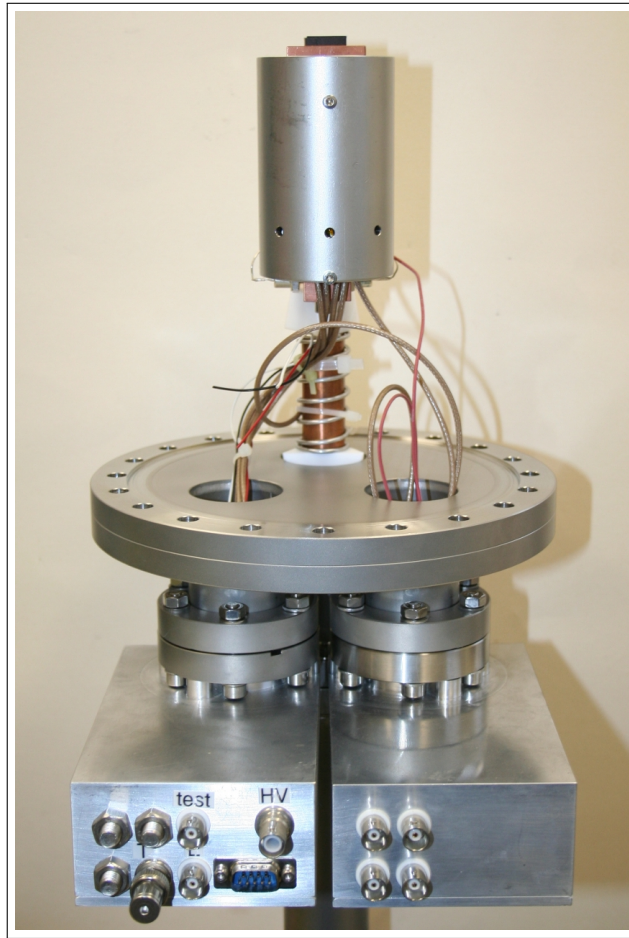


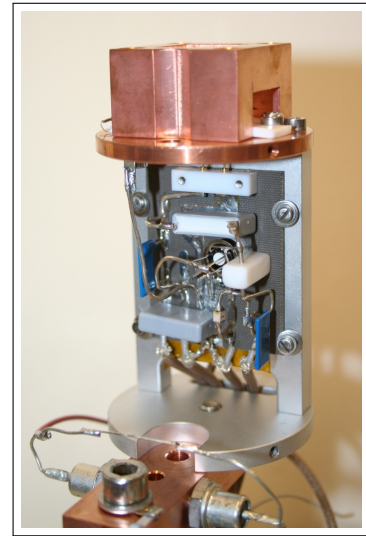
Figure 7.1.: (a) Vacuum setup: 1 - vacuum chamber, 2 - turbomolecular pump, 3 - cold finger, 4 - electronics housing, e.g. for preamp main stage. (b) Detector mount: 1 - electric shielding (stainless steel), 2 - intersection and heat conductor (copper), 3 - cold shield (copper), 4 - first preamplifier stage, 5 - APD. The red arrows indicate the direction of incident light.

thoroughly covered, the setup is light tight to allow for sensitive measurements with very low background.

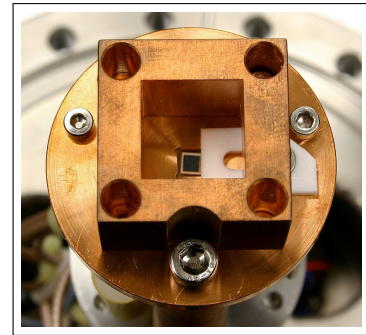
The vacuum chamber, schematically shown in figure 7.1, is equipped with a Leybold TW 300 turbomolecular pump and a Pfeiffer MVP 040-2 diaphragm pump. A Leybold IONIVAC ITR 90 pressure gauge is used to monitor the pressure. During measurements the vacuum gauge has to be switched off to avoid disturbance of the measurements by photons emitted from the gauge's filament. On the bottom of the chamber a CF 160 cluster flange is connected on which all electronic components are mounted (figure 7.1 (a) and figure 7.2 (a)). The APD and the first preamplifier stage are housed in a special structure surrounded by an electrical shielding, which is connected to a copper cold finger that is inserted into a liquid nitrogen dewar to cool the components (figure 7.1 (b) and figure 7.2 (b)). The connection between the cold finger and the detector mount is equipped with two Zener diodes which serve as heaters and can be used for temperature control during cooldown and can also be used to moderately bake out the system. For temperature readout PT 1000 sensors are located near the heaters and on the upper copper plate of the detector mount next to the APD. The cold finger itself, a 13 pin electrical feedthrough and a quad BNC feedthrough are each mounted on one of the CF 40 extensions. Outside the vacuum, two aluminum electronics cases are connected to the two feedthroughs, containing the main stage of the preamplifier and connections to



(a) Detector flange with detector mount.



(b) First preamp stage.



(c) Mounted S0223 APD.

Figure 7.2.: Photographs of the detector flange: (a) The complete detector flange with electronics housings and the detector mount, (b) detector mount with the first preamp stage without shielding and copper connection to the top plate, (c) mounted S0223 type APD with cold shield and teflon clamp.

the temperature sensors and heating diodes, respectively (see figure 7.2). On the top side of the chamber the CF 40 part opposite to the APD is sealed with a viewport, which can be equipped with either a LED with a small aperture or an optical fiber coupling the output of a grating spectrograph onto the detector.

The APD is installed on the top copper plate of the detector mount. A small teflon piece is used to press it onto this plate in order to improve the thermal connection and to fix the APD to suppress microphonic effects (see figure 7.2 (c)). An aluminum part serves as connection between the aluminum base plate of the detector mount and the top plate holding the detector. It also holds the first stage of the preamplifier, which in this way allows for the APD to be directly connected to the first stage. The electrical connection between the first preamp stage inside the vacuum and the main stage outside is done via a multi-pin electrical feedthrough with coaxial cables of about 25 cm to 30 cm length. The layout of the

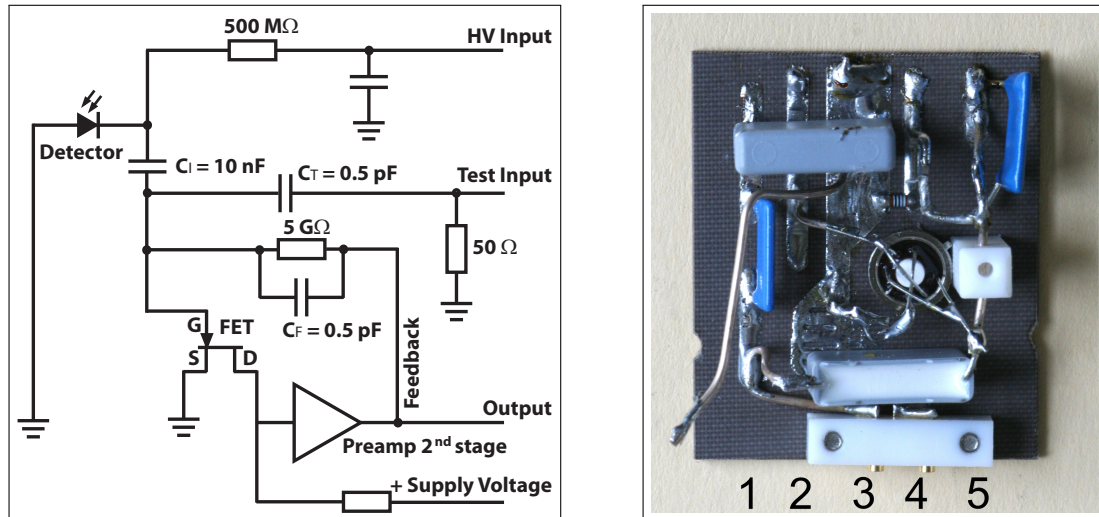


Figure 7.3.: Left: Scheme of the preamplifier. The single FET represents the parallel U430 JFET and the triangle is a symbol for the second stage of the preamplifier. Right: A photograph of the preamplifier's first stage. 1 – HV connection, 2 – FET drain (signal), 3 – ground, 4 – test pulse input, 5 – feedback line.

preamplifier will be discussed in section 7.1.2.

The setup can be operated at any temperature between -178°C , which is the lowest temperature reached during cooling with liquid nitrogen, and about $+100^{\circ}\text{C}$ with a precision of $\pm 0.5^{\circ}\text{C}$ using a LabVIEW based PID temperature control program. To avoid damage to the APD, the temperature control ensures a maximum temperature gradient of $2^{\circ}\text{C}/\text{min}$ at the detector while cooling down.

7.1.2. Low noise preamplifier

For detection of single-photons all noise sources have to be reduced as far as possible. One of these sources is the electronic noise of the preamplifier. In the early stages of the project several preamplifier types have been investigated [Ham08]. The commercially available Amptek CoolFET [Amp05] was ruled out, as well as two custom made solutions based on the A250 IC chip also used in the CoolFET, one with only the first preamp stage inside the vacuum, the other one with both the main and the first stage inside the vacuum. While problems with the CoolFET arose from the long cabling from the detector inside the vacuum to the preamp outside, the problems with the two custom solutions were due to the fragility of the A250 IC, of which several devices were destroyed. The circuitry of the low noise preamplifier board finally used is based on the layout developed for the Mainz Neutrino Mass Experiment [Wei90, Sch90]. It is a charge sensitive device, which is divided into two stages. The first amplification stage (see figure 7.3) consists mainly of two matched Vishay U430 n-channel JFET transistors assembled in a TO-48 package [Vis01] which are connec-

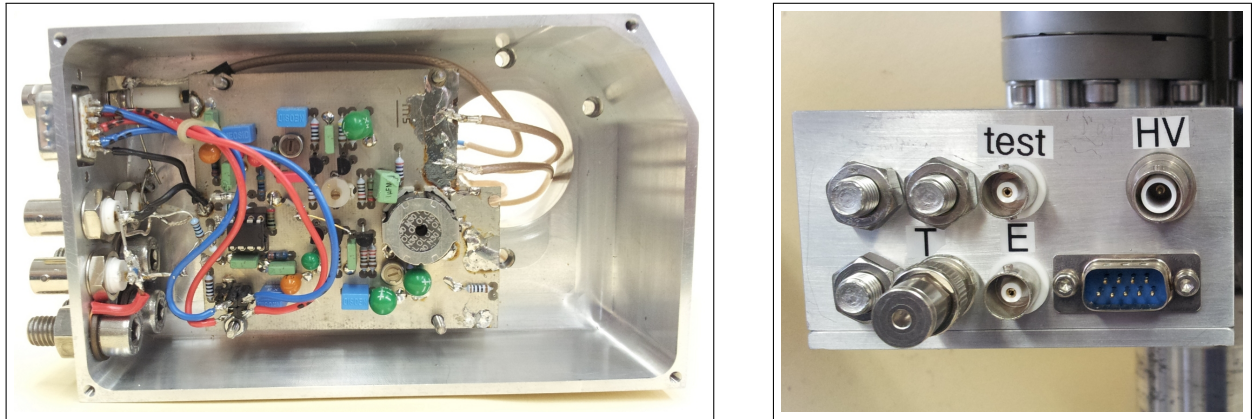


Figure 7.4.: Left: Aluminum casing with the main stage of the preamplifier. Right: The casing holding the main stage connected to a DN 40 CF flange with an electrical feedthrough. A D-Sub 9 connector is used to connect the main preamp stage to the standard supply voltages of ± 12 V and ± 24 V as provided by a NIM based spectroscopy amplifier. The High Voltage (HV) connector is directly connected to the HV line of the first stage as is the test input to the corresponding first stage connection. During all measurements, the energy (E) signal output was used. The timing (T) output is unused so far.

ted in parallel to reduce the noise. The second stage is mounted outside the vacuum in a special aluminum case directly connected to a CF 40 part with an electrical feedthrough (see figure 7.4). The connections on the casing of the preamp's main stage can also be seen in figure 7.4. The high voltage (HV) input is directly connected to the high voltage line of the first stage. The same holds for the test input, which is connected to the test input line of the first stage. A D-Sub 9 connector is used to connect the main preamp stage to the standard supply voltages of ± 12 V and ± 24 V as provided by a NIM based spectroscopy amplifier. During the measurements described in the next chapter, the energy output of the signal (E) was given preference to the timing output (T). The second stage is a discrete constructed fast amplifier with high transition steepness. An additional non-inverting output stage based on a Raytheon OP47 IC is used to ensure a certain loading capacity of the preamplifier output. A circuit digram of the complete preamplifier can be found in appendix B.1. During the tests of several APD types the noise behavior of the preamplifier was investigated thoroughly. A few essential solutions to preamplifier noise problems shall be evaluated here, all dealing with the alignment of the components and the quality of the soldering of the first preamp stage:

- To counter the effect of microphonic noise even on a very low level, it was found that the stiffness of the connections on the first preamp stage is essential. Hence, for all connections between components 1 mm silver strand was used as can be seen in figure 7.3.

- The optimized layout of the first stage's components can be seen on the right side of figure 7.3. Here the three crucial parts are the FET and the two capacitors of the test pulse input and the feedback line, respectively.
 - The FET itself is most vulnerable to microphonic effects and, therefore, has to be positioned and soldered very carefully. The best way to do that is to place the FET flat onto the circuit board directly over the hole later holding a small aluminum oxide plate. Now the connections of the FET have to be fixed in a way that the FET is already seated tight. To further stabilize the FET, when mounting the circuit board to the base plate, the small aluminum oxide plate, which is slightly thicker than the circuit board, is placed in the hole beneath the FET from the backside. Thus, after mounting, the plate presses the FET slightly upwards ensuring a good fixation and providing thermal coupling to the aluminum base plate, which is connected to the cold finger.
 - The capacitors of the test pulse input and the feedback line are also a potential source of noise. During the tests small 0.5 pF capacitors (SMD¹ variant with the dimensions $1.8 \times 1.1 \times 0.9 \text{ mm}^3$) were used, which were recently replaced with larger 0.5 pF or 1 pF capacitors, also SMD variants with the dimensions $3.1 \times 2.8 \times 2.1 \text{ mm}^3$, for easier handling. However, in all cases it turned out that the relative positioning and alignment of the capacitors has a relatively large influence on the preamp's noise behavior. Besides a stiff connection, the best noise levels are achieved when the planes of the capacitors are tilted by 90° relative to each other.

To quantify the noise contribution of the preamplifier, a Tektronix AFG 3102 function generator is used to generate an electronic test pulse which is connected to the preamp's test input. This pulse simulates a 100 keV signal that can also be used for calibration purposes. Since the mean energy for creating an electron-hole pair in Silicon is 3.76 eV at 77K [Ber68] the charge that has to be deposited on the capacitance C_T for a 100 keV signal (see figure 7.3) is given by

$$Q = \frac{1 \cdot 10^5 \text{ eV}}{3.76 \text{ eV}} \cdot e = 4.3 \cdot 10^{-15} \text{ C}, \quad (7.1)$$

where e is the elementary charge. Thus the amplitude of the pulse loading the capacitance $C_T = 0.5 \text{ pF}$ has to be

$$U = \frac{Q}{C_T} = \frac{4.3 \cdot 10^{-15} \text{ C}}{0.5 \cdot 10^{-12} \text{ F}} = 8.6 \text{ mV}. \quad (7.2)$$

¹surface-mounted device

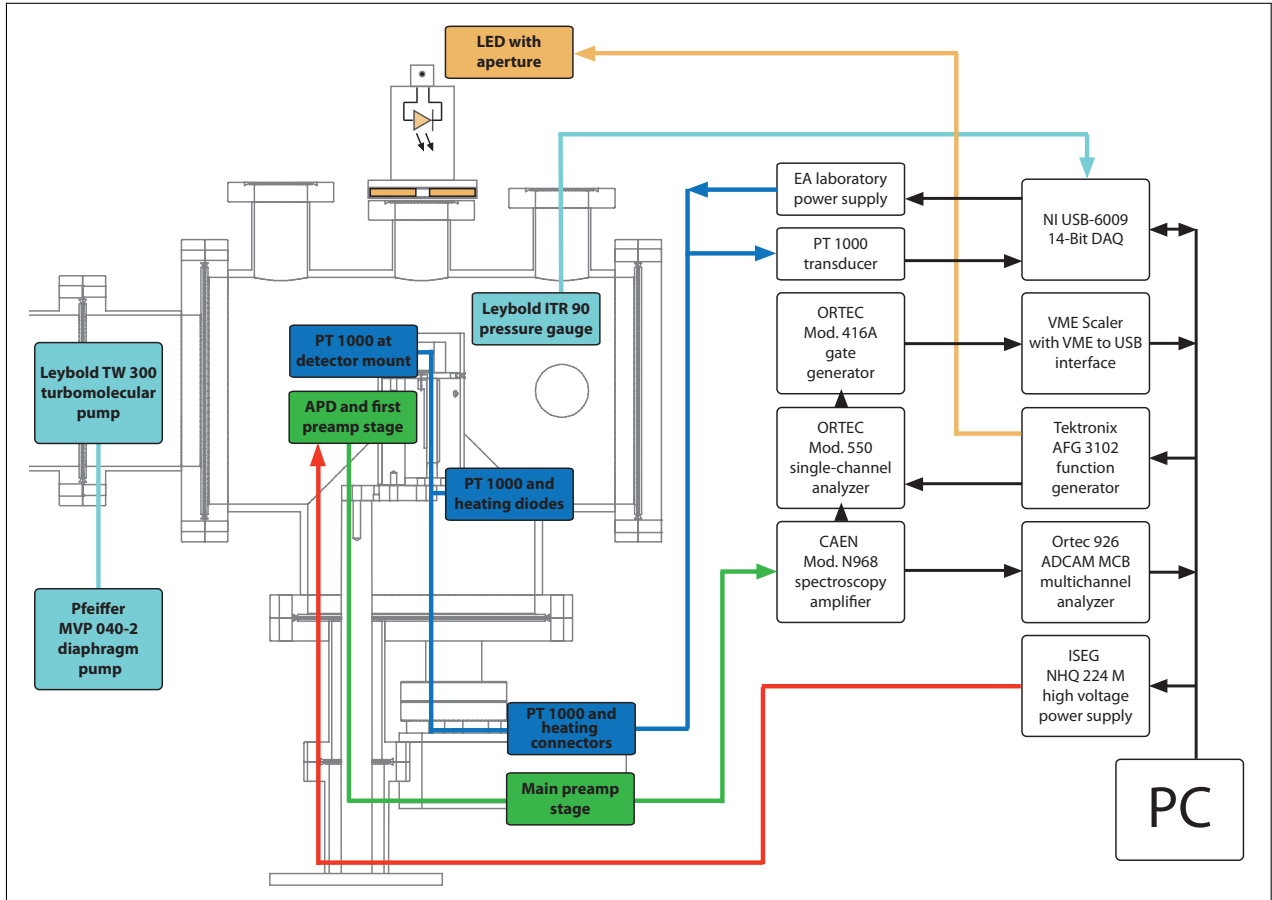


Figure 7.5.: Overview of the test setup control and data acquisition system. The DAQ devices utilized differ between different measurement types as described in sections 7.1.3.2 and 7.1.3.3. The directions of the arrows denote the in- or output function of the devices. The colors indicate the different parts of the system: yellow – photon sources, cyan – vacuum related devices, red – high voltage, blue – temperature control and green – signal processing.

In case of the use of 1 pF capacitors, the test pulse amplitude has to be reduced to 4.3 mV. The test pulse settings are shown in Tab. 7.1. The function generator is set to a pulse amplitude of 1 V and the signal is attenuated to 8.6 mV by two (20 ± 1) dB attenuators to allow a stable operation of the function generator. The rise time of this test pulse is 5 ns and the decay constant is 40 μ s. With this reference pulse the noise contribution of the preamplifier electronics without an attached detector has been determined to be $\sigma = 281$ eV, corresponding to 75 electrons [Jöh12].

7.1.3. Test setup control and DAQ

The front end electronics and data acquisition (DAQ) of the test setup depends on the needs of the respective measurement that should be performed. A schematic view of the devices used and their interconnections is shown in figure 7.5. Depending on the needs of the

Table 7.1.: Settings of the function generator for LED and Test pulses to determine gain and noise of the APD.

	Test pulse	LED pulse
rise time (ns)	5	5
decay const. (μ s)	40	40
frequency (kHz)	0.8	1.6
amplitude (V)	1	1.1 - 0.8

respective measurement, the detector setup is controlled and largely automatized through a LabVIEW based control software. The software was initially used only for temperature control, but was enhanced with several functions like bias voltage control, ADC readout, current and pressure readout.

For temperature readout, the resistivity of two PT 1000 sensors is converted into a voltage between 0 V and 5 V by a transducer² and this voltage is then read by a LabVIEW controlled NI USB-6009 14-Bit Multifunction DAQ. The heaters are also controlled by the USB-6009 module using an analog output to control a EA-PS 3016-10 B laboratory power supply, which provides the heating current. The output of the pressure gauge already meets the input range of the Ni USB-6009. The high voltage of the test setup is provided by a ISEG NHQ 224M high voltage power supply, connected to the control computer via RS 232. Other devices remotely controlled are an Ortec 926 ADCAM MCB multichannel analyzer (MCA), which is read out via a USB interface, as well as a SIS 3150 USB VME interface. Additionally, the Tektronix AFG 3102 function generator can also be controlled by LabVIEW via USB, which will later be used in several measurements.

In the following, the program written to control the main functions of the setup and to allow for basic ADC measurements will be explained in detail. Afterwards, the procedure to measure the APD gain will be described and the most general version of the program used to acquire signal and dark count rates providing a variety of measurement settings and allowing for automated runs of time-consuming measurements will be introduced.

7.1.3.1. The main control program

The functions of the main control program of the test setup can be accessed through the user interface shown in figure 7.6. These functions can be associated to the following tasks:

- **Log-file settings:** The log-file settings can be found at the upper left side of the interface. Depending on the preselected log entries (high voltage log can only be selected in case of enabled high voltage control), a file is automatically generated in a

²The circuit diagram of the transducer can be found in appendix B.2

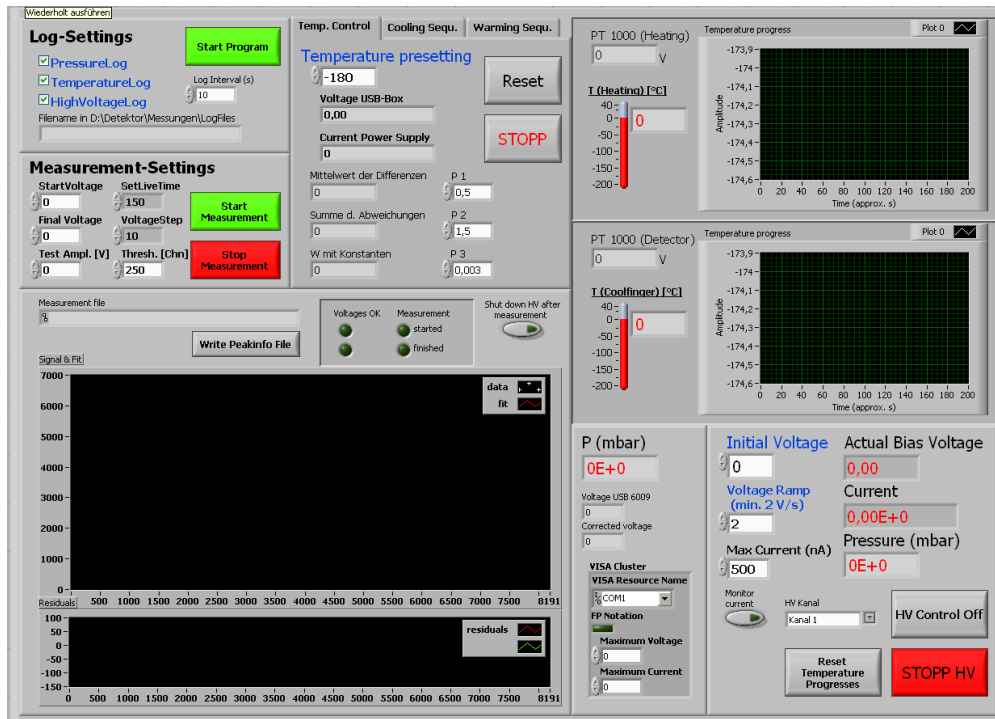


Figure 7.6.: Screenshot of the control program user interface.

sub-folder of the specified folder, with the name containing date and time of the initial entry. The log-file contains an additional entry with the period chosen in the “Log Interval” filed.

- **Temperature control:** The temperature control part of the interface consists of three tabs labeled “Temp. Control”, “Cooling Sequ.” and “Warming Sequ.”, all relying on a PID controller³ based algorithm.
 - The cooling sequence (“Cooling Sequ.”) tab can be used to cool down the setup in a controlled way. The minimum temperature, that should be reached can be defined in the “Final Temperature” field. To avoid damage to the APD, the cooling sequence ensures a maximum temperature gradient at the detector as preset in the “Max Δ T/min“ field while cooling down, which is by default set to 2°C/min. Below temperatures of -130°C the heating is completely switched off due to the very slow further change in temperature. When the final temperature is reached, the program switches to the temperature control tab and sets the cooling sequence final temperature as temperature to hold.
 - The warming sequence (“Warming Sequ.”) is essentially the counter part to the cooling sequence, ensuring a controlled warming, again with a preset temperature

³Proportional–integral–derivative controller

gradient, up to a defined temperature. As in the cooling sequence, the program switches to temperature control mode once the preset temperature is reached.

- The temperature control (“Temp. Control”) tab is used to keep the setup at a given temperature. This tab does not cool down or warm up the setup properly with a preselected temperature gradient and should therefore only be used after reaching the temperature to keep with either the cooling or the warming sequence.

The current temperature at the detector mount and at the heating installation along with the corresponding temperature history can be monitored in the displays and graphs at the upper right side of the interface.

- **High voltage control:** The high voltage control section is located at the lower left side of the interface. Once activated with the “HV Control” button (has to be done before the LabVIEW program is executed), the desired voltage can be set in the “Initial Voltage” field. The HV will be ramped with the speed set in the “Voltage Ramp” field. The displays on the very right show the current voltage and current values. If the “Monitor Current” button is enabled, the high voltage will be shut down with 10 V/s, if the current exceeds the preset “Max. Current” value. This feature has to be applied with caution, since the current rises when changing the preset voltage, which then may lead to an immediate shutdown. Initially, the subroutine was used to shut down the high voltage in case of a certain pressure increase, that may lead to discharges. Unfortunately, this feature can not be used during automated measurements as described in sections 7.1.3.2 and 7.1.3.3, since the filament of the pressure gauge induces background. The interface settings for the RS 232 communication with the HV module can be adjusted in the “VISA Cluster” panel.
- **Pressure monitoring:** In case the pressure gauge is turned on, the current pressure can be monitored in the “P (mbar)” display.
- **Amplitude spectra acquisition:** Since initially one of the main measurements used to characterize the APDs was the determination of the APDs’ gain and noise by taking amplitude spectra of the APD signal, the control program is equipped with the ability to automatically perform these measurements. Therefore, the program can be set to scan the bias voltage automatically from an initial “Start Voltage“ to a “Final Voltage” with a predefined “Voltage Step” width. The lifetime of the MCA data taking per voltage step can be preselected. The input labeled “Test Ampl.“ will be explained in section 7.1.3.2. A threshold channel can be selected, below which all entries will be ignored by the sub-program fitting the peaks of the spectrum. The subroutine makes use of the peak finding algorithm provided by an external software package called

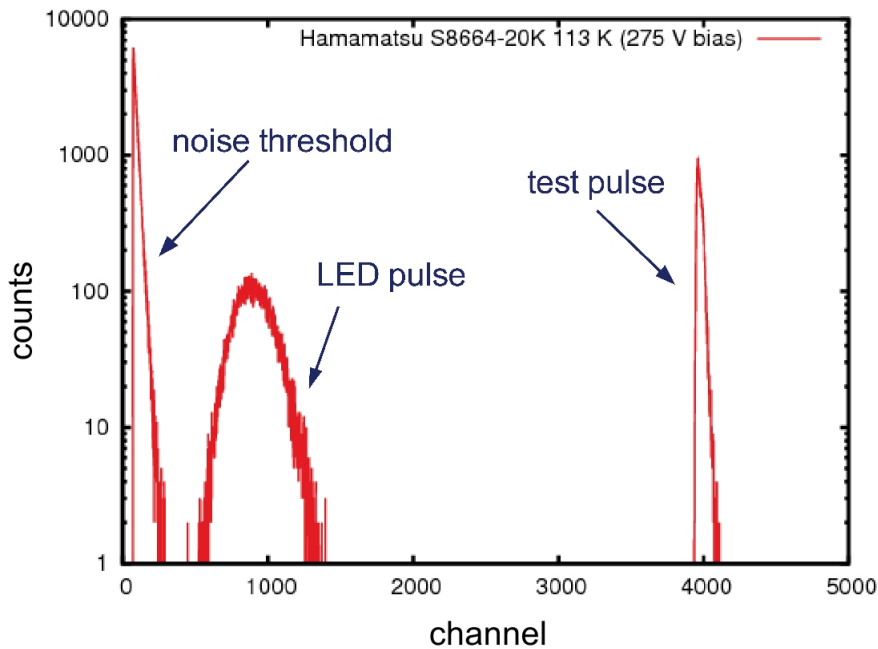


Figure 7.7.: Contributions to a typical gain measurement amplitude spectrum.

Fityk [Fit09]. The ADC spectrum, the fitted curves and the fit residuals are displayed in the lower left panels of the LabVIEW interface. The parameters of the fit function are written to a measurement file. The high voltage can automatically be shut down after the measurement cycle by enabling the corresponding switch. The four LED symbols represent the general status of the measurement.

7.1.3.2. Gain measurements

To determine the dependence of the gain of the detector on the detector bias voltage, detector signals were induced by light from a 628 nm LED pulsed with 1.6 kHz. The LED was later also used as single-photon source as described in section 7.2.2, but was first operated with a higher light yield. The settings of the voltage pulse driving the LED can be found in table 7.1 along with the settings of the test pulse applied to the test input of the preamplifier at the same time, to characterize the noise contribution of the preamplifier. The preamplifier signals were amplified and shaped by the CAEN N968 spectroscopy amplifier. The gain of the amplifier was set to 50 and the optimum shaping time for these measurements was determined to be $2 \mu\text{s}$. The amplified signals were recorded as amplitude spectra with the Ortec 926 ADCAM MCB multichannel analyzer (MCA) using the control program described in the previous section. To avoid pile up, the pile up rejection (PUR) input of the MCA was connected to the inhibit (inh) output of the CAEN amplifier. One of the resulting spectra is displayed in figure 7.7 and exhibits the following features:

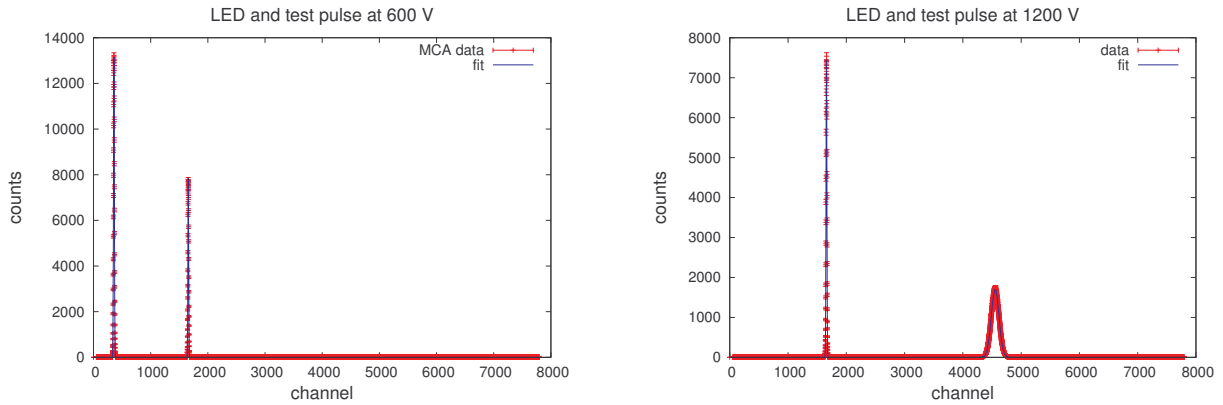


Figure 7.8.: Two amplitude spectra taken at 600 V (left) and 1200 V bias (right). It can be seen that the test pulse peak stays at the same position at around channel 1650 independent of the bias voltage, while the position of the LED pulse peak shifts to the right with increasing bias voltage. The peak also becomes smaller and broader due to the increasing fluctuations in the APD’s internal amplification process.

- Noise threshold: At the left hand side of the spectra an exponential decaying contribution can be seen, corresponding to the electronics noise of the system.
- LED signal peak: The peak of the APD signal induced by the LED is typically broader than the peak from the preamplifier test pulse, since besides the electronic noise it contains contributions of the photon statistics of the light pulse and the fluctuation of the APD’s internal multiplication process.
- Test pulse peak: As described in section 7.1.2, the test pulse simulates a signal with a certain energy, in this case $E = 100$ keV.

With the light yield kept constant, the signal amplitude of the detector increases with increasing gain, i.e. increasing bias voltage. Thus, the position of the peak associated with the LED signal in the amplitude spectrum shifts to the right (see figure 7.8). The relative gain at a certain bias voltage is then determined by the ratio of the signal amplitude at this voltage to the signal amplitude at a voltage, where it can be safely assumed, that no avalanche multiplication takes place. If the signal amplitude exceeds the dynamic range of the ADC, the light yield of the test pulse is lowered by reducing the test pulse amplitude. An additional spectrum at the same bias voltage is taken with the reduced test pulse amplitude and the ratio of the test pulse peak positions is added as correction factor to the following gains. The setting of the test pulse amplitude can be logged in the main program’s logfiles using the "Test Ampl." field in the program’s interface. For the measurements presented in the following, a bias voltage of 10 V has been chosen as reference point. As, at low voltages, there will also be recombination effects this method can not be used to determine absolute

gains. For the latter, the precise voltage, at which the effects of recombination and the onset of amplification of the APD cancel each other, has to be known. This point will be subject of further investigation.

7.1.3.3. Signal and dark count rate measurements

Besides measuring the relative gain by taking amplitude spectra, the other basic measurement that has been performed, were scaler based rate measurements of the dark count rate and the count rate with activated single-photon source. These measurements were performed with different threshold settings of a leading edge discriminator, at different bias voltages and with different settings of the single-photon source.

For this purpose, the main amplifier signals were discriminated by an ORTEC Mod. 550 single channel analyzer (SCA). The threshold of the SCA was externally set by the Tektronix AFG 3102 function generator by applying a DC voltage to the external threshold input of the SCA. To avoid double counts from over/undershoots of the main amplifier signal, the logic signals of the discriminator were elongated by an ORTEC Mod. 416A gate generator. These signals were then counted by a VME based SIS 3803 16 channel scaler board and read out by a LabVIEW program via the SIS 3150 USB VME interface.

To suppress count rate bursts during short time periods that can be caused by external disturbances, an adapted measurement cycle for these types of measurement was implemented in the corresponding programs. The dark count rate, as well as the signal rate were read out periodically (typically every second). This way count rate bursts, exceeding the average value of all other count rates by more than an order of magnitude, could be sorted out. The count rates obtained by the program were then written to a spreadsheet file for further analysis. The user interface of one of the programs written for this measurements can be seen in figure 7.9. Several other versions of the program exist but differ only in minor details due to adjustments for slightly different measurement cycles. The functions of the program utilizing the pulsed LED as light source are explained in the following:

- **Global Settings:** This section is used to select the input devices and the output file. The "VISA resource name" field is used to chose the connection to the Tektronix AFG 3102 function generator to control the SCA threshold. The fields with gray background (except the "value" display) show the status of the SIS 3150 USB to VME interface.
- **High Voltage Control:** The functions of the high voltage control are the same as explained for the control program in section 7.1.3.
- **Measurement Settings:** Most of the controls are self-explanatory. The number of

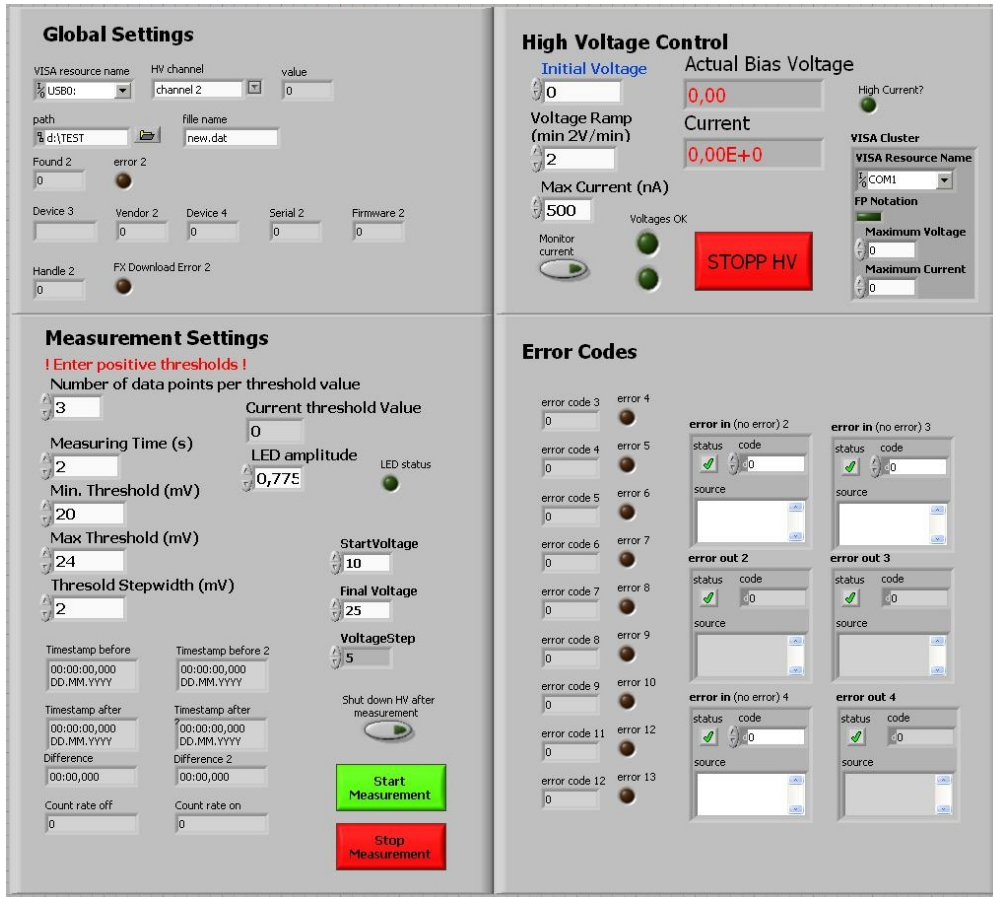


Figure 7.9.: User interface of one of the programs written to subsequently measure dark count rates and count rates with light source with different bias voltage, SCA threshold and light source settings.

data points for the dark count rate measurement and the count rate with external light source can be set, each with a duration as selected in the "Measuring Time" field. The dark count measurements are executed subsequently before enabling the light source, which is either supplied via the AFG 3102 in case of the LED light source or an additional EA laboratory power supply, switching the light bulb of the grating spectrograph, that will both be introduced later. This measurement will be repeated for each of the preselected SCA threshold settings, for each preselected bias voltage and, in this case, for each LED pulse amplitude predefined in the program code.

- **Error Codes:** Displays errors that may occur due to connection problems between the program and either the AFG 3102 or the SIS 3150. In case of an error the program has to be restarted.

7.2. Single-photon sources

In this section the basic concept of the single photon sources later used to determine the photo detection efficiency of the APDs will be explained. Afterwards, the two realizations of this concept, a pulsed LED with an aperture and a light bulb with an attached grating spectrograph, will be described. Measurements with a reference detector with known single-photon counting capability and quantum efficiency are used to characterize the single-photon sources.

7.2.1. Single-Photons from a pulsed low level light source

In order to determine the single-photon detection capability and the corresponding detection efficiency of a photon detector, the ratio of the number of photons emitted by a single-photon source and the number of photons detected with that detector has to be determined. However, this requires knowledge of the emission characteristics of the single-photon source. For other applications like in the field of quantum information sophisticated single photon sources based on e.g. parametric down conversion [Pit02, Pit05] or quantum dots [Bec02, Ben05] are investigated and used.

Compared to these approaches, this section deals with a relative simple realization of a single-photon source, which will be used in the next chapter to determine the photo detection efficiency of RMD S0223 type APDs. The idea is based on the emission characteristics of LEDs operated with low supply voltages and of thermal light sources. The number of photons emitted into a small solid angle, e.g the solid angle of the detector under investigation, is Poissonian distributed:

$$P_{\mu}(n) = \frac{\mu^n}{n!} e^{-\mu}. \quad (7.3)$$

If the expectation value μ of the Poissonian distribution is chosen suitably, the possibility of two photons emitted into this solid angle simultaneously becomes negligible. E.g. for $\mu = 0.1$ the possibility that no photon is emitted into the detector's solid angle is $P(0) = 0.905$. The possibility for one photon hitting the detector is $P(1) = 0.090$ and for two photons $P(2) = 0.005$.

The detection rate of a detector exposed to such a light source can be described by

$$\dot{N} = \dot{N}_P + \dot{D}, \quad (7.4)$$

where \dot{N} is the total count rate, \dot{N}_P the count rate due to the light source and \dot{D} the dark

count rate. \dot{N}_P is given by

$$\dot{N}_P = r \cdot \sum_{n=1}^{\infty} [\varepsilon_n \cdot P_{\mu}(n)], \quad (7.5)$$

where r is the rate of light source pulses and $P_{\mu}(n)$ the probability to emit n photons into the solid angle of the detector. ε_n is the probability for n photons, simultaneously hitting the device, to be detected. To calculate ε_n we have to consider how many photoelectrons are produced by the incident photons, and what the chances are for these photoelectrons to contribute to a measurable signal. The number of photoelectrons k produced by n incident photons follows a binomial distribution $f(k; n, QE)$ that depends on the quantum efficiency (QE) of the detector. If the efficiency for detection of a signal produced by k photoelectrons is labeled by $\varepsilon_{e,k}$, one obtains for ε_n :

$$\varepsilon_n = \sum_{k=1}^n \varepsilon_{e,k} \cdot f(k; n, QE). \quad (7.6)$$

The probability $\varepsilon_{e,k}$ to actually detect a certain number of photoelectrons produced in the detector depends on the collection efficiency and the amplification of the device. In photomultiplier kind of devices ε is called photo electron collection efficiency. To calibrate the single-photon source, a reference detector (Det_{Ref}) with the same solid angle coverage as the detector to be later exposed to the source is needed, that can detect single-photons with a known QE. For this purpose a PerkinElmer channel photomultiplier (CPM 1993 P [Perk3]) was used. The collection efficiency for photoelectrons produced from the cathode is for this detector >95% [Jes08]. It is therefore assumed that each event, where at least one photoelectron is produced, is detected, $\varepsilon_{e,k}(\text{Det}_{\text{Ref}}) \approx 1$. The probability that no photoelectron is produced from n photons is given by

$$f(0; n, QE) = (1 - QE)^n \quad (7.7)$$

Therefore the probability that at least one photoelectron is produced and subsequently detected is in this case given by

$$\varepsilon_n(\text{Det}_{\text{Ref}}) \approx 1 - (1 - QE)^n \quad (7.8)$$

and thus

$$\dot{N}_P(\text{Det}_{\text{Ref}}) \approx r \cdot \sum_{n=1}^{\infty} [(1 - (1 - QE)^n) \cdot P_{\mu}(n)]. \quad (7.9)$$

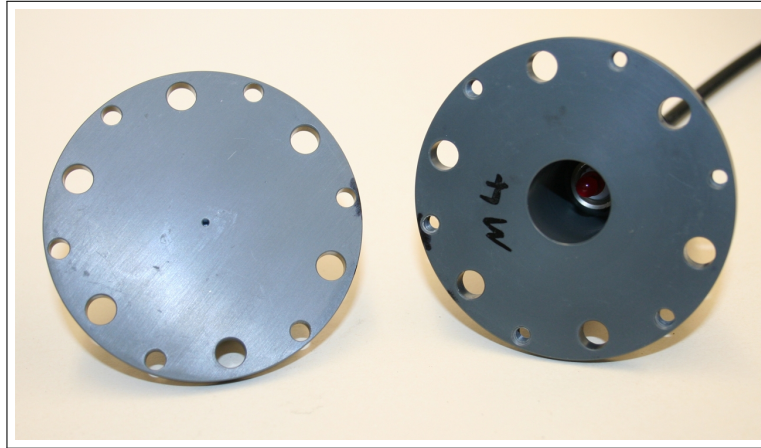


Figure 7.10.: The LED used as single-photon source with mounting structure and aperture.

$\dot{N}_P(\text{Det}_{\text{Ref}})$ is therefore determined by the expectation value μ , the QE of the detector and the rate r of the pulse driving the light source. On the other hand, if the rate $\dot{N}_P(\text{Det}_{\text{Ref}})$ is measured at a given rate r and with the known QE, μ can be determined. By attenuating the light source (e.g. by lowering the supply voltage of the LED) the expectation value μ can be reduced so far that emission of mainly single-photons into the detector's solid angle can be achieved. This will be demonstrated in the next section at the example of a pulsed LED, which was used as single-photon source to determine the photodetection efficiency of the RMD S0223 type APDs.

7.2.2. A pulsed 628 nm LED with aperture

To determine the photo detection efficiency of the APDs at a single optical wavelength, a single-photon light source has been realized using a red LED (628 nm) that is operated by applying short (40 ns) pulses with an amplitude of 850 mV and a pulse rate of $r = 100$ kHz (see table 7.2)[Jöh12]. To calibrate this single-photon sources as described in the previous section, a channel photomultiplier (CPM) manufactured by PerkinElmer [Perk1] was used. These devices have a high amplification of the order $1 \cdot 10^7$ that makes them ideal for photon

Table 7.2.: Settings of the function generator to generate LED pulses that result in mainly single-photon events incident on the APD.

Single-Photon pulse settings	
rise time (ns)	5
fall time (ns)	5
width (ns)	40
frequency (kHz)	100
amplitude (mV)	840 - 950

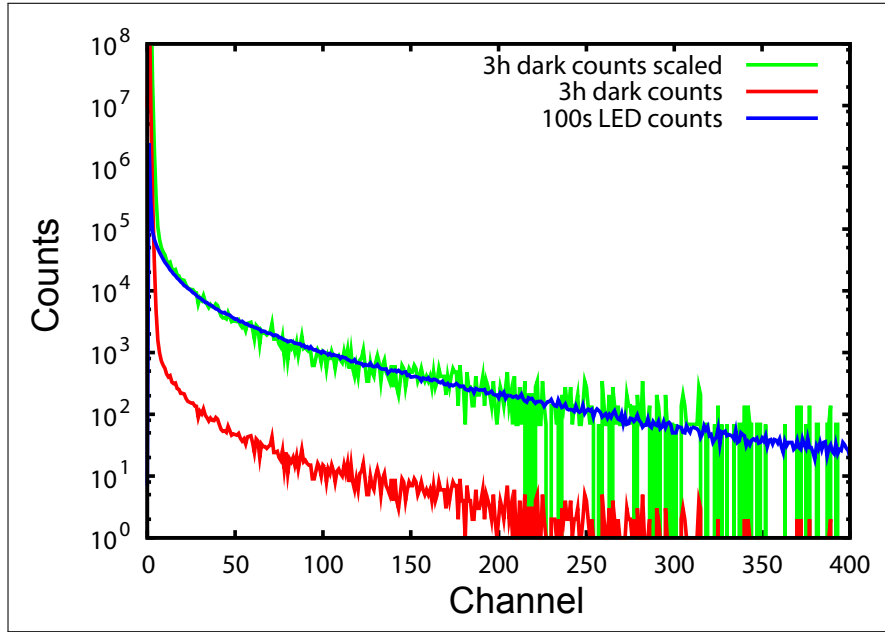


Figure 7.11.: APD spectra taken with and without illumination by single-photons generated with the pulsed LED. The amplitude distribution of the scaled dark count spectrum matches the shape of the single-photon events. [Jöh12]

counting. They feature a collection efficiency larger than 95% [Jes08] and, therefore, the approximation $\varepsilon_{e,k}(\text{CPM}) \approx 1$, used in equation 7.7, is still valid to a sufficient degree. The active area of the CPM has, for this measurement, been limited using an aperture such that the same solid angle coverage as with the APDs is obtained. With these settings we measure a signal rate of the $\dot{N}_P(\text{CPM}) = 50$. With a quantum efficiency of $(3.0 \pm 0.5)\%$ of the CPM at 628 nm, this result corresponds to $\mu = 0.017$, with $P(0) = 0.983$ and $P(1) = 0.016$. This means that every 63rd pulse of the LED emits a single-photon into the solid angle of the detector, while the probability of two or more photons to hit the detector is with $P(2) = 1.37 \cdot 10^{-4}$ negligible.

An additional method to prove that the light source emits single-photons is to compare an APD amplitude spectrum taken without LED light to a spectrum with illumination over a longer measurement time. Without illumination, electron hole pairs are generated in the APD by thermal excitation of electrons into the conduction band. These thermally generated electrons cannot be distinguished from electron hole pairs generated via the photo effect. A dark count spectrum should, therefore, after a certain time have the same amplitude distribution as a spectrum of the single-photon source. This is demonstrated in Fig. 7.11, that shows a comparison between a single-photon spectrum and a scaled version of the dark count distribution obtained in a 3 h measurement. The amplitude distribution of single-photon signals at 1480 V bias is extracted by subtracting a dark count spectrum taken with

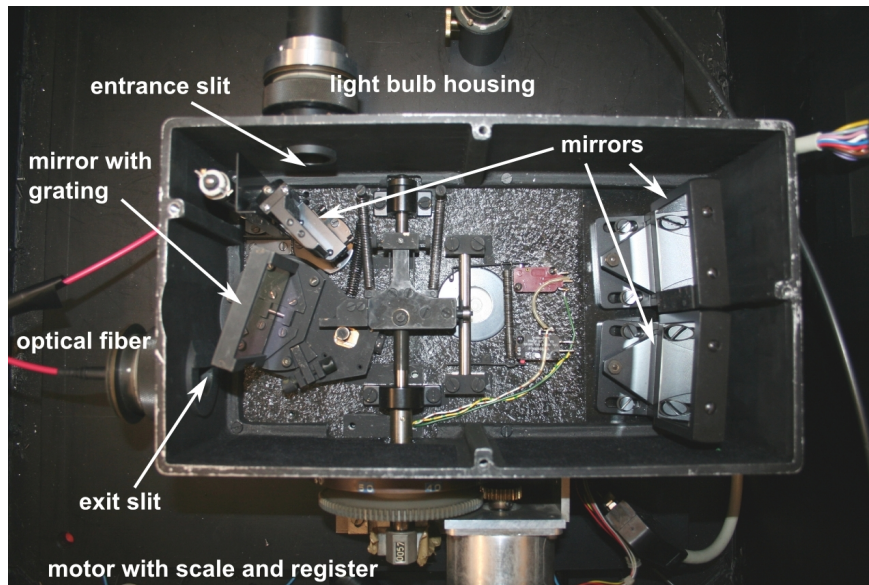


Figure 7.12.: Picture of the grating spectrograph with its housing opened inside a light tight blackened metal box.

the same measurement lifetime.

7.2.3. A grating spectrograph with light bulb

The considerations made in section 7.2.1 still hold when going from a pulsed light source to a continuous source (light bulb) as long as the count rate at the detector stays the same. This has been used to set up a second single-photon source using a grating spectrograph in combination with a tungsten light bulb [Jos10]. The grating spectrograph is used to select a certain wavelength from the continuous spectrum and to determine the photodetection efficiency as a function of the wavelength, in the case of the RMD S0223 type APDs especially at 1020 nm. The 2 Watts light bulb emits in first approximation a black body spectrum, which has its emittance maximum in the infrared regime. The spectrograph uses concave mirrors to collimate the incident light on a mirror with a diffraction grating and to focus the diffraction maximum to the exit slit. The grating spectrograph shown in figure 7.12 is equipped with a step motor to rotate the grating, while a scale with register attached to the motor can be used to determine the current wavelength, after the spectrograph has been calibrated. The calibration was performed using a mercury vapor lamp [Kus11]. The motor can be controlled by a LabVIEW program. The spectrograph casing itself is placed inside a light tight metal box. The exit of the spectrograph is equipped with an optical fiber (Thorlabs multi-mode fiber BFL37-800), that is used to guide the light to the detector inside the test setup's vacuum chamber. To avoid disturbance by ambient light, the fiber is coated with a black hose and aluminum foil.

The light intensity at the exit of the grating spectrograph has been measured using a calibrated *Thorlabs FDS 100-CAL* photodiode [Kus11]. The light from the spectrograph was subsequently attenuated by optical slits in the setup. Knowing the relative light intensities at different wavelengths, the light source can be calibrated for single-photon emission in the near infrared by determining the single-photon rate in the optical regime. The settings in the optical regime are again checked with the CPM 1993 P channel photomultiplier. The additional uncertainty in the incident photon rates resulting from this procedure is estimated to be on the 10% level.

RMD S0223 AVALANCHE PHOTO DIODES AS SINGLE-PHOTON DETECTORS

The following chapter is divided into three sections. The first section provides a short introduction on avalanche photo diodes. The second section will give an overview about the general characterization of the RMD S0223 APDs regarding dark current, gain and noise behavior. The third section will introduce the measurements performed to determine the photodetection efficiency of the APDs and the corresponding estimation on the time required to detect a signal above background at the SpecTrap experiment based on the photon rate estimations presented in section 6.2.1. The results of this chapter are published in [Jöh12].

8.1. Avalanche photo diodes

Avalanche photo diodes (APDs) are high-speed, high sensitivity photodiodes. Compared to PIN photodiodes, APDs are able to measure lower light levels due to their internal gain mechanism, achieved by applying a reverse voltage [Ham04]. The resulting strong electric field then leads to an avalanche multiplication of primary generated charge carriers. They are used in a broad range of applications, e.g. optical communications and are often used to replace PMTs in their classical fields, e.g. as scintillation light detectors. They are available in different layouts depending on the active area and the wavelength to be detected.

In contrast to standard PIN photo diodes the layer structure of APDs typically differs slightly. The PN^+ junction is on the P doped side followed by an intrinsic layer I (see figure 8.1). The N^+ denotes heavy doping of the N-doped layer. The APD finishes with a P^+ layer next to the intrinsic one. The reverse voltage is applied between the P^+ and the N^+ layer. The schematic electrical field behavior is also shown in figure 8.1. An incident photon should

interact within the intrinsic layer, which is significantly wider than the other layers, and create an electron-hole (e^- -h) pair. The charges are drifted towards the N^+ region (e^-) and the P^+ region (h), respectively. With the electric field within the intrinsic layer not being large enough to induce secondary charge creation, the charge carriers reach a certain drift velocity. When the electrons enter the PN^+ region, the electric field strength drastically rises and the electrons are now accelerated above the electron-hole creation threshold, inducing an avalanche multiplication of the initial e^- [Ren02]. The multiplication or gain M should be high enough to create a sufficient large charge pulse that can be further amplified and detected by the following preamplifier electronics. This is of special relevance for the detection of low light levels or even photon counting, where the number of initial charge carriers is very low.

The avalanche process induces the so called afterpulsing effect also known from PMTs. In PMTs this effect is caused by ionized residual gas atoms being accelerated towards the photo cathode and thus creating additional free primary electrons to be multiplied [Leo87]. In APDs, however, the cause is somewhat different. Here the main reason for afterpulsing are electrons that are captured within metastable states in the semiconductor (especially at impurities) and will eventually be released by thermal excitation after a certain time. The release time depends on the properties of the states and on the device temperature. While at higher temperatures the probability of the trapped electrons to be released within the APD's dead time, at low temperatures the release will most likely occur after the dead time, triggering an additional avalanche that is still correlated with the initial photon event [Dra00]. If the expected photon rate to be detected is low enough, the counting of afterpulses can be inhibited by blocking the acquisition of new pulses for a certain time interval.

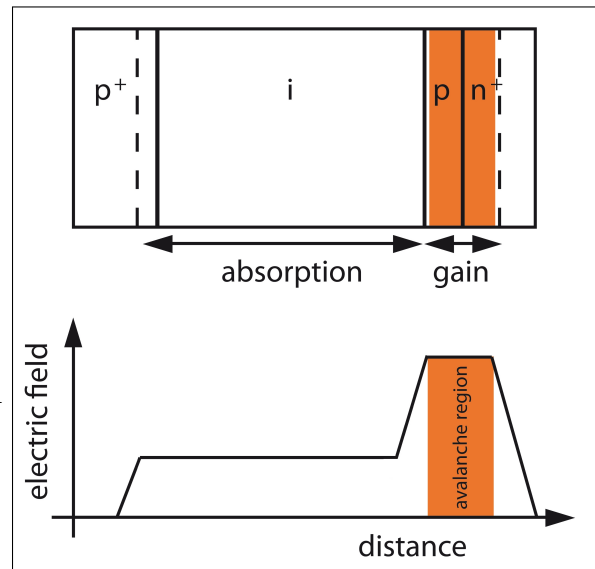


Figure 8.1.: Schematic cross section and electric field of an APD. Depending on the APD type, the light enters the device either at the P^+ or the N^+ side.

8.1.1. Dark counts and experimental measuring time

In typical applications of APDs the light intensity causing the APD signals is the quantity of interest. Therefore, much effort has been put in the theoretical description of the dark

current, induced among others by the avalanche multiplication process, disturbing the light induced APD signal [McI66, Hak90, Perk4]. In this case, however, the APDs are used to detect single-photons. The question is, if a signal caused by an electron avalanche can be discriminated from the noise of the amplification electronics. The precise height of this signal is in this case of no interest. Henceforth, not the dark current but the dark count rate is the central value to take into account in background discussion.

In the end, the aim is to detect low rates of single photons at the SpecTrap experiment to determine various fine and hyperfine transitions with as little measurement time as possible. Therefore, the impact of the dark count rate D and the signal rate S on the measuring time has to be considered. In order to distinguish a signal from the background within a time t with a certain significance $n\sigma$ the number of detected photons $\dot{N}_P \cdot t$ must be at least

$$\dot{N}_P \cdot t = S \cdot t \cdot \varepsilon = n \cdot \sqrt{(D + S \cdot \varepsilon) \cdot t} \approx n \cdot \sqrt{D \cdot t} \quad \text{for } D \gg S \cdot \varepsilon, \quad (8.1)$$

where N_P is again the count rate due to the light source, S is the rate of photons incident on the detector, t the measuring time, ε the detection efficiency of the detector and D the dark count rate. This leads to a measuring time t of at least

$$t = \frac{n^2}{\varepsilon^2} \cdot \frac{(D + S \cdot \varepsilon)}{S^2} = \frac{n^2 \cdot (D + S_{net})}{S_{net}^2} \quad (8.2)$$

with $S_{net} = S \cdot \varepsilon$. The measuring time is thus proportional to the ratio of the dark count rate and the background corrected signal rate S_{net} squared. In other words, to minimize the measuring time its inverse has to be maximized:

$$\frac{1}{t} \propto \frac{S_{net}^2}{(D + S_{net})} \quad (8.3)$$

8.1.2. Linear and Geiger mode operation

APDs are typically operated in either the linear or the Geiger mode (Gm). When operated in linear mode, the APD is biased below the breakdown voltage and the response of the APD is proportional to the incident light intensity. The gain of the APDs rises with the applied bias voltage.

In contrast to the linear operation mode, in Geiger mode the APD is biased slightly above breakdown voltage. The very high electrical field at this bias leads to a self-sustaining avalanche triggered by a single primary charge carrier. This process can be quenched passively or with an active quenching circuit. Passive quenching is done by a resistor placed in series with the APD. The current drawn by the APD causes a voltage drop across the resistor and

the APD bias drops below the breakdown voltage, thus eliminating the avalanche process. The bias voltage then slowly recovers and the detector is ready to be ignited again. In the case of active quenching an external circuit lowers the bias voltage after ignition of an avalanche in the diode. The circuitry then waits for a defined hold-off time before the bias voltage is raised again to its operational level, which also helps to minimize the effects of afterpulsing. With this method, effective gains of 10^5 to 10^6 can be achieved.

Typical applications of GmAPDs are telecommunications, where they are used as connection between optical fibers and standard electronics. However, APDs suitable for Geiger mode operation are in general not designed to detect low photon rates, due to their high dark count rates. Also the active areas of these types of APDs are very small, since due to the high dark count generation, devices larger than 1 mm diameter can not be operated at room temperature [Bri04]. To counter the drawback of the small size for different applications, multi-pixel Geiger mode APDs have been developed, comprised of an array of small Geiger mode pixels. They are used e.g. in medical imaging, high energy physics and astrophysical applications [Bri07].

Besides their small active diameters (of typically < 0.1 mm, e.g. [MPD13]), GmAPDs made from silicon tend to have lower QEs than APDs especially at long wavelengths and are therefore not suited for efficient application at SpecTrap.

In the following it will be shown, that under suitable conditions detection of low rates of single-photons is possible with large area APDs operated in linear mode.

8.2. Basic APD characterization

The first steps in characterizing these devices have been measurements of basic properties of the APDs, i.e. dark current and gain behavior. In addition with the determination of the signal to noise ratio a suitable set of settings was obtained, referred from here as the operation point.

During these investigations several of the APD types listed in section 6.2.3.2 were already ruled out due to their insufficient performance. The S1315 APDs provided by GSI were bare silicon devices without backing, making them very fragile and hard to handle. Besides this, the overall noise performance was not acceptable and the dark current behavior was erratic and unreproducible. This may have been caused by damage due to high voltage discharges in earlier measurements with the diodes, that had already been in use at GSI. Therefore, the Hamamatsu S8664-20k APD was tested, featuring a robust TO package casing. This type was much easier to handle, but features a low QE in the infrared region. The Hamamatsu S11518-30 type APDs are suitable for long wavelengths, were operated at high gains (≈ 4500) and were also able to detect single photons, but since the gain and the signal to noise ratio

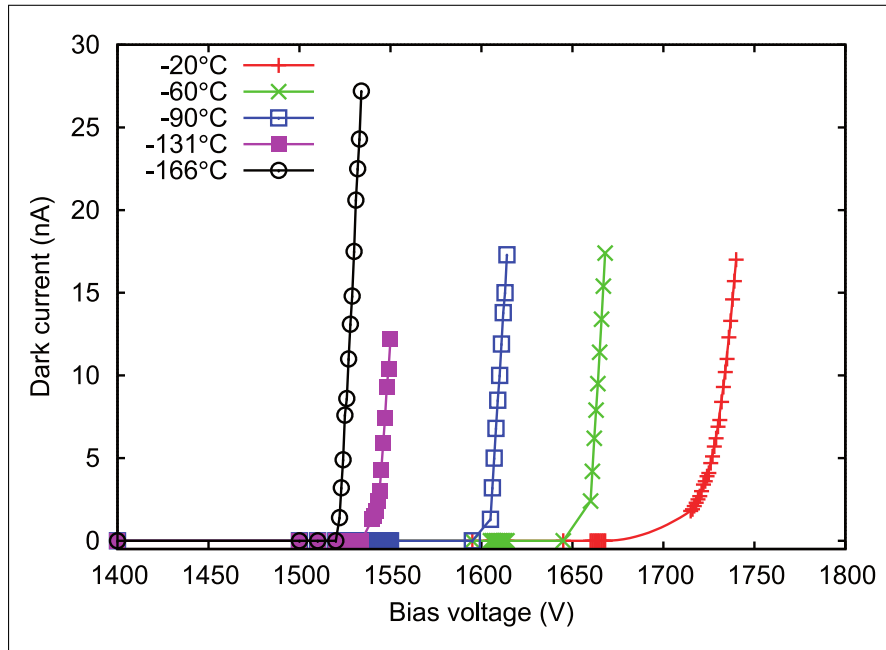


Figure 8.2.: Typical dark current behavior of a S0223 APD at different temperatures. The breakdown voltage decreases with temperature by about 1.4 V/°C [Jöh12].

(SNR) of the RMD APDs described below turned out to be significantly better, it was decided to focus on the latter [Kus11].

In the following the characterization of the RMD S0223 APD will be described in detail. This APD has an active diameter of $2 \times 2 \text{ mm}^2$ and features high quantum efficiencies of 75% between 830 nm and 905 nm and 20% at 1064 nm [RMD03]. As will be shown in the following sections, this APD can be stably operated in single-photon mode and is therefore the baseline for detection of fluorescence photons at SpecTrap up to 1100 nm.

8.2.1. Dark current

The first measurement to perform on an APD is the determination of the dark current behavior and the breakdown voltage. This was done at different temperatures between room temperature and -176°C . The dark current as well as the breakdown voltage rapidly drops with temperature (Figure 8.2.). The dark current was measured with the current meter embedded in the ISEG NHQ224 high voltage supply, which provides a resolution of 100 pA. It is obvious that with decreasing temperature the breakdown voltage of the APD also decreases. At the same time, the slope of the dark current becomes much steeper when approaching the breakdown voltage. When cooling the APD to low temperatures, this behavior allows to operate the diode very close to the breakdown voltage and thus high gain factors are achieved.

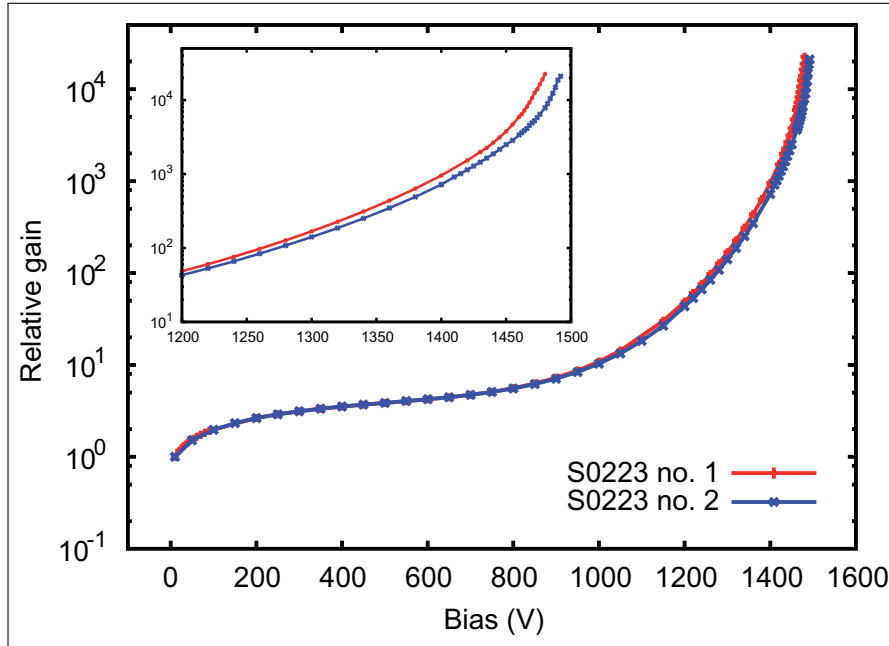


Figure 8.3.: Relative gain of two different S0223 type APDs.

8.2.2. Relative gain

For the APD gain measurements, signals are induced by shining light from a pulsed LED onto the diode as described in section 7.1.3.2. In the electronics setup used for this measurement the preamplifier signals are then further amplified and shaped by a CAEN Mod. N968 spectroscopy amplifier. The optimum shaping time was determined to be $2 \mu\text{s}$. The amplified signals are finally recorded using an ORTEC 926-M32-USB multichannel analyzer. The gain of the APDs was determined as a function of the applied bias voltage. The gain is given by the ratio of the position of the APD signal peak induced by an LED light pulse at different bias voltages relative to the position at 10 V bias. If, at higher gains, the signal amplitude starts to exceed the dynamic range of the ADC, the amplitude of the pulse driving the LED is lowered. The ratio between LED pulse positions in the spectra at two different amplitudes but equal bias voltage is used as correction factor in the calculation of the gain. Figure 8.3 shows the results of the gain measurement for two different S0223 type APDs, with the low noise setup and cryogenic cooling to about -176°C . Relative gains of $M \geq 2 \cdot 10^4$ were observed.

8.2.3. Determination of the APD's operation bias

The bias voltage used to operate the APDs in the following measurements was determined by the following considerations:

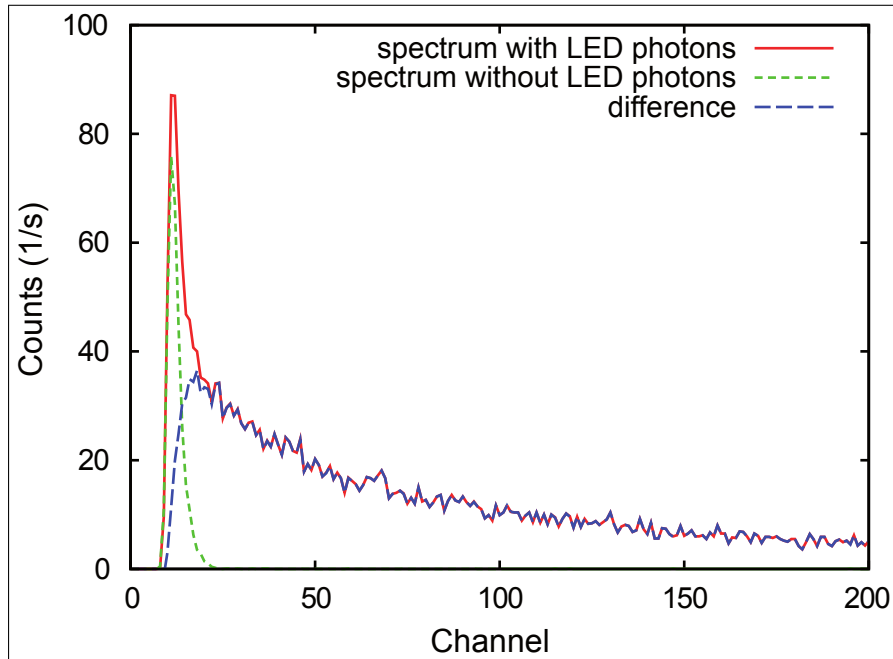


Figure 8.4.: Amplitude spectrum at 1480 V bias with and without single-photon source together with the difference spectrum showing only photon events. [Jöh12]

- The operation bias should not be chosen too close to breakdown since the breakthrough voltage depends on the APD temperature and small temperature drifts should not be able to shift the operation bias beyond this voltage.
- On the other hand the operation bias should be close to the breakthrough voltage in order to be able to use high gain values for the single-photon measurements.

It was found that a bias voltage of 1480 V at -176°C is a reasonable compromise between these two conflicting requirements, with a distance of about 10 V to the breakthrough voltage. With this setting still a high relative gain of $M \approx 2.2 \cdot 10^4$ can be achieved. During the measurements presented in the following this choice has allowed for stable operation of the setup for several weeks.

The value of the breakdown voltage varies between different APDs of the same type by some 10 V. At room temperature values between 1840 V and 1870 V are stated in the datasheet of the procured APDs. The breakdown voltage decreases with temperature by about $1.4 \text{ V}/^{\circ}\text{C}$ (see figure 8.2).

8.3. Determination of single-photon detection efficiency

Up to now only the general characteristics of the RMD S0223 APD were investigated. For the low expected fluorescence photon rates of some of the transitions of interest the detectors

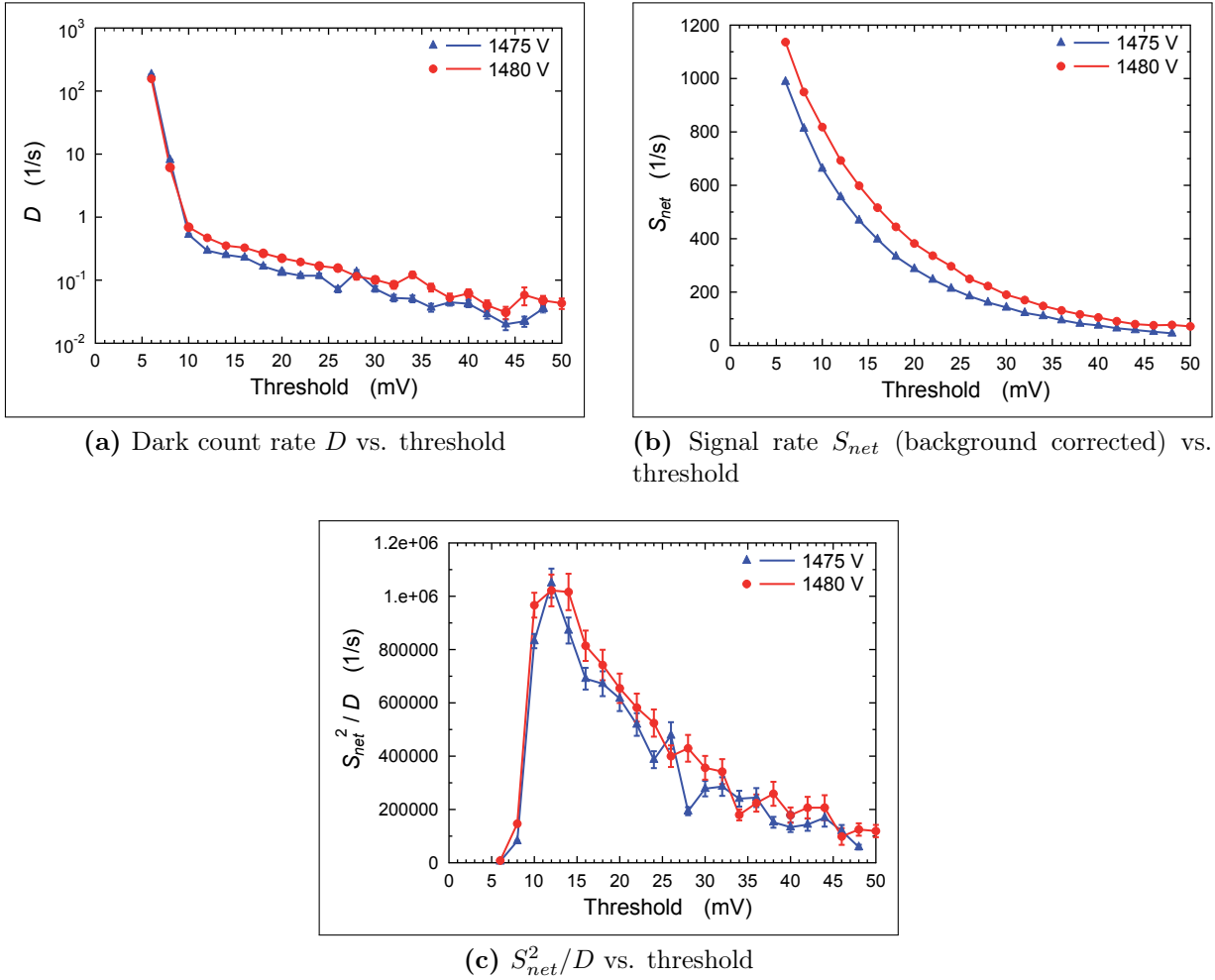


Figure 8.5.: Comparison of the obtained rates vs. threshold for two different bias voltages: a) Dark count rate D , b) Signal rate S_{net} (background corrected), c) S_{net}^2/D [Jöh12].

to be used have to be capable of detecting single-photons, which has to be proven.

8.3.1. Single-photon detection efficiency at 628 nm

A low intensity LED can be used as single-photon source as shown in the previous chapter. In the following the photo detection efficiency of the APDs will be discussed. From the measurements with the channel photomultiplier, described in section 7.2.2, the rate of photons incident on the APD at different LED pulse amplitudes can be extracted. To determine the APD count rates at a given signal amplitude, the main amplifier signals were discriminated using an ORTEC Mod. 550 single-channel analyzer. The output of the discriminator was connected to an ORTEC Mod. 416A gate generator, that was used to elongate the logic signals to avoid double counts from over/undershoots of the main amplifier signal or from afterpulses in the APD. These signals were then counted by a SIS 3803 scaler module.

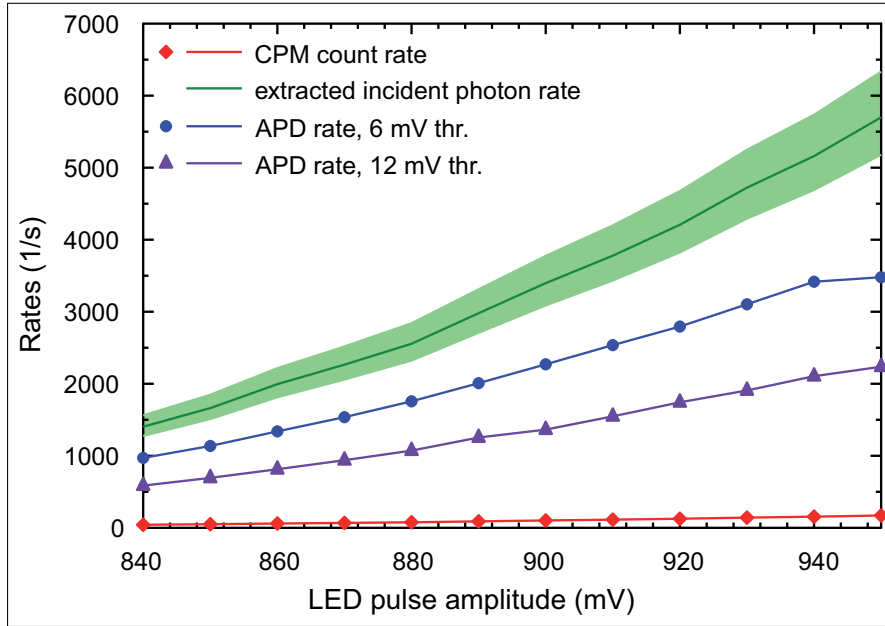


Figure 8.6.: The CPM count rates for different LED pulse amplitudes are shown in red. With a CPM QE of $(3 \pm 0.3)\%$ the number of incident photons is represented by the green band. Comparing the blue and purple datapoints representing the background corrected APD count rates at 6 mV and 12 mV discriminator threshold, respectively, with the incident band, the APD’s photo detection efficiency can be determined. The statistical error bars of the count rates are of the same size as the data points [Jöh12].

The count rates with and without LED light were taken for discriminator threshold settings from 6 mV to 50 mV with the measurement program described in section 7.1.3.3. When lowering the threshold, the background rate as well as the signal rate increases. In case the photon signal can be cleanly separated from the background, the LED signal rate should remain constant when further decreasing the discriminator threshold and only the background rate should rise. In the present case, where the signal peak is not clearly separated from the background (see figures 8.4 and 7.11), the preferred discriminator threshold setting cannot be determined easily. Since the amount of single-photon signals lost due to threshold settings should be as little as possible, the threshold has to be set to a value where the LED signal rate is highest for a reasonable dark count rate. As stated in section 8.1.1, the measuring time can be minimized by maximizing $\frac{S_{net}^2}{D}$, which is determined by the dark count rate (figure 8.5(a)) and the background corrected single-photon rate (figure 8.5(b)). Figure 8.5(c) shows $\frac{S_{net}^2}{D}$ as a function of the applied discriminator threshold for the investigated RMD S0223 APD operated at 1475 V and 1480 V, respectively. To achieve the maximum photo detection efficiency the detector should therefore be operated at the minimum threshold of 6 mV, where the dark count rate is still at an acceptable value of $\approx 230 \text{ s}^{-1}$. On the other hand, to minimize the measurement time required for signal detection at the SpecTrap setup a threshold of 12 mV should be used with these APDs and under the described operating

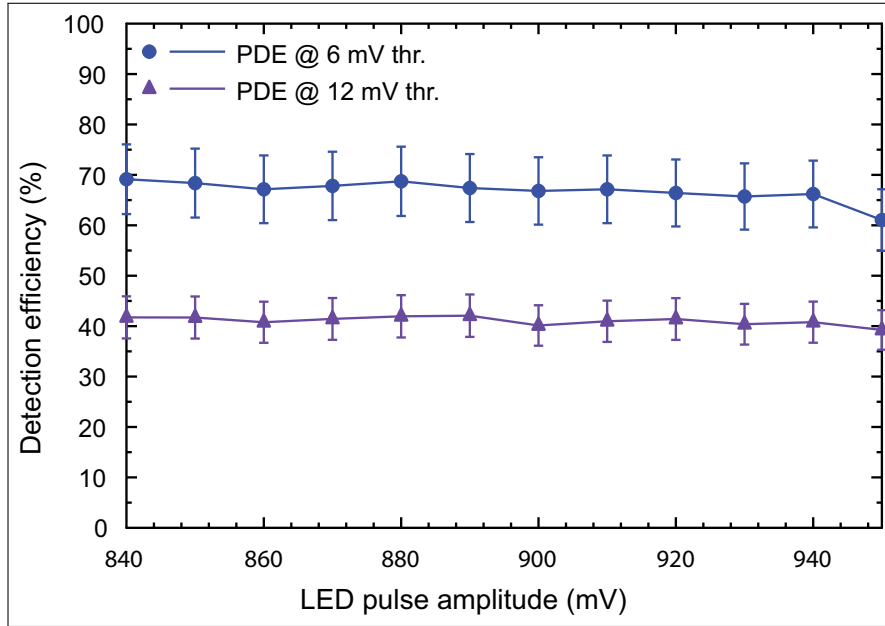


Figure 8.7.: Photo detection efficiencies for different LED pulse amplitudes derived from the count rate data shown in figure 8.6. The APD has an average photo detection efficiency of $(67 \pm 7)\%$ in the case of 6 mV threshold and $(41 \pm 4)\%$ in the case of 12 mV threshold [Jöh12].

conditions, since the optimum depends quadratically on the expected signal rate. For each threshold value the photo detection efficiency of the APD can be calculated by dividing the incident photon rate measured with the reference CPM during the single photon source characterization by the background and deadtime corrected signal rate of the APD. The results obtained from these measurements are shown in Fig. 8.6, for threshold values of 6 mV and 12 mV and for different LED pulse amplitudes ranging from 840 mV to 950 mV. The diamond shaped markers represent the measured count rates of the CPM. Assuming the mentioned QE of $(3.0 \pm 0.3)\%$ for the CPM, the photon rate incident onto the active area of the APD has been determined and is shown as the green band.

Comparing the count rates of the APD at these two thresholds (6 mV: blue circles, 12 mV: purple triangles) with the incident photon rates, a value of the photo detection efficiency can be extracted for each LED amplitude, which are shown in figure 8.7. The average of these values gives a photo detection efficiency of $(67 \pm 7)\%$ for 6 mV threshold which fits well with the QE of 68% at 628 nm interpolated from the datasheet of the S0223 APDs [RMD03]. At 12 mV threshold the photo detection efficiency drops to $(41 \pm 4)\%$.

8.3.2. Single-photon detection efficiency at 1020 nm

Since the APDs will be used for fluorescence light detection up to about 1100 nm, verification of single-photon counting also in this wavelength region is necessary. In order to do this

without access to a calibrated single-photon source an auxiliary solution was developed to at least coarsely prove the near infrared single-photon sensitivity. Therefore, the grating spectrograph with a light bulb is used as single-photon source as described in section 7.2.3.

Table 8.1.: Results of the photo detection efficiency (PDE) determination for different wavelength with the grating spectrograph. The corresponding dark count rates are also shown.

Wavelength (nm)	6 mV threshold		12 mV threshold	
	APD PDE ε (%)	Average APD dark rate (1/s)	APD PDE ε (%)	Average APD dark rate (1/s)
560	61 ± 12	≈ 230	37 ± 7	≈ 0.7
628	74 ± 15		45 ± 9	
1020	13 ± 3		8 ± 2	

The APD count rates with and without illumination by the light bulb were taken at 560 nm, 628 nm and 1020 nm. The photo detection efficiency at 628 nm can be determined directly by using the previously calculated photon rate incident on the CPM. The incident photon rates at 560 nm and 1020 nm are calculated using the intensity ratios known from the measurement with the calibrated photodiode (see section 7.2.3).

The results regarding the photo detection efficiency and the dark count rate of the S0223 APD at 560 nm, 628 nm and 1020 nm are shown in table 8.1 for the two threshold settings also used in the previous section. The values of the photo detection efficiency at 628 nm agree well with the values obtained in the measurements with the LED as single-photon source. The photo detection efficiency of $(13 \pm 3)\%$ measured for 1020 nm at 6 mV threshold is lower than the QE of 20% stated in the APD datasheet.

Especially when operating at low thresholds, drifts in the dark count rates are observed that are caused by fluctuations of the experimental parameters. During performance tests and especially during the measurement runs at the SpecTrap experiment these drifts have to be controlled by repeatedly measuring the dark count rates in between normal operation. Average values of the dark count rate at 6 mV and 12 mV threshold are given in table 8.1.

8.3.3. Detection time at SpecTrap

Now, the measuring time per laser wavelength step needed to detect a signal of the transition of e.g. hydrogen-like lead at the SpecTrap experiment can be estimated. At the optimal threshold setting of 12 mV, as shown in figure 8.5, the dark count rate is negligible compared to the dominating background from laser stray light of the excitation laser in the SpecTrap setup. Therefore, the previous dark count rate D has to be transformed to

$$D \rightarrow D \cdot \varepsilon \cdot \xi, \quad (8.4)$$

where ξ is the fraction of the light yield at the optical exits of the SpecTrap setup that can be focused on a detector of a certain diameter. Equation 8.2 can then be rewritten to

$$t = \frac{n^2}{\varepsilon^2} \cdot \frac{\varepsilon \cdot (D + S) \cdot \xi}{S^2 \cdot \xi^2} = \frac{n^2 \cdot (D + S)}{\varepsilon \cdot S^2 \cdot \xi}. \quad (8.5)$$

In this case, with a $2 \times 2 \text{ mm}^2$ size APD, $\xi = 95\%$ [Ham08]. The laser stray light background is estimated from a test measurement with Mg^+ ions to be of the order $D = 1.3 \cdot 10^4 \text{ s}^{-1}$. Taking the expected fluorescence photon rate $S = 7000 \text{ s}^{-1}$ for the $^{207}\text{Pb}^{81+}$ hyperfine transition as listed in table 6.1, a photodetection efficiency $\varepsilon = 8\%$ (see table 8.1) and a desired significance of $n = 3$ into account, equation 8.5 gives a minimum measuring time $t \geq 48 \text{ ms}$ per laser wavelength.

AN APD DETECTOR SETUP FOR SPECTRAP

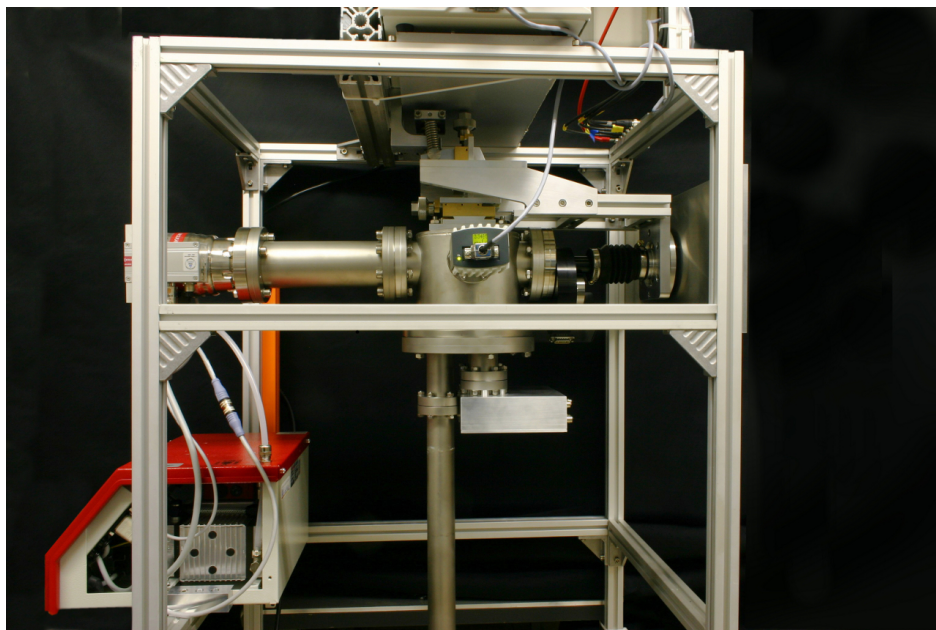


Figure 9.1.: Photograph of the APD detector setup mounted in the test laboratory at the University of Münster.

For the use of the RMD S0223 APDs at the SPECTRAP setup a special detector system (figure 9.1) was designed and built based on the experience gathered with the APD test setup described in section 7.1. Since noise contributions of microphonic and capacitive effects have been minimized in that setup, the intention was to change as little as possible on the existing detector mount, preamplifier alignment and cabling. Only the small copper part housing the heating diodes (compare figures 9.4 and 7.2) had to be replaced, since the detector mount

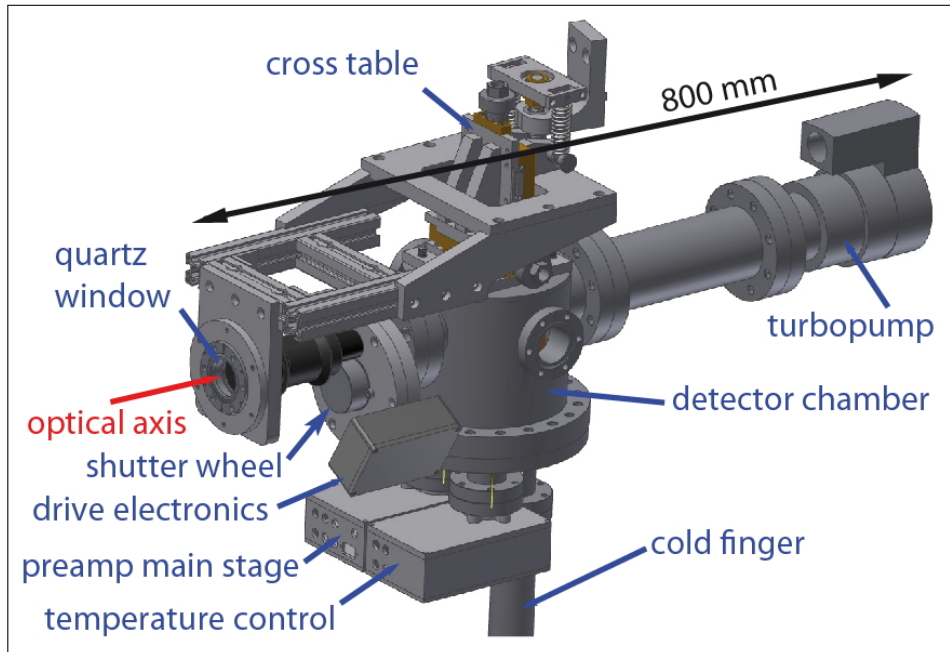


Figure 9.2.: Scetch of the vacuum chamber and its components.

had to be tilted by 90° . The overall system consists of three main components, the vacuum chamber, the detector flange and the shutter mechanism (see figure 9.2), which are described in detail in the following.

9.1. Detector vacuum chamber

The small vacuum chamber is pumped down to $\sim 10^{-7}$ mbar in order to prevent gas from condensing on the APD, the preamplifier and other cold surfaces of the detector mount, when the detector is operated at cryogenic temperatures. The main part is built of a 155 mm high stainless steel cylinder with an inner diameter of again 155 mm. The cylinder is closed on the upper end. A DN CF 160 flange is welded to the lower side attachment of the detector flange described in the next section. This main part of the vacuum chamber is further equipped with two DN CF 63 and two DN CF 40 flanges, oriented like a cross, with same sized flanges opposite to each other. A Pfeiffer HiPace80 turbomolecular pump is attached to a 210 mm CF 63 pipe extension mounted at the rear CF 63 flange to keep it further away from the magnets of the SpecTrap setup. The turbo pump is part of a Pfeiffer “HiCube” pumping station, also containing a small diaphragm pump and a control unit. Depending on the gas load introduced e.g. by the preamp components, it provides a vacuum of some 10^{-7} mbar. A small quartz window with a diameter of 34 mm that is equipped with four thread holes for mounting the shutter mechanism, is installed at the opposite CF 63 flange. The window is sealed with a rubber O-ring, reducing the aperture of the window to 14 mm

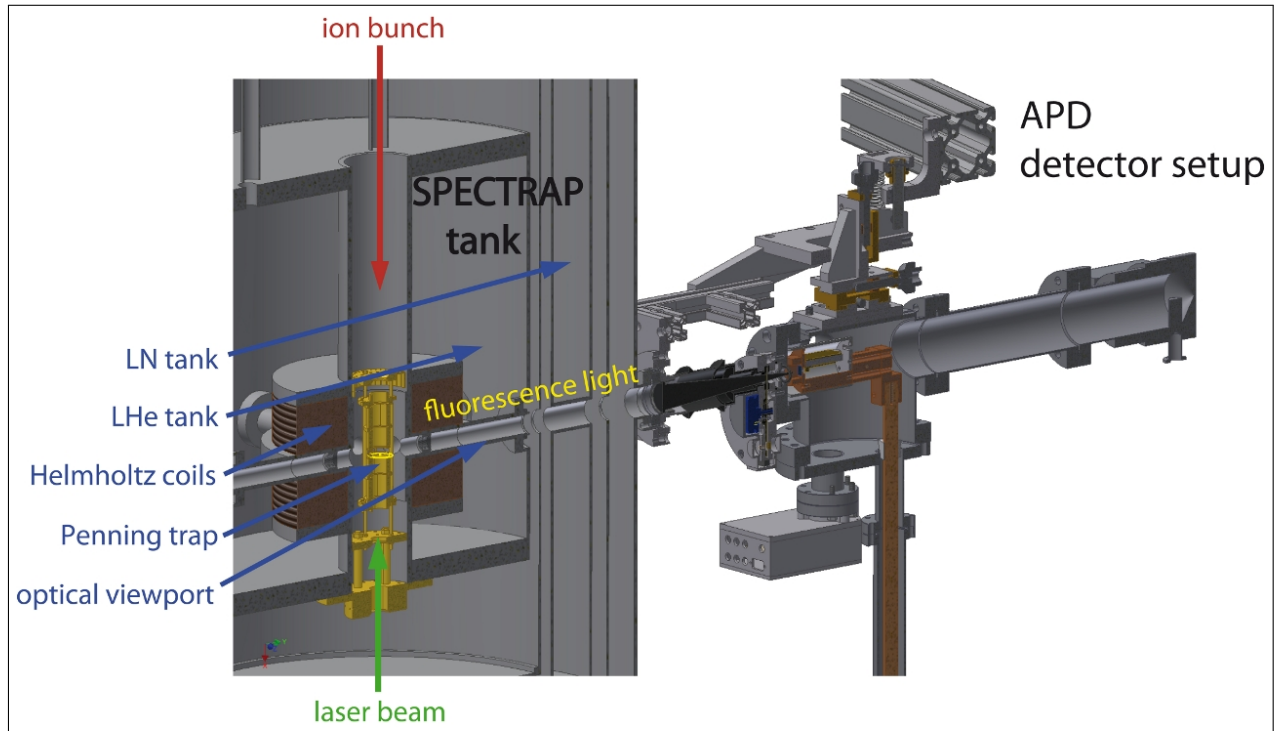


Figure 9.3.: Cross section of the detector setup and the SpecTrap experiment.

on the vacuum side. One of the two CF 40 flanges is used to connect a Leybold ITR200 S pressure gauge to the vacuum chamber, while the other CF 40 flange is currently unused. The shutter mechanism will be explained in detail in section 9.3.

The whole setup is mounted to the exit window of one of the optical viewports at SPECTRAP as shown in the sectional view in Fig. 9.3. The weight of the setup is held by two springs connected to the SpecTrap support structure. The elevation of the chamber can be roughly aligned by an adjusting screw. To be able to precisely adjust the position of the APD to the focal point of a lens located at the exit window of the SpecTrap viewport, a cross table mounted on top of the vacuum chamber is used to provide alignment of the chamber and the connected shutter mechanism by up to ± 12 mm in x , y and z direction.

9.2. Detector flange

The detector flange of this setup has the same layout as the detector flange in the test setup described in section 7.1.1. Since in the test setup a lot of effort was made to optimize the detector mount and the electronics cabling to reduce microphonic effects and pick-up of electronic noise, the idea was to change the layout as little as possible. The only change that was applied is an adapted design of the copper part housing the heating, that now tilts the preamplifier first stage with the APD by 90° to account for the needs of a horizontally

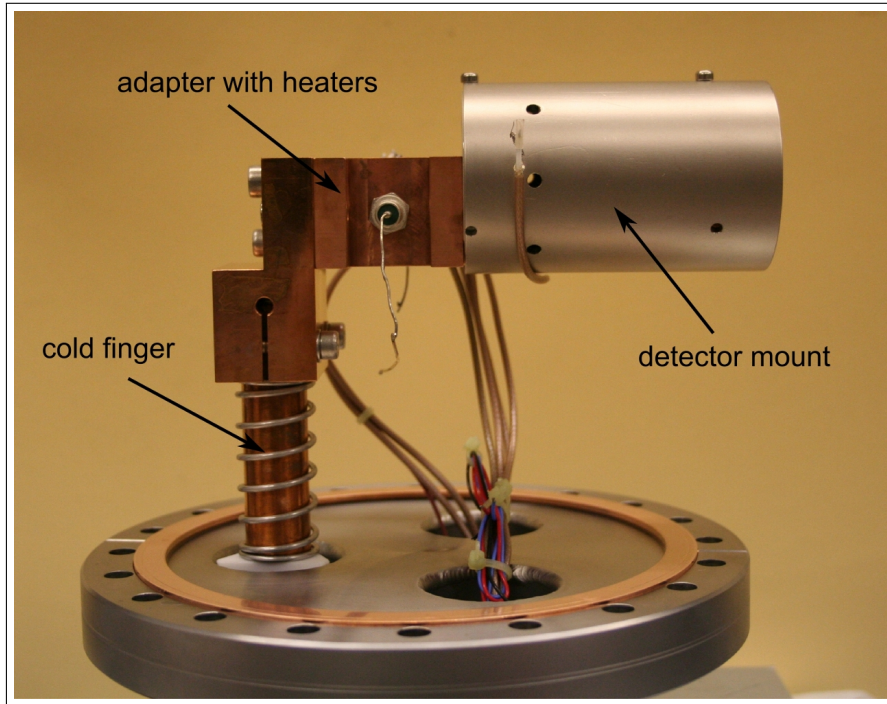


Figure 9.4.: Photograph of the modified detector flange.

aligned detector in the SpecTrap experiment (see figure 9.4). A teflon wedge, which is placed over the cold finger on the vacuum side and fixed with a spring was introduced to reduce vibrations of the cold finger, that induce microphonic noise. This problem is believed to be more essential at the SpecTrap experiment than in the lab, since the SpecTrap platform is vulnerable to tremors as was noticed during measurements in Summer 2011.

Like the setup used in the test chamber, the detector mount is equipped with two Zener diodes, that serve as heating installation. They are placed at the new adapter between detector mount and cold finger.

9.3. Optics and shutter mechanism

The whole detector setup is mounted to the exit window of one of the optical viewports at SPECTRAP. Since the RMD S0223 type APDs are rather small, the light emerging from the viewport has to be focused onto the detector by a $f = 200$ mm plano-convex lens, attached to the viewport. To keep the system light tight while at the same time assuring flexibility to enable adjustment of the detector position in any direction with respect to the viewport mounting, the latter is connected to the shutter by a rubber bellow. The purpose of the shutter mechanism is to protect the detector from excessive stray light during the excitation of the stored ions by a laser pulse.

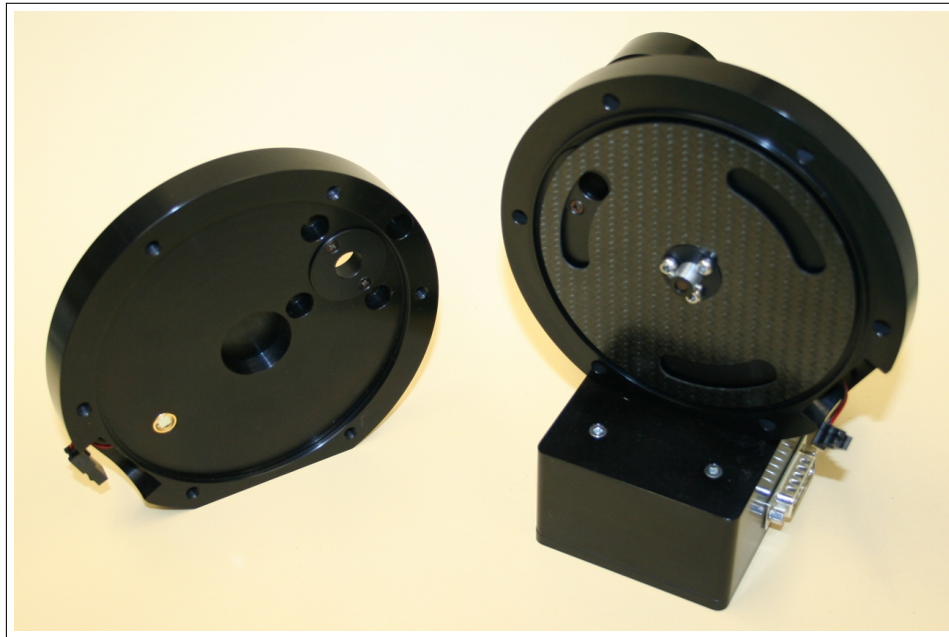


Figure 9.5.: Photograph of the opened shutter mechanism.

The shutter system consists of a mechanical shutter wheel, which is driven by a “maxon EC 45 flat” motor controlled by a “maxon DECS 50/5 1-Q-EC amplifier” board. It is equipped with three slits, each covering an angle of 60° , equidistantly arranged on a radius of 60 mm on the wheel. The aperture of the shutter is 10 mm. The shutter wheel is housed in a casing made of black anodized aluminum, also providing a small box-like extension containing the motor control electronics board. A D-Sub 15 connector is used to connect the control board as well as a light barrier with the control module described in the following section. The light barrier provides the shutter frequency and can be used to synchronize the shutter mechanism with additional experiment components, e.g. a laser shutter. The motor itself is mounted outside the shutter housing and is covered with a μ -metal shielding to reduce the influence of the magnetic field of the SpecTrap magnet.

The shutter wheel in combination with the motor was designed to allow shutter frequencies ranging from 6 Hz to 125 Hz. The corresponding shutter intervals spread from 140 ms with opening and closing times of 13 ms to 6.6 ms with opening and closing times of about 0.7 ms where the aperture is completely free or completely covered by the shutter wheel.

9.4. Setup remote control

The environmental conditions of the detector setup can be monitored and controlled via a NIM-sized control module (Fig 9.6). It is equipped internally with a NI USB-6009 14-Bit Multifunction DAQ module that allows to remotely control the functions of the detector

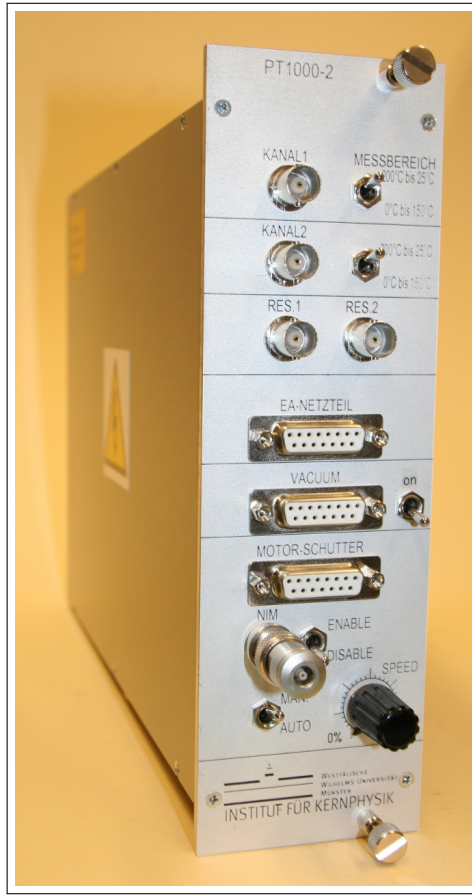


Figure 9.6.: Photograph of the NIM size control module.

setup in the same way as at the test setup (see section 7.1.3). The control module itself features:

- Two BNC connectors to connect PT 1000 sensors to the module. Transducers inside the module provide the Multifunction DAQ with voltages from 0 V to 5 V proportional to the PT 1000 resistance and thus the temperature. Two different temperature ranges can be selected for each channel via switches.
- A D-Sub 15 connector labeled “EA Netzteil” is foreseen to remotely control an EA laboratory power supply via the Multifunction DAQ. The power supply serves as current source for the heating installation at the detector mount.
- Another D-Sub 15 connector labeled “Vakuu” can be used to operate and read out a ITR 200 pressure gauge. Since the gauge’s emission disturbs photon measurements, it can be turned off by a switch.
- A third D-Sub 15 connector labeled “Motor Shutter” serves as connection to the motor and the light barrier of the shutter mechanism. The shutter frequency can be directly

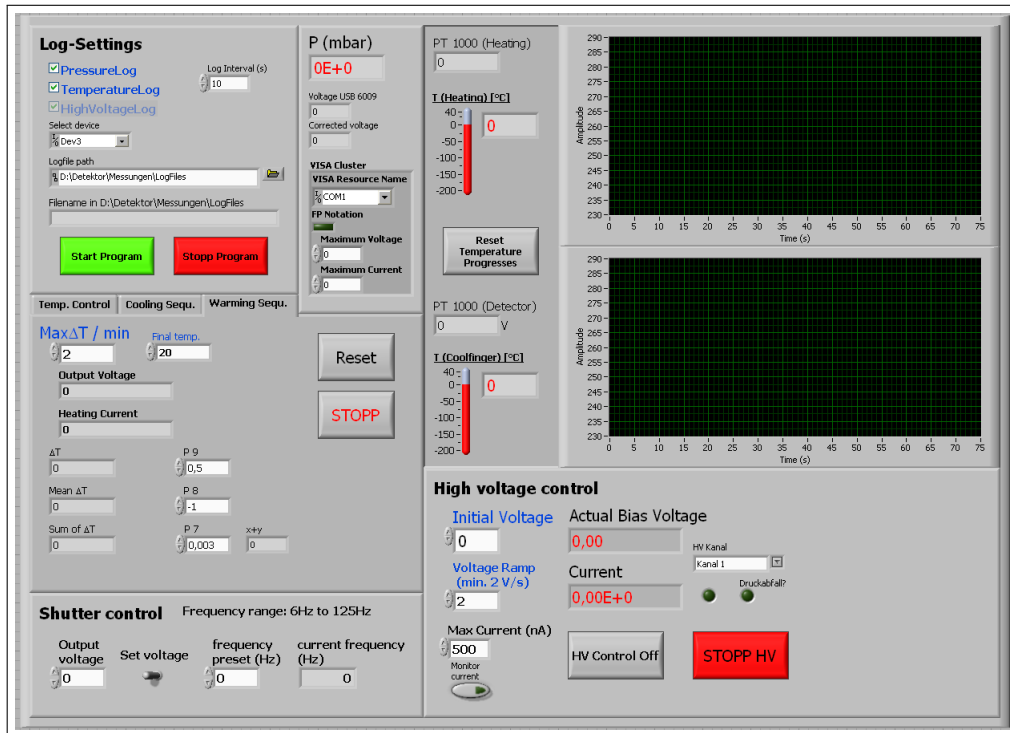


Figure 9.7.: User interface of the control program.

picked off from a BNC connector to use it, e.g. for another shutter mechanism to block the laser. The shutter frequency can be set manually via the potentiometer or automatically via the Multifunction DAQ. The mode can be changed by a switch. Another switch is used to enable or disable the motor of the shutter mechanism. When enabled, the motor automatically starts rotating with the selected speed or at least a minimum rotation speed.

- The front plate is equipped with two additional BNC connectors (“Res1” and “Res2”) that can be internally connected to free ports of the NI 6009 for various purpose as needed.

Since the basic layout of the setup is the same as the test setup, the control programs described in section 7.1 can be reused with only minor changes. The calibration of the temperature sensors had to be redone and the channels of the physical input/output device, i.e. the NI USB-6009 inside the NIM housing, had to be adjusted. An additional program was written to control the shutter mechanism, with parts also implemented in a main control program, that can be used to control the overall setup. A screenshot of the user interface can be seen in figure 9.7. Comparing the interface with figure 7.6 shows, that the main functions of the program are the same. The program was rearranged to provide a simple way to control the detector setup in a final experiment run. Besides layout changes, the only

major difference is the lack of the control to automatically take amplitude spectra with the Ortec MCA. This function has been removed, while in the lower left corner, now the shutter control can be found. The input can be switched between setting the motor supply voltage or a desired shutting frequency. The current frequency can be monitored in the corresponding display.

CONCLUSION AND OUTLOOK

This work has contributed to two laser spectroscopy experiments at GSI, the LIBELLE experiment and the SpecTrap experiment. The first part of this work focused on the LIBELLE experiment and its results. The second part dealt with the development of an APD based photon counting system for the SpecTrap experiment. The results of this work along with an outlook on the subject are presented in the following:

The LIBELLE experiment: The LIBELLE experiment has been the latest effort to determine the transition wavelength of the $2s$ hyperfine transition in $^{209}\text{Bi}^{80+}$, which has been successful due to the novel parabolic mirror detection system. The bismuth ions were stored in the ESR and excited by a tunable laser system. The wavelengths of the $1s$ transition in hydrogen-like Bi^{82+} and the $2s$ transition in lithium-like Bi^{80+} in the laboratory frame have been determined to be:

$$\lambda_{\text{lab}}^{\text{H-like}} = (591.1442 \pm 0.0645) \text{ nm}$$

$$\lambda_{\text{lab}}^{\text{Li-like}} = (641.1112 \pm 0.0627) \text{ nm}$$

To transform the latter wavelengths to the ion's rest frame, the ion velocity has to be known, which depends on the velocity of the electrons in the electron cooler at the ESR. The electron velocity is given by the effective acceleration voltage U_{eff} applied to the electron cooler. Calibration difficulties and several corrections to the applied voltage potential, have led to a significant uncertainty on the calculated ion velocity. The wavelengths in the ions' rest frame have nevertheless been determined to be

$$\lambda_0^{\text{H-like}} = (243.744 \pm 0.050) \text{ nm}$$

$$\lambda_0^{\text{Li-like}} = (1554.655 \pm 0.322) \text{ nm.}$$

The main contribution to the uncertainty of the transition wavelengths in the ion's rest frame, $\lambda_0^{\text{H-like}}$ and $\lambda_0^{\text{Li-like}}$, originate in the uncertainty of the applied electron cooler voltage. Therefore, it is currently considered to repeat the LIBELLE experiment with a special focus on the calibration and determination of the electron cooler voltage to significantly increase the accuracy of the experiment [Gep13].

The parabolic mirror system: The success of the LIBELLE beamtime in measuring the HFS transition wavelength in $^{209}\text{Bi}^{80+}$ has been achieved, among others, due to the novel parabolic mirror system. This parabolic mirror system was installed at the ESR in the summer of 2010 and had been tested previous to the LIBELLE beamtime during a special relativity experiment performed with Li^+ ions stored in the ESR. The LIBELLE beamtime has shown, that after an initial ion cooling phase of about 40 s seconds, the mirror can be safely moved into the beam position without significantly disturbing the beam.

The performance of the mirror system regarding the signal and background count rates are very close to the estimates obtained from simulations performed in the design phase of the system. E.g. the signal rate of (58 ± 13) cps taken at the resonance at 2.2 mA ion current can be scaled up to (79 ± 18) to match the ion current of 3 mA assumed in the simulations and is found to be comparable to the simulated signal rate of 86 cps.

The success of the novel detection system lead to a request to adapt its general idea to other experimental demands, namely the detection of XUV photons, which is currently pursued. Therefore, the copper mirror will be replaced with a metal plate, where XUV photons will create secondary electrons, which are then guided to an multichannel plate detector also placed inside the vacuum by electron optics. Simulations concerning the design of the detector are already finished [Vol13] and the mechanical design is ongoing.

The SpecTrap experiment: The SpecTrap experiment is a Penning trap experiment built to perform laser spectroscopy measurements on a variety of charged ions with suitable transition wavelengths. The ions are cooled inside the trap to very low temperatures. SpecTrap has been set up at GSI as one of several experiments making use of the HITRAP facility currently under construction. Within the framework of the SpecTrap collaboration, the Nuclear Physics Institute of the University of Münster provides the experiment with detectors for detection of fluorescence light down to the single-photon level, covering the wavelength regime from ultraviolet to near infrared wavelengths. Within this work a detector system for wavelengths ranging from 240 nm to 400 nm, consisting of a Channel Photomultiplier (CPM) module with a suitable mounting structure, was supplied to SpecTrap and has already been

used during first commissioning measurements.

In the course of these measurements, about 2600 Mg^+ ions have been stored inside the SpecTrap Penning trap by stacking up to 180 successive bunches from a local pulsed ion source, and have been cooled down to 0.1 K. The trap loading cycle has been improved by optimizing the fluorescence signal taken with the CPM detector setup. Storage times of up to 145 s were achieved [Caz12].

Further tests of the SpecTrap setup are ongoing and with the commissioning of the beamline connecting SpecTrap to an existing electron beam ion source (EBIS), also multiply charged ions will be available at SpecTrap. First tests with C-like $^{40}\text{Ca}^{14+}$, which has a transition at 569.44 nm, or with B-like $^{40}\text{Ar}^{13+}$, which has a transition at 441.24 nm, are planned. Finally, with the start-up of the HITRAP facility the highly charged ions listed in table 2.2 will be available and hyperfine transitions in these ions will be investigated with an estimated accuracy of $\frac{\Delta\lambda}{\lambda} = 10^{-7}$, starting with the hyperfine transition in H-like $^{209}\text{Bi}^{82+}$, since a suitable laser system is already available in the SpecTrap collaboration [Caz12].

APD detector setup for SpecTrap: A setup to investigate different types of APDs has been built consisting of a small vacuum chamber also with a cryogenically cooled detector mount. An extremely low noise preamplifier has been developed based on an existing design of the Mainz Neutrino Mass Experiment, which features a noise contribution of only $\sigma = 281$ eV. The test setup has been largely automatized to allow for uninterrupted measurements. Two single-photon sources have been set up, based on the emission characteristics of LEDs operated with low supply voltages and of thermal light sources, that emit mainly single-photons into the solid angle of the detector. Among others, this setup has been used to characterize RMD S0223 type APDs with an active area of (2×2) mm².

The characterization of the RMD S0223 APD showed that these devices can be operated at high relative gains of up to $2.2 \cdot 10^4$ allowing for single-photon counting. The photodetection efficiency at 560 nm, 628 nm and 1020 nm has been determined. The photodetection efficiency of $(67 \pm 7)\%$ at 628 nm is of the same order as the quantum efficiency stated in the datasheet of the APD (68%). At 1020 nm, the transition wavelength of the 1s hyperfine splitting in $^{207}\text{Pb}^{81+}$, the PDE was determined to be $(13 \pm 3)\%$

Based on these APDs a photon counting system for the SpecTrap experiment has been developed to allow for fluorescence light detection in the wavelength range from 400 nm to 1100 nm. The system features a cryogenically cooled detector mount with an RMD S0223 type APD as fluorescence light detector, which can be aligned to a focusing lens at the exit window of the optical viewport at SpecTrap by a cross table. This system is based on the APD test system and laid out to the requirements and experimental conditions at the SpecTrap experiment. It is equipped with a shutter wheel and a NIM-sized control unit for

protection of the detector from laser straylight. Final adjustments to this setup are currently being implemented.

A detector with a larger active area would ease the measurements at SpecTrap a great deal, since the alignment of the detector does not have to be as precise as with the rather small S0223 type APD and even the light yield at the detector would slightly increase. Therefore, the RMD S0812 APDs ($8 \times 8 \text{ mm}^2$ active area) are currently investigated [Sur13] to check their overall performance and their noise levels, which are expected to be higher due to the higher capacitance of the devices. Also the photodetection efficiency and single photon counting capability of these devices are investigated.

OPERATING PROCEDURE FOR THE APD SETUP

This section describes a procedure to be followed when starting to operate the RMD S0223 APD. Due to changes in the environmental and experimental conditions, the operating point of the APD as well as the optimal threshold settings of the discriminator, which are referred to in chapter 8, should be redetermined. Therefore, the following steps should be followed:

1. To check the preamplifier performance, the preamp noise without the detector should be measured.
2. After assembling the APD to the mounting structure and cooling down the setup, at least the dark current as function of the bias voltage should be measured to determine the APD's breakdown voltage.
3. Additionally, to verify high gain values, the gain as function of the bias voltage should be determined.
4. Now the operation point has to be determined. As mentioned in chapter 8, a reasonable choice for the operation point is 10 V below the breakdown voltage. However, the gain at the operation point should also be taken into account. It may be desirable to shift the operation point closer to the breakdown voltage in order to achieve higher gains.
5. Oscilloscope pictures of the preamplifier and the main amplifier signals at the APD's operation point should be taken.
6. Single photon ADC spectra at the operation bias should also be taken.

A. Operating procedure for the APD setup

7. The dark count rate and the count rate with single-photon illumination by a calibrated single-photon source have to be measured at the operation bias for several discriminator threshold settings in order to determine the optimum threshold for a high photodetection efficiency, following the measurements in section 8.3.
8. Now, the operation parameters are determined and the APD is operational.

APPENDIX B

CIRCUIT DIAGRAMS

B.1. Preamplifier

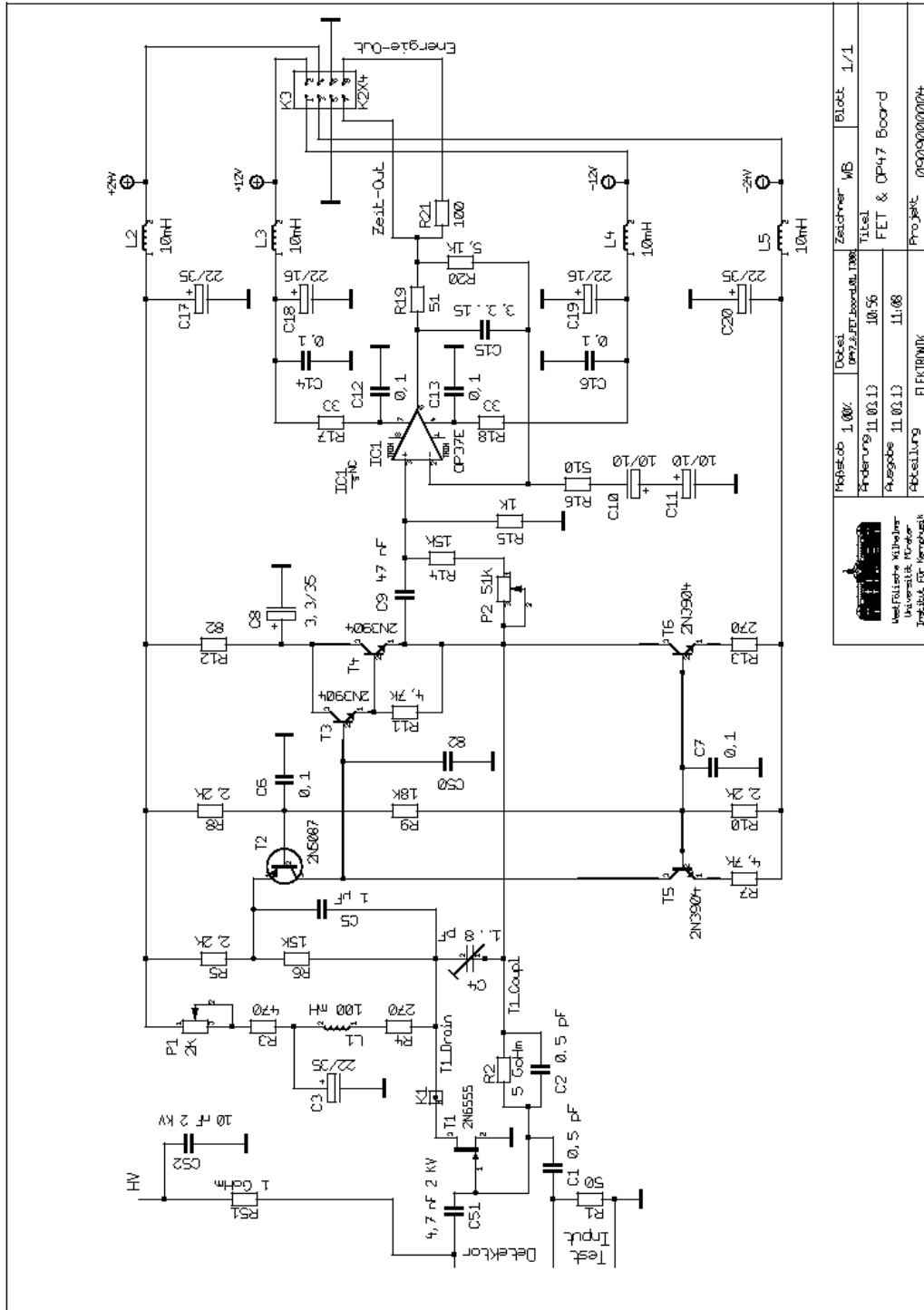


Figure B.1.: Circuit diagram of the preamplifier board.

B.2. PT 1000 transducer

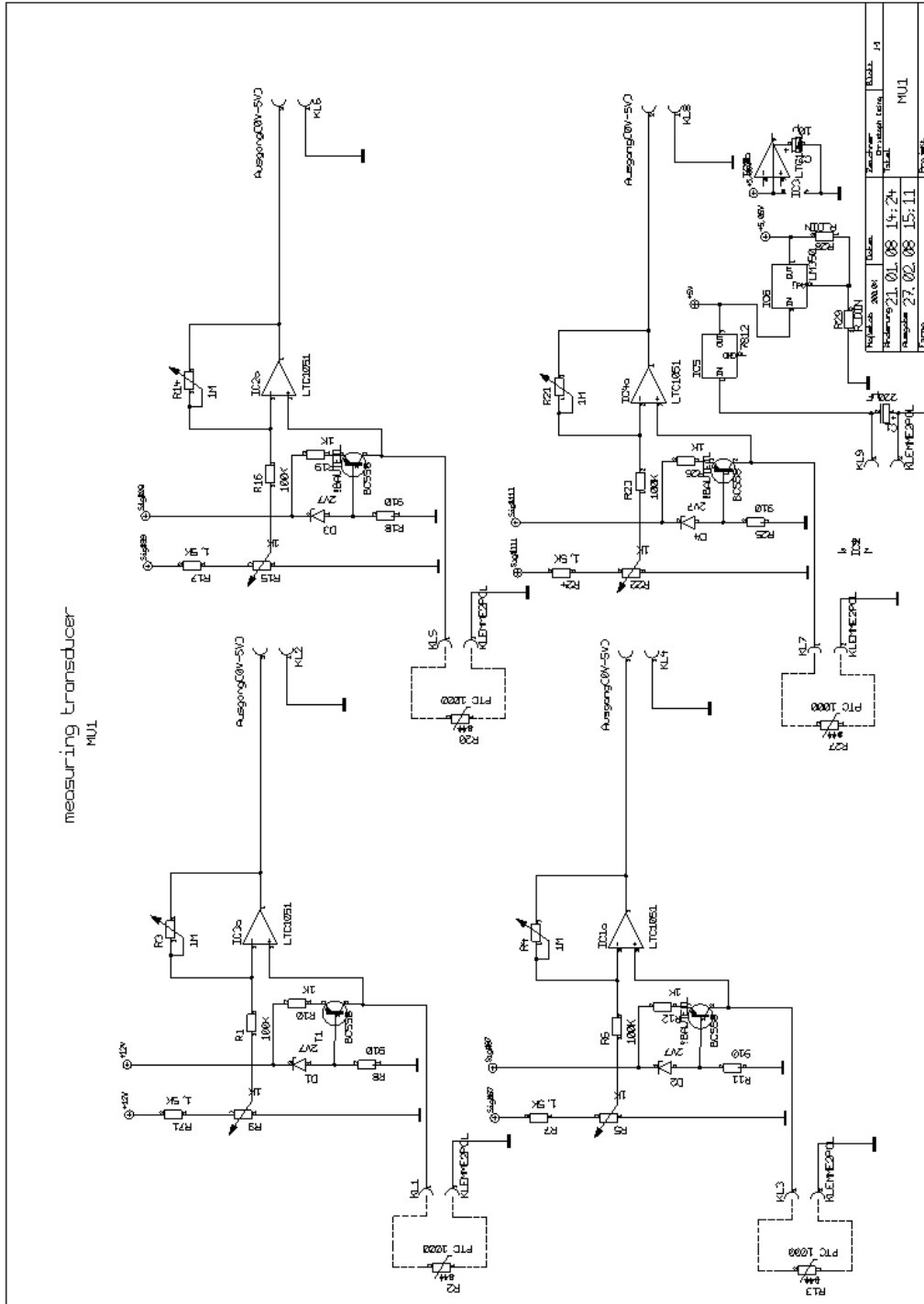
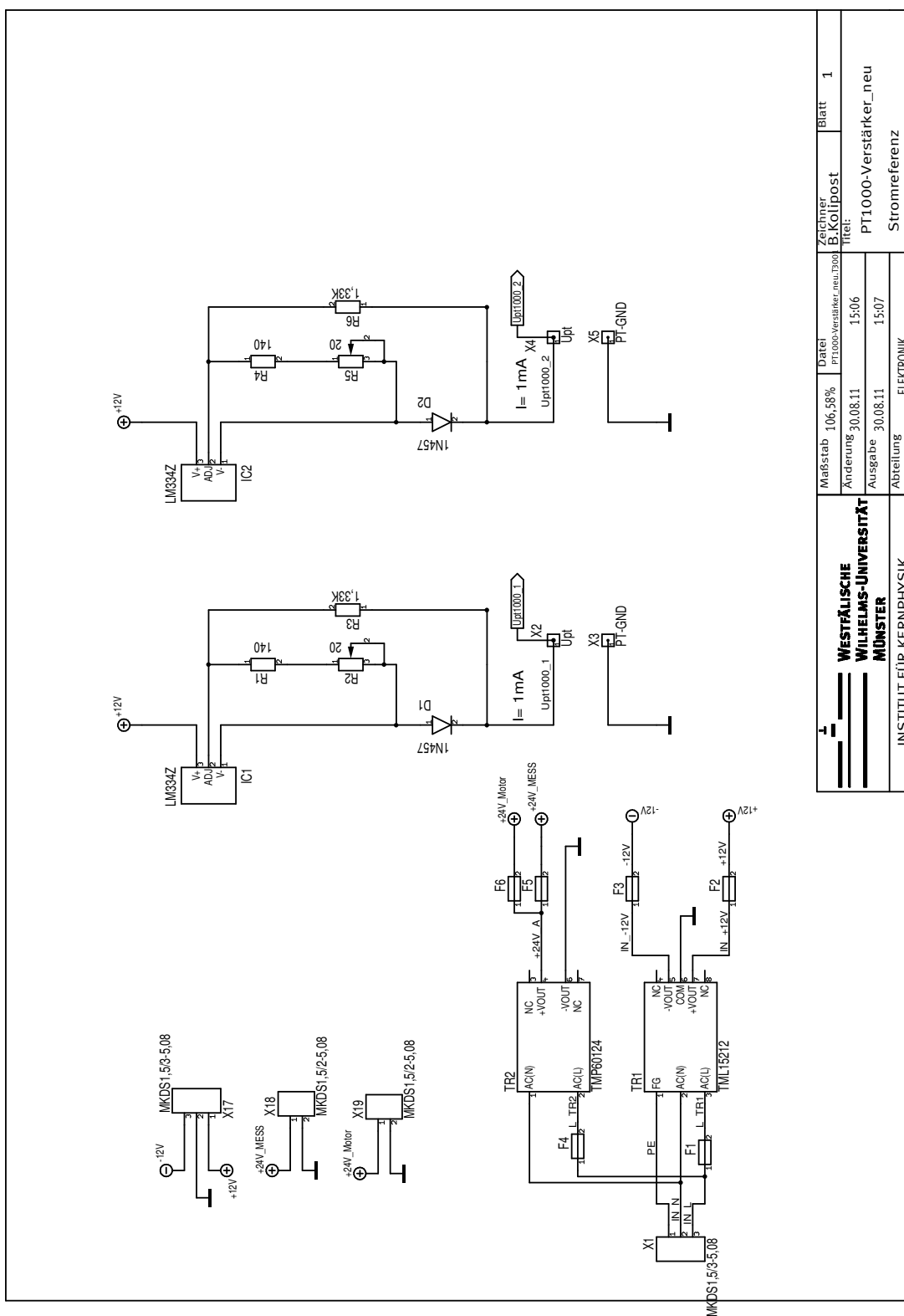


Figure B.2.: Circuit diagram of the PT 1000 transducer used in the test setup.

B.3. APD setup NIM size control module

Table B.1.: Connections of the NI USB 6009 Multifunction I/O board

Connections NI USB 6009			
pin-no.	signal	circuit board conn.	front plate conn.
1	GND	X3	
2	AI0	X2	
3	AI4	N.C.	
4	GND	X5	
5	AI1	X4	
6	AI5		
7	GND		Vacuum D-Sub 15 Pin 12
8	AI2		Vacuum D-Sub 15 Pin 2
9	AI6		
10	GND		
11	AI3		
12	AI7		
13	GND		EA-Netzteil D-Sub 15 Pin 11
14	AO0		EA-Netzteil D-Sub 15 Pin 2
15	AO1		Motor-Schutter D-Sub15 Pin 6
16	GND		
17	P0.0		
18	P0.1		
19	P0.2		
20	P0.3		
21	P0.4		
22	P0.5		
23	P0.6		
24	P0.7		
25	P1.0		Motor-Schutter D-Sub15 Pin 7
26	P1.1	X11	
27	P1.2		
28	P1.3		
29	PFIO	X11	
30	+2,5V		
31	+5V		
32	GND	X15	



WESTFÄLISCHE WILHELMS-UNIVERSITÄT MÜNSTER		INSTITUT FÜR KERNPHYSIK			
Maßstab	106,58%	Datum	PT1000-Verstärker_neu_1300	Blatt	1
Änderung	30.08.11	15:06	Zeichner B.Kolipost		
Ausgabe	30.08.11	15:07	Titel: PT1000-Verstärker_neu		
Abteilung			ELEKTRONIK		
			Stromreferenz		

Figure B.3.: Circuit diagram of the PT 1000 transducer used in the test setup (1).

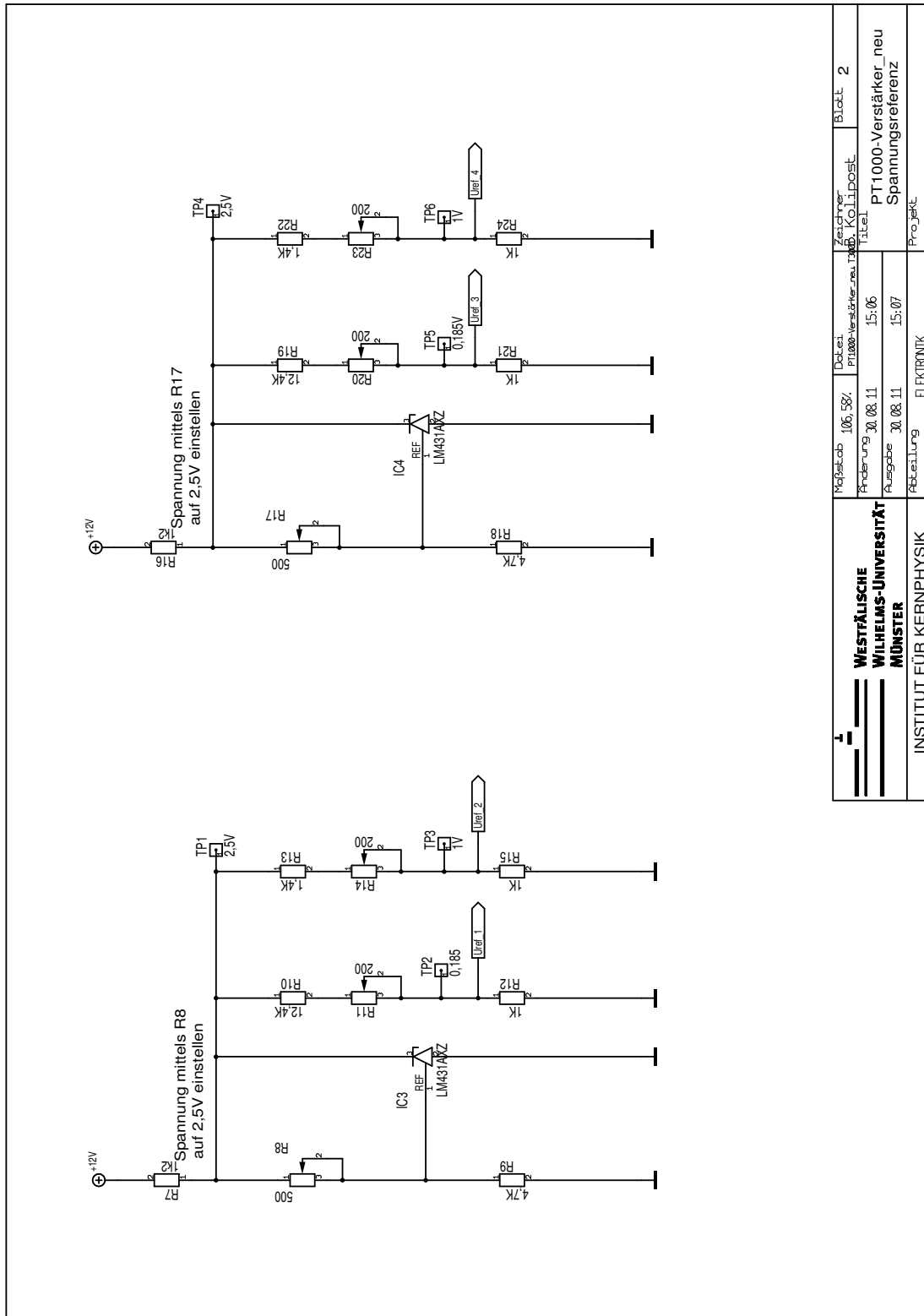


Figure B.4.: Circuit diagram of the PT 1000 transducer used in the test setup (2).

<p>WESTFÄLISCHE WILHELMS-UNIVERSITÄT MÜNSTER</p> <p>INSTITUT FÜR KERNPHYSIK</p>	MiBstLab 106.58%	DatZeit	Zeichner	Blatt 2
	Prüfung 30.08.11	Prüfung 30.08.11	15:06	PT1000-Verstärker_neu
	Ausgabe 30.08.11	Ausgabe 30.08.11	15:07	Spannungsreferenz
	Abteilung	ELEKTRONIK	Projekt	

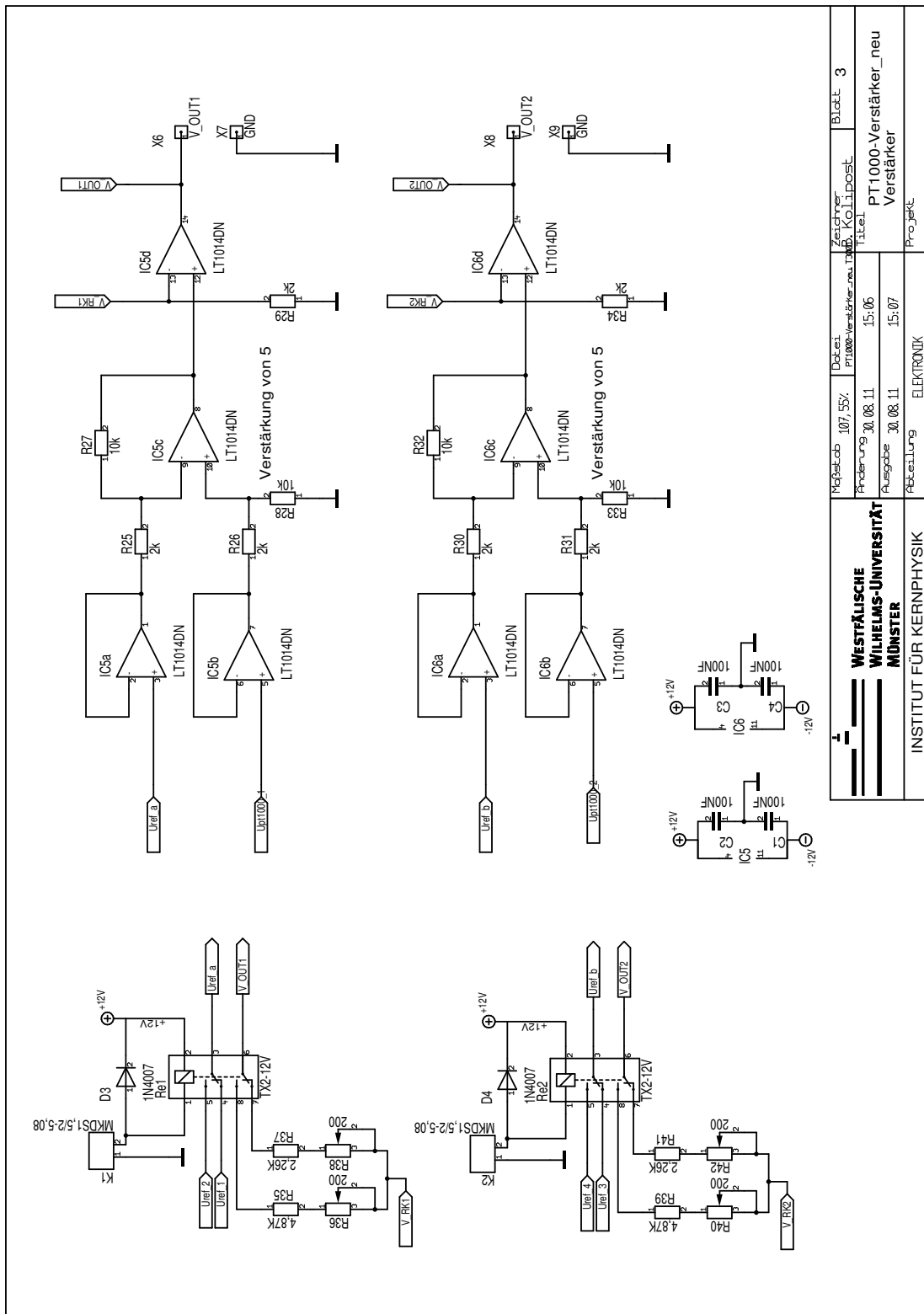


Figure B.5.: Circuit diagram of the PT 1000 transducer used in the test setup (3).

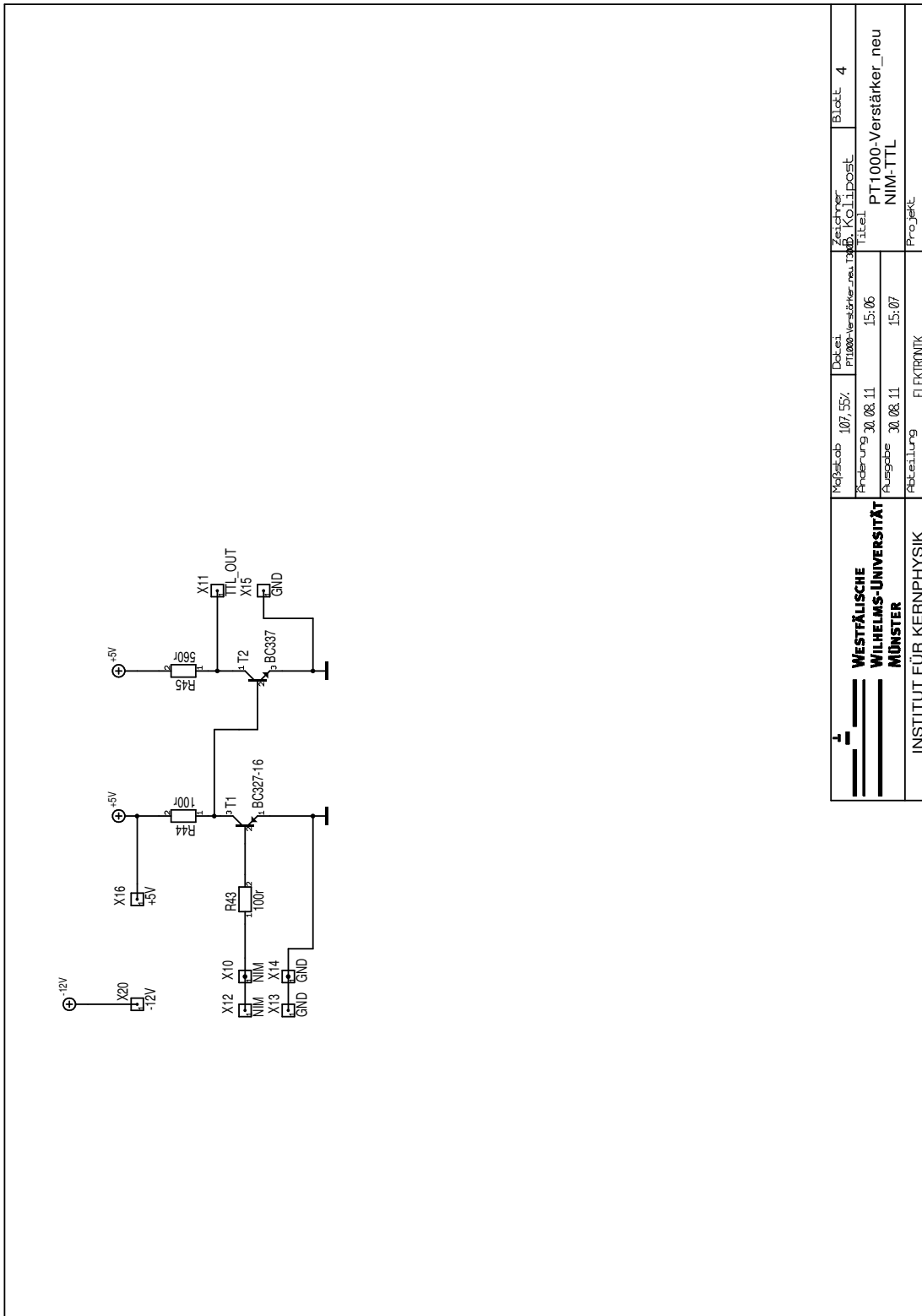



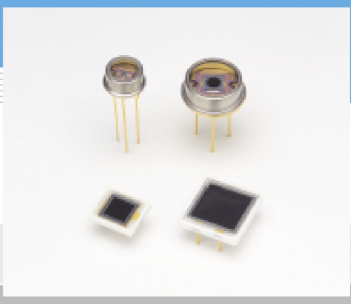
Figure B.6.: Circuit diagram of the PT 1000 transducer used in the test setup (4).

 WESTFÄLISCHE WILHELMS-UNIVERSITÄT MÜNSTER		INSTITUT FÜR KERNPHYSIK	
Maßstab	107,55%	Datum	30.08.11
Prüfung	30.08.11	Prüfung	15:06
Ausgabe	30.08.11	Ausgabe	15:07
Abteilung	ELEKTRONIK	Zeichner	SOIIPost
		Titel	PT1000-Verstärker_neu
		Projekt	NIM-TTL
			Blatt 4

APPENDIX C

DATASHEETS

PHOTODIODE



Si APD

S8664 series

Short wavelength type APD

Features

Applications

- High sensitivity at visible range
- Low noise
- High gain
- Low capacitance

- Low-light-level measurement
- Analytical equipment


General ratings / Absolute maximum ratings

Type No.	Dimensional outline /Window material *1	Package	Effective *2 active area size (mm)	Effective active area (mm ²)	Absolute maximum ratings		
					Operating temperature T _{opr} (°C)	Storage temperature T _{stg} (°C)	
S8664-02K	①/K	TO-5	φ0.2	0.03	-20 to +60	-55 to +100	
S8664-05K			φ0.5	0.19			
S8664-10K			φ1.0	0.78			
S8664-20K			φ2.0	3.14			
S8664-30K	②/K	TO-8	φ3.0	7.0			
S8664-50K			φ5.0	19.6			
S8664-55	③/E	Ceramic	5 × 5	25			-20 to +80
S8664-1010	④/E		10 × 10	100			

Electrical and optical characteristics (Typ. T_a=25 °C, unless otherwise noted)

Type No.	Spectral response range λ (nm)	Peak *3 sensitivity wavelength λ _p (nm)	Photo sensitivity S M=1 λ=420 nm (A/W)	Quantum efficiency QE M=1 λ=420 nm (%)	Breakdown voltage V _{BR} I _D =100 μA		Temperature coefficient of V _{BR} (V/°C)	Dark *3 current I _D		Cut-off frequency f _c (MHz)	Terminal *3 capacitance C _t (pF)	Excess *3 Noise index λ=420 nm	Gain M λ=420 nm
					Typ. (V)	Max. (V)		Typ. (nA)	Max. (nA)				
S8664-02K	320 to 1000	600	0.24	70	400	500	0.78	0.1	1	700	0.8	0.2	50
S8664-05K								0.2	1.5	680	1.6		
S8664-10K								0.3	3	530	4		
S8664-20K								0.6	6	280	11		
S8664-30K								1	15	140	22		
S8664-50K								3	35	60	55		
S8664-55								5	50	40	80		
S8664-1010								10	100	11	270		

*1: K: Borosilicate glass E: Epoxy resin
 *2: Area in which a typical gain can be obtained.
 *3: Values measured at a gain listed in the characteristics table.



IR-enhanced Si APD



S11518 series

Enhanced near IR sensitivity, using a MEMS technology

HAMAMATSU has developed various types of Si detectors that offer enhanced near-infrared sensitivity due to a MEMS structure formed on the back side of the photodiode. The S11518 series are a family of Si APDs with improved sensitivity in the near infrared region.

The S11518 series delivers a quantum efficiency of 40% at 1.06 μm and so provides significantly higher sensitivity to YAG laser light (1.06 μm) compared to our conventional product (S8890 series, quantum efficiency of 20%).

Features

- ➔ High sensitivity in the near infrared region
- ➔ High gain

Applications

- ➔ YAG laser monitor
- ➔ Long wavelength light detection

Structure / Absolute maximum ratings

Type no.	Window material*1	Package	Photosensitive area*2 (mm)	Absolute maximum ratings	
				Operating temperature T _{opr} (°C)	Storage temperature T _{stg} (°C)
S11518-10	K	TO-5	φ1.0	-20 to +85	-55 to +125
S11518-30	K	TO-8	φ3.0		

Note: Exceeding the absolute maximum ratings even momentarily may cause a drop in product quality. Always be sure to use the product within the absolute maximum ratings.

*1: K=borosilicate glass

*2: Area in which a typical gain can be obtained

Electrical and optical characteristics (Typ. T_a=25 °C, unless otherwise noted)

Type no.	Spectral response range λ (nm)	Peak sensitivity wavelength*3 λ_p (nm)	Breakdown voltage V _{BR} I _D =100 μA		Temp. coefficient of V _{BR} I _D =100 μA (V/°C)	Dark current*3 I _D		Terminal capacitance*3 C _T (pF)	Cut-off frequency*3 f _c R _L =50 Ω (MHz)	Excess noise figure*3 \times $\lambda=890$ nm	Gain M $\lambda=890$ nm
			Typ. (V)	Max. (V)		Typ. (nA)	Max. (nA)				
S11518-10	600 to 1150	980	500	800	3.5	5	50	1.5	230	0.3	100
S11518-30						15	150				

*3: Values measured at a gain listed in the characteristics table

List of Figures

1.1. Basic QED processes	2
2.1. Energy levels of the Hydrogen atom	8
2.2. Expectation values of electric and magnetic field strengths in HCl	10
3.1. GSI overview	18
3.2. ESR overview	19
3.3. LIBELLE laser setup	20
3.4. LIBELLE laser control program	22
3.5. ESR mirror section	25
3.6. Relativistic effects: Doppler shift	26
3.7. Emission and detection angles	27
3.8. Relativistic effects: distribution of polar angles	28
3.9. Simulation results for the mirror section	31
3.10. Simulation results for the parabolic mirror system	32
3.11. Parabolic mirror system (schematic)	34
3.12. Parabolic mirror system (pictures)	35
3.13. Forward detection system	36
3.14. Schematic of the DAQ system	39
3.15. Scan structure	41
4.1. Time evolution of the detector count rates	45
4.2. Beamtime PMT count rates	46
4.3. Timing spectrum	47
4.4. Flow chart of the scan step extraction	50
4.5. Bunch stacking	52
4.6. Bunch fits	53
4.7. χ^2_{red} -distribution of bunch fits	54
4.8. Resonance fit example	55
4.9. Li-like time regions	58
4.10. Li-like area fits	60

LIST OF FIGURES

4.11. Li-like laboratory wavelengths	63
4.12. H-like resonance fits	65
5.1. Schematic overview of the electron cooler voltage control	68
5.2. Scheme of a high voltage voltmeter	69
5.3. Calibration fit for $U_{\text{set}} \rightarrow U_{\text{DVM}}$	70
5.4. Calibration fit for $U_{\text{DVM}} \rightarrow U_{\text{PTB}}$	72
5.5. Wavelength results for Bi^{82+}	76
5.6. Wavelength results for Bi^{80+}	77
6.1. HITRAP location	83
6.2. SpecTrap setup	84
6.3. SpecTrap Penning trap	85
6.4. Cross section of one of the viewports of the SpecTrap cryostat	89
6.5. Light rays of two point sources within the ion cloud to the detector	91
6.6. <i>kojac</i> simulation results	92
6.7. Simulated magnetic field strength	94
6.8. CPM detectors	95
6.9. Silicon APD types	96
6.10. Infrared detectors	97
7.1. Detector test setup	100
7.2. Detector flange and detector mount	101
7.3. Preamplifier scheme and first stage	102
7.4. Preamplifier main stage and connectors	103
7.5. Overview of the test setup control and DAQ system	105
7.6. Test setup control program	107
7.7. Contributions to an amplitude spectrum for gain determination	109
7.8. Amplitude spectra for gain determination	110
7.9. Signal and noise rate measurement program	112
7.10. LED mount	115
7.11. Dark count spectra	116
7.12. Grating spectrograph	117
8.1. Scheme of an APD	120
8.2. Dark current of a S0223 APD	123
8.3. Relative gain of two S0223 type APDs	124
8.4. Single-Photon spectrum	125
8.5. Comparison of different rates vs. threshold	126

8.6. Single-Photon measurement	127
8.7. Photo detection efficiency	128
9.1. Detector setup: photograph of the setup	131
9.2. Detector setup: vacuum chamber	132
9.3. Detector setup: cross section	133
9.4. Detector setup: detector flange	134
9.5. Detector setup: shutter	135
9.6. Detector setup: NIM size control module	136
9.7. Detector setup: control program user interface	137
B.1. Circuit diagram: preamplifier	147
B.2. Circuit diagram: PT 1000 transducer	149
B.3. Circuit diagram: PT 1000 transducer (1)	151
B.4. Circuit diagram: PT 1000 transducer (2)	152
B.5. Circuit diagram: PT 1000 transducer (3)	153
B.6. Circuit diagram: PT 1000 transducer (4)	154

List of Tables

2.1. Previous values of the $2s$ hyperfine splitting in $^{209}\text{Bi}^{80+}$	13
2.2. HCI to test QED	14
3.1. Estimated photon rates for $^{209}\text{Bi}^{80+}$	30
3.2. Simulation results: Mirror section vs. parabolic mirror system	33
3.3. TDC and scaler assignment	38
4.1. Measurement data files	44
4.2. Li-like runs	59
4.3. Li-like fit results	61
4.4. H-like runs	64
4.5. H-like fit results	64
5.1. Electron cooler settings during the LIBELLE beamtime	75
5.2. Transition wavelength values for Bi^{82+} and Bi^{80+}	78
6.1. Count Rate Estimates	93
7.1. Pulse settings	106
7.2. Single-Photon pulse settings	115
8.1. PDE and dark rates with spectrograph	129
B.1. Connections of the NI USB 6009	150

Bibliography

- [All03] J. Allison et al., *GEANT4 - a simulation toolkit*, Nuclear Instruments and Methods in Physics Research **A506**, 2003.
- [Amp05] A250CF CoolFET User Manual -Preliminary Rev. A3, Amptek, Bedford, MA, USA 2005.
- [And10] Z. Andjelkovic et al., *Towards high precision in-trap laser spectroscopy of highly charged ions*, Hyperfine Interactions Vol.196 1-3, p.81-91, Springer Netherlands 2010, <http://www.springerlink.com/content/uw5210jq4n0tt224/>.
- [And12] Z. Andelković, *Setup of a Penning trap for precision laser spectroscopy at HITRAP*, PhD thesis, Johannes Gutenberg Universität Mainz, 2012.
- [Ani10] D. Anielski, *Entwicklung eines Detektoraufbaus zur Bestimmung der 2s-Hyperfeinstrukturaufspaltung von $^{209}\text{Bi}^{80+}$ am Experimentierspeicherring an der GSI*, Diploma thesis, WWU Münster, February 2010, http://www.uni-muenster.de/Physik.KP/AGWeinheimer/Files/theses/Diplom_Denis_Anielski.pdf.
- [Bal08] Balzers heat protection filters, available from www.opticsbalzers.com.
- [Bec02] C. Becher et al., *A quantum dot single-photon source*, Physica **E 13**, p. 412-417, 2002.
- [Ben05] A.J. Bennett et al., *High-efficiency single-photon sources based on InAs/GaAs quantum dots in pillar microcavities*, Physica **E 26**, p. 391–394, 2005.
- [Bha12] S. Bharadia et al., *Dynamics of laser-cooled Ca^+ ions in a Penning trap with a rotating wall*, Appl. Phys. **B 107**, p. 1105-1115, 2012.
- [Bei98] P. Beiersdorfer et al., *Measurement of QED and Hyperfine Splitting in the $2s_{1/2}$ - $2p_{3/2}$ X-Ray Transition in Li-like $^{209}\text{Bi}^{80+}$* , Phys. Rev. Lett. **80** 3022, 1998.
- [Bei00] T. Beier, Physics Reports **339**, p. 79-213, 2000.

- [Ber68] G. Bertolini and A. Coche, eds., *Semiconductor Detectors*, (Elsevier–North Holland, Amsterdam, 1968).
- [Bra83] B.H. Bransden, *Physics of Atoms and Molecules*, Longman Group Limited, New York, 1983.
- [Bra00] C. Brandau, *Messungen zur Photorekombination hochgeladener lithiumähnlicher Atome*, PhD thesis, Justus-Liebig-Universität Gießen, 2000.
- [Bri04] I. Britvitch et al., *Avalanche photodiodes now and possible developments*, Nucl. Instr. and Meth. in Physics Research **A 535**, p. 523-527, 2004.
- [Bri07] I. Britvitch et al., *Characterisation of Geiger-mode avalanche photodiodes for medical imaging applications*, Nucl. Instr. and Meth. in Physics Research **A 571**, p. 308-311, 2007.
- [Caz12] R.M. Cazan *Preparation of Cold Mg⁺ Ion Clouds for Sympathetic Cooling of Highly Charged Ions at SPECTRAP*, PhD thesis, Johannes Gutenberg Universität Mainz, 2012.
- [Dem10] W. Demtröder, *Experimentalphysik 3 - Atome, Moleküle und Festkörper*, 4th edition, Springer-Verlag, Berlin 2010.
- [Dra00] D. Dravins et al., *Avalanche Diodes as Photon-Counting Detectors in Astronomical Photometry*, Proc. SPIE 4008, p. 298-307, 2000.
- [Du96] Y. Du et al., *Multi-Layer Multi-Branch Data Acquisition System MBS*, GSI Report 1996, http://www-win.gsi.de/daq/Docs/jb96_mbs.pdf
- [Fit09] Fityk curve fitting and data analysis, Program for data processing and nonlinear curve fitting, <http://fityk.nieto.pl>
- [Gab08] G. Gabrielse et al., *New Measurement of the Electron Magnetic Moment and the Fine Structure Constant*, Phys. Rev. Lett. **100**, 128801, 2008.
- [Gen11] T.R. Gentile et al., *Magnetic field effects on large area avalanche photodiodes at cryogenic temperatures*, Nucl. Instr. and Meth. **A 652**, p. 520-523, 2011.
- [Gnu12] Gnuplot, a portable command-line driven graphing utility, 2012, <http://www.gnuplot.info>.
- [Gep12] C. Geppert, *Laser Spectroscopy on relativistic Bi^{82+/80+} Ions at the Storage Ring ESR/GSI*, research seminar talk at the WWU Münster, April 2012.
- [Gep13] C. Geppert, Johannes Gutenberg Universität Mainz, private communication, February 2013.

-
- [Hak90] N.Z. Hakim et al., *Generalized Excess Noise Factor for Avalanche Photodiodes of Arbitrary Structure*, IEEE Trans. Electron Devices **37**, No. 3, p. 599-610, 1990.
- [Ham04] Characteristics and use of Si APD (Avalanche Photodiode), Technical Information SD-28, Hamamatsu Photonics K.K., 2004.
- [Ham07] Photomultiplier Tubes: Basics and Applications, Third Edition, Hamamatsu PMT handbook, 2007, http://sales.hamamatsu.com/assets/pdf/catsandguides/PMT_handbook_v3aE.pdf.
- [Ham08] D. Hampf, *Untersuchung der APD S1315 von RMD im Hinblick auf ihren Einsatz als Detektor am SPECTRAP Experiment*, Diploma thesis, WWU Münster, June 2008, http://www.uni-muenster.de/Physik.KP/AGWeinheimer/theses/Diplom_Daniel_Hampf.pdf.
- [Ham11] Hamamatsu Photonics, H10330A datasheet, 2011, http://sales.hamamatsu.com/assets/pdf/parts_H/H10330A-25_-45_-75_TPM01042E02.pdf
- [Han13] V. Hannen et al., *Detection system for forward emitted photons at the Experimental Storage Ring at GSI*, to be submitted to JINST.
- [Jam06] F. James, *Statistical Methods in Experimental Physics*, 2nd edition, Singapore: World Scientific, p. 324, 2006.
- [Jes08] H. Jesch, PerkinElmer, private communication, 2008.
- [Jöh12] R. Jöhren et al., *APDs as Single-Photon Detectors for Visible and Near-Infrared Wavelengths down to Hz Rates*, Journal of Instrumentation, Volume 7, P02015, 2012.
- [Jos10] M. Joswowitz, *Kalibrierte Photonenquellen für Testmessungen von XENON- und SpecTrap-Detektoren*, Diploma thesis, WWU Münster, August 2010, http://www.uni-muenster.de/Physik.KP/AGWeinheimer/Files/theses/Diplom_Marcus_Joswowitz.pdf.
- [Kin06] T. Kinoshita et al., *Improved α^4 term of the electron anomalous magnetic moment*, Phys. Rev. **D 73**(1), 013003-27, 2006.
- [Kla94] I. Klaft et al., *Precision Laser Spectroscopy of the Ground State Hyperfine Splitting of Hydrogenlike $^{209}\text{Bi}^{82+}$* , Phys. Rev. Lett. **73** 2425, 1994.
- [Krä07] J. Krämer, *Aufbau und Test einer Ionenfalle für die Laserspektroskopie an hochgeladenen Ionen*, diploma thesis, Johannes Gutenberg Universität Mainz, 2007.

- [Kug12] Kugler GmbH, Heiligenberger Str. 100, 88682 Salem, Germany, <http://www.kugler-precision.com>.
- [Kus11] F. Kuschewski, *Untersuchungen von Avalanche Photodioden zum Einzelphotonennachweis*, Bachelor thesis, WWU Münster, Juli 2011, http://www.uni-muenster.de/Physik.KP/AGWeinheimer/Files/theses/Bachelor_Frederik_Kuschewski.pdf.
- [Lam47] W.E. Lamb et al., *Fine Structure of the Hydrogen Atom by a Microwave Method*, Phys. Rev **72**, p 241, 1947.
- [Leo87] W.R. Leo, *Techniques for Nuclear and Particle Physics Experiments*, Springer Verlag, Berlin, 1987.
- [Loc13] M. Lochmann, PhD thesis in preparation, Johannes Gutenberg Universität Mainz, in preparation.
- [Loc12] M. Lochmann, *private communication*, November 2012.
- [Lop10] R. López Coto, *Test and commissioning of the detector system in the $^{209}\text{Bi}^{80+}$ experiment at the Experimental Storage Ring (ESR) at GSI*, Master Thesis, WWU Münster, November 2010, http://www.uni-muenster.de/Physik.KP/AGWeinheimer/Files/theses/Master_Ruben_Lopez_Coto.pdf.
- [LTU12] LT Ultra Precision Technology GmbH, Wiesenstrasse 9, 88634 Herdwangen-Schönach, Germany, <http://www.lt-ultra.com>.
- [Mar00] J. Marler et al., *Studies of avalanche photodiode performance in a high magnetic field*, Nucl.Instr. an Meth. **A 449**, p. 311-313, 2000.
- [McI66] R.J. McIntyre, *Multiplication Noise in Uniform Avalanche Diodes*, IEEE Trans. Electron Devices, ED13, p. 164-168, 1966.
- [Mei12] B. Meier et al., *Nuclear magnetic resonance apparatus for pulsed high magnetic fields*, Rev. of Scient. Instr. **83**, 083113, 2012.
- [Min12] S. Minami, *VUPROM as 16-ch Multi-Hit Double-Buffer TDC and Scaler*, GSI Helmholtzzentrum für Schwerionenforschung GmbH, February 2012.
- [MPD13] Micro photon devices, PDM datasheet, <http://www.micro-photon-devices.com/media/pdf/PDM.pdf>
- [Mue79] R. Müller, Rauschen, Springer 1979.

-
- [Nör07] W. Nörtshäuser, *Laserspektroskopie hochgeladener Ionen an HiTrap*, Research seminar talk at the Nuclear Physics Institut, WWU Münster, 2007.
- [Nör08] W. Nörtshäuser, *Laser spectroscopy of lithium-like bismuth at the ESR*, experiment proposal, 2008.
- [Nör09] W. Nörtshäuser, *private communication*, GSI, Darmstadt, 2009.
- [Nör11] W. Nörtshäuser, *Laser spectroscopy for QED tests in highly charged ions*, *Hyperfine Interact.* **199**, p. 131, 2011.
- [Nör12] W. Nörtshäuser, *Ground-State Hyperfine Transition in Li-like Bismuth*, HCI 2012 conference proceedings, to be published.
- [Nov08] C. Novotny, *Towards a new test of time dilation - Laser spectroscopy on lithium ions stored at a velocity of 33.8% of the speed of light*, PhD thesis, Johannes Gutenberg-Universität Mainz, August 2008.
- [Nov09] C. Novotny et al., *Sub-Doppler laser spectroscopy on relativistic beams and tests of Lorentz invariance*, *Phys. Rev. A* **80**, 2009
- [Perk1] PerkinElmer: CPM datasheet, <http://optoelectronics.perkinelmer.com/content/relatedlinks/cpmdatasheet.pdf>.
- [Perk2] PerkinElmer Handbook: The Channel Photomultiplier and its Operation, PerkinElmer, 2006.
- [Perk3] PerkinElmer: Channel Photomultipliers - Overview and Specifications, PerkinElmer Optoelectronics, 2006, http://www.perkinelmer.com/CMSResources/Images/46-6538APP_AvalanchePhotodiodesUsersGuide.pdf
- [Perk4] PerkinElmer: Avalanche photodiode - A User Guide, PerkinElmer Optoelectronics, 2001.
- [Pit02] T.B. Pittman et al., *Single photons on pseudodemand from stored parametric down-conversion*, *Phys. Rev. A* **66**, 042303, 2002
- [Pit05] T.B. Pittman et al., *Heralding single photons from pulsed parametric down-conversion*, *Optics Communications* 246, p. 545-550, 2005.
- [Pov06] B. Povh, K. Rith, C. Scholz, F. Zetsche, *Teilchen und Kerne*, Springer, Berlin Heidelberg, 2006.

- [Qui01] W. Quint et al., *HITRAP: A Facility for Experiments with Trapped Highly Charged Ions*, *Hyperfine Interactions* **132**, p. 457-461, 2001.
- [Ren02] D. Renker, *Properties of avalanche photodiodes for applications in high energy physics, astrophysics and medical imaging*, *Nucl. Instr. and Meth.* **A 486**, p. 164-169, 2002.
- [RMD01] RMD product information: Silicon Avalanche Photodiodes (APDs), <http://www.rmdinc.com/products/p006.html>.
- [RMD03] RMD Inc., Silicon Avalanche Photodiode datasheet, 2003.
- [San09] R. Sánchez, GSI Darmstadt, private communication, 2009.
- [San12] R. Sánchez, GSI Darmstadt, private communication, 2012.
- [Sap01] J. Sapirstein et al., *Hyperfine splitting in lithiumlike bismuth*, *Phys. Rev.* **A 63**, 032506, 2001.
- [Sch90] M. Schrader, *Rauschoptimierung eines ladungsempfindlichen Vorverstärkers für Halbleiterdetektoren und digitale Filterung des analogen Ausgangssignals*, Diploma thesis, Johannes Gutenberg Universität Mainz, February 1990.
- [Sch08] Schott long pass filters, datasheet available from www.schott.com.
- [See99] P. Seelig, *Laserspektroskopie der 1s-Hyperfeinstrukturaufspaltung an wasserstoffähnlichem $^{207}\text{Pb}^{81+}$* , PhD thesis, Johannes Gutenberg Universität Mainz, 1999.
- [Sha98] V.M. Shabaev et al., *Transition energy and lifetime for the ground-state hyperfine splitting of high-Z lithiumlike ions*, *Phys. Rev.* **A 57**, p. 149-156, 1998.
- [Sha00] V.M. Shabaev et al., *Calculation of the hyperfine structure of heavy H- and Li-like ions*, *Hyperfine Interact.* **127**, p. 279, 2000.
- [Sha01] V.M. Shabaev et al., *Towards a Test of QED in Investigations of the Hyperfine Splitting in Heavy Ions*, *Physical Review Letters*, Volume 86, Number 18, p. 3959-3962, 2001.
- [Ste04] M. Steck et al., *Electron cooling experiments at the ESR*, *Nucl. Instr. and Meth.* **A 523**, p. 357-365, 2004.
- [Sur13] M. Surholt, diploma thesis at the WWU Münster, in preparation.
- [Tho12] Thorlabs GmbH (German division), Hans-Boeckler-Str. 6, 85221 Dachau/Munich, Germany, <http://www.thorlabs.com>.

-
- [Tom00] M. Tomaselli et al., *Hyperfine structure of Li-like bismuth*, Hyperfine Interact. **127**, p.315, 2000.
- [VAb12] VAb Vakuum-Anlagenbau GmbH, Marie-Curie-Str. 11, 25337 Elmshorn, Germany, <http://www.vab-vakuum.de>.
- [Vis01] Vishay Siliconix, U430 Matched N-Channel Pair datasheet, 2001.
- [Vog05] M. Vogel et al., *A proposed precision laser spectrometer for trapped highly charged ions*, Review of Scientific Instruments **76** (2005) 103102.
- [Vol11] A.V. Volotka et al., *Test of many-electron QED effects in the hyperfine splitting of heavy ions*, GSI Scientific Report 2011, S. 386, 2012.
- [Vol13] J. Vollbrecht, PhD thesis at the WWU Münster, in preparation.
- [Wei98] G. Weinberg et al., *Electron capture from H_2 to highly charged Th and Xe ions trapped at center of mass energies near 6 eV*, Phys. Rev. **A 57**, p. 4452-4461, 1998.
- [Wei90] C. Weinheimer et al., *Measurement of energy resolution and dead layer thickness of LN_2 -cooled PIN photodiodes*, Nucl. Instr. and Meth. **A 311**, p. 273-279, 1992.
- [Wen13] W.Q. Wen et al., *Optical measurement of the longitudinal ion distribution of bunched ion beams in the ESR*, Nucl. Instr. and Meth. **A 711**, p. 90-95, 2013.
- [Win96] T. Winkler, *Untersuchung zur Elektronenkühlung hochgeladener schwerer Ionen*, PhD thesis, Universität Heidelberg, 1996.
- [Win99] H. Winter, *Laserspektroskopie an schweren Ionen: Laserinduzierte Zweistufen-Rekombination, Hyperfeinaufspaltung und g-Faktor des gebundenen Elektrons*, PhD thesis, Technische Universität Darmstadt, 1999.

Acknowledgements

Experimental physics, especially when organized in collaborations between different institutions, requires teamwork and therefore involves a lot of people. I would like to thank all who have contributed to this work.

First of all, this work would not have been possible without the strong support of Prof. Christian Weinheimer, who offered me a PhD position and the opportunity to work on this interesting and challenging project. He always took the time to discuss problems or to come up with new ideas. His profound knowledge in data and error analysis saved me e.g. from capitulating on the extrapolation of the electron cooler voltage. His lab experience often led to a miraculous disappearance of experimental especially electrical hitches. He also helped me personally a great deal beyond physics related issues.

I am also very grateful to Prof. Wilfried Nörtershäuser, who gave me the opportunity to join the LIBELLE beamtime and to work on the analysis of the experimental data.

I would like to express my gratitude to Dr. Volker Hannen, who is coordinating the collaboration activities with GSI and with whom I therefore worked very closely over the last years. Especially during the starting time he supported me a lot with the lab work and helped me figure out problems when I couldn't see the wood for the trees. I also learned a lot from his experience in programming and data analysis. I would also like to thank him for some guitar lessons during the rehearsals of the institute band and for joining me at weekends in the lab or to help me sort out final analysis difficulties.

I further like to thank the non-physicist members of the institute, the technicians and the members of the electronics and mechanical workshops for their help and support. I especially like to thank Daniel Bonaventura, who did the construction of the APD detector setup for the SpecTrap experiment, Bodo Kolipost, who designed and built the NIM control module for the latter setup and Wladimir Buglak, who helped me a lot concerning preamplifier issues.

I also thank all my colleagues, who worked with me on the project through the years. Here in Münster these are namely Daniel Hampf, who started the whole APD characterization business, Denis Anielski, Rubén Lopéz Coto and especially Jonas Vollbrecht, whom I wish all the best for the continuing of the detector development. From the people at GSI I would like to thank, besides the whole LIBELLE and SpecTrap crew, especially Matthias Lochmann, Zoran Andelkovic, Radu Cazan, Christopher Geppert, Rodolfo Sánchez, and Manuel Vogel. Furthermore I would like to thank all the other people of the AG Weinheimer and the nuclear physics institute for the friendly and productive working atmosphere, fruitful conversations and distracting institute parties.

I also like to thank Silvia Beara and Jonas Vollbrecht for proofreading this work.

Des weiteren möchte ich meinen Eltern für ihre Unterstützung während meines gesamten Studiums danken, ohne die ich nicht soweit gekommen wäre. Bei dir, lieber Elias, möchte ich mich dafür entschuldigen, dass ich, besonders kurz vor der Abgabe dieser Arbeit, oft wenig Zeit für dich hatte. Zum Schluss, liebe Margarete, möchte ich dir danken, für deine Geduld mit mir in den Jahren und für deine Unterstützung. Ich weiß, was du aufgegeben und auf dich genommen hast um mir diese Arbeit zu ermöglichen.

